EVANGELOS RIGAS

Dual Beam Swept Source Optical Coherence Tomography for Microfluidic Velocity Measurements

School of Aerospace, Transport and Manufacturing
Centre for Engineering Photonics

OCT for 2D and 3D Velocity Measurement in Microfluidic Flows

PhD
Academic Year: 2017–2018

Supervisors: Dr. H. D. Ford
Prof. R. P. Tatam

November 2018

School of Aerospace, Transport and Manufacturing
Centre for Engineering Photonics

OCT for 2D and 3D Velocity Measurement in Microfluidic Flows

PhD

Academic Year: 2017–2018

EVANGELOS RIGAS

Dual Beam Swept Source Optical Coherence Tomography for Microfluidic Velocity Measurements

Supervisors: Dr. H. D. Ford
Prof. R. P. Tatam

November 2018

Abstract

Microfluidic flows are an increasing area of interest used for “lab-on-a-chip” bio-analytical techniques, drug discovery, and chemical processing. This requires optical, non-invasive flow-visualization techniques for characterising microfluidic flows. Optical Coherence Tomography (OCT) systems can provide three-dimensional imaging through reasonably-opaque materials with micrometre resolution, coupled to a single optical axis point using optical fibre cables. Developed for imaging the human eye, OCT has been used for the detection of skin cancers and endoscopically in the human body. Industrial applications are growing in popularity including for the monitoring of bond-curing in aerospace, for production-line non-destructive-testing, and for medical device manufacturing and drug encapsulation monitoring.

A dual beam Optical Coherence Tomography system has been developed capable of simultaneously imaging microfluidic channel structures, and tracking particles seeded into the flow to measure high velocity flows, using only a single optical access point. This is achieved via a dual optical fibre bundle for light delivery to the sample and a custom high-speed dual channel OCT instrument using an akinetic sweep wavelength laser. The system has 10 µm resolution in air and a sweeping rate of 96 kHz. This OCT system was used to monitor microfluidic flows in 800 µm deep test chips and Poiseuille flows were observed.

Acknowledgements

I thank my family and friends for their encouragement and for supporting me on every step I made.

I would like to thank my supervisors Helen Ford and Ralph Tatam for their support and guidance throughout the PhD and for providing me with the opportunity to work on this project. Special thanks must go to Helen, as she was by my side whenever I had a work related or even a personal problem. Additionally, I am grateful to Jonathan Hallam and Tom Charrett for their advices and support at various stages of the project. Furthermore, my thanks go to Steve Staines for his help on the fibre bundles and the OCT instrument and to Matthew Partridge for the preparation of the colloidal suspensions. Also, I would like to thank Thomas Kissinger for kindly giving me his FPGA board and expertise on the subject. Moreover, I thank Daniel Francis for helping with the pictures presented in this thesis. I would also like to thank my fellow PhD students, James Barrington, Nicolas Davis, Antonio Rendon Romero, Alex Tothill as well as the newcomers, James Bremner, Sam Gibson, and Kieran Wiseman for making the lab environment enjoyable. Finally, I thank everyone at Engineering Photonics for providing a great working experience.

I gratefully acknowledge funding during this PhD project from the Centre for Engineering Photonics and from the Engineering and Physical Sciences Research Council (EPSRC) UK, via grant EP/L014637/1.

Table of Contents

List of Figures

List of Tables

Special Terms

n-tuple frame The combination of overlapped B-scan frames from all the light beams for a given B-scan frame capture at time t.

A-scan The Amplitude plot of the z-depth in a sample for a single point along the scanning axis.

B-scan Represents the cross-section of a sample. It is acquired by scanning a light beam across the body of a sample while acquiring the reflected spectra for each position along the scanning path.

Beam A ray of light used to generate a 2-dimensional light sheet that is scanned across the sample.

Beam offset The distance ΔS between the two beams of a Fibre pair.

Beam separation The distance ΔS between the two beams of a Fibre pair.

Burst B-scan rate This B-scan rate applies only to the 2-component high velocity tracking technique and is related to the time between B-scans of different beams.

Dual beam A pair of light beams separated by distance D_{beam}.

Dual frame The combination of B-scan frames from both light beams for a given time t.

Fibre bundle An optical fibre cable, also known as fibre optic cable, is an assembly similar to an electrical cable, but containing one or more optical fibers that are used to carry light.

Fibre pair A fibre ferrule for multi-mode fibres, that contains a pair of bare single-mode fibres secured in place with epoxy.

Frame A 2-dimensional image representing the cross-section of the sample. It is also known as a B-scan.

Light plane A light sheet generated by a light beam that is scanned across a sample.

Polysorbate 20 Polysorbate 20 is known commercially as Tween 20 and is commonly used as a detergent and emulsifier in a number of domestic, scientific, and pharmacological applications.

List of Acronyms

Notation	Description	Page List
µPIV	micro-Particle Image Velocimetry	1, 2, 9, 10, 22, 76, 137
ADC	Analogue-to-Digital Converter	72, 117
CCD	Charge-Coupled Device	9, 10, 14, 20, 93, 124
CMOS	Complementary Metal-Oxide Semiconductor	20
DAC	Digital-to-Analogue Converter	105, 110, 170
DAQ	Data Acquisition card	63, 73, 95, 96, 116, 117, 119
DBR	Distributed Bragg Reflector	26, 30, 31
DDM	Differential Dynamic Microscopy	8
DFB	Distributed Feedback Bragg	23, 31
DFT	Discrete Fourier Transform	39, 44, 181
DIHM	Digital In-line Holographic Microscopy	8
DIV	Data Invalid Vector	47, 170
DTFT	Discrete-Time Fourier Transform	38, 39, 181
DVV	Data Valid Vector	34, 47, 48, 96, 119, 121, 143
ENOB	Effective Number of Bits	73
FD-OCT	Fourier Domain Optical Coherence Tomography	13, 19, 20
FDML	Fourier Domain Mode Locking	23–25, 76
FFT	Fast Fourier Transform	36, 39, 44, 96, 119, 122, 143, 145, 147, 181
FPGA	Field-programmable Gate Array	105, 113, 170

Notation	Description	Page List
FWHM	Full Width at Half-Maximum	29
HDF	Hierarchical Data Format	121, 170
ILP	In-Line Polariser	127
IPA	Isopropyl Alcohol	91
LDV	Laser Doppler Velocimetry	8, 11, 22, 137
LSV	Laser Speckle Velocimetry	8
MEMS	Micro-Electro-Mechanical Systems	23, 28
NA	Numerical Aperture	56–58, 62, 63, 68, 87, 98
NEP	Noise-equivalent Power	100, 101
OCM	Optical Coherence Microscopy	58, 63
OCT	Optical Coherence Tomography	2–6, 12–14, 16, 17, 20–23, 51, 52, 60, 61, 63, 67, 72, 75, 76, 86, 89, 110, 116, 121, 123, 131, 132, 134, 137, 141, 142, 144, 152, 158, 167, 169
ODT	Optical Doppler Tomography	13, 22
OPD	Optical Path Difference	13, 38, 43
PBS	Phosphate Buffered Saline	140
PIV	Particle Image Velocimetry	1, 3, 8, 9, 137, 168, 172
PM	Polarisation Maintaining	127
PMMA	Poly(Methyl Methacrylate)	5, 133, 142
PNR	Peak to Noise Ratio	38, 44, 45
PSC	Polarisation State Controller	102, 126
PSD	Power Spectral Density	42, 46
PSF	Point Spread Function	29, 36, 38, 44, 45, 97
PSR	Peak to Side-lobe Ratio	38, 44, 45

Notation	Description	Page List
PTV	Particle Tracking Velocimetry	10, 167, 172
RIN	Relative Intensity Noise	46, 71
SD-OCT	Spectral Domain Optical Coherence Tomography	14, 17, 19, 21, 29, 44
SNR	Signal to Noise Ratio	30, 38, 47, 48, 52, 72, 94, 96, 97, 169, 171
SOA	Semiconductor Optical Amplifier	23
SQNR	Signal-to-Quantization-Noise Ratio	72
SS-OCT	Swept Source Optical Coherence Tomography	3–6, 14, 19, 21, 24, 28, 37, 44, 51–53, 64, 67–69, 73, 80, 86, 167, 169, 171
SSE	Sum of Squared Errors of prediction	97
TD-OCT	Time Domain Optical Coherence Tomography	13–15
VCSEL	Vertical-Cavity Surface Emitting Laser	21, 23, 24, 76
VT-DBR	Vernier-Tuned Distributed Bragg Reflector	28

List of Symbols

Sign	Description	Unit	Page List
k_B	Boltzmann's constant	J/K	70
c	Speed of light in vacuum	m/s	29
q	Elementary charge of an electron	C	70
$\hbar$	Planck's constant	$\mathrm{m}^2 \cdot \mathrm{kg/s}$	72
n	Index of refraction		28, 35, 57, 62
ΔS	Beam separation	µm	76–80, 84–86
ΔT	Time difference between sub-frames	s	77, 78, 83, 84
W	B-scan image width	pixel	65, 66, 73, 75, 78, 79, 83
z_coh	Instantaneous coherence length	s	30
t_coh	Coherence time	s	29
b	Confocal parameter	m	56, 60, 62
f	Focal length	m	56, 57, 61, 62, 123
w	Gaussian beam spot size	m	58
w_0	Gaussian beam waist radius	m	58–61
z	Nominal path length difference	m	35
ϕ	Phase	rad	54, 55
$\Delta\phi$	Phase difference	rad	54
δz	OCT Axial (Depth) resolution	µm	30, 67
δx	OCT Transverse (Lateral) resolution	µm	61, 62, 67, 80, 84, 123
z_R	Rayleigh range	m	58, 61, 62
f_Ascan	Laser sweep frequency	Hz	64–66, 75, 77, 79

Sign	Description	Unit	Page List
f_{Bscan}	B-scan sweep frequency	Hz	65, 84
T_{Bscan}	B-scan period	s	78
Θ_{div}	Total angular spread	rad	59, 61
θ_{div}	Half-divergence angle	rad	57, 59, 62
δt	Time step between frames	s	153
ρ	Volumetric mass density	$\mathrm{kg/m^3}$	135
η	Dynamic viscosity of the fluid	$\mathrm{Pa \cdot s}$	156
t_{V}	Particle response time	s	136
G	Pressure gradient	Pa	156
Re_{r}	Relative Reynolds number		135
St_{V}	Stokes number		136
A	Channel surface area	$\mathrm{m^2}$	160
υ	Flow average velocity	m/s	160
$\Delta\upsilon$	Instantaneous velocity	m/s	155
$u(y)$	Velocity distribution	mm/s	156
Q	Volume flow rate	µl/min	156, 160
Θ	Galvanometer optical scan angle	rad	116
$\langle \Delta i^2_{\mathrm{ex}} \rangle$	Excess photon noise	W	70
$\langle \Delta i^2_{\mathrm{sh,opt}} \rangle$	Optical shot noise	$\mathrm{C \cdot A \cdot Hz}$	70
$\langle \Delta i^2_{\mathrm{th}} \rangle$	Thermal noise	W	69
I	Scanned distance on the sample surface	m	116
t_{avg}	Averaging time	s	101
BW	Measurement bandwidth	Hz	101
λ_0	Centre wavelength	m	30, 35
$\langle I \rangle$	DC current of photodetector	A	70
λ	Optical wavelegth	m	28, 59
Δf	Bandwidth of noise	Hz	70
$\Delta\nu$	Optical bandwidth	Hz	70
P_{min}	Minimum detected optical power	W	101
T	Absolute temperature of resistor	K	70

Dedicated to my supervisor Helen D. Ford

Chapter 1

Introduction

1.1 Motivation

Over the last two decades, the interest in flows at the sub-millimetre scale has grown swiftly. Until now, the industry was mainly focused on ink-jet printing technology, but nowadays the emphasis is shifting to new areas of application, including artificial organs [1], miniaturized fuel cells [2], heat-exchangers for electronic devices [3], and recently "lab-on-chip" bio-analytical techniques [4]. For these applications the channel dimensions vary from a few mm to a few µm and with flow velocities ranging from a few mm/s to as slow as tens of µm/s. In µm-scale channels, inter-facial phenomena have a greater impact upon the flow when compared to macroscopic flow theory and experimental methods are needed to support the theoretical models.

In macroscopic flows, the measurement of the velocity components is achieved either by physical flow-measurement probes that interact partially with the flow but without significantly altering the result or by using non-intrusive techniques such as Doppler and Particle Image Velocimetry (PIV). For microscopic flows, the former techniques are not achievable, mostly due to miniaturization issues and is rather unfavourable, as at these scales a device that interacts with the flow alters the characteristics of the flow being measured. Along with the development of microfluidic devices, an initiative has taken place to introduce an optical, non-invasive solution to measure the flow. One technique that stands out, mostly because of its multi-velocity-component capability and the sub-µm spatial resolution, is micro-Particle Image Velocimetry (µPIV).

As the channel size decreases to hundreds of microns, several difficulties arise. In macroscopic PIV, a laser light sheet defines the measurement plane. In microfluidic channels, this sheet has to be only a few microns thick to maintain good spatial resolutions. For 3D µPIV measurements, off-axis viewing is necessary, but in this

case, multiple access ports are needed. Additionally, the diameters of scattering particles must be in the range of few µm down to a few hundred nm, for correct flow tracking. Such problems can be overcome with background noise rejection via confocal microscopy along with fluorescent particles. However, the use of such particles, places restrictions on the illumination wavelength, reducing the technique's flexibility.

Alternatively, a novel approach is to utilize Optical Coherence Tomography (OCT) instead of confocal fluorescence µPIV, as OCT demonstrates high background rejection due to the short coherence length of the laser source being employed. Additionally, the OCT signal incorporates the Doppler shift information, which has already been used for single-component flow measurement. The main drawback of this method is the acquisition rate of A-scans, which is limited to a few 10s of kHz. With recent advancements in acquisition technology that rate has gone over 100 kHz [5], but in that case the signal-to-noise ratio (SNR) drops significantly [6].

In summary, the use of OCT for flow measurement offers the following advantages. OCT has the potential to enable three-dimensional flow velocity measurements, using a single access port. Optical Coherence Tomography (OCT) offers high-resolution imaging of the wall structure, while capturing the velocity information at the same time. Additionally, OCT has a high background rejection, as well as high SNR without requiring any fluorescent particles; and at the operating wavelength of OCT, most of the microfluidic devices that are based in silica appear transparent, thus allowing the measurement in such devices.

1.2 Objectives

The core objectives of this project, in order of importance, can be summarized as follows:

- Achieve 2D and 3D flow measurement of a microfluidic channel, while requiring a single-port optical access, i.e. the sample is imaged from a single side.
- Improve the acquisition speed of the system utilizing novel image multiplexing techniques.
- Put the finished OCT systems under test, using a range of laboratory test flows.
- Acquire a series of test flows, and calculate the flow profiles with the use of particle tracking techniques.

1.3 Contents of the Thesis

This thesis starts with a detailed review of optical techniques for microfluidic velocity measurements as well as advancements in OCT imaging speed and previous applications of OCT in microfluidics. The first chapter (Chapter 2) contains the overview of optical techniques used for microfluidic measurements. Then it reviews previous work done in this area using PIV. Furthermore, as the main subject of this thesis is the application of OCT in microfluidic measurements, a review on the advancements in OCT imaging speed and previous work in microfluidics is presented.

In Chapter 3, the akinetic all-semiconductor laser is reviewed, as this is the laser source used in this work, while the end of the chapter the performance of an akinetic laser is discussed followed by experimental results. The next chapter (Chapter 4), starts with the necessary theory behind a single beam Swept Source Optical Coherence Tomography (SS-OCT) system and highlights all the physical aspects for these systems such as system resolution, depth of field, noise, etc. Optical coherence tomography is one of a class of optical tomographic techniques. The principle of OCT is low coherence interferometry where electromagnetic waves are superimposed causing the phenomenon of interference in order to extract information. A typical OCT system consists of a Michelson interferometer with a low-coherence broadband light source. The light of the laser is split by a beam-splitter into a reference and a sample beam. The reflected light from both the reference and the sample is recombined at the photodetector and interference fringes are produced. To extract the depth information the interferometric signal is Fourier transformed, with the amplitude approximately proportional to the difference in refractive index inside the sample.

A typical fibre-optic SS-OCT system consists of a swept wavelength laser, a coupler (beam-splitter), polarisation state controllers, a photodetector, and a galvanometer. Such a system can be seen in Figure 1.1. A pair of mirrors mounted on a galvanometer is used to scan the sample beam across the surface of the sample for the generation of a cross-sectional image; the depth information from the interferometer is one-dimensional.

As it will be discussed later in Chapter 4, there are different modes of operation for a multiple beam system depending on the number and orientation of the sample beams. With single beam systems the acquisition of the OCT image is dependent on the sweep frequency of the laser. To increase the acquisition speed, without changing the laser parameters, multiple beams are introduced, each dedicated to a sub-region of the final OCT image. Figure 1.2 shows the difference between a single and triple beam system. The latter, requires less time for the acquisition of an OCT image with the same dimensions as the former. The final sections detail how a multiple beam system can be used for particle tracking velocimetry.

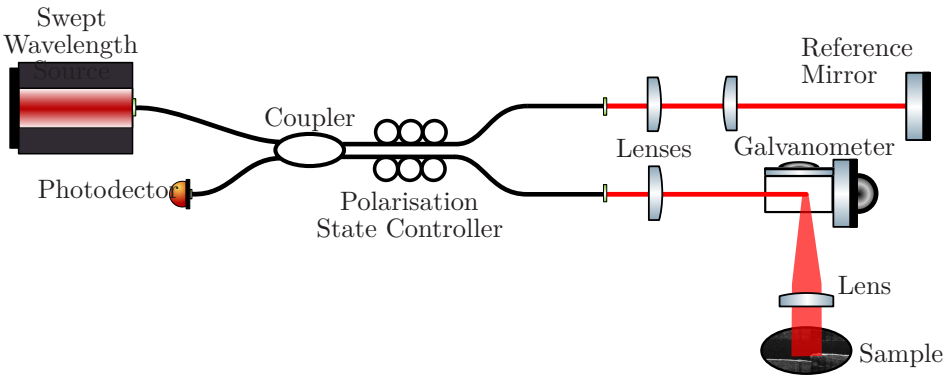

Figure 1.1: *Schematic diagram of a typical Swept Source Optical Coherence Tomography system.*

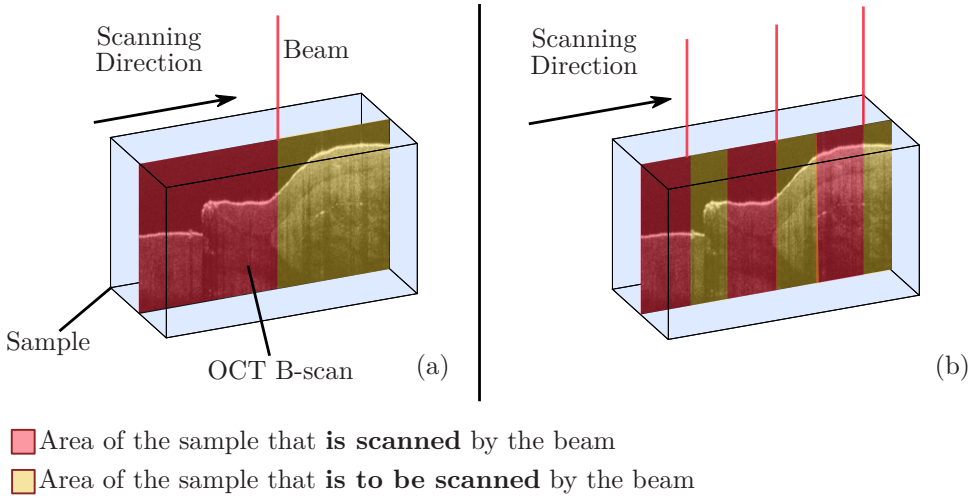

Figure 1.2: *In (a), the scanning procedure of a single beam OCT. Whereas in (b), a system with three beams is shown—it requires $^1/_3$ of the time.*

Chapter 5 discusses the design of a dual beam SS-OCT system using fibre-optic components. The design principles are detailed and the process of implementing such a system is shown. Polarisation effects induced by the fibre are introduced and the steps to resolve the issues are discussed. This is followed by a different interferometer design that solves the polarisation issues and its implementation is discussed. Additionally, for this implementation there was an effort to integrate the design into a prototype instrument. Finally, this chapter concludes with the measurement of the beam waists to determine the lateral resolution of the setup.

Chapter 6 is the final experimental chapter where the implemented dual beam OCT system is used for the measurement of particle velocities in microfluidic chambers. Typically, these chambers are from hundreds down to tens of microns deep. As an example, the schematic diagram of a microfluidic chamber chip that was used for

the velocity measurements can be seen in Figure 1.3. The chip has a 800 µm deep rhombic chamber with dual inputs/outputs. It is primarily used for the mixing of biological substances.

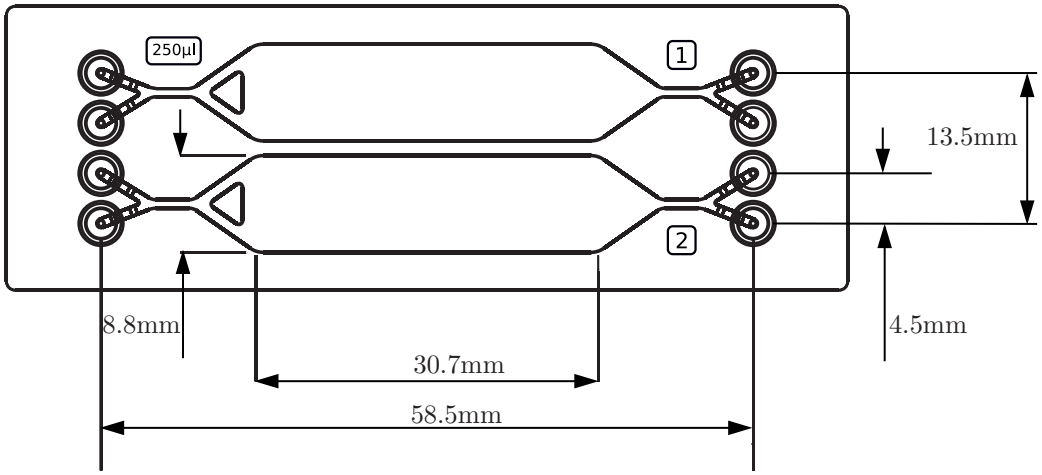

Figure 1.3: *Top view of Poly(Methyl Methacrylate) (PMMA) Rhombic Chamber Chip with 250 µl chamber. This microfluidic chip has two channels that are 800 µm deep. The length and width of each channel is 30.7 mm and 8.8 mm respectively. The lid thickness is 175 µm.*

At the beginning of the chapter, the procedure of producing a colloidal suspension with latex particles is detailed along with the specifications of the microfluidic equipment that was used for the experiments. Later, the algorithm behind the particle tracking is described for both single beam and dual beam systems. Then, the resulting velocity profiles calculated using the particle tracking algorithm are presented. Such a profile can be seen in Figure 1.4, where the recorded particle velocities, shown as blue dots, are used to calculate the polynomial fit—solid line–that corresponds to the Poiseuille flow profile for a microfluidic chamber chip with a square cross-section. The shaded region around the fit corresponds to the 95% confidence interval. Furthermore, the application of the dual beam OCT system for the analysis of flow rate fluctuation induced by a syringe pump is shown.

Finally, Chapter 7 concludes with a summary of what has been accomplished by the work presented in this thesis along with the experimental results. Also, future applications of this work and specifically of the dual beam SS-OCT system are discussed.

Summarising, in this thesis the individual chapters cover the following areas:

Chapter 2 reviews available optical techniques used for microfluidic velocity measurements and focuses on Optical Coherence Tomography as an alternative.

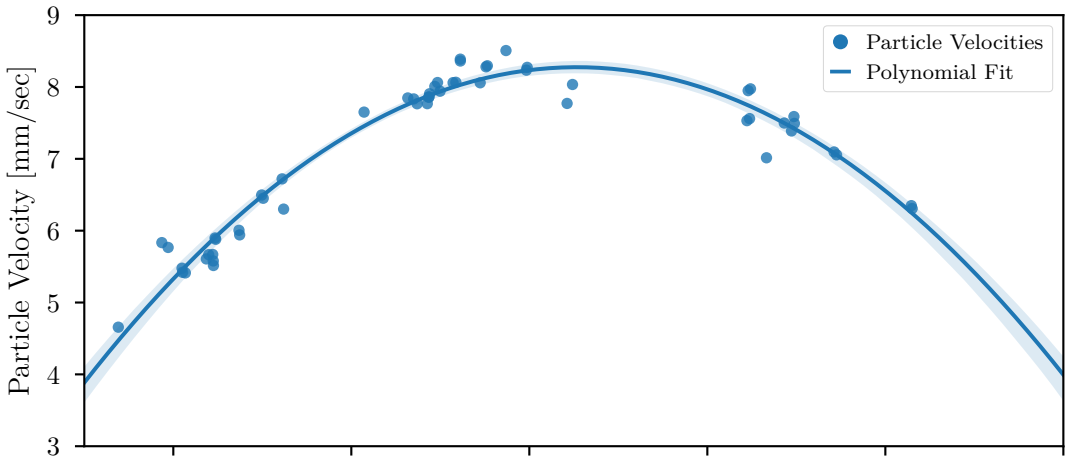

Figure 1.4: *Polynomial fit of the recorded particle velocities for the Poiseuille flow profile of a microfluidic chip with square cross-section. The shaded region corresponds to the 95% confidence interval.*

Chapter 3 discusses the development of akinetic swept source lasers and how they can improve the imaging speed and image quality of Optical Coherence Tomography systems.

Chapter 4 details the relevant single beam Swept Source Optical Coherence Tomography (SS-OCT) theory, the multiple beam configurations, and explains the concepts of optical resolutions and imaging speed improvements for each configuration.

Chapter 5 presents two dual beam SS-OCT systems, from their design to the implementation along with the problems that occurred throughout the development and how these problems were resolved.

Chapter 6 describes the process of using the implemented dual beam OCT system to capture a series of measurements using a test microfluidic setup. Then, details the principles of a particle tracking algorithm, that is used on the measurements to detect the particle positions through a series of frames, in order to extract the velocity profiles of the microfluidic channels. Finally, an experimental demonstration of the effects of flow pressure fluctuation induced by a syringe pump are presented.

Chapter 7 concludes this thesis by summarising the results and providing an outlook into future applications for the proposed system.

Chapter 2

Review of Optical Techniques for Microfluidic Flow Measurements

2.1 Microfluidic Applications

The knowledge of how a fluid flows and behaves in channels with dimensions of tens of micrometres—microfluidics—has evolved as a distinct field of study. In microfluidics, miniature devices are used to perform complex processes such as mixing, separating, and transporting biological substances and chemical samples. Flow characterization is required to maximize the efficiency and optimize the design of those devices. Key application areas include, but not limited to:

Open microfluidics In open microfluidics, at least one boundary of the system is removed, exposing the fluid to air or another interface (i.e. liquid) [7–9]. Applications of open microfluidics include open-channel microfluidics, rail-based, paper-based, and thread-based microfluidics [10–12].

Continuous-flow microfluidics This technology is based on the manipulation of continuous liquid flow through micro-fabricated channels. The liquid flow is induced by external pressure sources such as external mechanical pumps, integrated mechanical micro-pumps, or by combinations of capillary forces and electro-kinetic mechanisms [13].

Digital microfluidics Alternatives to closed-channel continuous-flow systems; discrete, independently controllable droplets are manipulated on a substrate using electro-wetting. As an analogy to digital microelectronics, this approach is referred to as digital microfluidics. An example application used electro-capillary forces to move droplets on a digital track [14].

Paper-based microfluidics Paper-based microfluidic devices are an alternative

for portable, cheap, and user-friendly medical diagnostic systems [12]. Applications of paper-based microfluidics include portable glucose detection [15] and environmental testing [16].

Cellular biophysics By rectifying the motion of individual swimming bacteria [17], microfluidic structures can be used to extract mechanical motion from a population of motile bacterial cells [18]. Thus, bacteria-powered rotors can be built [19,20].

Optics The combination of microfluidics and optics is known as optofluidics. Examples of optofluidic devices are tunable micro-lens arrays [21,22].

Acoustic droplet ejection (ADE) Acoustic droplet ejection uses a pulse of ultrasound to move low volumes of fluids—typically nanoliters [23] or picoliters [24]—without any physical contact. ADE technology has been used for the transfer of proteins [25], high molecular weight DNA and live cells [26] without damage or loss of viability.

Fuel cells Microfluidic fuel cells use laminar flow to separate the fuel and its oxidant to control the interaction of the two fluids without a physical barrier as would be required in conventional fuel cells [27,28].

2.2 Flow Measurements Techniques

Due to the small dimensions and complex geometries, analytical models to predict the properties of the flow of complex fluids are insufficient. Additionally, the materials used to manufacture microfluidic channels alter the surface tension and roughness, changing the properties of the flow. Many techniques have been used in the past to analyse the actual flow of microfluidic devices.

Through the years, much effort has been put to invent non-invasive technologies for velocity measurements in flow channels. The most common techniques are Particle Image Velocimetry (PIV) and Laser Doppler Velocimetry (LDV). Other lesser-known techniques are Differential Dynamic Microscopy (DDM), Digital In-line Holographic Microscopy (DIHM), and Laser Speckle Velocimetry (LSV) [29–31].

2.2.1 Flow Measurements with µPIV

In Particle Image Velocimetry (PIV), the fluid is seeded with small particles that are assumed to follow the fluid dynamics. Under normal light conditions these particles are invisible; for the measurement the fluid is illuminated so that the tracer particles become visible. Then, using a camera the motion of the particles is recorded and used

for the calculation of the velocity field (speed and direction) of the flow under test. Typically, PIV apparatus consists of a Charge-Coupled Device (CCD) camera, a laser with a cylindrical lens that converts the light beam to a light sheet in order to limit the physical region illuminated, a synchronizer to act as an external trigger for control of the camera and laser, the seeding particles, and the fluid under investigation.

For micrfofluidics, a variation of PIV known as micro-Particle Image Velocimetry (µPIV) is used. However, in µPIV, the system (Figure 2.1) is based around an epifluorescent or epifluorescence illumination microscope; it uses the fluorescence of the specimen in an arrangement of optical components that permits illumination from above the specimen. Additionally, the light that is absorbed by the fluorescent dye is emitted at a longer wavelength, which makes it possible to distinguish tracer particles from other objects (e.g. interfaces).

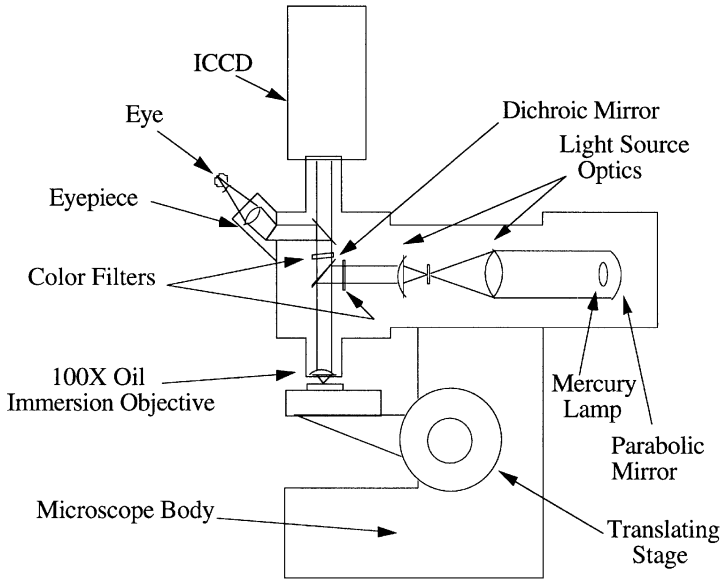

Reprinted by permission from Springer Nature: Springer, A particle image velocimetry system for microfluidics, J. G. Santiago, S. T. Wereley, C. D. Meinhart et al (1998)

Figure 2.1: *Schematic of the micro-PIV recording system using: an epifluorescent microscope, a high numerical aperture lens, a continuous-illumination mercury arc lamp, and an intensified/cooled CCD camera.*

Fluorescing particles that excite at a specific wavelength and emit at another are injected inside the microfluidic channel. The light emitted by the light source is reflected through a dichroic mirror, travels through an objective lens that focuses on the point of interest, illuminating the device and "charging" the particles. The emission from the particles, along with reflected light travels back though the objective, the dichroic filter and through a colour filter that blocks the reflected light allowing

only the light from the particles to reach the CCD camera. Utilizing the ability of objective lens to focus on one plane at a time, thus creating a 2-dimensional plane, µPIV is able through autocorrelation and cross-correlation techniques to measure the velocity vectors and determine the velocity of the flow.

Using this µPIV technique, the spatial resolution and the accuracy of the fluid velocity measurements is limited by the diffraction limit of the recording optics, noise in the particle-image field, the interaction of the fluid with the finite-sized seed particles, and Brownian motion [32]. µPIV is capable of high-resolution imaging [33,34]; the spatial resolution was typically below 2 µm. Some applications of µPIV include but are not limited to three-dimensional measurements and visualization of internal flow of a moving droplet [35], high-speed measurements of transient flow in microfluidic devices [36], and velocity measurements of red blood cells and plasma of *in vitro* blood flow [37].

2.2.2 Flow Measurements with PTV

Particle Tracking Velocimetry (PTV) as the name suggests is a velocity measurement technique where individual particles are tracked. PTV can be used for both two- and three-component particle tracking. In two-dimensional (2D) PTV, the flow field is measured in a two-dimensional slice of the flow (using a camera), usually illuminated by a laser sheet and tracer particles are tracked individually for several frames to determine the flow profile. Similarly, in three-dimensional (3D) PTV, multiple cameras are used to record a three-dimensional volume. The illuminated space in 3D-PTV is a thick light slab rather than a thin light sheet and is determined by the thickness of the illuminated spaced, by the field of view and by the depth of focus of the cameras. The tracking of particles in three-dimensional space is achieved using photogrammetric techniques [38].

One of the difference between PTV and PIV is that PTV depends on Lagrangian measurement principle, which each seeded particle could be followed through the time. Whereas PIV, is based on Eulerian measurement principle, which the velocity v is a function of position x and time t. Comparatively, both techniques are able to measure flow velocities under laminar or even turbulent flow regimes [39]. In a comparative study by Alberini et al., PTV can be used acquire average flow fields which are in good agreement with PIV; within a divergence less than 5% [40]. Under this study PTV was used to measure flow fields during the blending of Newtonian and non-Newtonian fluids in a standard baffled cylindrical vessel. The difference in tracer particle size, 10 µm for PIV and 200 µm for PTV, affects the overall resolution of the measurements. For PTV, the scale of measurement is directly connected to the size of particles and calibration target which limits the capability of PTV to determine smaller turbulent scales. However, the size limitation in this case was imposed by

the camera used for PTV. In this thesis, this limitation is eliminated as OCT is used to capture the images for the particle tracking. Specifically, for the experiments presented here 10 µm particles were used which is the same as PIV in Alberini's case. Additionally, traditional PTV requires the same amount of access ports as PIV, i.e two for 2D tracking, one for illumination and one for imaging. However, in the case of PTV using OCT the number of access ports drops to one, even for 3D tracking.

In conclusion, PTV is a valid technique for the measurement of flow fields. When used in laminar or low turbulence flows it can achieve the same accuracy as PIV. With advances in blob tracking algorithms, PTV is less computationally intensive and easier to implement. One of the downsides of PTV is that requires high seeding densities in order to be accurate, especially in turbulent regimes [41]. In that case PIV may be a more appropriate measurement approach.

2.2.3 Flow Measurements with µLDV

Laser Doppler Velocimetry (LDV), also known as laser Doppler anemometry (LDA), is the technique where the Doppler shift of the light scattered from a moving particle in a laser beam is used to measure the velocity of particles in transparent or semitransparent flows. Doppler velocimetry is based on the principle of optical heterodyne detection, for one-component velocity measurement, a pair of coherent beams intersect to form a fringe pattern inside the measurement volume (Figure 2.2). A seed particle passes through the fringe pattern, causes light to backscatter and pulsate. This pulsating light is measured using a photodetector and the frequency of the pulsation along with the fringe spacing is used to compute the particle velocity.

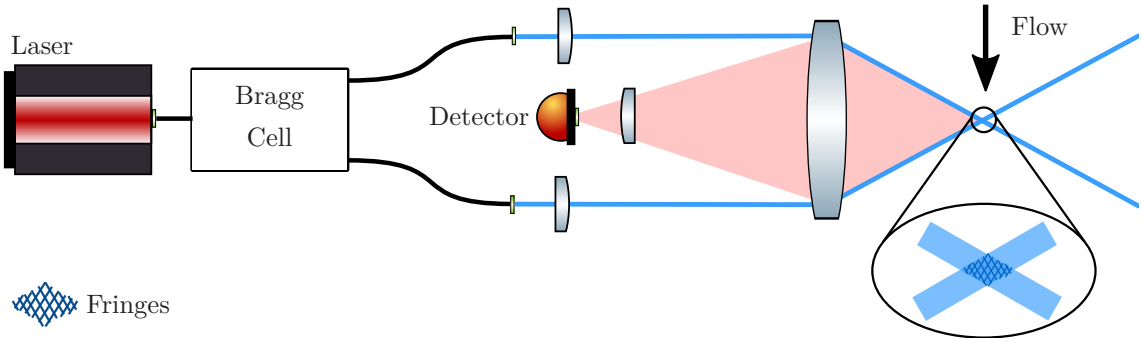

Figure 2.2: *Schematic diagram of optical setup for laser Doppler velocimetry. The cross-hatched region at the interesection of the beams are the intereference fringes.*

LDV has the disadvantage of directional ambiguity; particles moving either forwards or backwards in respect with the flow will produce a pulsating wave with

identical frequencies. To combat this ambiguity however, an accousto-optic modulator (usually a Bragg cell) is used to add a known frequency shift to one of the two beams causing the fringes to move in one direction. In this case, the velocity is calculated by subtracting the modulator frequency from the measured one.

For multiple component velocity measurements, a pair of beams (two beams per probe) is used at a different wavelength for each velocity component. Hence, each beam pair is separated into three colours: e.g. green (514.5 nm), blue (448 nm), and purple (447.5 nm). For each velocity component a different optical access direction is needed, e.g. three probes at top, left, and front of the sample for a three-component velocity measurement. However, when compared to PIV, it requires one less access point for the same amount of velocity components. For one dimensional velocity measurement, PIV requires two different access points—usually orthogonal to each other—one for particle illumination and one for measurement.

Laser Doppler velocimetry has been demonstrated for measurements of microfluidic flows; in 1995, a solid-state laser Doppler anemometer was used for measuring laminar flow in a 175 µm deep channel [42]. In 1999, the flow behaviour of a low-density polyethylene melt was investigated in a specifically developed flow channel [43]. The investigation of the velocity fields was performed in the steady state of flow and the system was reliable for measurements of velocities down to 250 µm/s.

Similarly, measurements of injection nozzle flows have been presented, where instead of a parallel fringe system, diverging and converging fringes are employed. A spatial resolution of 4 µm in the x direction and 16 µm in the y direction have been demonstrated [29]. With spatial resolutions smaller than 10 µm this sensor is suitable for nano- and microfluidics. In the same year (2008), using laser Doppler velocimetry and flow induced birefringence simultaneous measurements of velocity and stress distributions in polyisobutylene were presented [44].

Finally, measurements of flow rate inside a microchannel by using a laser Doppler technique has been presented [45]. Instead of parallel fringe systems, two superposed fan-like fringe systems with opposite gradients were employed to determine the velocity distribution inside the microchannel directly. To discriminate both fringe systems, the sensor utilised a time division multiplexing technique. Interestingly, the spatial resolution of the system was 960 nm. The flow rate measurements presented were in the range of 30 µl/min.

2.3 OCT for Microfluidics

Recent advancements in speed and resolution of Optical Coherence Tomography (OCT) have enabled the use of the technique in microfluidic measurements. Previ-

ously, OCT was used in biomedical applications e.g. skin, eye, etc. Any movement from the patients would cause a degradation on the image, i.e. an involuntary eye movement will cause the OCT image to become blurry. With the recent development of high-speed cameras and high-speed/high-resolution analogue-to-digital converters the sample does not need to be stationary. For flow measurements a variant of optical coherence tomography is used.This variant takes advantage of the Doppler shift in the fringes of the interferometer, thus the technique is known as Optical Doppler Tomography (ODT).

2.3.1 Time Domain and Fourier Domain OCT

There are two main types of OCT, Time Domain Optical Coherence Tomography (TD-OCT) and Fourier Domain Optical Coherence Tomography (FD-OCT). In TD-OCT the path length of the reference arm is varied in time by translating the reference mirror longitudinally as shown in Figure 2.3. The optical setup typically consists of an interferometer, e.g. Michelson, with a low coherence, broad bandwidth light source. The light is split into a reference and sample arm and the reflected light is recombined at the photodetector. Specifically, the two arms will have an Optical Path Difference (OPD) that will result in a proportional phase difference. When the recombined light is captured using a square-law detector, such as a photodiode, the phase difference can be extracted from the measured signal. For the two-beam interference of monochromatic waves the output of the detector will be

$$I = I_1 + I_2 + 2\sqrt{I_1 I_2}\cos\Delta\Phi\,, \tag{2.1}$$

where I is the total irradiance at the detector, I_1 and I_2 the irradiance of each beam and $\Delta\Phi$ the phase difference between the two paths [46]. Depending on the path difference, the temporal coherence of the source, and the polarisation overlap the visibility V of the fringes varies from 0 to 1, thus (2.1) can be rewritten as

$$I = I_1 + I_2 + 2|V(\mathrm{OPD})|\sqrt{I_1 I_2}\cos\Delta\Phi\,, \tag{2.2}$$

where $V(\mathrm{OPD})$ is the visibility of the fringes as a function of optical path difference. In low coherence interferometry, the interference fringes will appear only when the path difference lies within the coherence length of the light source. The main disadvantage of this technique is the scanning mirror which requires a mechanical stage for the translation and leading to low scan rates. A similar technique to TD-OCT substitutes the photodetector for an image sensor allowing the acquisition of images without beam scanning [47,48]. However, the images are not cross-sectional but “en-face” i.e. orthogonal to the light beam of illumination like images of classical microscopy.

In FD-OCT the broadband interference is acquired spectrally resolved either by encoding the optical frequency in time with a spectrally scanning source or with a

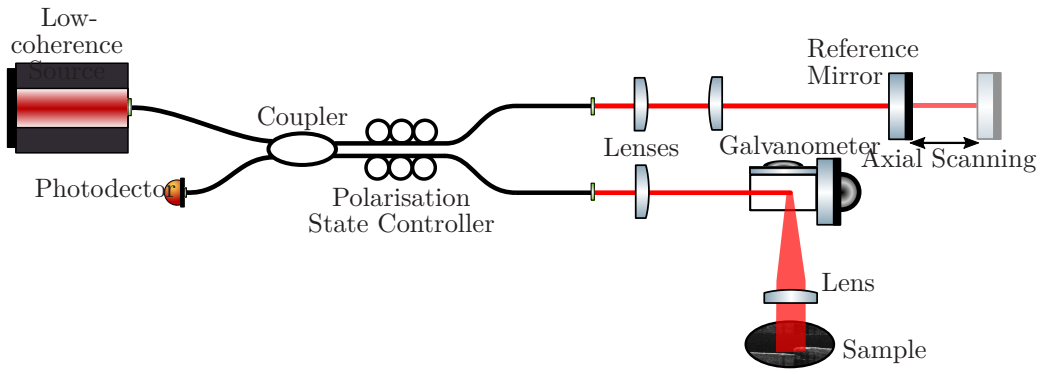

Figure 2.3: *Schematic diagram of the optical setup for Time Domain Optical Coherence Tomography.*

dispersive detector, like a grating and a linear detector array. The former is known as Swept Source Optical Coherence Tomography (SS-OCT), while the latter is known as Spectral Domain Optical Coherence Tomography (SD-OCT). For both techniques, the depth scan can be immediately calculated by a Fourier transform from the acquired spectra, without movement of the reference arm, thus improving imaging speed.

In a typical SD-OCT system the spectral information is extracted by distributing different optical frequencies onto a detector stripe, e.g. line-array CCD, via a dispersive element like a diffraction grating as shown in Figure 2.4. The full depth information is acquired from a single exposure which allows high speed imaging, however the signal to noise ratio is reduced due to the lower dynamic range of stripe detectors with respect to single photosensitive diodes. Additionally, the dispersive elements in the spectroscopic detector usually do not distribute the light equally spaced in frequency on the detector, thus the signal has to be resampled before processing [49].

In SS-OCT, the swept wavelength source is substituted for the low coherence source removing the need for a diffraction grating and camera. Instead a simple photodiode is used simplifying the optical setup (Figure 2.5). However, the problem of scanning is essentially translated from the reference arm (TD-OCT) into the swept wavelength source (SS-OCT).

2.3.2 Optical Doppler Tomography

Optical Doppler Tomography combines Doppler velocimetry with Optical Coherence Tomography to obtain high-resolution tomographic images of static and moving constituents in high scattering media. The principle of operation is that when backscattered light from a moving particle interferes with the reference beam, a shift

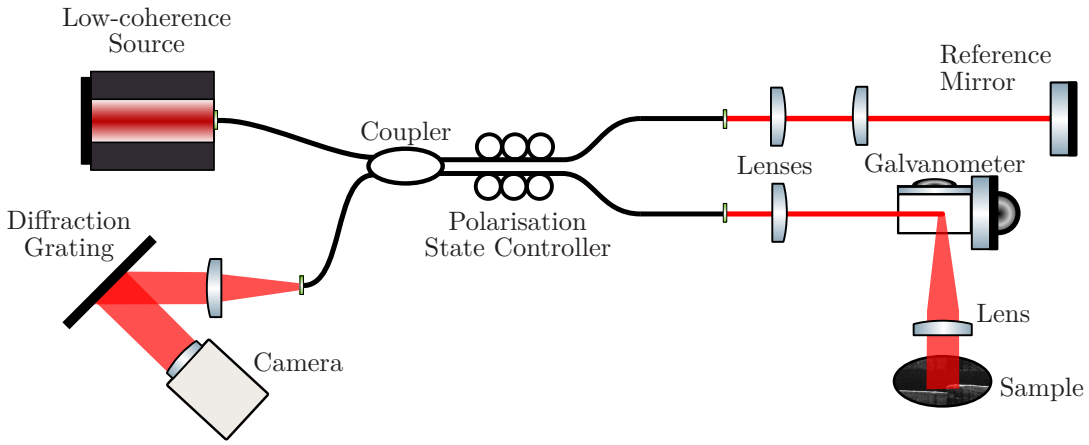

Figure 2.4: *Schematic diagram of a typical Spectral Domain Optical Coherence Tomography system.*

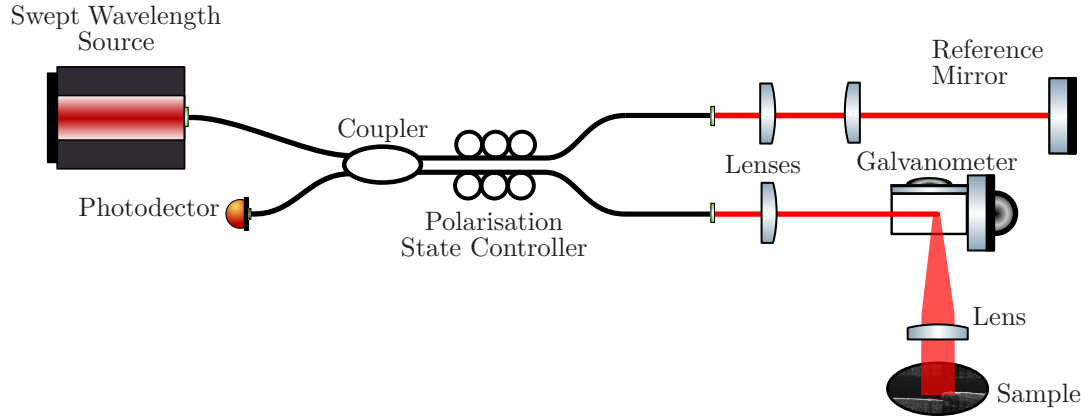

Figure 2.5: *Schematic diagram of a typical Swept Source Optical Coherence Tomography system.*

in frequency f_{D} of the interference fringe intensity from that of the optical phase modulation is made.

$$f_{\mathrm{D}} = \frac{1}{2\pi}(k_{\mathrm{s}} - k_{\mathrm{i}})v\,, \tag{2.3}$$

where k_{i} and k_{s} are wave vectors for incoming and scattered light and v is the velocity vector of the moving particle [50]. The detection of the Doppler frequency shift permits measurements of the particle flow velocity at discrete spatial locations [51,52]. As it can be seen in Figure 2.6 the system is identical to a standard TD-OCT setup with the primary difference lying in the use of a phase modulator and in digital signal processing. The electro-optical phase modulator is introduced to produce a stable carrier frequency. ODT similar to OCT has both a time-domain and Fourier-domain method. In time-domain ODT, a delay line is incorporated in the reference arm to generate a delay and a phase-resolved algorithm is used to determine the

Doppler frequency shift. In the Fourier-domain method, the reference mirror is fixed and the Fourier-domain fringe signal,is obtained either by a spectrometer (SD-ODT) or by a frequency sweeping light source (SS-ODT).

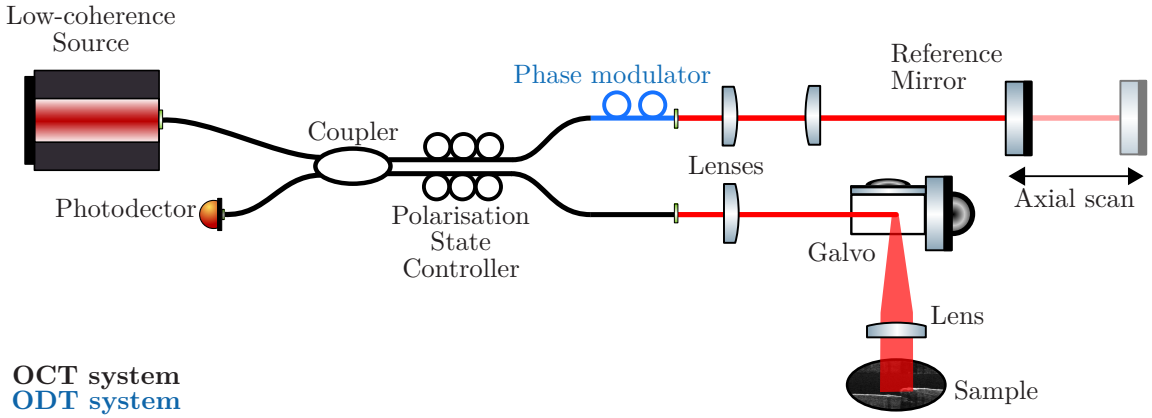

Figure 2.6: *Schematic diagram of the optical setup for Doppler Optical Coherence Tomography. The system is similar to an Time Domain Optical Coherence Tomography system apart from the phase modulator on the reference arm.*

One of the limitations of using Doppler shift to determine the flow is that the technique is only sensitive to longitudinal flow velocity. For quantifying the flow using ODT the flow direction must be known. However, in many biological applications flow direction is not known, thus ODT alone is not enough to fully quantify the flow. A solution to this problem is Doppler variance which can be used to determine the transverse flow [53]. The technique is based on the fact that Doppler OCT imaging uses a relatively high numeric aperture lens (to increase the lateral resolution) in the sample arm. The beam from different sides of the edges will produce different Doppler shifts, f_1 and f_2.

An interesting sub-field of microfluidics concerns the behaviour of blood flow in micro-channels. The flexibility of ODT systems, due to simple setup and component requirements along with the ability to perform *in vivo* measurements, allowed them to become dominant in this area. OCT/ODT systems have demonstrated non-invasive imaging of *in vivo* blood flow dynamics and tissue structures with high spatial resolution (2 µm to 10 µm) in biological systems [54], bidirectional colour Doppler imaging of flow in biological tissues with micrometer-scale resolution [55], *in vivo* blood flow measurements of human hand with high velocity sensitivity [56], cerebral blood flow measurements [57], and localized fluid flow and shear stress measurements within porous scaffolds [58]. Finally, Doppler OCT, has also been used to measure complex flows in microfluidic channels [59–61] and mixing devices [62].

2.3.3 Microfluidic Measurements Using OCT Techniques

Recently, a joint time and spectral domain OCT setup was used to measure the velocity of retinal and choroidal blood flow [63], and monitor the flow in a semitransparent micro-channel device [64]. Furthermore, OCT has been used for quantitatively characterizing the microfluidic-scale flow generated by motile cilia [65]. Motile cilia are cellular organelles that generate directional fluid flow across various epithelial surfaces including the embryonic node and respiratory mucosa. Two-dimensional, two-component flow velocity field characterization using OCT-based particle tracking velocimetry was demonstrated with a maximum recorded velocity of 300 µm/s. The latest application of OCT in microfluidics deals with the measurement of the flow dynamics in a microfluidic chip [66]. This system used a high speed SD-OCT with axial resolution of 1.2 µm in air and acquisition rates in the range of 120 kHz. For the experiments, a 1% intra-lipid suspension was used in 20 µm deep and 50 µm wide microfluidic channels. This recorded a flow rate of 0.63 µl/min (≈10 mm/s), determined from the cross-sectional velocity map; the value of 0.67 µl/min was set on the syringe pump.

Apart from the single beam systems,a multi-beam non-overlapping system was demonstrated in 2010, where an ultra-high speed 1050 nm swept source OCT was used for retinal and anterior segment imaging at 100 000 to 400 000 axial scans per second [67]. The system had a short cavity laser and was able to produce 100 000 axial scans per second. Buffering the laser sweep doubled the axial scans per second for a sweep of 200 kHz. Sweep buffering in SS-OCT is a technique that utilises long spools of fibre—typically hundreds to thousands metres long—to delay and interleave the wavelength sweep [68], usually the interlacing of the sweep is achieved with a 50% beam-splitter as shown in Figure 2.7 (B). The same sweep buffering technique is also applied to Fourier Domain Mode Locking (FDML) lasers increasing the effective sweep rate. Furthermore, to double the sweep frequency again, a second beam was added and allowed 400 000 axial scans per second. The different system configurations can be seen in Figure 2.7.

2.4 Resolution and Speed of OCT

As mentioned in previous sections, the tracer particles can travel with relatively high velocities inside the microfluidic chambers. The velocities can reach tens of millimetres per second, thus in order to capture the light scattered from these particles the optical system must be capable of high speed imaging. Additionally, as the particles become smaller than 15 µm in order to fit in the microfluidic channels with depths approaching a few tens of micrometres, the spatial resolution of the system must be sufficiently small to identify them.

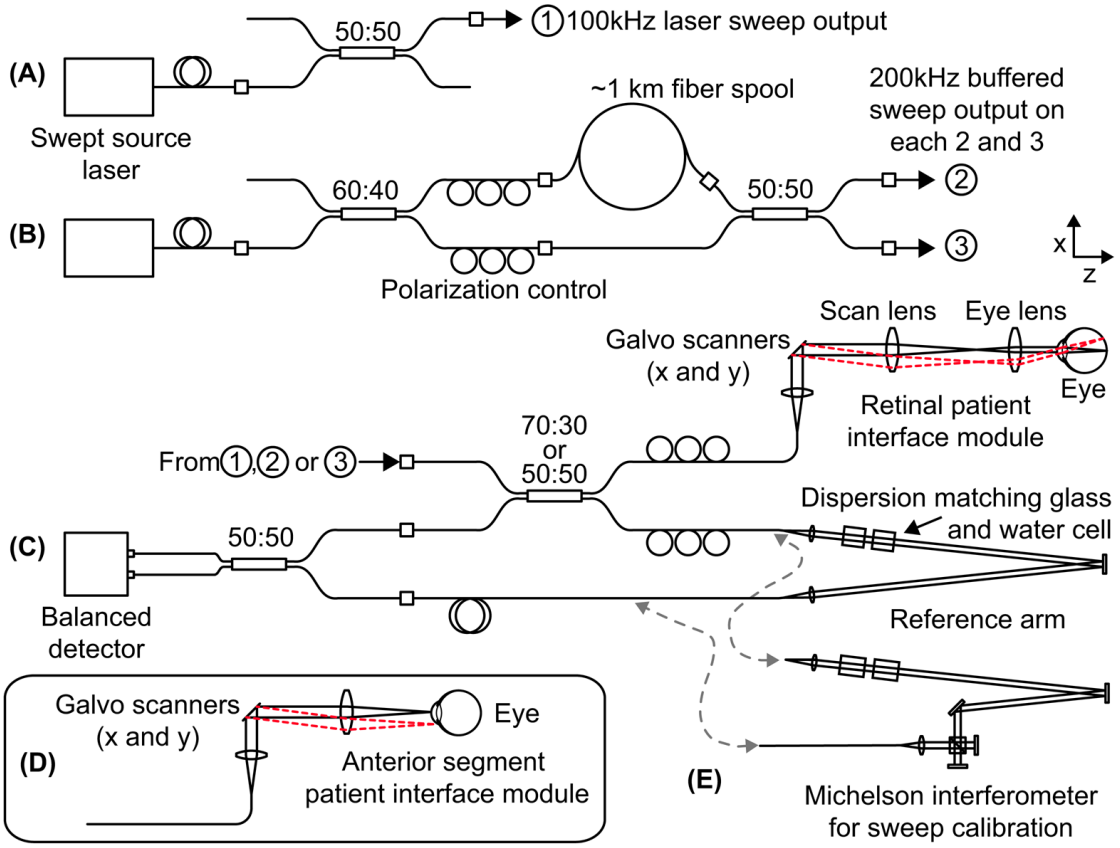

"Ultra-high Speed 1050nm Swept Source / Fourier Domain OCT Retinal and Anterior Segment Imaging at 100,000 to 400,000 Axial Scans Per Second." by Potsaid, Benjamin et al. [67], used under CC BY-NC-SA 3.0.

Figure 2.7: *System layout. (A) Swept laser source for 100 kHz OCT imaging. (B) Swept laser source for 200 kHz and 400 kHz OCT imaging. (C) System configuration for retinal imaging. (D) Patient interface for anterior segment imaging. (E) System configuration for sweep calibration.*

In an OCT system there are five crucial parameters affecting its performance.

- Longitudinal (axial) resolution
- Transverse (lateral) resolution
- Dynamic range
- Measurement speed
- Centre wavelength of the light source

For the last 15 years, considerable efforts have been put into research to increase the

longitudinal resolution of OCT to sub-µm levels, but also to break the measurement speed barrier of the few kHz acquisition rate. The longitudinal resolution is related to the coherence length and is inversely proportional to the optical bandwidth of the laser source. Super-luminescent diodes (SLD) operating around 850 nm with a bandwidth of 30 nm are often used, providing 10 µm to 20 µm axial resolution [69].

Higher resolutions have been achieved by substituting ultra-short pulsed lasers for super-luminescent diodes. In 1999, ≈1 µm resolution has achieved using a 350 nm broad-bandwidth Ti:sapphire femtosecond laser [70]. The use of high-numerical-aperture lenses along with a confocal geometry improves the axial as well as the lateral resolution. This OCT variant is called optical coherence microscopy. Such a system was demonstrated with a microscope based on a Linnik[1] interferometer, and it produced *en-face* images without scanning and with a resolution of 1 µm in the longitudinal direction and 0.5 µm in the transverse [48]. The same year scientists achieved sub-µm resolution using a commercial 10-fs Ti:sapphire laser in combination with a photonic crystal fibre. The emission spectrum ranged from 500 nm to 950 nm, resulting in a lateral resolution of 2.5 µm and an axial resolution of ≈0.75 µm in free-space, that is the equivalent of 0.5 µm in biological tissue [71].

Undoubtedly, ultra-high resolution improves image quality but reduces the signal-to-noise ratio (SNR) as the detection bandwidth increases, when standard time domain detection techniques are employed. Hence, the reduction in imaging speed. However, if Fourier domain techniques are used, while they offer the same resolution, the lack of a moving reference allows the system to operate at higher speeds [5]. Additionally, for a single detector TD-OCT system, the full optical bandwidth reaches a single detector element and interference occurs between electromagnetic fields of the same optical frequency or wavelength. Moreover, the shot noise generated by the power density at one particular wavelength is present at all electronically detected frequencies, and therefore adversely affects the SNR at all other carrier frequencies [72]. By spectrally separating each wavelength in space (SD-OCT) substituting the detector with an array of detectors or in time (SS-OCT) with a single detector, the cross shot noise is eliminated and the SNR is increased [6,73].

There are two methods to construct a Fourier Domain Optical Coherence Tomography (FD-OCT) system: Spectral Domain Optical Coherence Tomography (SD-OCT) and Swept Source Optical Coherence Tomography (SS-OCT). With the former the detection is being performed using a spectrometer with a multichannel analyser. As for the latter a fast tunable laser is being used.

Both systems provide directly the spectral fringe pattern enabling a plethora of novel applications. Spectral domain systems have being used in applications ranging from imaging blood flow using Doppler techniques [56,74,75] to inspecting printed

[1] a bulk Michelson interferometer with microscope objectives in both arms

electronics with sub-micron resolution [76]. Also, the complex Fourier domain signal can be measured directly doubling the axial depth range [77,78]. However, ultra-high resolution OCT imaging requires light of broad spectral bandwidth, therefore dispersion compensation is important in order to achieve ultra-high resolution. The effects of unmatched dispersion up to first order on the OCT signal are modifications such as scaling and delaying of the coherence function by the group velocity. Practically, the first order dispersion effects are minimal if limited to small unmatched path lengths. However, for second and higher order dispersion, OCT signals are substantially distorted; particularly for unmatched path lengths exceeding several millimetres in highly dispersive glasses or away from the minimum dispersion wavelength in optical fibres [79]. In time domain OCT many dispersion compensation techniques have been developed; either analogue, such as matching the materials and path lengths of the interferometer's arms, or digital, using numerical algorithms. The latter scenario has an implication though, as the acquired signal has to be broken down to its frequency components, before numerical compensation can take place. This adds a significant overhead and slows down the systems speed. Alternatively, in Fourier domain OCT the spectral fringe signal is captured directly during acquisition, thus making FD-OCT well suited for numerical dispersion compensation. Experimental demonstrations show that ultra-high resolution spectral domain OCT can provide at least 100x increase in imaging speed when compared to ultra-high resolution time domain OCT. Moreover, numerical dispersion compensation has shown to compensate relatively large dispersion mismatches [80–82].

A natural consequence of the advancements in scan rates was the transition from 2D (cross-sectional images of the sample acquired by scanning the beam in one dimension) to 3D (series of cross-sectional images to represent a volume acquired by scanning the beam in two dimensions) OCT, which can provide additional image information, such as OCT cross-sections, OCT fundus[2] images, and three-dimensional structure representations [83]. The only impediment to achieving higher speeds, in spectral domain OCT, was the Charge-Coupled Device (CCD) cameras, which was being used at the time. The CCD is composed of a photoactive region (capacitor array) and a transmission region that acts like a shift register. An image is projected onto the photoactive region charging the capacitor array proportionally to the light intensity. The control circuit shifts the charge of each element to the next; the last element on the array dumps its charge into a charge amplifier where the charge is converted to voltage and digitised. While CCD line scan cameras offered low noise, high sensitivity, and high dynamic range, the line scan rates were limited to the 10 kHz to 70 kHz range. OCT systems featuring such cameras demonstrated axial scan rates of 16 kHz with 2048 camera pixels [80] and 75 kHz with 512 camera pixels [84].

Meanwhile, the resurgent popularity of Complementary Metal-Oxide Semicon-

[2]The fundus is an area of the interior surface of the eye, which includes the retina, optic disc, macula and fovea, and posterior pole

ductor (CMOS) technology due to recent advancements on integrated circuits, changed the field of imaging sensors. The main advantage of CMOS technology is that it has the potential to achieve faster sustained imaging speeds than CCD technology because it is possible to directly integrate digital communication circuitry, gain stages, A/D converters, and photosensitive pixels on the same chip [85]. Although CMOS technology offers high imaging speed, it generally suffers from low sensitivity and higher noise than CCD [86], reducing its suitability for OCT.

Nonetheless, as the CMOS technology matures, an increasing amount of research systems substitutes CCD with CMOS cameras with astounding results, such as volumetric imaging with axial scan rates ranging from 70 kHz up to 312 kHz with 4096 and 576 camera pixels respectively [87]. This high-speed volumetric imaging enables time resolved measurements of dynamic processes (4D-OCT) [88].

However, swept source OCT systems can achieve similar acquisition speeds only limited by the sweep rate of the laser source. Additionally, swept laser sources are especially important for imaging in the 1.3 µm wavelength range and above, where low cost CCDs are not available. Swept source OCT can be found in a multitude of applications [89,90], but more noticeable is the use in the field of ophthalmic imaging. In ophthalmology OCT is being used to capture the entire anterior of the eye in high axial resolution; providing morphological information of the eye interior (e.g. cornea). A popular swept source technology is the Vertical-Cavity Surface Emitting Laser (VCSEL). It has been used for *in vivo* high speed retinal, anterior segment and full eye imaging. The MEMS[3] tunable VCSEL enables long coherence length—>100 mm have been recorded [91,92], adjustable spectral sweep range and adjustable high sweep rates (50 kHz to 1200 kHz) [92–94].

In summary, time domain OCT techniques struggle to deliver high resolution imaging at high speeds due to the limits of the moving reference arm. Yet, Fourier domain OCT techniques are able to deliver high speed acquisition rates, mostly due to the lack of mechanical movement to change the length of the reference arm and increased signal to noise ratio. Additionally, Fourier domain OCT eases the dispersion compensation using numerical techniques as the spectral fringe pattern is directly available. However, while the axial scan rates of both SD-OCT and SS-OCT are increasing, both faced many difficulties along the way. For SD-OCT the limitations are due to imaging sensor (CCD or CMOS), as for SS-OCT the bottleneck is because of the laser sweeping rate. Yet, the technological advancements led to real-time *in vivo* 3D-OCT setups to be realized.

[3]Micro-Electro-Mechanical systems

2.5 Summary

A brief summary of the most widely-used flow measurement techniques reviewed in Sections 2.2.1, 2.2.3 and 2.3 is given in Table 2.1.

Table 2.1: *Comparison of widely-used optical techniques for flow measurements.* Abbreviations used: (+) Advantages, (−) Disadvantages

Technique	Notes
µPIV	(+) High-resolution imaging (below 2 µm) [33,34] (+) Ultra high-speed imaging (> 1000 fps) [36] (−) For multi-component velocity measurements requires additional optical access port
LDV	(+) Sub-micrometre resolution (960 nm) [45] (−) Particle direction ambiguity
LDV with Bragg cell	(+) Solves direction ambiguity [43] (+) Multi-component velocity measurements [95,96] (−) For multi-component velocity measurements requires additional probe and three different lasers
ODT	(+) High-resolution imaging (2 µm to 10 µm in biological tissue) [54] (−) Requires additional processing for Doppler shift
OCT	(+) High-resolution imaging (0.7 µm in free-space) [71] (+) High-speed imaging (up to 520 kHz) [93,94] (−) Ability of multi-component velocity measurements with single access port

Chapter 3

Akinetic Swept Source for OCT Applications

3.1 Introduction

There are two types of light sources, based on super-luminescent diodes, that are being used in Optical Coherence Tomography (OCT). Broad-wavelength for frequency domain OCT (FD-OCT) and swept-wavelength sources for swept-source OCT (SS-OCT). An ideal swept-wavelength laser for OCT would sweep over a wide wavelength range, be linear in frequency with low relative intensity noise (RIN), low side modes, and high coherence length–all at the highest possible sweep rate supporting the imaging requirements [97].

Throughout the years different approaches have been utilized to build lasers for OCT. Those include ring lasers [98], grating-based Littman–Metcalf [99–102], Micro-Electro-Mechanical Systems (MEMS) [103,104], polygon mirror [73,105] pump with VCSEL combined with a MEMS and an Semiconductor Optical Amplifier (SOA) [91], crystal deflection [106], Fourier Domain Mode Locking (FDML) [107,108], Distributed Feedback Bragg (DFB) arrays [109], and resonant-sine lasers [110–112].

The main limitation of all the above systems is the mechanical movement of the optical filter elements that control the laser wavelength scan. This deteriorates the image quality at the beginning and end of the A-scan due to the creation and depletion of momentum and the hysteresis inherent to such systems. However, existing techniques such as reference interferometers exist that can mitigate the problem and linearise the sweeps. The reference interferometer, usually a Mach-Zehnder, generates a variable rate optical clock that is used to drive the acquisition system.

Another limitation lies in the long cavity lengths required, that result in cavity

instabilities due to mechanical vibrations–made from piezo- or mechanically actuated gratings and mirrors–and temperature fluctuations, as the refractive index varies with temperature [113], atmospheric pressure, and is affected by gas turbulence.

Specifically, the mechanical mechanisms provide a pathway to couple vibrations into the laser cavity, add expense and complexity, provide a point of wear and fatigue which limits the lifetime, and necessitate an undesirably long laser cavity. A solution to these problems is the development and implementation of all-semiconductor *akinetic* laser technology. The term "akinetic" comes from the Ancient Greek $\alpha\kappa\check{\iota}\nu\eta\sigma\acute{\iota}\tilde{\alpha}$ (akinesia, "quiescence") and describes the absence of movement in a system.

An all-semiconductor laser uses an integrated semiconductor optoelectronic design approach without the use of coupling to an external cavity–the only things moving are photons and electrons. The entire sweep in an akinetic laser is programmable with the use of an on-board electronic chip that controls the driving currents of the diode. Due to the short waveguide design the akinetic laser minimises temperature variations and mechanical vibrations achieving excellent spectral performance. The semiconductor wafer-scale production nature of the laser also allows the cost of such devices to drop with time due to economies of scale [114,115].

This chapter describes the advantages and compromises of using all-electronic wavelength tuning in conjunction with a semiconductor chip implementation of a swept-wavelength OCT source.

3.2 Overview of Non-Kinetic Lasers

One of the critical components for a Swept Source Optical Coherence Tomography (SS-OCT) is the tunable laser source. The centre wavelength and the tuning range of the laser determines the axial resolution of OCT as it is proportional to the bandwidth. Additionally, there is a need for high sweep repetition rates increasing the acquisition speed and broadens the applications that it can be used (e.g. high velocity flow tracking). Furthermore, the laser must have a long instantaneous coherence to allow imaging at greater depths. Last, it is preferable for the sweep to be linear in frequency or wavelength as it reduces image artefacts and noise from the resulting cross-sectional images (B-scans).

All of these requirements are satisfied, in varying degrees, by non-kinetic swept sources such as Fourier Domain Mode Locking (FDML), MEMS-based tunable lasers like Vertical-Cavity Surface Emitting Laser (VCSEL), and others.

3.2.1 Fourier Domain Mode Locking (FDML)

The most important performance specifications required for OCT significantly differ from the ones typically needed in other tunable laser applications. As discussed in previous sections, the most important factors are the sweep rate, the tuning range, and the linewidth. For SS-OCT a high performing swept source has a wavelength sweep range of ≈100 nm, a wavelength sweep repetition rate of ≈100 kHz, and an instantaneous linewidth of ≈100 pm. A tuning range of 100 nm at a centre wavelength of 1 µm corresponds to 10% relative wavelength tuning, about 30 THz optical frequency. A 100 kHz sweep repetition rate translates to a frequency tuning speed of 3 THz/µs [116].

The FDML technique overcomes the physical limitation of cavity build-up dynamics allowing high sweep repetition rates up to 1 MHz. The principle of FDML is to synchronize the optical round-trip time of light circulating in the laser cavity with the filter sweep operation period of the optical bandpass [108]. Thus, one tuning period of the laser takes exactly as long as the light needs to propagate through the laser cavity. Specifically, light with a certain wavelength is transmitted through the optical bandpass filter and then propagates through a very long laser cavity, realized by an optical delay line. Meanwhile the optical bandpass filter is swept over one entire cycle, covering all desired wavelengths. When the light arrives back at the filter, the filter transmits this wavelength again. This means light does not have to build up from ASE background; it is still there from the last wavelength sweep, i.e. the entire wavelength sweep is optically stored inside the laser cavity. For sweep rates of hundreds of kHz a 3 km spool of optical single mode fibre is used. To make all wavelength components circulate at the same frequency, the chromatic dispersion of the fibre delay lines has to be compensated [117].

FDML lasers have certain advantages for OCT applications compared to other techniques. When the cavity is properly compensated for dispersion, the high number of effective round-trips leads to the effect of repetitive spectral filtering (mode competition) making the spectral linewidth of FDML laser narrower. The narrower linewidth improves the roll-off performance in OCT applications, resulting in a longer imaging depth. In FDML, almost all groups of laser gain media can be used with length up to meters, such as rare earth-doped fibre amplifiers, non-linear Raman amplifiers, etc. This allows high output powers (>100 mW), which improves the noise sensitivity in OCT applications [118]. Finally, at the operating wavelengths of 1.31 µm and 1.55 µm FDML lasers are entirely built of standard telecommunications components.

3.2.2 Vertical-Cavity Surface Emitting Laser (VCSEL)

The vertical-cavity surface-emitting laser (VCSEL) is a type of semiconductor laser diode with laser beam emission perpendicular from the top surface. For a 1310 nm MEMS-VCSEL laser the structure includes an indium phosphide (InP) substrate, used as the gain region, where a wide-gain aluminium indium gallium arsenide (AlInGaAs) mirror is epitaxially grown on and joined by wafer bonding. The VCSEL is optically pumped at 980 nm. Similarly, a 1310 nm MEMS-VCSEL laser is optically pumped at 850 nm [119]. Additional metal and dielectric layers on top of this VCSEL structure complete the optical cavity. This cavity includes a suspended top dielectric mirror, separated from the underlying VCSEL structure by an air gap, which can be contracted by electrostatic force as a voltage is applied between the actuator contacts.

These lasers can achieve coherence lengths of >100 mm and axial scan rates up to 1.2 MHz The only downside is that at 1.2 MHz the sweep are non-linear. But using custom drive waveforms the sweep can be linearised; with such linearised drive waveforms 200 kHz axial scan rates have been demonstrated [92].

Instead of using an optical pump at lower wavelengths, the MEMS-VCSEL can be electrically pumped. Optical pumping provides a number of performance advantages over electrical pumping, including enhanced tuning range and spectral purity. The absence of resistive heating associated with electrically pumped devices, e.g. Distributed Bragg Reflector (DBR), also increases available gain and again promotes wide tuning range. However, electrical pumping simplifies the cavity design and lowers the cost allowing VCSEL lasers to be used in consumer devices like computer mice, laser printers, etc.

Finally, wide mirror reflectivity bandwidth is critically important for wide tuning range. A high refractive index contrast mirror with a short optical field penetration depth is also critical to reduce the overall effective cavity thickness and increase the FSR, which further increases tuning range. Wide bandwidth can be achieved with a hybrid metal/deposited dielectric mirror [120], or alternatively with a high contrast grating (HCG) [121].

3.3 All-semiconductor Swept-Laser Technology

The concept of all-semiconductor lasers can be traced back to late 1980s, where Larry Coldren, a professor at the University of California Santa Barbara, started working to create a widely tunable all-semiconductor laser [122]. After years of development Coldren and his team founded the company Agility Communications

Inc. that manufactured widely tunable all-semiconductor lasers. In parallel, other companies (Syntune, Santur, Oclaro) worked on similar designs [123–125].

Around the same period companies such as Smart Fibres were able to develop and commercialize slowly tuning swept lasers utilizing all-semiconductor technology [126]. Additionally, Luna Technologies and AXSUN Technologies [127] similarly adapted semiconductor technology. In 2008, Insight Photonic Solutions working in conjunction with Dennis Derickson, a professor at the California Polytechnic State University, developed an all-semiconductor swept-wavelength laser with high repetition rates, narrow OCT system point spread functions (PSFs), and long coherence lengths [128]. The laser was later made available commercially [129–131].

For the project discussed in this thesis there were two options as to which type of laser to use, either a Santec swept laser with a scanning rate of 20 kHz or an all-semiconductor laser developed by Insight Photonics with a scanning rate of 100 kHz. The advantages and disadvantages of each laser can be seen in Table 3.1. During development both lasers were used in different setups but with main focus on the akinetic laser due to high sweep rate advantage.

Table 3.1: *Akinetic laser (Insight Photonics SLE-101) compared to a non-akinetic (Santec HSL-2100-HW) laser.*

Laser	Advantages (+) / Disadvantages (-)
Akinetic Swept Laser	(+) Adjustable bandwidth (10 nm to 100 nm) (+) High sweep rate (100 kHz) (+) Flat power profile (−) Medium resolution (10 µm) (−) Requires removal of invalid sweep points
Santec Swept Laser	(+) Bandwidth (>110 nm) (+) High resolution (<8 µm) (−) Low sweep rate (20 kHz) (−) Gaussian power profile (−) Component availability at centre wavelength (1.33 µm)

The following sections will explain the theory of operation and the unique characteristics behind the technology of the akinetic laser as it is used in the experimental setups described in Sections 5.3 and 5.4.

3.3.1 Wavelength Tuning

In this section the performance characteristics of an all-semiconductor akinetic laser will be explored along with the impact in OCT system performance. The all-semiconductor laser is a vital part of a swept-source OCT system (SS-OCT), as its performance impacts the imaging capabilities and quality of such a system. The majority of laser designs employed in SS-OCT systems involve a moving or kinetic structure which is responsible for providing wavelength-dependent feedback, resulting in a wavelength change in the radiant emission. As the tuning element on these systems (e.g. MEMS) is a moving physical object, the sweep rate is limited by the speed and range of motion of this object. Contrary, in a Vernier-Tuned Distributed Bragg Reflector (VT-DBR) the wavelength change is provided by an index-of-refraction change in a semiconductor material, which changes a grating spacing (Figure 3.1) and varies the cavity length and thus changes λ according to

$$\frac{m\lambda}{2} = nL\,, \tag{3.1}$$

where m is the mode index integer, λ is the free-space wavelength, n is the effective index of the waveguide, and L is the cavity length [132]. In such a system the tuning is achieved by changing either the cavity's refractive index $\Delta n/n$, the cavity length $\Delta L/L$, and the mode index $\Delta m/m$:

$$\frac{\Delta\lambda}{\lambda} = \frac{\Delta n}{n} + \frac{\Delta L}{L} + \frac{\Delta m}{m}\,. \tag{3.2}$$

A VT-DBR relies on dynamic variation of each of these three variables simultaneously. This can be achieved by electrically heating the vernier mirrors and the gain medium using drive currents.

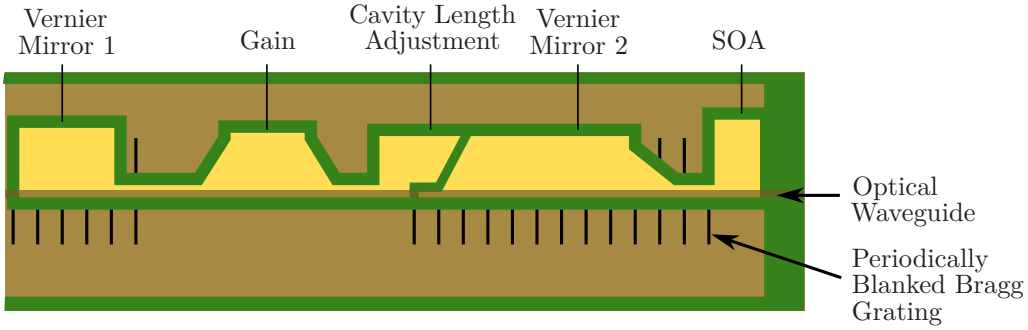

Figure 3.1: *Semiconductor structure of the VT-DBR akinetic laser. The amplifier (SOA) is electrically pumped and has a similar structure to Fabry–Pérot laser diode but with anti-reflection design elements at the end faces [129].*

3.3.2 Coherence Length and Imaging Depth Range

In SD-OCT, the optical bandwidth of the laser source determines the axial resolution of the system. The linewidth of a laser, is the width—typically the Full Width at Half-Maximum (FWHM)—of its optical spectrum. The linewidth is strongly related to the temporal coherence, characterized by the coherence time or coherence length as shown in Equation (3.3).

$$L_{\text{coh}} = c \cdot \tau_{\text{coh}} = \frac{c}{\pi \cdot \Delta\nu}\,, \tag{3.3}$$

where c is the speed of light in vacuum, t_{coh} the coherence time, and $\Delta\nu$ the (full width at half-maximum) linewidth, i.e. optical bandwidth [133]. This coherence length is the propagation length after which the magnitude of the coherence function has dropped to the value of $1/e$.

However, in swept wavelength sources the optical bandwidth of the source corresponds to the tuning range $\Delta\lambda$ of the laser. A typical output spectrum for swept wavelength sources with a Gaussian-like profile can be seen in Figure 3.2. The tuning range is defined from edge to edge (full range), at $-3\,$dB FWHM, or at $1/\mathrm{e}^2$ level.

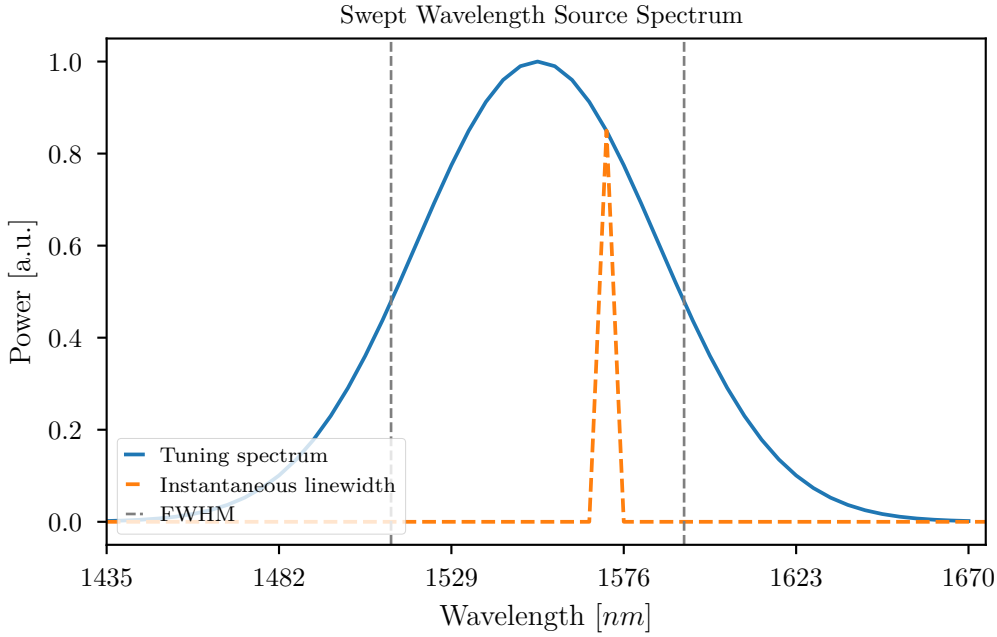

Figure 3.2: *Tuning spectrum of a swept wavelength source with a Gaussian-like power profile. The tuning range (black dashed lines) is defined from edge to edge (full range), at −3 dB (full width at half maximum: FWHM), or at* $1/\mathrm{e}^2$ *level. The orange dashed line represents the instantaneous linewidth of the laser.*

The tuning range is related to the Point Spread Function (PSF) through the Fourier transform if no windowing functions are applied. Assuming a Gaussian spectrum

with $1/e^2$ width of $\Delta\lambda$, the axial resolution, defined as the FWHM of point spread function, is given by

$$\delta z \approx 0.75 \frac{\lambda_0^2}{\Delta\lambda}\,, \tag{3.4}$$

where δz is the axial resolution of OCT, λ_0 the centre wavelength of the swept source, and $\Delta\lambda$ the tuning range, i.e. optical bandwidth [133].

For a swept wavelength laser with a tuning range of $\Delta\lambda = 127\,\text{nm}$ at $\lambda_0 = 1300\,\text{nm}$ (3.4) yields $\delta z \approx 10\,\mu\text{m}$; the same resolution is achieved with $\Delta\lambda = 180\,\text{nm}$ at $\lambda_0 = 1550\,\text{nm}$.

During the wavelength sweep, the laser emits a narrowband spectrum instantaneously which is known as instantaneous linewidth (Figure 3.2). This finite linewidth of the instantaneous output causes the visibility of interference to decrease with path length difference. The instantaneous coherence length function is related to the instantaneous spectrum through the Fourier transform, just like the point spread function is to the overall tuning spectral envelope. The coherence length is defined as the optical delay when interference visibility drops by 3 dB (50%). Hence, the coherence length corresponds to a full depth range with visibility greater than > 0.5. Since OCT is a reflective interrogation technique, the so-called imaging depth captures the double path in the interferometer and is therefore half the coherence length of the source, i.e., a swept source with a coherence length of 20 mm has an imaging depth of 10 mm. Because Signal to Noise Ratio (SNR) is proportional to the square of the visibility, longer coherence length is required in OCT. The instantaneous coherence length, z_{coh} , is related to the FWHM instantaneous linewidth, $\delta\lambda$, via

$$z_{\text{coh}} \approx 0.44 \frac{\lambda_0^2}{\delta\lambda}\,, \tag{3.5}$$

where λ_0 is the instantaneous centre wavelength and $\delta\lambda$ the FWHM instantaneous linewidth [133,134].

As a numerical example, $\delta\lambda = 0.1\,\text{nm}$ at $\lambda_0 = 1300\,\text{nm}$ yields $z_{\text{coh}} \approx 7.4\,\text{mm}$; the same coherence length is obtained with $\delta\lambda = 0.14\,\text{nm}$ at $\lambda_0 = 1550\,\text{nm}$. At longer wavelengths the instantaneous coherence length is longer for the same linewidth. Long instantaneous coherence length is a key aspect of an SS-OCT system. It facilitates deep imaging (anterior eye segment, full axial eye length), it enables advanced OCT measurement techniques, such as superimposed multipath OCT, polarization-sensitive OCT [135], or phase-sensitive OCT [136].

A distributed Bragg reflector laser utilises at least one Distributed Bragg Reflector (DBR) outside the gain medium (the active region). A DBR is a light-reflecting device based on Bragg reflection at a periodic structure. In most cases, the Bragg mirror is more specifically a quarter-wave mirror, providing the maximum amount of reflection for the given number of layers. The main difference between a DBR

laser and a DFB is that the whole active medium is embedded in a single distributed reflector structure.

DBR laser diodes are usually single-frequency lasers with diffraction-limited output, and often they are wavelength-tunable. The tuning within the free spectral range is usually accomplished by either change of injection current into the gain section (DBR current tuning), or through change in temperature of the entire device by altering the heat-sink temperature (DBR temperature tuning). The dominant tuning mechanism is the refractive index change due to temperature variation. To further increase the tuning range, a separate, electrically heated, phase section can be added between the gain and grating sections allowing an increase of 8 nm [137].

Alternatively, electro-optic tuning can also be accomplished. Mode-hop free tuning over a larger wavelength region is possible by coordinated tuning of the Bragg grating and the gain structure. There are more sophisticated device designs, exploiting a Vernier effect with sampled gratings (SG-DBR laser), that offer a tuning range as wide as e.g. 40 nm, although not without mode hops. The linewidth of a DBR diode is typically a few Megahertz due to the relatively short laser resonator, typically on the order of 1 mm.

Coherence length is affected by the laser cavity and time-based shifting of the centre wavelength [138], thus using distributed Bragg reflector (DBR)-like structures to construct the cavity of the laser results in a narrow line width. In addition, the small dimensions of the laser cavity, along with it being manufactured on a semiconductor wafer, substantially reduces cavity length variation due to the repeatability offered by the advanced techniques employed by silicon chip manufacturers.

By using an all-semiconductor laser the cavity can be as small as 2 mm in length and be monolithically constructed within the semiconductor (Figure 3.3), minimizing the mechanical variation that might limit coherence length. In an all-semiconductor akinetic laser the coherence length can be user-adjustable. The laser behaviour is finely controlled, as the laser has a built-in platform to control sweep characteristics. The ability to finely tune the coherence length programmatically can help reduce unwanted signals that create ghosting[1] in OCT images and are typically caused by inter- and intra-cavity reflections [139]. The lack of moving parts in akinetic lasers solves this issue. As such the same coherence length can be achieved whether running 4k sweeps per second (S/s) or 100 kS/s.

[1]Ghosting is the phenomenon where a replica of the image appears, offset in depth position, that is super-imposed on top of the main image. The main cause is reflections from cavities in the propagation path.

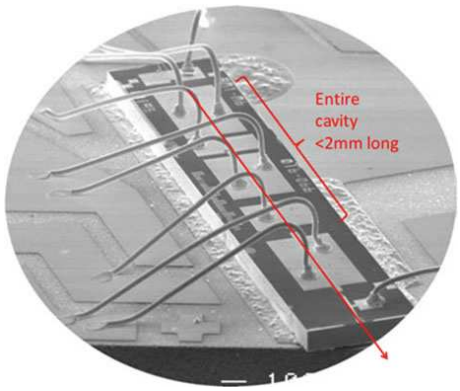

Reprinted by permission from Springer Nature: Springer, Akinetik Swept Sources. In: Drexler W., Fujimoto J. (eds) Optical Coherence Tomography, Minneman M. et al. (2015)

Figure 3.3: *SEM image of the bonded laser chip. The optical path is less than 2 mm long and in a single mechanical part, reducing cavity variation and leading to high coherence length, as well as eliminating the typical inter- and intra-cavity reflections that can create ghosting with other swept lasers [131].*

3.3.3 Sweep Speed and Duty Cycle

Sweep speed plays a significant role in OCT systems as it helps to overcome various problems inherent to such systems. Rapid sweeping can reduce blur from movement [140] the same way as high-speed cameras do with fast-moving objects. OCT is commonly used for retinal imaging where slow imaging speeds along with eye movements can lead to blurry images thus reducing OCT performance. Additionally, a fast sweep reduces the measurement time needed, thus reducing impact on patients. It enables 3D volumetric imaging [111,141,142] hundreds of A-scans can be acquired in a fraction of a second.

Unlike some mechanically driven lasers, the speed, the number of points, and the wavelength range of the akinetic laser module used in the following chapters are controlled by a change of current within the laser cavity affecting five separate parameters. This akinetic laser can be programmed for any sweep speed over a range from 4000 to 100 000 sweeps per second. The low repetition rate value of 4000 sweeps per second is not a fundamental limitation and could be made arbitrarily low. Additionally, the number of wavelength points per sweep is inversely proportional to the sweep rate leading to increased image depth, as discussed in Section 3.3.4, but at slower refresh rates.

The sweep speed of swept laser sources is constrained by the duty cycle of the sweep. Traditional swept lasers use a mechanical tuning mechanism that needs to be accelerated and decelerated at the beginning and end of the sweep, while keeping

the momentum constant for the majority of the sweep. Mechanical vibrations on this mechanism affect sweep rate stability. The electrostatic actuator in MEMS-based lasers is inherently non-linear, since the suspended mirror displacement varies as the square of the applied voltage. However, the MEMS-VCSEL, like other MEMS-based tunable lasers, can be linearised through drive waveform pre-shaping [119]. In the past, the delays during acceleration and deceleration stages of the sweep were inconsequential compared to the delays in the data acquisition system. Nowadays, sampling rates are sufficiently fast that distortions caused by acceleration and deceleration are detectable.

An akinetic laser allows fast tuning between wavelengths, thus the time from the end of a sweep to the beginning of a sweep is relatively short, permitting a high duty cycle with little dead time between sweeps. When combined with streaming-type data acquisition systems discussed in Section 5.4.7, the all-semiconductor laser increases total throughput and imaging speed (Figure 3.4). As mentioned before, the software controlled nature of those lasers allows the duty cycle to be adjusted and it can be set to almost any value from 5% to 95%. Using a smaller duty cycle, in some occasions, can be advantageous, e.g. if the acquisition system is using an embedded processor with limited processing power. In contrast, kinetic swept lasers often have a characteristic sweep rate that varies significantly over the duration of the sweep. This non-linear behaviour often leads to a non-homogeneous coherence length across the sweep [131].

3.3.4 Linearity and k-Clock

Linearity in frequency (k-space) is a key requirement for swept source OCT applications. Most traditional swept lasers require either an external optical k-clock to clock the data acquisition or to post-process the linear-in-time data. This optical clocking or k-clocking is typically performed using a Mach-Zehnder interferometer to detect the frequency sweep and clock the the analogue–to–digital converter (ADC) at a variable rate corresponding to the frequency sweep rate. There are swept lasers that fit in a butterfly package so the reference interferometer can integrated with the laser removing the need for an external optical k-clock generator. Unlike other swept sources, the akinetic laser used for the experiments has an internal reference interferometer for the generation of the electronic k-clock but is only used internally.

The in-built software of the laser forces the wavelength to be correct for equal frequency steps at each of the evenly spaced clock transitions. This reduces the cost and complexity of OCT systems as they need fewer components in order to be functional. Additionally, this eliminates the problem with non-uniform triggering of the acquisition where the clock of ADC is not in sync with the k-clock of the laser, leading to non-linearity in frequency samples. The akinetic laser can generate

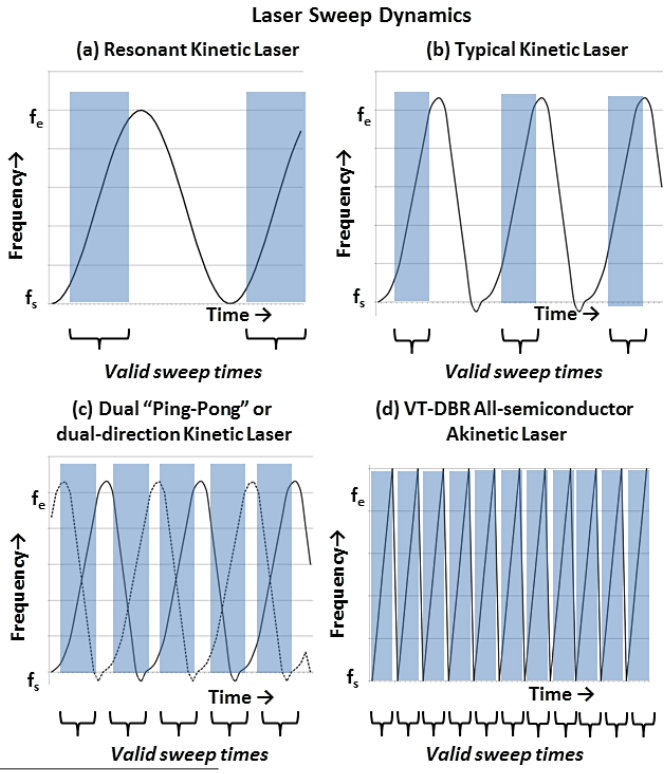

Adapted by permission from Springer Nature: Springer, Akinetik Swept Sources. In: Drexler W., Fujimoto J. (eds) Optical Coherence Tomography, Minneman M. et al. (2015)

Figure 3.4: *Resonant kinetic laser sweep has sine structure with a typical 30% non-linearity, (b) Typical kinetic laser sweep sequence with relatively low duty cycle, (c) "Ping-Pong" sequence with doubled-up lasers or bi-directional sweeps sometimes used to minimize effects of kinetic-tuning swept lasers, and (d) tuning of the VT-DBR swept laser [129].*

the constant rate clock signal to drive the acquisition electronics. This is achieved by generating an additional signal that indicates when a frequency sample is valid or not; this is known as the Data Valid Vector (DVV). However, if the data valid vector is not synchronised with the sweep then it will lead to non-linearities in the frequency samples. Finally, if the signals are synchronised and properly used at the acquisition stage, it can reduce the computation time—as the post-processing to uniformly space the data in k-space is not required.

The akinetic laser can output a start sweep trigger that is deterministically aligned to the k-clock. The start-sweep signal generates a pulse just a clock cycle before the first valid k-clock and can be used as a trigger for the acquisition system to capture a new frame (B-scan). As non-kinetic lasers allow high-speed sweep rates, the imaging depth range is no longer constrained by the coherence length but by the Nyquist limit of the detection of the interferogram [143]. This is true only if the detection amplifier bandwidth does not limit the imaging depth range.

3.3.5 Mode Hops and Phase Stability

By having software control on every aspect of the sweep in an akinetic laser, mode hops are eliminated as the software constantly monitors and ensure that no mode hops happen. Long before the laser could even begin a mode hop, the control optimizes the sweep to ensure optimum side-mode-suppression ratio (SMSR). Furthermore, using the data valid vector, the points in the sweep where an erroneous jump to a different wavelength occurs are filtered out, minimising the amount of phase discontinuities. Yet, for this to hold true, there is the requirement that the DVV must be synchronised with the sweep in order to remove the invalid wavelength points. Phase stability is crucial in OCT applications, such as phase microscopy or Doppler OCT, as it is advantageous to have consecutive wavelength sweeps that are aligned perfectly. To ensure phase stability the laser must have wavelength repeatability, this means that every sweep point must match the corresponding wavelength for each subsequent sweep. The displacement sensitivity of a phase-sensitive OCT system is calculated using

$$\delta z = \frac{\delta\phi\lambda_0}{4\pi n} + \frac{\delta\lambda}{\lambda_0} z\,, \tag{3.6}$$

where $\delta\phi$ is the phase uncertainty in the interferogram measurement, $\delta\lambda$ is the wavelength repeatability, z is the nominal path length difference, n is the index of refraction, and λ_0 is the centre wavelength [132].

The fundamental phase uncertainty of an OCT system is defined to be $1/\sqrt{SNR}$ [144]. To achieve SNR-limited displacement sensitivity, variations in the wavelength repeatability must be minimized as shown in Equation (3.6).

3.3.6 Trigger Jitter

As the sweep rate of a swept wavelength laser increases the jitter of the triggering signal becomes a major factor in SNR [145]. With sweep rates of hundred of thousands per second the clock signals need to be precise. A time delay of more than 1.25 ns can lead to erroneously interpreting the acquired signals. This is especially problematic for mechanically swept lasers that require external optical k-clocks, as the trigger signal has to propagate through different devices. By generating the electronic k-clock internally akinetic lasers minimise the trigger jitter to ±300 fs, while on an optical k-clock, it is difficult to achieve better than 18 ps to 50 ps jitter due to zero drift and other factors [146]. Equation (3.7) describes the dependence of SNR on analogue frequency bandwidth (f) and jitter $\Delta t_{\text{jitter}}^{\text{RMS}}$.

$$\text{SNR}_{\text{dB}} = -20 \cdot \log_{10}(2\pi f_{\text{BW}} \Delta t_{\text{jitter}}^{\text{RMS}}) \tag{3.7}$$

3.3.7 Selectable Power Profiles

The optical power of the swept laser can affect multiple properties of an OCT system. The total power and the shape output profile can limit the maximum penetration depth and the resolution respectively. With precise control over the shape and the power we can accomplish:

- Reduced image artefacts with level power
- Custom profiles allow optimization of PSF and suppression of side-lobes
- Flat, strong output power can reduce relative intensity noise trade-offs and improve penetration depth

With akinetic lasers the output power is directly controlled by the on-board chip and can be selected through software. With a flat power profile artefacts in the PSF can be reduced, further improving the image quality. The ability to have a flat power profile is significant in SS-OCT as the amplitude variation is not eliminated by balanced detection–only the zero value is corrected [146]. The varying amplitude envelope of other lasers remains in the interferogram, reducing image quality (Figure 3.8).

Another approach, that is possible with akinetic all-semiconductor lasers, is to use a custom power profile to pre-emphasize (i.e. increase output power for specific wavelengths) the optical signal to compensate for wavelength and polarization-dependent losses in the OCT interferometer. This compensation can be applied to either flat-top or Gaussian profiles.

3.4 Sweep Quality of Akinetic Laser

For the implementation of the dual beam OCT systems described in Sections 5.3 and 5.4 an akinetic laser is used. In the following sections, the physical properties of the laser and its principles of operation are discussed. The quality of the sweep is determined by the PSF which corresponds to the Fast Fourier Transform (FFT) of the interference fringes generated by a Michelson interferometer. However, as it will be discussed further in Section 3.4.4, a portion of the sweep points are invalid. Thus, a data invalid vector (DIV) is applied that extracts the valid points before the calculation of the Fast Fourier Transform (FFT). If these invalid points are not removed properly from the raw signal the image quality of OCT is degraded, this can be seen in Section 3.4.4.

3.4.1 In-Situ Sweep Programmability

With most lasers the sweep speed, duty cycle, and power profile is fixed. The only way to change the number of points is by changing the optical k-clock hardware. In contrast, akinetic all-semiconductor lasers, for the reasons mentioned in previous sections, are able to program the sweep in real-time. As a comparison Table 3.2 summarises the parameters that can be adjusted in the akinetic all-semiconductor laser used for this project and compares it with the non-akinetic swept laser used in previous projects.

Table 3.2: *Akinetic laser (Insight Photonics SLE-101) specificactions compared to a non-akinetic (Santec HSL-2100-HW) laser*

Parameter	Akinetic Swept Laser	Santec Swept Laser
Points per Sweep	1 to 130 000	N/A
Max. Optical Power (mW)	11	8
Coherence Length (mm)	40	8
Centre Wavelength (µm)	1.52 to 1.62	1.31
Sweep Width (nm)	10 to 100	>110
Sweep Speed (kHz)	4 to 100	20
Sweep Power Profile	Flat Top	Gaussian
Sweep Direction	forward or backward in λ	forward in λ

The akinetic laser (Insight Photonics SLE-101), used for the OCT system described in Chapter 5, features a longer coherence length of 40 mm compared to 8 mm typical for a non-akinetic swept wavelength laser. As discussed in Section 3.3.2, the coherence length is an important parameter that dictates the imaging depth of the SS-OCT system. Furthermore, the akinetic laser has adjustable centre wavelength ranging from 1.52 µm to 1.62 µm as well as variable sweep width with a range up to 82 nm. In order to have the highest attainable depth resolution by the OCT system the sweep width is set to its maximum value, i.e. 82 nm. Hence, the centre wavelength is set to 1550 nm.

Additionally, the akinetic laser has an adjustable sweep rate with a maximum of 100 kHz, leading to high-speed axial scans (A-scans). However, the sweep rate, sweep width, and points per sweep form a performance trilemma, i.e. increasing one of the three parameters, decreases the other one of the two or both. Thus, is not possible to have the maximum number of points per sweep at the maximum sweep rate and sweep width.

Finally, the laser has a flat-top power profile instead of the more common Gaussian profile. The laser has to perform a sweep calibration before it is used. At that stage the laser calculates the driving currents for the laser diode to achieve a uniform

power across all wavelength points of the sweep. Additionally, the laser has an internal Michelson interferometer that is used for feedback in the calculation of the profile. The advantage of the flat power profile is that after acquisition of the interference signal a custom windowing function can be applied to the data that can suppress the side-lobes in the Fourier domain, thus the Signal to Noise Ratio (SNR) is increased. Contrarily, when the laser sweep already has a custom power profile (e.g. Gaussian), a windowing function cannot be used in post-processing. However, having an appropriate power profile can increase the SNR without the requirement of additional post-processing on the datasets.

3.4.2 Point Spread Function (PSF) Quality

The limit of image quality in a swept laser OCT system can be determined by the axial PSF [147]. The PSF of an OCT system corresponds to the power spectrum of an interferogram produced by an interferometer with a single reference reflector. As will be explained in the following sections, the interferogram produced when the OPD of the interferometer is close to zero is equal to the autocorrelation function of the light source; thus, it relates to the coherence of the light source. So, the optical path length difference over which the optical PSF drops to 50% is the coherence length of the source. Two values that can be extracted from a PSF diagram are the Peak to Side-lobe Ratio (PSR) and Peak to Noise Ratio (PNR), where the latter is a good indication for the Signal to Noise Ratio (SNR) of the system. High peak to side-lobe and peak to noise ratios facilitate an image with low artefacts and high contrast.

3.4.2.1 Discrete Fourier Transform and Properties

For a deterministic continuous signal, $x(t)$, the Fourier transform $\mathcal{F}$ is used to describe its spectral content [46]. The forward Fourier transform is given by

$$X(f) = \mathcal{F}[x(t)] = \int_{-\infty}^{\infty} x(t)\mathrm{e}^{-\mathrm{j}2\pi ft}\,\mathrm{d}t\,. \tag{3.8}$$

Similarly, the inverse Fourier transform $\mathcal{F}^{-1}$ is defined as

$$x(t) = \mathcal{F}^{-1}[X(f)] = \int_{-\infty}^{\infty} X(f)\mathrm{e}^{\mathrm{j}2\pi ft}\,\mathrm{d}f\,. \tag{3.9}$$

For discrete-time signals, i.e. the digitised interferometric signal the Discrete-Time Fourier Transform (DTFT) is used. The definition of the DTFT is similar to the

continuous-time transform with the main difference being the substitution of the integral with a summation:

$$X(f) = \mathcal{F}[x(t)] = \sum_{n=-\infty}^{\infty} x[n]\mathrm{e}^{-\mathrm{j}2\pi fn} \tag{3.10}$$

The DTFT itself is a continuous function of frequency, but typically in digital Fourier analysis discrete samples are calculated via the Discrete Fourier Transform (DFT), which is by far the most common method of modern Fourier analysis. It should be noted that the Discrete Fourier Transform (DFT) is only a method for calculating the Fourier transform and there are different algorithms that are utilised to compute the DFT; the most common algorithm is the Fast Fourier Transform (FFT). Both transforms are invertible. The inverse DTFT is the original sampled data sequence while the inverse DFT is a periodic summation of the original sequence.

3.4.2.2 Parseval's Theorem

For a complex signal $x(t)$, the complex conjugate $x^*(t)$ can be found from the inverse Fourier transform as

$$x^*(t) = \left(\mathcal{F}^{-1}[X(f)]\right)^* = \int_{-\infty}^{\infty} X^*(f)\mathrm{e}^{-\mathrm{j}2\pi ft}\,\mathrm{d}f\,, \tag{3.11}$$

where $X^*(f)$ is the complex conjugate of $X(f)$. However, if x(t) is real then $X(f) = X^*(-f)$. Based on Parseval's theorem [46] for complex-valued functions x(t), y(t) with Fourier transforms $\mathcal{F}[x(t)] = X(f)$, $\mathcal{F}[y(t)] = Y(f)$ the following property exists;

$$\int_{-\infty}^{\infty} x^*(t)y(t)\,\mathrm{d}t = \int_{-\infty}^{\infty} X^*(f)Y(f)\,\mathrm{d}f\,, \tag{3.12}$$

where $X^*(f)$ is the complex conjugate of $X(f)$. Furthermore, using the inverse Fourier transform and Equation (3.11), $x^*(t)$ and $y(t)$ can be written as

$$x^*(t) = \int_{-\infty}^{\infty} X^*(f)\mathrm{e}^{-\mathrm{j}2\pi ft}\,\mathrm{d}f \quad \text{and} \quad y(t) = \int_{-\infty}^{\infty} Y(f)\mathrm{e}^{\mathrm{j}2\pi ft}\,\mathrm{d}f\,. \tag{3.13}$$

The proof of Parseval's theorem involves the Fourier transform of the Dirac delta function. One of the properties of the Dirac delta function $\delta(t)$ is

$$x(t) = \int_{-\infty}^{\infty} \delta(t-t')x(t')\,\mathrm{d}t'\,. \tag{3.14}$$

The Fourier transform of the Dirac delta function is $\mathcal{F}[\delta(t)] = \Delta(f) = 1$. Additionally, $\delta(t)$ can be written as the inverse Fourier transform of $\Delta(f)$, i.e.

$$\begin{aligned} \delta(s) &= \int_{-\infty}^{\infty} \Delta(f) \mathrm{e}^{-\mathrm{j}2\pi f s} \,\mathrm{d}f \\ \overset{s=t-t'}{\Longrightarrow} \quad \delta(t-t') &= \int_{-\infty}^{\infty} (1) \mathrm{e}^{-\mathrm{j}2\pi f (t-t')} \,\mathrm{d}f \,. \end{aligned} \tag{3.15}$$

Starting with the left side of Parseval's equation and using the inverse Fourier transforms from (3.13), Equation (3.12) becomes

$$\begin{aligned} \int_{-\infty}^{\infty} x^*(t) y(t) \,\mathrm{d}t &= \int_{-\infty}^{\infty} \left(\int_{-\infty}^{\infty} X^*(f) \mathrm{e}^{-\mathrm{j}2\pi f t} \,\mathrm{d}f \right) \left(\int_{-\infty}^{\infty} Y(f') \mathrm{e}^{\mathrm{j}2\pi f' t} \,\mathrm{d}f' \right) \mathrm{d}t \\ &= \int_{-\infty}^{\infty} \int_{-\infty}^{\infty} \int_{-\infty}^{\infty} X^*(f) Y(f') \mathrm{e}^{-\mathrm{j}2\pi f t} \mathrm{e}^{\mathrm{j}2\pi f' t} \,\mathrm{d}f \,\mathrm{d}f' \,\mathrm{d}t \\ &= \int_{-\infty}^{\infty} \int_{-\infty}^{\infty} X^*(f) Y(f') \left(\int_{-\infty}^{\infty} \mathrm{e}^{-\mathrm{j}2\pi (f-f') t} \,\mathrm{d}t \right) \mathrm{d}f \,\mathrm{d}f' \,. \end{aligned} \tag{3.16}$$

Then, substituting $\delta(t-t')$ for $\int_{-\infty}^{\infty} \mathrm{e}^{-\mathrm{j}2\pi (f-f')t} \,\mathrm{d}t$ leads to

$$\begin{aligned} \int_{-\infty}^{\infty} x^*(t) y(t) \,\mathrm{d}t &= \int_{-\infty}^{\infty} \int_{-\infty}^{\infty} X^*(f) Y(f') \delta(f-f') \,\mathrm{d}f \,\mathrm{d}f' \\ &= \int_{-\infty}^{\infty} X^*(f) \left(\int_{-\infty}^{\infty} Y(f') \delta(f-f') \,\mathrm{d}f' \right) \mathrm{d}f \,. \end{aligned} \tag{3.17}$$

Lastly, applying (3.14) to (3.17) leads to the proof of the theorem, i.e.,

$$\int_{-\infty}^{\infty} x^*(t) y(t) \,\mathrm{d}t = \int_{-\infty}^{\infty} X^*(f) Y(f) \,\mathrm{d}f \,. \tag{3.18}$$

If both $x(t)$ and $y(t)$ are real, then $x(t) = x^*(t)$ and $y(t) = y^*(t)$ but $X(f) \neq X^*(f)$ and $Y(f) \neq Y^*(f)$, thus

$$\int_{-\infty}^{\infty} x(t) y(t) \,\mathrm{d}t = \int_{-\infty}^{\infty} X^*(f) Y(f) \,\mathrm{d}f \tag{3.19}$$

and further, if $g(t) = x(t) = y(t)$,

$$\int_{-\infty}^{\infty} |g(t)|^2 \,\mathrm{d}t = \int_{-\infty}^{\infty} g(t) g(t) \,\mathrm{d}t = \int_{-\infty}^{\infty} G^*(f) G(f) \,\mathrm{d}f = \int_{-\infty}^{\infty} |G(f)|^2 \,\mathrm{d}f \,. \tag{3.20}$$

3.4.2.3 Power Spectral Density and Autocorrelation

The discrete–time signal $\{x(t); t = 0, \pm 1, \pm 2, \dots\}$ is assumed to be a sequence of random variables with zero-mean,

$$\mathrm{E}\{x(t)\} = 0\,, \quad \text{for all } t\,.$$

Hereafter, $\mathrm{E}\{\cdot\}$ denotes the expectation operator which averages over the ensemble of realizations. Assuming a physical voltage source which follows $x(t)$ and applied to the terminals of a $1\,\Omega$ resistor, then the instantaneous power dissipated in that resistor would be given by $x^2(t)$ watts.

Thus, the time-averaged power P of a signal $x(t)$ can be given by the following [148],

$$P_x = \frac{1}{T}\int_0^T |x(t)|^2 \,\mathrm{d}t\,. \tag{3.21}$$

Using Parseval's theorem and Equation (3.20) the above can be rewritten as

$$P_x = \frac{1}{T}\int_0^T |x(t)|^2 \,\mathrm{d}t = \frac{1}{T}\int_{-\infty}^{\infty} |X(f)|^2 \,\mathrm{d}f\,. \tag{3.22}$$

Since the random process has been truncated to a finite time interval ($[0, T]$), there will generally not be any problem with the existence of the Fourier transform. Additionally, as P_x is a random variable as well to get the averaged power the expectation of $X(f)$ must be taken:

$$\langle P_x \rangle = \mathrm{E}\{P_x\} = \frac{1}{T}\int_{-\infty}^{\infty} \mathrm{E}\{|X(f)|^2\} \,\mathrm{d}f \tag{3.23}$$

To calculate the power of the un-truncated random process, the limit as $T \to \infty$ is taken,

$$\langle P \rangle = \lim_{T\to\infty} \frac{1}{T}\int_{-\infty}^{\infty} \mathrm{E}\{|X(f)|^2\} \,\mathrm{d}f = \int_{-\infty}^{\infty} \lim_{T\to\infty} \frac{1}{T}\mathrm{E}\{|X(f)|^2\} \,\mathrm{d}f\,. \tag{3.24}$$

Define S_{xx} as the integrand in Equation (3.24) [148], i.e.

$$S_{\mathrm{xx}}(f) = \lim_{T\to\infty} \frac{1}{T}\mathrm{E}\{|X(f)|^2\}\,, \tag{3.25}$$

and the average power will be

$$\langle P \rangle = \int_{-\infty}^{\infty} S_{\mathrm{xx}}(f) \,\mathrm{d}f\,. \tag{3.26}$$

As $S_{\mathrm{xx}}(f)$ is a function of frequency with the property that when integrated over all frequency the total power is obtained. Thus, $S_{\mathrm{xx}}(f)$ has the units of power per unit frequency, in other words is the power spectral density function (PSD) of the random process. Alternatively, using the discrete-time Fourier transform [149] the PSD can be defined as

$$S_{\mathrm{xx}}(f) = \lim_{N\to\infty} \mathrm{E}\left\{\frac{1}{N}|X(f)|^2\right\} = \lim_{N\to\infty} \mathrm{E}\left\{\frac{1}{N}\left|\sum_{t=1}^{N} x(t)\mathrm{e}^{-\mathrm{j}2\pi ft}\right|^2\right\} . \tag{3.27}$$

The autocorrelation $R_{\mathrm{xx}}(\tau)$ (or covariance $r(k)$ in discrete time [149]) for a wide-sense-stationary random processes[2] is given by

$$\begin{aligned} R_{\mathrm{xx}}(\tau) &= \mathrm{E}\left\{x(t)x^*(t-\tau)\right\} , \\ r(k) &= \mathrm{E}\left\{x(t)x^*(t-k)\right\} . \end{aligned} \tag{3.28}$$

Based on Wiener–Khintchine–Einstein theorem [148] for a wide-sense-stationary (WSS) random process $x(t)$ whose autocorrelation function is given by $R_{\mathrm{xx}}(\tau)$, the Power Spectral Density function of the process is

$$S_{\mathrm{xx}}(f) = \mathcal{F}[R_{\mathrm{xx}}(\tau)] = \int_{-\infty}^{\infty} R_{\mathrm{xx}}\mathrm{e}^{-\mathrm{j}2\pi f\tau}\,\mathrm{d}\tau . \tag{3.29}$$

Similarly, for a discrete-time signal the Power Spectral Density (PSD) is defined as the DTFT of the covariance sequence [149], i.e.,

$$S_{\mathrm{xx}}(f) = \mathcal{F}[r(k)] = \sum_{k=-\infty}^{\infty} r(k)\mathrm{e}^{-\mathrm{j}2\pi fk} . \tag{3.30}$$

3.4.2.4 Calculation of PSF for the Akinetic Laser

The akinetic laser used throughout the experiments has an internal Michelson interferometer that is used during the sweep calibration (Section 3.4.4). Thus, the laser captures the interferometric signal and calculates the point-spread function for the determination of the sweep quality. After the calibration, the raw signal is stored on the embedded computer inside the laser for troubleshooting purposes. As the interferometer is inside the laser, it has the advantage that the optical path difference is close to zero delay and both arms are dispersion matched; unlike external bulk-optic interferometers where they need dispersion compensation when the light propagates through different media. To demonstrate the use of the internal Michelson

[2] A stochastic process whose unconditional joint probability distribution does not change when shifted in time

interferometer and the process of generating the PSF, the raw interferometric signal was extracted from the on-board memory of the laser after a calibration and the PSF is presented here. The following interferometric signals were captured at different laser conditions to show the various performance states of the laser. The first was captured while the laser sweep was at a good condition, while the second when the laser performance was degraded.

The raw optical signal from the internal interferometer of the akinetic laser is shown in Figure 3.5. The laser was calibrated for a sweep rate of 100 kHz covering 82 nm sweep width at the centre wavelength of 1.55 µm. Because on the internal interferometer both arms are terminated with a mirror, the interference signal is a single-frequency sinusoid. From the graph it can be seen that there are no visible phase discontinuities and overall the signal appears to be clean.

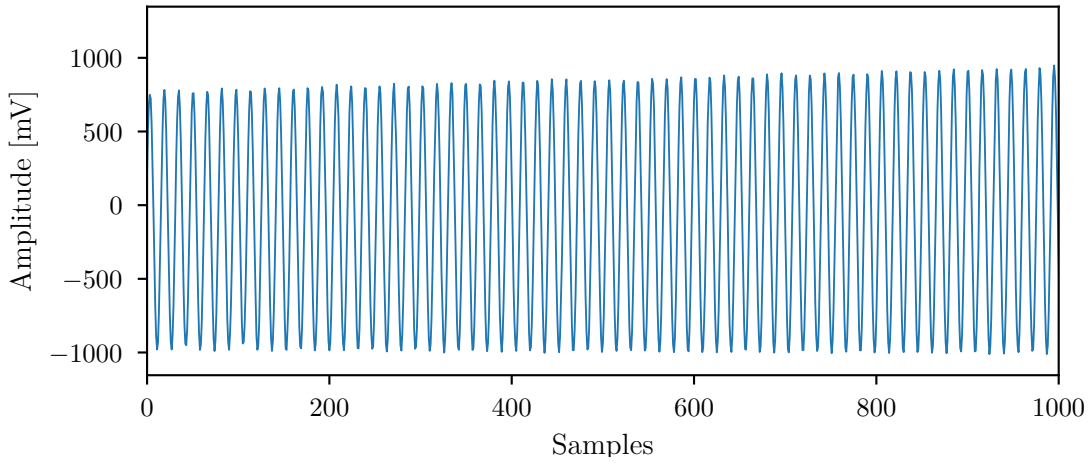

Figure 3.5: *Raw optical signal from the internal interferometer of an akinetic laser with a 100 kHz sweep frequency. As seen in the figure, there are no phase discontinuities leading to a high peak–to–side-lobe ratio as shown in Figure 3.6.*

In other imaging systems and in the domain of Fourier optics the Point Spread Function corresponds to the impulse response of the system that is applied to an object through convolution that yields an image:

$$\text{Image} = \text{PSF} * \text{object}\,.$$

Applying this concept to OCT means that the interferometric signal captured corresponds to the convolution of the light source with the object being scanned. Now, using an interferometer with zero Optical Path Difference (OPD), the resulting signal will be the autocorrelation (also known as coherence) function of the light source. This means that based on Wiener–Khintchine–Einstein theorem the “optical PSF”

(PSF_o) is equal to PSD which in turn is equal to the Fourier transform of the auto-correlation function. Thus, to calculate the PSF, the discrete Fourier transform is applied to the digitised interferometric signal. For the calculation of the PSF, a windowing function is applied to the raw signal and then the array is padded such as the total number of points is a power of 2. Depending on the window function a different result for the peak to side-lobe is obtained. The window applied here is Blackman-Harris as it particularly emphasizes the dynamic range in the PSF. Alternatively, a Hamming window can be applied but it generally produces a lower dynamic range than a Blackman-Harris window. More information about window functions and FFT padding can be found in Appendix A.

After the raw signal is windowed and padded, the Discrete Fourier Transform (DFT) is performed based on Equation (3.30). To describe the imaging performance of an SD-OCT or SS-OCT system, it is common to calculate the square of the magnitude after the FFT [150] or to use $20 \cdot \log_{10}$ [151] when plotting the "electrical PSF" (PSF_e). Finally, the power converted to logarithmic scale is

$$\mathrm{PSF}_\mathrm{e}^\mathrm{dB}(f) = 10 \cdot \log_{10} |S_{\mathrm{xx}}(f)|^2 . \tag{3.31}$$

The result of the PSF calculation for the signal from Figure 3.5 can be seen in Figure 3.6. Peak to side-lobe and peak to noise-floor ratios vary with the sweep rate, but typically the laser can achieve 45 dB to 60 dB and 55 dB to 80 dB respectively. Here, the Peak to Side-lobe Ratio is equal to 43 dB while Peak to Noise Ratio approximately 50 dB.

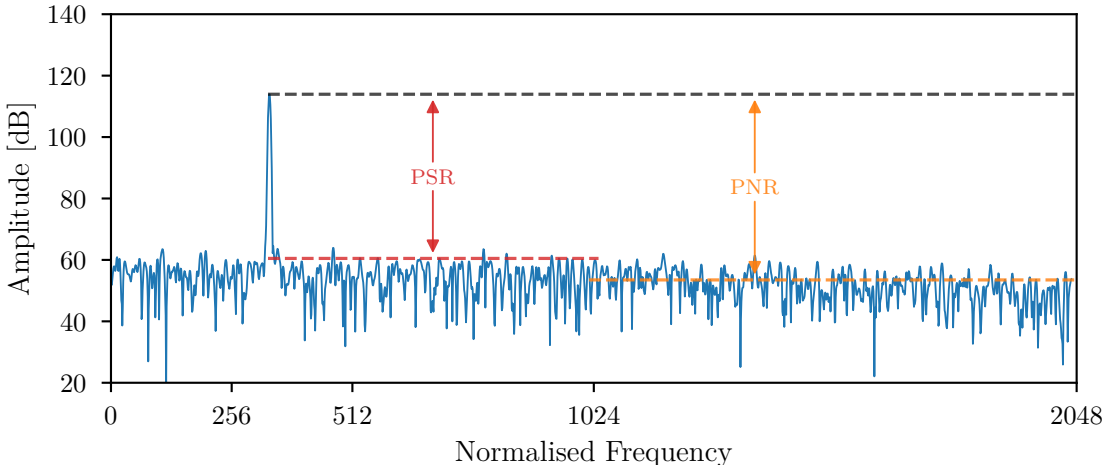

Figure 3.6: *Point-spread function (PSF) of an akinetic laser for a 100 kHz sweep. The peak–to–side-lobe ratio (PSR) and peak–to–noise (PNR) in this case are 43 dB and 50 dB respectively. These ratios facilitate an image with low artefacts and high contrast.*

However, depending on the room conditions like temperature or humidity the output of the laser can degrade. This can be fixed by performing frequent sweep

calibrations, especially between measurements if there is a long time interval between the two. To illustrate the problems that can arise, Figure 3.7 shows an excerpt from the acquired raw interferometric signal after a calibration. The signal contains a series of phase discontinuities and various random glitches.

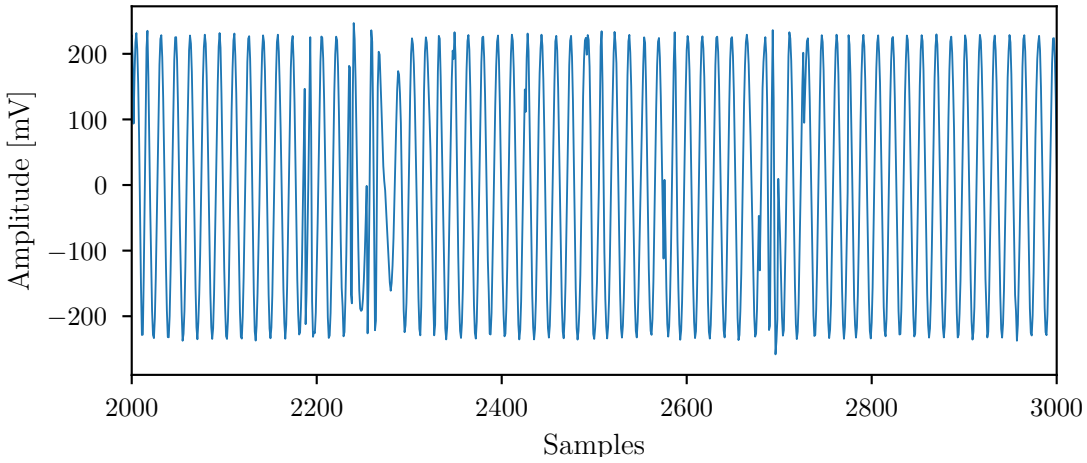

Figure 3.7: *Raw optical signal from the internal interferometer while the output of the laser was degraded. These phase discontinuities lead to OCT image artefacts and low image contrast and detail.*

These phase discontinuities lead to OCT image artefacts that lower the contrast and detail. Specifically, it lowers the peak to side-lobe ratio meaning that fine details in the image cannot be detected. This can be seen in the point-spread function shown in Figure 3.8 that was calculated from the raw interferometric signal shown in Figure 3.7. The Point Spread Function is degraded, compared to the one from Figure 3.6, as the Peak to Side-lobe Ratio (PSR) is equal to 21 dB compared to 43 dB, while Peak to Noise Ratio (PNR) is 44 dB compared to 50 dB. Interestingly, the noise floor on both point-spread functions is approximately the same, however the peak and the side-lobes are higher in the second one. It can be thought as the signal-to-noise ratio has been compressed. Notably, a decrease by 3 dB is equivalent to halving the power, thus a difference of 20 dB—as is the case for PSR—means that it decreased 100 times. When the laser output is degraded this much, a baseline calibration must be performed.

Usually, the laser must be calibrated before use and subsequently every few hours in order to maintain a clean output. This calibration is known as user calibration and it calibrates the output over the bandwidth of the sweep. However, over longer periods of time (e.g. weeks), as the output of the laser deteriorates, a different calibration must be performed. This is known as baseline calibration, it calibrates the output across the full bandwidth of the laser at the slowest sweep rate; this calibration can be thought as a factory reset.

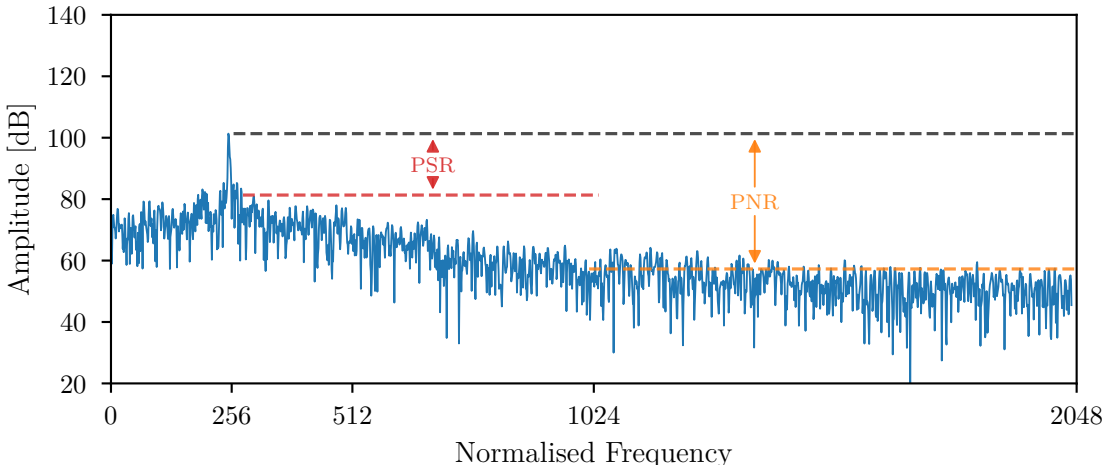

Figure 3.8: *Point-spread function (PSF) of an akinetic laser for a 100 kHz sweep. The peak–to–side-lobe ratio (PSR) and peak–to–noise (PNR) in this case are 21 dB and 44 dB respectively. This reduction is caused by phase discontinuities that appear on the raw interferometric signal.*

3.4.3 Relative Intensity Noise (RIN)

Relative Intensity Noise (RIN) describes the instability in the power level of a laser. Intensity noise is usually quantified as RIN, i.e. as noise of the power divided by the average power. Relative intensity noise is generated either from cavity vibrations or fluctuations in the laser gain medium. The optical power of the laser can be defined as

$$P(t) = \langle P \rangle + \delta P(t)\,, \tag{3.32}$$

where $\langle P \rangle$ is the average power and $\delta P(t)$ is the fluctuating quantity with zero-mean value. The relative intensity noise can then be statistically described with a Power Spectral Density (PSD) which depends on the noise frequency f. Based on Section 3.4.2.3, the relative intensity noise can be statistically described with the Fourier transform of the autocorrelation function of the normalized power fluctuations as

$$S_{\mathrm{I}}(f) = \frac{2}{\langle P \rangle^2} \int_{-\infty}^{\infty} \langle \delta P(t) \delta P(t+\tau) \rangle \cdot \mathrm{e}^{-\mathrm{j}\pi f \tau}\, \mathrm{d}\tau\,, \tag{3.33}$$

where $\langle P \rangle$ is the average laser power and δP is the normalised power.

Akinetic lasers can achieve low intensity noise inherent of the small cavity dimensions as RIN is generated by cavity vibrations or fluctuation. This means in OCT systems, RIN can be reduced by using balanced-detection as discussed in Section 4.3.7. In akinetic lasers with low RIN and a combination of a custom power profile, high-sensitivity can be achieved.

3.4.4 Data Valid Vector

The laser used for the measurements in later chapters has a particular mode of operation in order to generate the points of the sweep. By regulating the currents that drive the laser diode it switches from different modes of operation. When a mode change happens, momentarily, the output of the laser can be considered unstable or erratic. Thus, for those points the output is invalid and it must not be taken into account during post-processing the data.

The place of the invalid points across the sweep is predetermined at the calibration stage. To ease the post-processing an array containing the indices where those invalid points occur can be exported from the laser. This array is the Data Invalid Vector (DIV), or its complementary array, the Data Valid Vector (DVV)—it contains the indices of the valid points. The application of the DVV is important for the processing of the data, as without it the collected data are unusable due to incorrect wavelength points being present. Having the invalid points included on the Fourier transform alters the waveform reducing the SNR and introducing image artefacts.

To better illustrate the effects of the invalid points and the significance of the data valid vector an OCT image was captured using the system described in Section 5.4. The microfluidic chip from Section 6.7 was used as the test subject. The laser was set to sweep at 96 kHz over the bandwidth of 82 nm. The total number of sweep points was set to 4096—which is convenient for the acquisition as it is a power of two (2^{12}). Based on the DVV the number of valid points was 2785.

As there is a small delay—due to optical path length–between the laser generating a new wavelength point and that being captured by the acquisition card, the Data Valid Vector (DVV) cannot be applied directly to the captured data. Instead, as the DVV is an array, in order to match the valid points of the DVV with the valid points on the captured data the array element must be rolled over their axis by an amount of places equal to the delay. The array elements that roll beyond the last position are re-introduced at the first. Based on the delay of the optical setup the DVV must rolled by 87 places, thus for the illustration the following roll values were chosen: 67, 77, 87, and 97. For the comparison four data valid vectors are produced by rolling the original data valid vector the amount of places indicated. Then, the new data valid vectors are used to extract the valid sweep points from the captured data, thus generating four signals. These signals are Fourier transformed to generate four cross-sectional images (B-scans) where the pixel intensities correspond to the amplitude of the transform in dB. For the comparison the pixel values are normalised to the range $[0, 1]$. The result can be seen in Figure 3.9.

Above each image the histogram of the normalised pixel intensities is displayed. For the histogram, the pixel values are separated into 50 bins. The frequency axis of the histogram is in logarithmic scale to allow the full range of values to be displayed.

Based on the test object that was used for the measurement, the B-scan image must contain four horizontal lines. Two lines for the top and bottom of the chip and another two for the top and bottom of the microfluidic channel.

Specifically,

- 1st line: top of the chip
- 2nd line: top of the channel
- 3rd line: bottom of the channel
- 4th line: bottom of the chip

The chip is 2 mm thick with a 700 µm deep channel and the lid has a thickness of 175 µm. Hence, the lines must appear at 0 µm, 175 µm, 875 µm, and 2 mm. Only Figure 3.9c shows all the lines clearly as this image corresponds to the one with the correct DVV applied. Notably, it is also the one with a differently shaped histogram. The majority of pixels have an intensity below 0.75 which indicates that the SNR has improved and as a consequence the image has better contrast compared to the other three. Furthermore, the information from the histogram can be used to discard the noise of the image by isolating the pixels with intensities above a certain threshold as is later discussed in Section 6.5.1.

Additionally, Figure 3.9d has slightly more contrast than Figure 3.9b despite both using a DVV with 10 places distance above or below 87. When the DVV does not match the captured data, a portion of valid points is withdrawn instead of the invalid ones. Furthermore, the invalid points are not equally spread over the length of the sweep but there are clusters of invalid points instead. Thus, in Figure 3.9d the portion of valid points withdrawn is smaller than Figure 3.9b, leading to an image with a slightly better SNR.

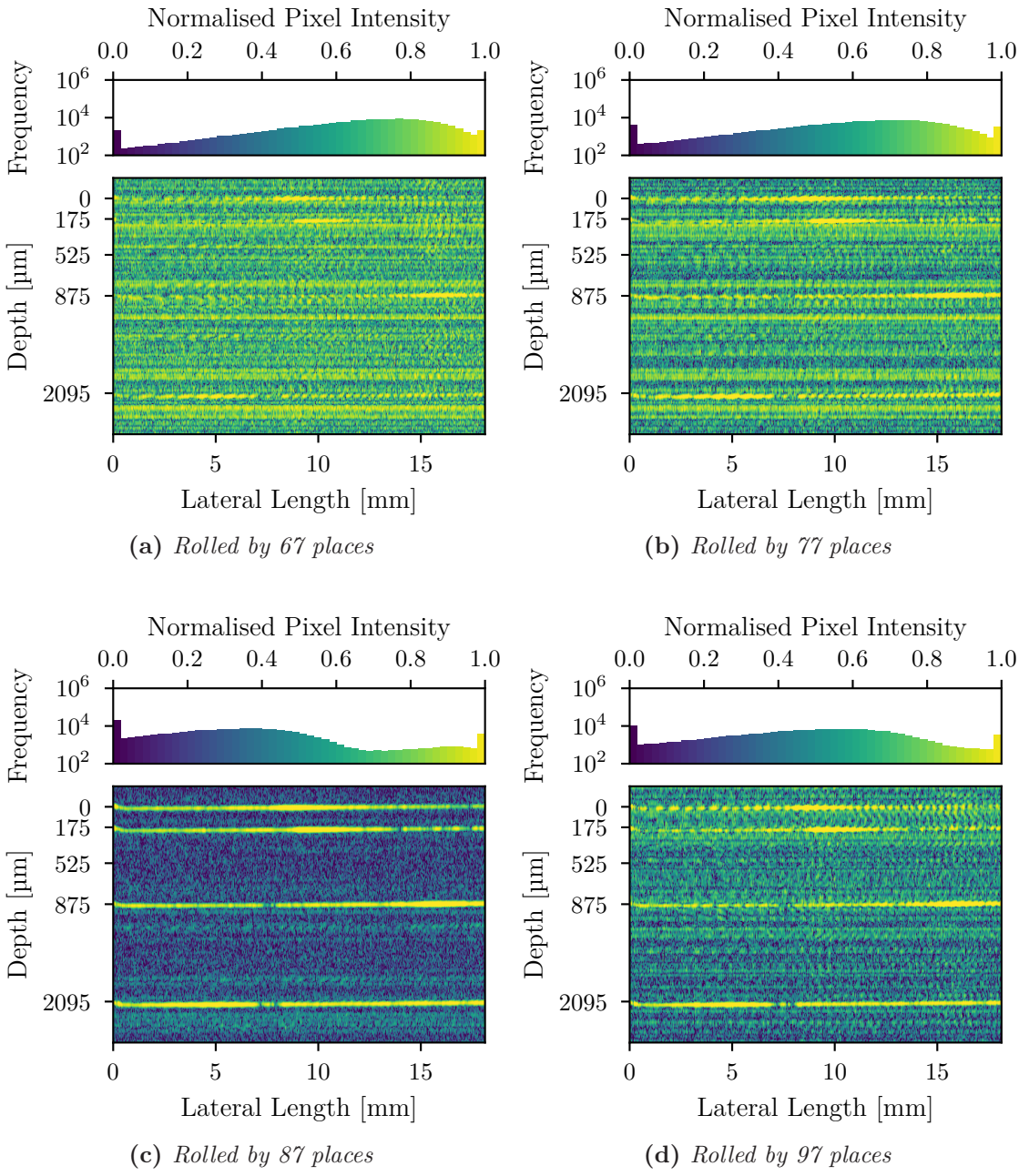

(a) *Rolled by 67 places*

(b) *Rolled by 77 places*

(c) *Rolled by 87 places*

(d) *Rolled by 97 places*

Figure 3.9: *B-scan image comparison of the effects of Data Valid Vector on OCT image quality. The DVV must extract only the valid points of the sweep as otherwise it leads to OCT images with poor contrast and low SNR (a,b,d). When the DVV is properly shifted to match the valid points of the sweep (c) the OCT image gains contrast and improved SNR. The histogram is a good indicator of the contrast in the image.*

Chapter 4

Multi-beam OCT

4.1 Introduction

In this chapter, the theory behind Multiple Beam Dual Optical Coherence Tomography systems is analysed. Depending on the arrangement of the beams, either *coplanar* or *parallel*, the system can achieve high speed flow acquisition, either in two (*coplanar*) or three dimensions (*parallel*), while requiring only a single access port to the sample.

In the first section, the theory for a single beam SS-OCT system is explained and serves as the base for the rest of the systems. In later sections, the different modes of multi-beam systems are discussed.

At the end of the chapter, the differences between the different systems and possible improvements for future research are discussed, before concluding with a brief summary.

4.2 Modes of Operation

The multiple beam system must be thought of as an n-beams system where n is the number of beams. These systems can be categorised based on the number of beams used as well as the orientation of them in relation to the scanning direction. There are four modes for multiple beam OCT systems. The first mode, where $n = 1$, is identical to the standard SS-OCT and its behaviour is the same regardless of the scanning direction, unlike the other modes. The main advantage of the multi-beam modes, is the acquisition speed increase that allows the tracking of particles with higher velocities.

Single Beam: This is a typical OCT setup where a single beam is scanned on a linear path over the sample producing an array of 1D scans that compose a 2D image.

Multi Beam — coplanar (non-overlapping): In this mode, multiple beams are arranged longitudinally to the scanning direction and spaced appropriately to allow the acquisition of image planes with no overlapping regions. The speed increase is proportional to the number of beams.

Multi Beam — coplanar (overlapping): Similar to non-overlapping but with smaller beam separation that allows the acquisition of image planes with a certain degree of overlap between them. The speed increase is inversely proportional to the distance between the beams.

Multi Beam — volumetric: Similar to the single beam system but able to capture multiple parallel image planes simultaneously, thus producing a volumetric representation of the sample.

4.3 Single Beam

In the simplest form of an SS-OCT system, light from a swept wavelength laser passes through a beam-splitter, that splits the light into two arms. The first is called the *reference arm* and is terminated with a mirror, whereas the second goes to the sample and is known as the *sample arm*. Such a system is only able to capture axial scans (A-scans) of a sample at a given location. In order to be able to produce two-dimensional cross-sections (B-scans), a galvanometer mirror must be placed before the sample to scan the beam across a path that will determine the captured length of the final image.

Figure 4.1a shows the diagram of a typical fibre optic SS-OCT system. A swept wavelength laser is connected to a beam-splitter that splits the light into two different paths, the reference and the sample. The use of the galvanometer mounted mirror allows the beam to be scanned along a path on the surface the sample, thus acquiring multiple A-scans for different locations. When those are assembled, they form a cross-sectional image better known as a B-scan. The reflected light from both the sample and reference, interferes in the beam-splitter and the result is output at the bottom left port of the beam-splitter where it is collected by the photodetector.

To increase the SNR of the system instead of a single photodetector, a specialised balanced detector, with two inputs, is utilised. Using a balanced detector requires the addition of a circulator (Figure 4.1b), as it requires two anti-phase signals. The use of the circulator eliminates the need of an attenuator to match the power between the balanced detector inputs. If a beam-splitter was used instead of the circulator

(Figure 4.1c) the attenuator would be required to match the optical power—the light for left input passes through a second beam-splitter. The balanced detector will subtract the two signals, as they are anti-phase the common parts will be amplified, whereas the noise will be subtracted.

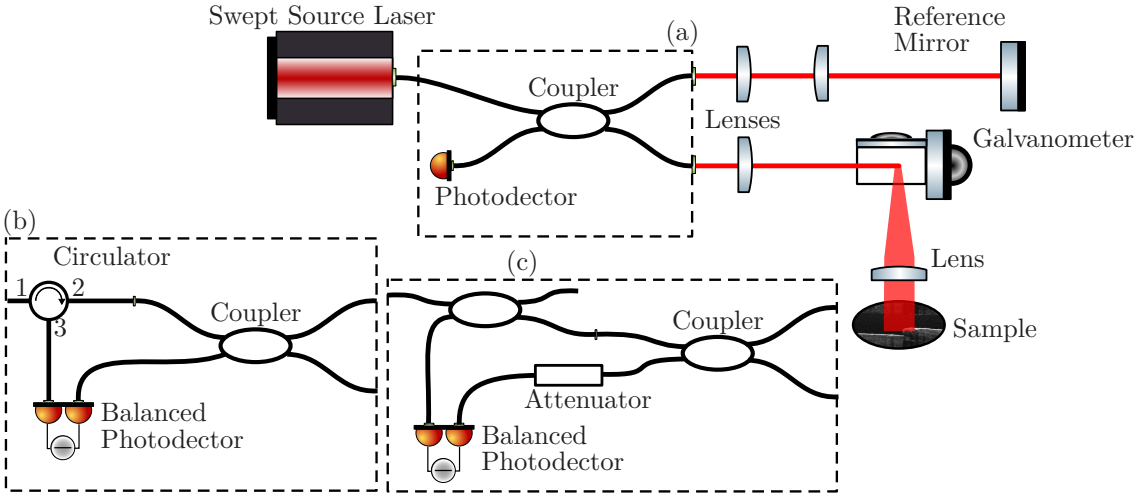

Figure 4.1: *The optical diagram for a typical SS-OCT system. Light from a swept wavelength laser passes through a beam-splitter, that splits the light to two arms. The first is called the* reference arm *and is terminated with a mirror, whereas the second goes to the sample and is known as the* sample arm. *A galvanometer mirror is placed before the sample and will scan across a path that will determine the captured cross-section. For balanced detection (a) is substituted for (b) or (c). However, (c) requires more components and wastes optical power.*

The performance of an SS-OCT system can be measured by either measuring or calculating a set of properties that govern the system. To characterise the speed, the A-scan/B-scan and acquisition rates must be measured. The depth of field is used to determine the image quality. Similarly, the depth, lateral, and B-scan resolutions determine the image resolution. Additionally, the noise of the system has to be measured.

4.3.1 Depth Resolution

The depth resolution is also called “axial resolution” and is dependent on the wavelength as well as the bandwidth of the swept source. In an interferometer like the one in Figure 4.2 the laser has a bandwidth $\Delta\lambda$ equal to $\lambda_2 - \lambda_1$. The two mirrors are located at a distance L_1 and L_2 from the beam splitter respectively.

When the light from a swept wavelength laser meets a beam splitter, it splits into two beams that travel a distance L_1 and L_2 respectively until they arrive at the

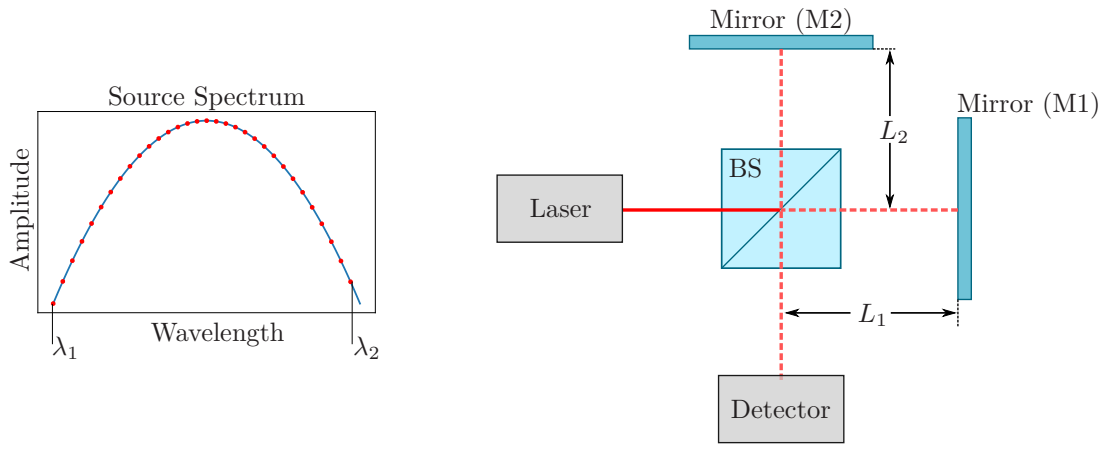

Figure 4.2: *Beam splitter interferometer and laser source spectrum.*

reflective surface of a mirror. Let λ_1 and λ_2 be the first and last wavelength of the sweep. The phase of a wave that is propagating in a medium with refractive index n is given by

$$\phi = \frac{2\pi n}{\lambda} x \,, \tag{4.1}$$

where λ is the wavelength of the wave and x is the total distance the wave has travelled [152]. Thus, the phase of the waves with wavelengths on either edge of the source bandwidth (λ_1, λ_2) for the first beam—after it has travelled from the beam splitter to the mirror (M1) and back—will be

$$\phi^{\lambda_1} = \frac{2\pi n}{\lambda_1}(2 \cdot L_1) = \frac{4\pi n}{\lambda_1} L_1, \quad \phi^{\lambda_2} = \frac{2\pi n}{\lambda_2}(2 \cdot L_1) = \frac{4\pi n}{\lambda_2} L_1 \,. \tag{4.2}$$

Likewise for the second beam, the phases are

$$\phi^{\lambda_1} = \frac{2\pi n}{\lambda_1}(2 \cdot L_2) = \frac{4\pi n}{\lambda_1} L_2, \quad \phi^{\lambda_2} = \frac{2\pi n}{\lambda_2}(2 \cdot L_2) = \frac{4\pi n}{\lambda_2} L_2 \,. \tag{4.3}$$

The phase difference between the two beams for each wavelength can be calculated using

$$\Delta\phi = \phi_2 - \phi_1 \,. \tag{4.4}$$

Substituting the values of ϕ_1 and ϕ_2 from (4.2) and (4.3) respectively into Equation (4.4) yields

$$\Delta\phi^{\lambda_1} = \frac{4\pi n}{\lambda_1} L_2 - \frac{4\pi n}{\lambda_1} L_1 = \frac{4\pi n}{\lambda_1}(L_2 - L_1) = \frac{4\pi n}{\lambda_1} \Delta L \quad \text{and} \tag{4.5}$$

$$\Delta\phi^{\lambda_2} = \frac{4\pi n}{\lambda_2} L_2 - \frac{4\pi n}{\lambda_2} L_1 = \frac{4\pi n}{\lambda_2}(L_2 - L_1) = \frac{4\pi n}{\lambda_2} \Delta L \,. \tag{4.6}$$

Finally, the difference in phase for both wavelengths $\Delta(\Delta\phi)$ will be

$$\begin{aligned}\Delta(\Delta\phi) = \Delta\phi^{\lambda_2} - \Delta\phi^{\lambda_1} &= \frac{4\pi n\Delta L}{\lambda_2} - \frac{4\pi n\Delta L}{\lambda_1} \\ &= 4\pi n\Delta L\left(\frac{\lambda_2 - \lambda_1}{\lambda_1\lambda_2}\right) \\ &= 4\pi n\Delta L\left(\frac{\Delta\lambda}{\lambda_1\lambda_2}\right).\end{aligned} \tag{4.7}$$

In order to sample the interference fringes, a sampling frequency f_s that will satisfy the Nyquist's criterion must be chosen. According to the criterion, perfect reconstruction is guaranteed possible for a band-limit $B < f_\mathrm{s}/2$. Let N the number of points captured with a sampling frequency f_s and M the number of fringes captured. Then, the number of fringes per acquisition is defined as

$$M = \frac{N}{2}\,. \tag{4.8}$$

Assume a sine wave with frequency ν, its phase will be

$$\phi = 2\pi\nu\,, \tag{4.9}$$

where the frequency ν in units of captured points is equal to $N/2$. Equalising Equations (4.7) and (4.9) and solving for ΔL to get the acquired depth yields

$$\begin{aligned} & 4\pi n\Delta L\left(\frac{\Delta\lambda}{\lambda_1\lambda_2}\right) = 2\pi\nu \\ \Longrightarrow \quad & 4\pi n\Delta L\left(\frac{\Delta\lambda}{\lambda_1\lambda_2}\right) = 2\pi\frac{N}{2} \\ \Longrightarrow \quad & 2\Delta L = \frac{\lambda_1\lambda_2}{n\Delta\lambda}\frac{N}{2} \\ \Longrightarrow \quad & \Delta L = \frac{N}{4}\frac{\lambda_1\lambda_2}{n\Delta\lambda} \end{aligned} \tag{4.10}$$

The maximum one-sided imaging depth Δz is equal to ΔL, so (4.10) can be rewritten as

$$\Delta z = \frac{N}{4}\frac{\lambda_1\lambda_2}{n\Delta\lambda} = \frac{\lambda_1\lambda_2}{4n\delta\lambda} \approx \frac{\lambda_0^2}{4n\delta\lambda}\,, \tag{4.11}$$

where $\delta\lambda = \Delta\lambda/N$ is the sampling wavelength interval [153] and λ_0 the centre wavelength of the source. If the instantaneous linewidth is smaller than the sampling interval the amplitude of the coherence function will decay with distance, limiting

the usable ranging depth. Additionally, the depth at which the sensitivity falls off by a factor of 1/2 or 6 dB in optical SNR units [79] is given by

$$\Delta z_{6\,\mathrm{dB}} = \frac{4\ln 2}{\pi}\frac{\lambda_1\lambda_2}{4n\delta\lambda} = \frac{\ln 2}{\pi}\frac{\lambda_1\lambda_2}{n\delta\lambda}\,. \tag{4.12}$$

Moreover, the coherence length l_c is equal to

$$l_\mathrm{c} = \frac{\lambda_1\lambda_2}{2n\Delta\lambda} \approx \frac{\lambda_0^2}{2n\Delta\lambda}\,, \tag{4.13}$$

as the imaging depth captures the double path in the interferometer and is therefore half the coherence length of the source. Furthermore, the axial resolution of OCT is equal to the 6 dB falloff point of the coherence length for a Gaussian beam . However, depending on the type of the laser a correction factor must be applied [154], thus the axial resolution can be generalised as

$$\delta z = \gamma \cdot \frac{2\ln(2)}{\pi n}\frac{\lambda_0^2}{\Delta\lambda}\,, \tag{4.14}$$

where γ is the correction factor and accounts for the fact that many broadband SLEDs do not have a perfect Gaussian shape but rather a more flat-top profile. For lasers with a Gaussian power profile γ is unity, while for flat-top profiles a factor of $\gamma = 1.186$ is typically used.

Using Equation (4.14) the axial resolution can be calculated for different centre wavelengths and light source bandwidths, the result is shown in Figure 4.3. It shows the axial resolution versus light source bandwidths for centre wavelengths of 980 nm, 1310 nm, and 1550 nm; typical of those used in OCT instrumentation. Based on the graph, micron scale axial resolution requires broad optical bandwidths and bandwidth requirements increase dramatically for longer wavelengths.

4.3.2 Lateral Resolution and Depth of Field

Lateral resolution, also known as “transverse resolution” is the same as in optical microscopy and is determined by the diffraction limited spot size of the focused beam. The diffraction limited minimum spot size is proportional to wavelength and inversely proportional to the Numerical Aperture (NA) or the focusing angle of the beam. The depth of field of the system is equal to the confocal parameter b and is proportional to the Rayleigh range Z_R.

4.3.2.1 Numerical Aperture

When a collimated beam with diameter d is incident onto an objective lens with a focal length f, then the beam will be focused on a point along the optical axis after

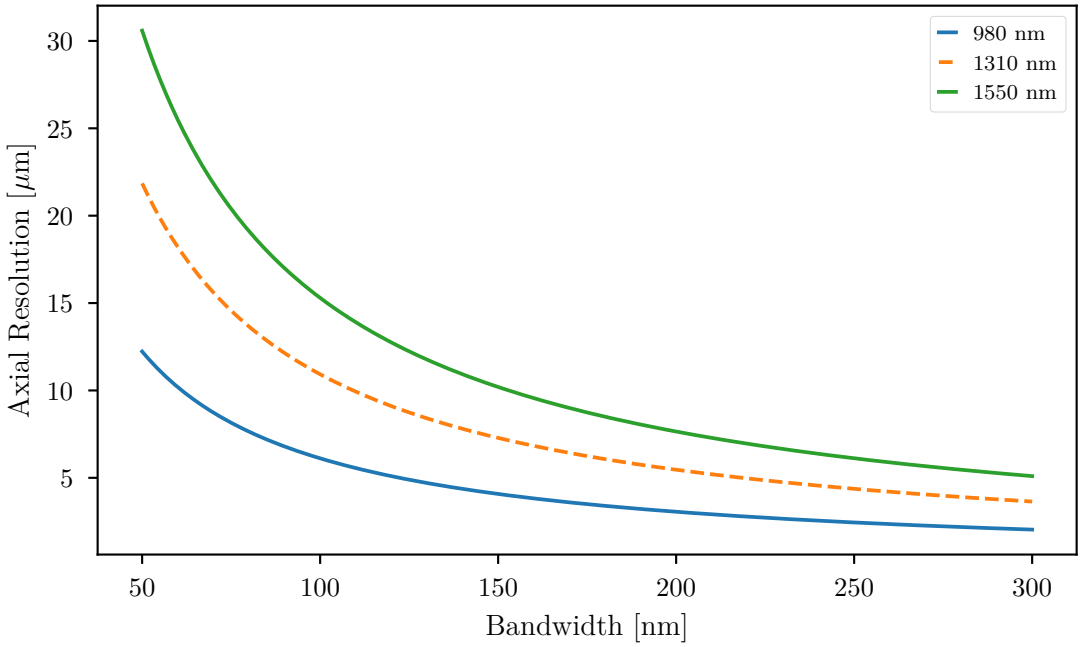

Figure 4.3: *Axial resolution versus light source bandwidths for centre wavelengths of 980 nm, 1310 nm, and 1550 nm. Micron scale axial resolution requires broad optical bandwidths and bandwidth requirements increase dramatically for longer wavelengths.*

the lens at a distance equal to the focal length. The Numerical Aperture (NA) of a lens with a focusing angle θ [46] is given by

$$\mathrm{NA} = \mathrm{n}\sin\theta_{\mathrm{div}} = \mathrm{n}\sin\left(\arctan\left(\frac{\mathrm{d}}{\mathrm{f}}\right)\right) \approx \mathrm{n}\frac{\mathrm{d}}{2\mathrm{f}}\,, \tag{4.15}$$

where n is the refractive index of the medium in with the beam propagates, usually this is air so $n = 1$, d the size of the incident beam on the lens, and f is the focal length. The approximation holds when the numerical aperture is small.

A diagram of the focusing beam can be seen in Figure 4.4. The collimated beam will be focused to a focal point F that is located a distance equal to the focal length f. For small focusing angles in radians ($\theta_{\mathrm{div}} \ll 1\,\mathrm{rad}$) the NA is equal to $d/(2f)$. The focusing angle is also known as the "half-divergence angle".

4.3.2.2 Paraxial Approximation

In geometric optics, the paraxial approximation is a small-angle approximation used in Gaussian optics and ray tracing of light through an optical system (such as a

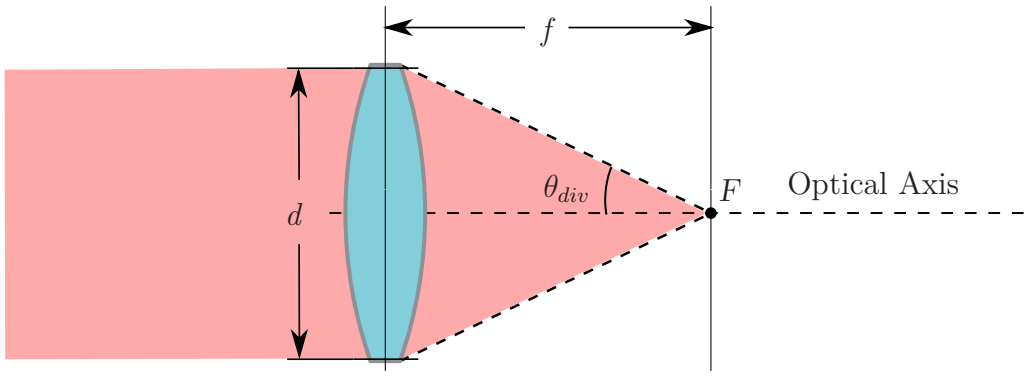

Figure 4.4: *A collimated beam passes through a focusing lens. The diameter of the incident beam on the objective lens is equal to d. The beam will be focused to a focal point F after the lens at a distance f, equal to the focal length of the lens. The angle* θ_{div} *between the optical axis and the marginal ray is called "half-divergence angle".*

lens). A paraxial ray is a ray which makes a small angle (θ) to the optical axis of the system, and lies close to the axis throughout the system [155]. The paraxial approximation allows three important approximations for angles in radians that simplify the calculation of the ray's path. These approximations are

$$\sin\theta \approx \tan\theta \approx \theta \quad \text{and} \quad \cos\theta \approx 1\,. \tag{4.16}$$

In OCT lateral resolutions below 10 µm can be achieved with low numerical aperture optics (0.1–0.3). Techniques such as Optical Coherence Microscopy (OCM), can achieve sufficient transverse resolutions (<5 µm) in the range of 0.2 to 0.5 NA and lower, despite the rapid degradation of the axial resolution seen in confocal microscopy [156]. At these NA ranges the approximation error is below 5 %, thus throughout the following sections the paraxial approximation will be used to simplify the equations.

4.3.2.3 Gaussian Beams

An important attribute of Gaussian beams is the variation of the spot size $w(z)$ with distance. Let the lowest-order Gaussian beam that is characterised by a spot size w and has a planar wavefront in the transverse dimension z. The spot size w for any given distance along z axis is given by

$$w(z) = w_0\sqrt{1+\left(\frac{z}{z_{\mathrm{R}}}\right)^2}\,, \tag{4.17}$$

where w_0 is the beam waist radius, z the distance along the transverse axis, and z_{R} the Rayleigh range [157]. For simplicity, at $z = 0$ the radius of the spot size is equal to w_0 and is the diffraction limited spot size of a focused beam. This point is known

as the beam waist and w_0 is the beam waist radius. All the important factors of the Gaussian beam will be related to the beam waist and Rayleigh range.

As shown in Figure 4.5, the spot size is at its minimum for $z = 0$ when the beam waist is equal to $2w_0$. The total angular spread Θ_{div} of the beam is twice the half-divergence angle θ_{div}. Interestingly, with a tighter spot size the beam expands rapidly due to diffraction. Additionally, the beam will be collimated over a shorter distance in the near-field. Increasing the spot size allows the beam to be focused over a longer distance.

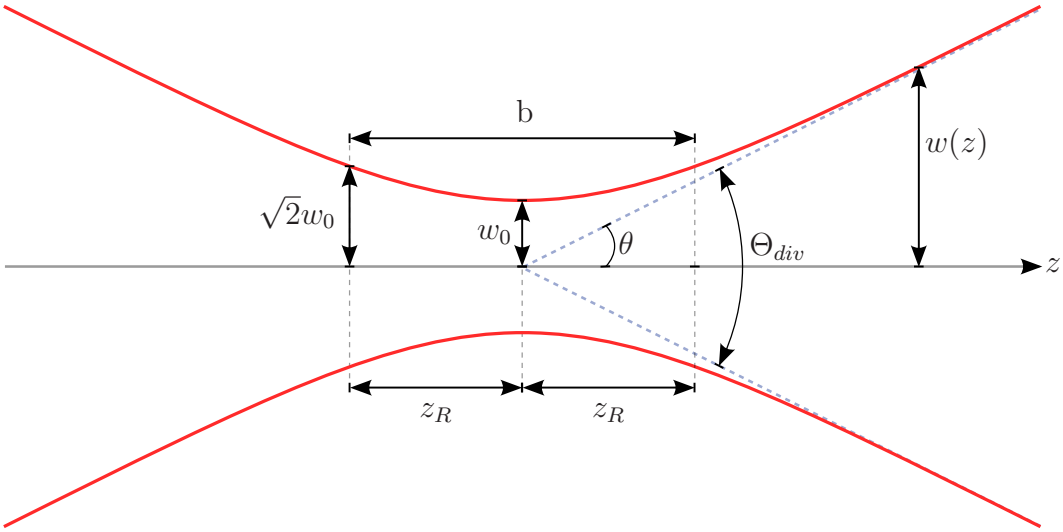

This is a derivative of "Diagram of Gaussian beam waist parameters" by Rodolfo Hermans, used under CC BY-SA 3.0. The derivative is licensed under CC BY-SA 3.0 by Evangelos Rigas.

Figure 4.5: *Gaussian beam width $w(z)$ as a function of the distance z along the beam. At a distance from the waist equal to the Rayleigh range z_{R}, the width W of the beam is $\sqrt{2}$ larger than it is at the focus where $w = w_0$, the beam waist. The distance between the two points $z = \pm z_{\text{R}}$ is called the confocal parameter b or depth of field of the beam. Θ denotes the total angular spread.*

Moreover, starting from the beam waist, the distance at which the beam radius increases by $\sqrt{2}$ or equally the beam area doubles, is known as the "Rayleigh range" and is given by

$$z_{\text{R}} = \frac{\pi n w_0^2}{\lambda} \quad \text{"Rayleigh range"}\,, \tag{4.18}$$

where λ is the wavelength of the Gaussian beam and n the refractive index of the propagation medium [157]. The Rayleigh range marks the approximate dividing line between the "near-field" or Fresnel and the "far-field" or Fraunhofer regions for a beam propagating out from a Gaussian waist.

4.3.2.4 Depth of Field

Let a Gaussian beam that is focused from an aperture D down to a waist with diameter $2w_0$. The full distance between the $\sqrt{2}w_0$ spot size points, i.e. twice the Rayleigh range, is the quantity known as the confocal parameter [157] and is equal to

$$b = 2z_{\mathrm{R}} = \frac{2\pi n w_0^2}{\lambda}\,. \tag{4.19}$$

For OCT, the distance between the $\sqrt{2}w_0$ spot size points marks the region where everything inside will be in focus. This means that b is equal to the depth of field of the system. Based on Equation (4.19) the depth of field is inversely proportional to the central wavelength of the beam and proportional to the square of the spot radius, i.e. the spot area.

4.3.2.5 Far-Field Beam Angle: The "Top Hat" Criterion

At the far-field ($z \gg z_{\mathrm{R}}$), where the beam expands linearly with distance, using Equation (4.17), the $1/e$ spot size $w(z)$ for the field amplitude in the far field for a Gaussian beam coming from a waist with spot size w_0 is given by

$$w(z) = \frac{w_0 z}{z_{\mathrm{R}}} = \frac{\lambda z}{\pi n w_0}, \qquad z \gg z_{\mathrm{R}}\,. \tag{4.20}$$

For a diffraction-limited Gaussian beam, the $1/\mathrm{e}^2$ beam divergence half-angle is $\lambda/(\pi n w_0)$,

$$\theta_{\mathrm{e}^{-2}} \simeq \frac{\lambda}{\pi n w_0}\,, \tag{4.21}$$

where λ is the wavelength (in the medium) and w_0 the beam radius at the beam waist [157]. This equation is based on the paraxial approximation [155], and is thus valid *only* for beams with moderately strong divergence.

4.3.2.6 Far-Field Beam Angle: The 1/e Criterion

Another definition for the far-field beam angle is to use the 1/e or 86% criterion for the beam diameter, so that the far field half-angular spread is defined by the width corresponding to the $1/e$ point for the electric field amplitude at large z [157], i.e.

$$\theta_{\mathrm{e}^{-1}} = \lim_{z\to\infty} \frac{w(z)}{z} = \frac{\lambda}{\pi n w_0}\,. \tag{4.22}$$

The full angular spread Θ_{div} is twice the far-field beam angle, thus from (4.22) is equal to

$$\Theta_{\text{div}} = \frac{2\lambda}{\pi n w_0}\,. \tag{4.23}$$

Similarly, from Figure 4.5 and using basic trigonometry, $\theta_{\text{e}^{-1}}$ will be equal to

$$\theta_{\text{e}^{-1}} = arctan\left(\frac{w_0}{z_{\text{R}}}\right). \tag{4.24}$$

Using the paraxial approximation ($tan\theta \approx \theta$) leads to $\theta_{\text{e}^{-1}} = {}^{w_0}/_{z_{\text{R}}}$. Then, the full angular spread will approximately be

$$\Theta_{\text{div}} \approx 2\frac{w_0}{z_{\text{R}}}\,. \tag{4.25}$$

4.3.2.7 Lateral Resolution

In OCT the lateral resolution δx, as in conventional microscopy, is equal to the spot size at the beam waist [158]. This means that the lateral resolution is equal to

$$\delta x = 2w_0\,. \tag{4.26}$$

The smaller the spot size at the beam waist, the better the resolution, as a smaller size means that there is a smaller region that is averaged to produce a single point. The lateral resolution can be related to the half-divergence angle or the full angular spread using (4.22) and (4.23) and solving for $2w_0$ gives

$$\begin{aligned} \Theta_{\text{div}} &= \frac{2\lambda}{\pi n w_0} \\ \Longrightarrow \qquad w_0 &= \frac{2\lambda}{\pi n \Theta_{\text{div}}} \\ \Longrightarrow \qquad 2w_0 &= \frac{4\lambda}{\pi n \Theta_{\text{div}}} = \frac{2\lambda}{\pi n \theta_{\text{e}^{-1}}}\,. \end{aligned} \tag{4.27}$$

Substituting $2w_0$ from Equation (4.27) into (4.26) leads to

$$\delta x = 2w_0 = \frac{4\lambda}{\pi n \Theta_{\text{div}}}\,. \tag{4.28}$$

Using the lens from Figure 4.4 the lateral resolution can be rewritten to take into account the spot size of the incident beam d and the focal length f. From

Equation (4.15) and using the paraxial approximation the half-divergence angle θ_{div} is equal to $d/2f$. Additionally, this angle is the $\theta_{\text{e}^{-1}}$, thus (4.28) becomes

$$\left.\begin{aligned} \delta x &= \frac{2\lambda}{\pi n \theta_{\text{e}^{-1}}} \\ \theta_{\text{div}} &= \frac{d}{2f} \\ \theta_{\text{div}} &\equiv \theta_{\text{e}^{-1}} \end{aligned}\right\} \implies \delta x = \frac{2\lambda}{\pi n}\frac{2f}{d}\,. \tag{4.29}$$

Finally, the lateral resolution is equal to

$$\delta x = 2w_0 = \frac{4\lambda}{\pi n}\frac{f}{d}\,, \tag{4.30}$$

where d is the spot size of the beam on the objective lens, f is the focal length [158].

From Equation (4.30) it can be seen that the beam waist is inversely proportional to the collimated beam spot area hitting the lens. This means that the resolution increases proportionally with the lens aperture. Conversely, the resolution will increase by lower the focal length of the lens.

The NA of a lens used for focusing a laser beam determines the minimum possible beam radius in the focus (beam waist) to $\lambda/(\pi\text{NA})$, assuming a collimated Gaussian beam (i.e. having diffraction-limited beam quality) with correct input beam radius hits the lens. In such cases, the numerical aperture is not defined via a marginal ray, but based on the maximum beam divergence half-angle which the lens can handle without truncation or excessive aberrations. The higher the Numerical Aperture (NA) the finer the transverse resolution.

The numerical aperture of a Gaussian beam is defined to be $\text{NA} = \text{n}\sin\theta_{\text{e}^{-1}}$, where n is the index of refraction of the medium through which the beam propagates. Substituting NA for $\theta_{\text{e}^{-1}}$ in $\theta_{\text{e}^{-1}} = w_0/z_{\text{R}}$ and subsequently solving for z_{R} gives the Rayleigh range in relation to the numerical aperture. This means that the Rayleigh range is related to the numerical aperture by

$$z_{\text{R}} = \frac{w_0}{\text{NA}}\,. \tag{4.31}$$

Finally, the confocal parameter b can be expressed in relation to the lateral resolution as

$$b = \frac{\pi n \delta x^2}{2\lambda}\,, \tag{4.32}$$

where δx is the lateral resolution [158]. The depth of field is proportional to the square of the lateral resolution and increasing the Numerical Aperture increases the transverse resolution. However, increasing the transverse resolution (decreasing the spot size), decreases the depth of field.

4.3.2.8 Summary

To summarise, the lateral (transverse) resolution and depth of field are dependent on the optics used such as lenses and the beam quality. The collimation and the lens will affect the Numerical Aperture (NA) and subsequently will affect the spot size at the beam waist that corresponds to the resolution. Diffraction forces a trade-off between resolution and depth of field.

OCT imaging is usually performed with low Numerical Aperture (NA) focusing and the confocal parameter is much longer than the coherence length. A high-NA focusing limit achieves fine transverse resolution for a reduced depth of field. High Numerical Aperture (NA) focusing is used in Optical Coherence Microscopy (OCM) for en face imaging [159].

4.3.3 A-scan Acquisition

In the time needed to acquire the depth information below the sample's surface at a single point the laser has completed a full frequency sweep over the available bandwidth. The transverse resolution dictates the diameter of the sampled point and the frequency components of the sines and cosines—that compose the interferometric signal—correspond to a different depth in the sample. Additionally, the raw interferometric signal captured over the period of the scan needs to be Fourier transformed in order to extract the depth information. The magnitude of the transformed signal is known as an A-scan. A change in refractive index within the sampled material will lead to a peak at the frequency that corresponds to that depth. The amplitude of the peak is approximately proportional to the change of the refractive index.

An interferometer like the one in Figure 4.2 will produce an interferometric signal similar to Figure 4.6, where the time domain signal and the calculated A-scan can be seen. Assuming mirror (M1) is the sample and mirror (M2) the reference; the interference signal is a sinusoid with a frequency that depends on the distance between the sample and the beam-splitter. The frequency of each peak corresponds to a location in the sample where a change on the refractive index occurs indicating an interface between two mediums. The height of the peak indicates the difference in refractive index between the two interfaces.

The sampling frequency f_s and number of sample used to capture the interference signal affects the maximum acquired depth (Equation (4.10)). For optimal results, the sampling frequency must be chosen based on Nyquist criterion to allow the representation of the highest frequency present in the interferometric signal.

Assuming a Data Acquisition card (DAQ) able to acquire at a sampling rate that

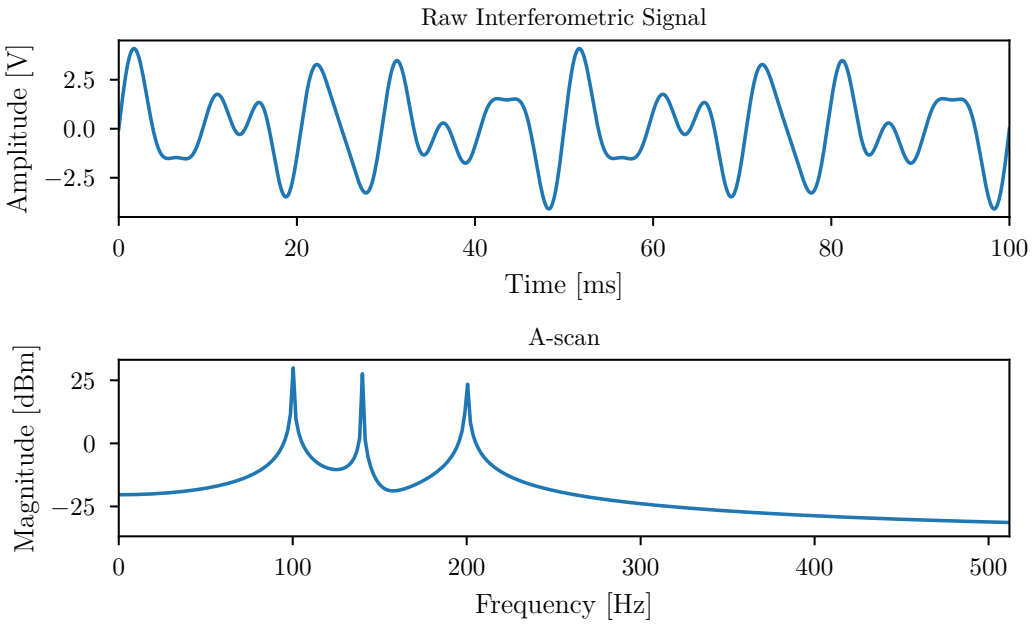

Figure 4.6: *At the top, an example interferometric signal for an interferometer, like the one on Figure 4.2, is shown. To extract the depth information the signal is Fourier transformed and its magnitude can be seen on the bottom graph. The frequency of each peak corresponds to a location in the sample where a change on the refractive index occurs indicating an interface between two mediums. The height of the peak is related to the difference of the refractive index between the two interfaces.*

satisfies Nyquist's sampling criterion[1], the maximum A-scan acquisition rate for this system is limited to the frequency of the swept wavelength laser. The A-scan rate (f_{Ascan}) of a SS-OCT is equal to the sweep rate of the laser.

4.3.4 B-scan Acquisition

To generate a cross-sectional image of a sample, the laser beam is scanned across the length of the sample with the use of a galvanometer. As the mirror of the galvanometer rotates, the beam is directed to a new location on the sample. The range of motion of the galvanometer will dictate the region to be sectioned, while the sweep frequency, the number of A-scans that will be captured. This means that the range of the galvanometer controls the width of the cross-section image and the sweeping frequency the distance between two adjacent sample location. Joining the

[1]To satisfy the Nyquist sampling criterion, for a given sampling frequency f_s, perfect reconstruction is guaranteed possible for a band-limit $B < f_s/2$

A-scans together forms what is known as a B-scan image—with a width equal to the number of A-scan and height equal to the number of points of the Fourier transform.

Figure 4.7 shows a laser beam that is scanned along a linear path on the sample's surface. In order to generate a high quality image, the sweep range and frequency of the galvanometer must be selected, in such a way, that it allows the distance between two adjacent sample locations to be equal to the lateral resolution.

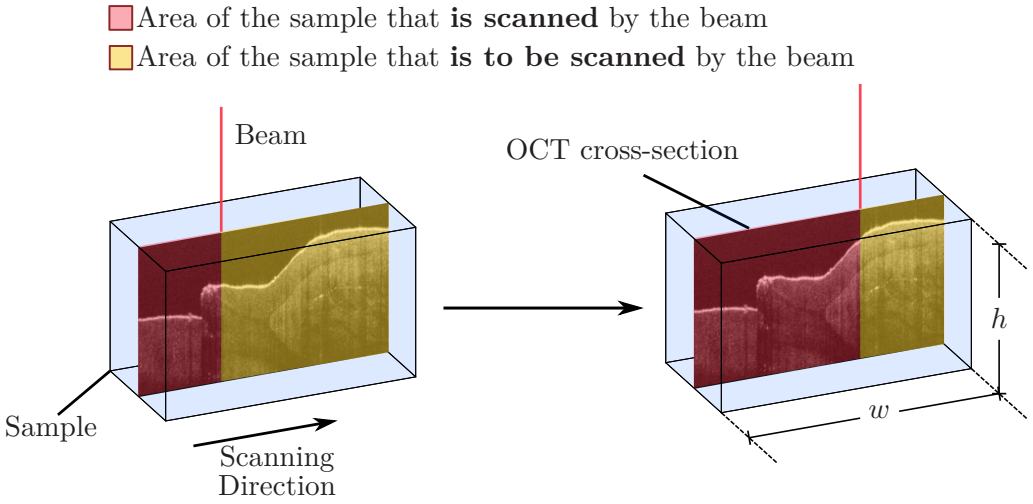

Figure 4.7: *A sample is represented as a transparent blue box. The cross-sectional image within the box corresponds to the internal structure of the sample. A single light beam passes through while the galvanometer scans the light from left to right. The region where the beam has scanned the sample is highlighted with red, while the region to be scanned is highlighted with yellow.*

4.3.5 A-scan and B-scan Rate

As the number of A-scans per B-scan correspond to the width of the resulting image, we can define the B-scan acquisition rate (f_{Bscan}) in relation to image width (W).

$$f_{\text{Bscan}} = \frac{1}{T_{\text{Bscan}}} = \frac{f_{\text{Ascan}}}{W}\,, \tag{4.33}$$

where f_{Bscan} is the repetition rate of each B-scan, T_{Bscan} the period of the B-scan, f_{Ascan} the A-scan rate and W the width of the B-scan image in units of A-scans. Solving for B-scan period from Equation (4.33) yields

$$T_{\text{Bscan}} = \frac{W}{f_{\text{Ascan}}}\,, \tag{4.34}$$

where f_{Ascan} is the swept source frequency and W is the width of the resulting B-scan image in number of A-scans in the B-scan. From (4.34), the B-scan acquisition rate is inversely proportional to the B-scan image width. In order to increase the B-scan rate, the frequency of the swept source has to increase, as decreasing the width of the image will lower the image pixel count along the axial and transverse axis.

4.3.6 B-scan Resolution

On a B-scan image, every column corresponds to one A-scan and every row represents the normalised frequency of Fourier transform. The magnitude of the Fourier transform is usually normalised over the range 0–255, as this is the range for an 8-bit greyscale image. Alternatively, the magnitude is used with a false colour representation to allow for greater detail.

A B-scan image, as it is the digital representation of the sampled cross-section, is saved as a digital image. In digital imaging, the term resolution is falsely used to describe the number of pixels in images instead of the spatial resolution. This "resolution" is commonly referred to by the two pixel counts, for the width and height of the image. Occasionally, the product of the two numbers is used, e.g. for an image 1280 pixels wide and 720 pixels tall, the "resolution" in pixel is 0.92 MPixels. Usually, an image with a high pixel count is considered to have a higher resolution—i.e. a resolution of 1920×1080 pixels is known as Full-High Definition, whereas 1280×720 pixels is known as High Definition [160]. In contrast, camera manufacturers prefer to use the terms "Number of Effective Pixels" when referring to the capturing elements of the imaging sensors and "Number of Recorded Pixels" for the pixel count of the resulting image [161].

4.3.6.1 Pixel Count and Resolution

Digital images can be thought of as mosaics composed of tiny squares called picture elements (pixels). The computer screen is divided into a grid of pixels, as the image sensors are divided into a grid of photosites[2]. The captured pixels have no physical dimensions, although in most cases the number of pixels is equal to the number of photosites since each photosite corresponds to a pixel in the final image. Thus, a better way to represent the resolution of a B-scan is using the underlying spatial resolution.

Since the pixels do not have physical dimensions, if they are squeezed into a smaller area, the image gets smaller and the perceived sharpness increases (from the same viewing distance). Images on high-resolution screens and printouts look sharper

[2] An individual light-sensitive element in a digital image sensor.

only because the available pixels are smaller and grouped into a small area—not because there are more pixels. As pixels are enlarged, they cover a larger area and the perceived sharpness decreases (from the same viewing distance). When enlarged past a certain point, the individual pixels are distinguishable—the image becomes pixelated.

For two image sensors with different size of photosites but the same sensor area, the one with smaller photosites can fit more of them in the same surface area and that will lead to images with sharper curves and finer detail. If the two image sensors have the same photosite count, the sensor area covered with smaller photosites will be smaller compared to the one with larger photosites. When viewing images (from the same distance) produced by these two sensors, the smaller one will look sharper. However, when the smaller is viewed from a closer distance, its sharpness can be made to appear identical to the larger one when viewed from farther away.

To change the dimensions of an image—making it smaller or larger for a given output device—pixels must be added or subtracted. This process is called *resampling*. To make an image larger, extra pixels are added and the colour of each is calculated using the colours of the neighbouring pixels. This will always lead to image degradation. In contrast, to make an image smaller some pixels are removed and the apparent quality is otherwise retained.

4.3.6.2 Physical Resolution of a B-scan

In SS-OCT, as there is no image sensor and there is no direct link between pixels and physical dimensions. Instead, physical dimensions of the pixels are linked to the axial and transverse resolutions of the OCT system. Thus, the image resolution is dependent on source wavelength, bandwidth, and optics (e.g lenses). Every row of pixels in a B-scan image has physical length equal to the distance travelled by the beam. The spatial resolution along this transverse axis is equal to transverse (lateral) resolution of the system, i.e. the width of the pixel is equal to δx. Similarly, for a column of pixels, the physical length is equal to the captured depth and each pixel has a height equal to δz.

Interestingly, this allow images with non-square pixel ratio as the resolution between the two dimensions (Sections 4.3.1 and 4.3.2.7) are not linked, hence the two can be different. Essentially, in one dimension more pixels are needed to represent an equal amount of length along the other dimension. This leads to images that have a pixel count of 600×1024 which when converted to physical dimensions can be equal to 1.2 mm x 2.5 mm. From now on, when referring to B-scan resolution, the spatial resolution ($\delta x \times \delta z$) will be used.

Additionally, as the B-scan depth resolution is dependent on wavelength and

bandwidth there is the advantage to control the resolution of the system without changing the main components of the system. This can be achieved by adjusting the bandwidth with the use of optic filters. Likewise, for the lateral resolution, substituting the focusing lens before the sample for one with lower or higher Numerical Aperture (NA) will change the transverse resolution of the B-scan.

Summarising, the pixel count in an image doesn't reflect the resolution of an image. With the same number of pixels but with differing physical pixel dimensions the images will appear of higher or lower quality. In photography, due to design the photosites corresponds to the pixel used to represent it. Similarly in SS-OCT, but the relation between B-scan pixels and physical dimensions is governed by the depth and lateral resolution of the SS-OCT system.

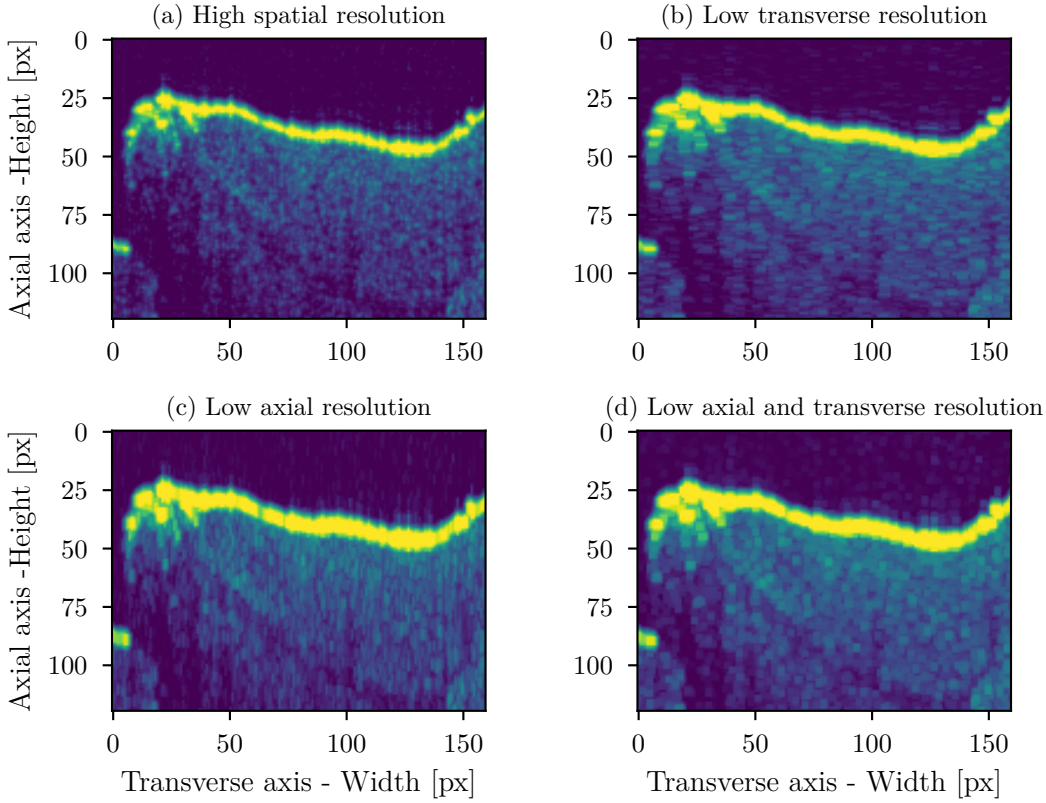

Figure 4.8: *All images have the same pixel count (160x120) albeit different spatial resolution. Image (a) is the original and the rest are processed accordingly to emulate the effects of lower spatial resolution. a) Higher depth and lateral resolution than the others. Although it is pixelated, the blocks appear square as both spatial dimensions have the same resolution. b) Lower transverse resolution means that the pixels along the width are elongated. c) Lower axial resolution makes the image to look streaky along the axial axis. d) Lower resolution on both axes. The image looks like the one at top left but with "bigger" pixels.*

To demonstrate why the pixel count of a B-scan image is not representative for image resolution, Figure 4.8 shows four B-scan images with the same pixel count (160x120) but with different spatial resolution. Starting from top left, image (a) has the highest spatial resolution from all four. When compared to bottom right (d), which has the lowest of all, it can be seen that the interface highlighted with yellow appears to be thinner and detailed.

While both (a) and (d) look "pixelated", the apparent pixel size for (d) is larger and the image looks blurry. As for (b) and (c), they have a lower resolution along the transverse and axial axis respectively. In (b) the apparent pixels look elongated and the internal structure of the sample appears blocky. Similar for (c), where pixels are stretched along the vertical axis.

4.3.7 Noise and Balanced Detection

Generally, on every SS-OCT system the noise can be split into four distinct sources.

Johnson–Nyquist noise also known as **thermal noise**. It is the electronic noise generated by the thermal agitation of the charge carriers (usually the electrons) inside an electrical conductor at equilibrium, which happens regardless of any applied voltage [162,163].

Optical Shot noise or **Poisson noise** is a type of noise which can be modelled by a Poisson process. In optics, shot noise describes the fluctuations of the number of photons detected from the detector due to their occurrence independent of each other [164,165]. Optical shot noise translates into current shot noise of the same statistics after photo detection.

Excess noise refers to the fluctuations in source light output intensity due to the beating of various spectral components having random phases [166].

Quantisation noise is a model of quantisation error introduced by the process of quantising the detector signal with the analogue-to-digital converter.

4.3.8 Johnson–Nyquist Noise

The Johnson–Nyquist noise is closely related to the detector. From Equation (4.35) it is evident that the only variable, in order to decrease the noise, is detector bandwidth either by selecting the appropriate detector or by limiting the bandwidth with the use of filters.

$$\langle \Delta i_{\mathrm{th}}^2 \rangle = \frac{v_n^2}{R} = 4k_{\mathrm{B}}T\Delta f\,, \tag{4.35}$$

where k_B is Boltzmann's constant in J/K, T is the resistor's absolute temperature in K, and Δf is the bandwidth in Hz over which the noise is considered.

4.3.9 Optical Shot Noise

Since shot noise is a Poisson process, due to the finite charge of an electron, one can compute the root-mean-square current fluctuations as being of a magnitude

$$\langle \Delta i^2_{\mathrm{sh,opt}} \rangle = 2q\langle I \rangle \Delta f \,, \tag{4.36}$$

where q is the elementary charge of an electron,Δf is the bandwidth in Hz over which the noise is considered, and $\langle I \rangle$ is the averaged DC current flowing. Typical OCT systems have a strong reference arm and weak backscattered imaging signals. According to the basic interferometric equation (2.1), the signal power is proportional to the square-root of the reference beam power in this case, where the shot noise due to the imaging signals can be neglected. However, the shot noise power also increases with the square-root of the reference power in this case (4.36). Therefore, the SNR due to shot noise is only dependent on the bandwidth, however, as the reference power is increased and thus the measured signal gets bigger all other noise sources relatively loose significance and this improves the overall SNR up to the optimum given by the shot-nose. Hence shot-noise limited operation is reached [167].

The theoretical SNR gain of SD-OCT and SS-OCT compared to TD-OCT rests upon the assumption of shot noise-limited detection in each detection channel. This limit requires sufficient reference arm power to assure shot noise dominance but usually requires significant reference arm attenuation to minimize excess noise [79].

4.3.10 Excess Photon Noise

The excess photon noise for a purely spontaneous source is given by

$$\langle \Delta i^2_{\mathrm{ex}} \rangle = \frac{(1+\alpha^2)\langle I \rangle^2 \Delta f}{\Delta \nu_{\mathrm{eff}}} \,, \tag{4.37}$$

where $\Delta\nu$ is the effective linewidth in Hz, Δf is the bandwidth in Hz over which the noise is considered, α is the degree of polarization, and $\langle I \rangle$ is the average DC current flowing [166].

To reduce the excess noise, the DC current must be minimised and this is achieved with balanced detection. Notably, the optical bandwidth can reduce the excess noise and from Equation (4.14) can be seen that the bandwidth increases the resolution.

For the balanced detection to be successful one condition applies. The two signals have to be anti-phase. That way when they are subtracted from each other the common signal (DC) is removed and we get only the AC signal (Figure 4.9).

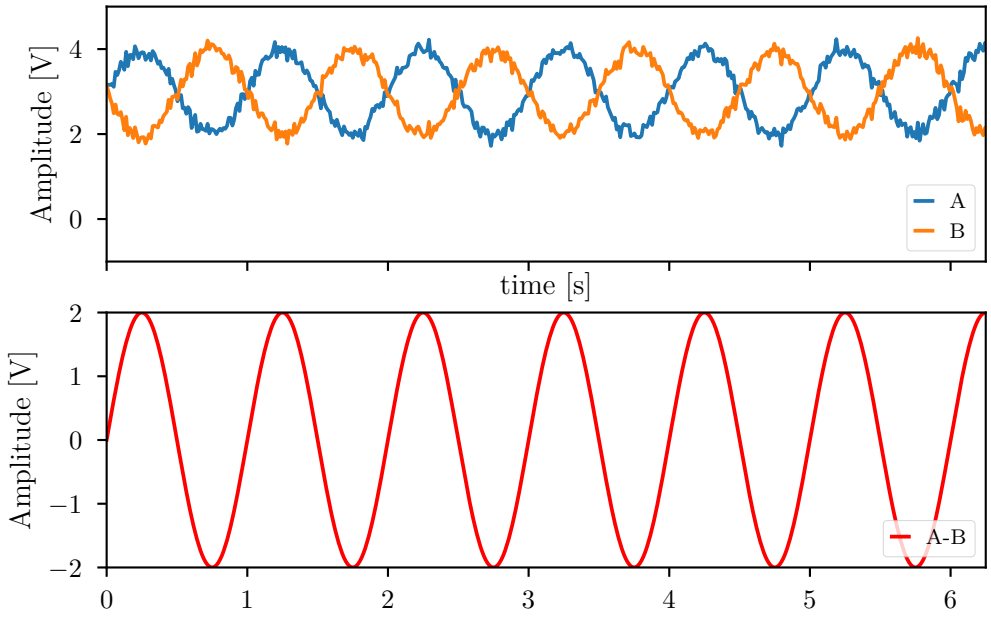

Figure 4.9: *The subtraction of two anti-phase signals (A, B) with a DC offset of three Volts and added noise, leads to the same signal as A (A-B) but with the DC component and noise removed and the signal has double the amplitude.*

4.3.11 Relative Intensity Noise (RIN)

By definition, RIN represents the total amount of photon noise per unit bandwidth and can be calculated using

$$\mathrm{RIN} = \frac{\langle \Delta i_{\mathrm{th}}^2 \rangle + \langle \Delta i_{\mathrm{sh}}^2 \rangle + \langle \Delta i_{\mathrm{ex}}^2 \rangle}{\langle I \rangle^2 \Delta f} \,. \tag{4.38}$$

The term RIN and excess photon noise are used interchangeably in literature because typically the excess photon noise is the dominant signal-to-noise ratio (SNR) limiting factor at higher source powers.

When the Relative Intensity Noise (RIN) is limited by shot noise, the RIN is given by shot-noise-limited relative intensity noise as

$$S_{\mathrm{I,sn}}(f) = \frac{2\hbar\nu}{\langle P \rangle} \,, \tag{4.39}$$

where $\hbar$ is Plank's constant, ν noise frequency, and $\langle P \rangle$ average laser power.

This PSD is independent of noise frequency (white noise), and it increases with decreasing average power. This can be understood as the introduction of additional quantum noise in the attenuation process. Thus, when the SNR is limited by RIN, it does not depend on laser power. In contrast, when the SNR is limited by shot noise, it improves with increasing laser power.

In summary, to increase the SNR of an OCT system, the overall noise must be decreased. The different types of noise present depend mainly on the DC current and secondly on the bandwidth, both optical and electrical. To minimise the DC current, the solution is to decrease input power but this lowers the signals amplitude and subsequently decreasing the SNR. An alternative, uses a balanced detector that will reject the common signal (DC offset and noise) and will amplify the actual signal. In case of electrical bandwidth, that can be minimised using analogue or digital filters after the photodetector output and and before the signal acquisition.

4.3.12 Quantisation Noise

The Analogue-to-Digital Converter (ADC) has a finite number of quantising levels determined by the sampling resolution, i.e. the number of digital bits that will represent the full-range of the analogue signal. Increasing the number of bit lowers the rounding error, introduced by quantisation, between the analogue input voltage and the digitised value. The quantisation noise is non-linear and signal-dependent.

For an ideal ADC, where the quantisation error is uniformly distributed and the signal has a uniform distribution covering all quantisation levels, the Signal-to-Quantization-Noise Ratio (SQNR) can be calculated from

$$\mathrm{SQNR}_{\mathrm{max}}\,[\mathrm{dB}] = 20 \cdot \log_{10} 2^{Q} \approx 6.02 \cdot Q\,, \tag{4.40}$$

where Q is the number of quantisation bits. However, when the input signal is a full-amplitude sine wave the distribution of the signal is no longer uniform, and SQNR is given by

$$\mathrm{SQNR}_{\mathrm{max}}\,[\mathrm{dB}] = 20 \cdot \log_{10} 2^{Q} + 20 \cdot \log_{10} \left(\sqrt{\frac{3}{2}} \right) \approx 6.02 \cdot Q + 1.761\,, \tag{4.41}$$

assuming the quantization noise is still uniformly distributed [154].

As an example, for an ideal 8-bit ADC the maximum theoretical SQNR is 49.9 dB, whereas for an 12-bit ADC is 74 dB. Due to signal distortions and other noise contributions besides the quantisation noise, the maximum *effective* SQNR that is measured with an ADC is always smaller than the theoretical value. To calculate the effective

SQNR the number of bits Q is substituted with Effective Number of Bits (ENOB) which is a measure of the dynamic range of an ADC and its associated circuitry. ENOB specifies the resolution of an ideal ADC circuit that would have the same resolution as the circuit under consideration. Thus, effective SQNR is defined as

$$\mathrm{SQNR}_{\mathrm{eff}}\,[\mathrm{dB}] = 6.02 \cdot \mathrm{ENOB} + 1.761\,. \tag{4.42}$$

For SS-OCT, a sampling resolution of 8-bit can achieve comparable system sensitivity to a 14-bit ADC but the reduced imaging dynamic range can manifest itself as an increase in image artefacts due to strong Fresnel reflection [168]. The 12-bit DAQ used for the experiments has an ENOB of 9.52 leading to an effective SQNR ($\mathrm{SQNR}_{\mathrm{eff}}$) of 59 dB, compared to the theoretical SQNR of 74 dB.

4.4 Multi Beam Coplanar (Non-Overlapping)

A multiple beam coplanar system is an extension of the single beam SS-OCT (Section 4.3), except for having multiple coplanar beams distributed along the transverse axis to scan the sample. In the non-overlapping variant of the multi-beam system, the beams are equally spaced as shown in Figure 4.10. Similar to the single beam system, capturing a B-scan image requires a galvanometer to scan the beams laterally over the sample. The axial and transverse resolutions are the same as the single beam system and can be calculated using Equations (4.14) and (4.30).

4.4.1 B-scan Acquisition

Based on the three beam system of Figure 4.10, to acquire a single B-scan image, the beams will have to travel a distance equal to $W/3$, where W is the width of the B-scan and physically corresponds to the width of the cross-sectional plane captured. Each beam will be used to generate a regional B-scan image. When these regional B-scans are joined together, a bigger B-scan image is formed and will be similar to the B-scan captured using the single beam system. Separately, the beams can be treated as a single beam SS-OCT with a B-scan size of $(W/3) \times h$.

Substituting W for $W/3$ in Equation (4.34) yields

$$\begin{aligned} f_{\mathrm{Bscan}} &= \frac{f_{\mathrm{Ascan}}}{W/3} = \frac{3 f_{\mathrm{Ascan}}}{W}\,, \\ T_{\mathrm{Bscan}} &= \frac{W}{3 f_{\mathrm{Ascan}}}\,. \end{aligned} \tag{4.43}$$

As the regional images are captured simultaneously, the B-scan period of the final image will be equal to the regional. Comparing Equations (4.33) and (4.43), the speed

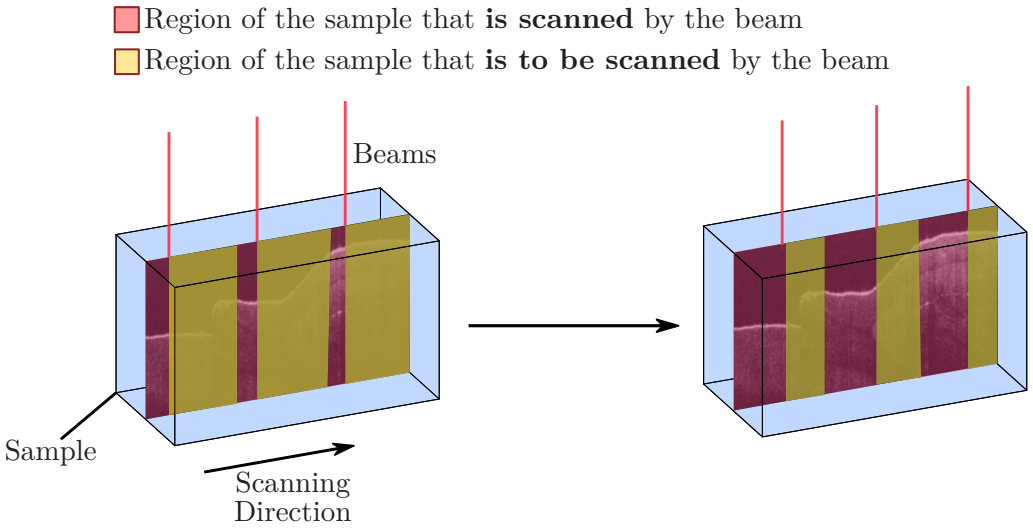

Figure 4.10: *A sample is represented as a transparent blue box. The cross-sectional image within the box corresponds to the internal structure of the sample. The light beams pass through while the galvanometer scans the light from left to right. The region each beam have scanned is highlighted with red, while the region to be scanned is highlighted with yellow.*

increase is proportional to the number of beams used. Using the same reasoning, in a system with two beams, the regional B-scan period will be equal to

$$f_{\text{Bscan}} = \frac{f_{\text{Ascan}}}{W/2} = \frac{2f_{\text{Ascan}}}{W}\,, \tag{4.44}$$
$$T_{\text{Bscan}} = \frac{W}{2f_{\text{Ascan}}}\,.$$

This can be generalised for n number of beams, hence the B-scan frequency or period for multi-beam non-overlapping systems is given by

$$f_{\text{Bscan}} = \frac{f_{\text{Ascan}}}{W/n} = \frac{nf_{\text{Ascan}}}{W} \quad \text{and} \tag{4.45}$$
$$T_{\text{Bscan}} = \frac{W}{nf_{\text{Ascan}}}\,,$$

where n is the number of beams used, $w_{\text{B-scan}}$ the width of the B-scan captured by a beam.

Equation (4.45) is valid *only* when the beams are equidistant and there is no overlap between regional B-scans. As the acquisition speed increase is linear and proportional to the number of beams used, there is an advantage of adding more beams. But the addition of beams, adds complexity to the light delivery mechanism.

In a system where the sweeping frequency is equal to 96 kHz, a B-scan width of 600 A-scans gives a B-scan rate of 160 Hz. For the same system, but with the addition of two more beams, the B-scan rate is equal to 480 Hz. Interestingly, for the number of beams equal to the width of the B-scan, i.e. 600, the B-scan rate is equal to $f_{\text{Ascan}} = 96\,\text{kHz}$, but this doesn't seem possible with current technology.

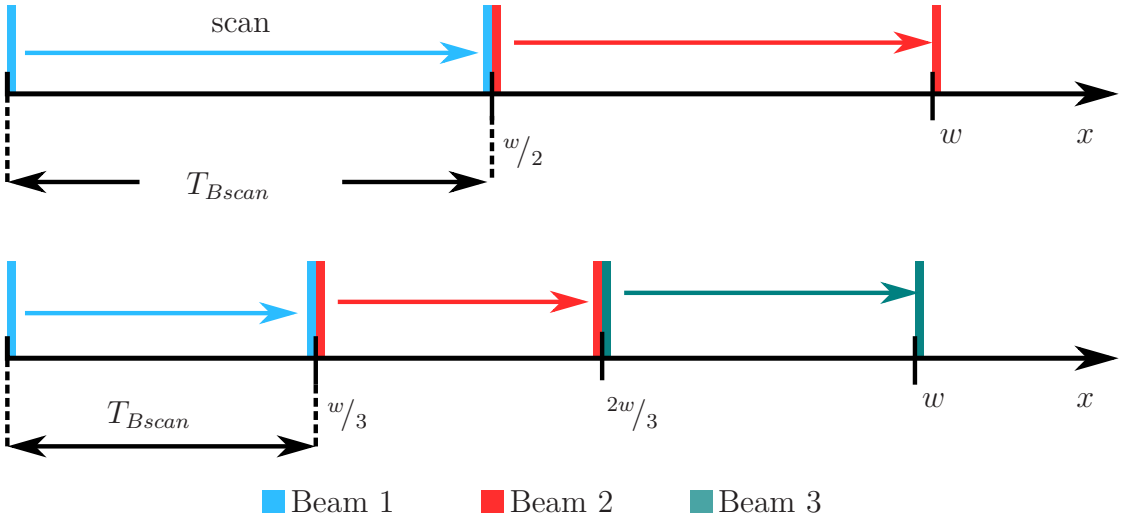

Figure 4.11: *The positions of two (top) and three (bottom) beams along the transverse axis x and relative to the width of the B-scan W. The B-scan period T_{Bscan} decreases—acquisition speed increases—when more beams are utilised. For the two beams, in a single scan, Beam 1 and 2 will travel a distance equal to $W/2$. Similarly, with three beams, Beams 1, 2 and 3 will be equal to $W/3$. In both cases, the total width captured is W, but at different speeds.*

Figure 4.11 highlights the B-scan period decrease with the addition of extra beams (2 and 3). For two beams, each beam covers a distance $W/2$ for a final B-scan image with width W. Similarly, for three beams, the distance covered by each beam is $W/3$ for the same image width W. However, the B-scan period for two beams decreased by 2, while adding a third reduced it by another 1.6 times.

4.4.2 Advantages and Disadvantages

As mentioned earlier, this mode has the advantage to decrease the time required to capture a B-scan, thus increasing the acquisition speed allowing faster moving particles to be imaged. A multi-beam non-overlapping system was demonstrated in 2010, where an ultrahigh speed 1050 nm swept source OCT was used for retinal and anterior segment imaging at 100 000 to 400 000 axial scans per second [67]. Buffering the laser sweep doubled the axial scans per second for a sweep of 200 kHz.

Furthermore, to double the sweep frequency again, a second beam was added and allowed 400 000 axial scans per second.

For microfluidics, the speed increase allows faster moving particles to be captured and tracked, thus flows with higher velocities can be analysed. However, this mode is limited due to current technology and the complexity of the optics required to add more than a couple of beams. Advancements in multi-core fibres might allow more beams to be used, while lowering the complexity of the system.

With current technology, a way to achieve B-scan rates that are close to the sweep frequency of the laser is to use a coplanar multi-beam system with overlapping acquisition regions. This mode is explained in detail in the section that follows.

4.5 Multi Beam Coplanar (Overlapping)

In microfluidics there is a need to track particles travelling with high velocities. To achieve the tracking of such particles, images of particles in the fluidic channel must be acquired with high frame rates. Current technologies, like µPIV, are able to capture at such high frame rates, although they require access through multiple ports in order to achieve this [169]. However, OCT systems require a single access port to capture two-dimensional information (Section 4.3.4), but they suffer from slow frame rates. The swept wavelength laser technology is the main cause for the slow B-scan rates (typically up to hundreds of Hz), as they usually incorporate mechanical parts for the generation of the sweep. Notably, newer technologies like non-kinetic swept sources, such as VCSEL or FDML, allow B-scan rates in the kHz range. To allow slower swept sources (tens or hundreds of kHz) to achieve higher B-scan rates, a variation of the multiple beam mode is introduced. All the optical properties remain the same as the single and multi beam non-overlapping systems. However, compared to multi beam non-overlapping system, the B-scan rate is equal to that of the single beam system (Equation (4.33)).

In this mode, the beams are not distributed along the scanning path; rather, each beam is placed next to the other at a distance ΔS. The distance ΔS will be known as the beam separation. As the beams are scanned along the whole width of the sampling region, multiple B-scans will be generated that correspond to the same overlapping region plus some non-overlapping portion of the sample.

As an example, a dual beam overlapping system will be used throughout this section to illustrate the key aspects of this mode. Figure 4.12 shows the resulting B-scan images for Beams 1 and 2, while highlighting the overlapping region. By capturing B-scan images in succession, each image can be thought of as frames like in an animation. Following this comparison, the B-scan images acquired using each

beam, in a single scan, will be known as sub-frames. Joining the sub-frames, will produce a B-scan image that will be known as the master frame.

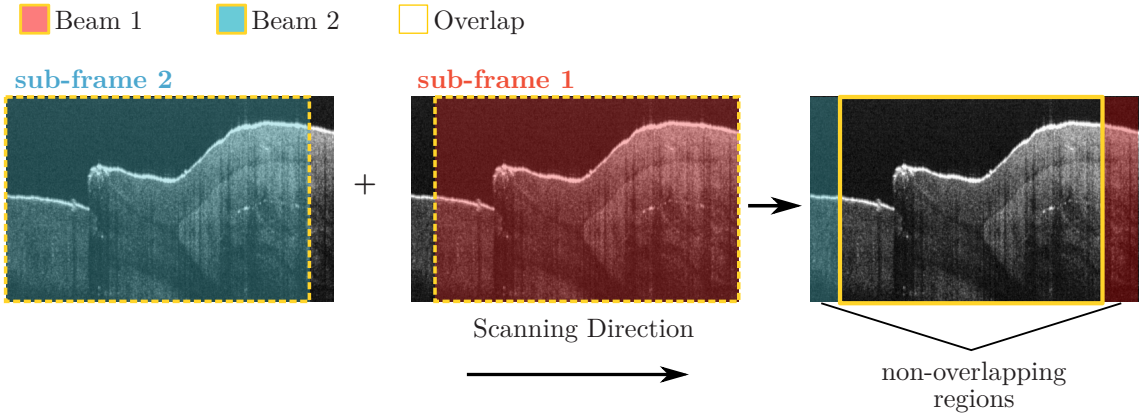

Figure 4.12: *Dual beam B-scan overlap when the beams are longitudinal to the scanning direction. A dual beam system where the first beam (Beam 1) is located ΔS away from (Beam 2), while the scanning direction is from left to right. Joining the two sub-frames, produces a single image with non-overlapping regions on either side of the overlapping one. ΔS determines the amount of time between two B-scan frames in a dual frame, i.e. the burst rate.*

Borrowing the definition of a tuple from mathematics, a tuple is a finite ordered list of elements. An n-tuple is an ordered list of n elements, where n is a non-negative integer. The n in this case corresponds to the number of beams used, thus the number of B-scan sub-frames produced. Tuples of different length have a different name; a 2-tuple is called an ordered pair or double and a 3-tuple is a triple or triplet. Subsequently, a dual beam system will produce double-frames and similarly a triple beam, a triple-frame, etc.

As mentioned earlier, the beam separation is equal to ΔS. While the beams travel with the same speed along the scanning axis when scanned, there will be a time difference ΔT between each sub-frame. This ΔT is the time required for the next sub-frame to be captured; $1/\Delta T$ corresponds to the rate at which new sub-frames are captured. This rate f_{Burst} will be known as the *Burst B-scan Rate*. The relation between ΔS and ΔT as a function of the axial scan rate f_{Ascan} can be defined as

$$\Delta T = \frac{\Delta S}{f_{\text{Ascan}}}\,, \tag{4.46}$$

where ΔS is the separation of the beams in B-scan pixels—each pixel corresponds to one A-scan—and f_{Ascan} is the sweep rate in units of A-scans per second. Equally, the Burst rate will be

$$f_{\text{Burst}} = \frac{1}{\Delta T} = \frac{f_{\text{Ascan}}}{\Delta S}\,. \tag{4.47}$$

It is evident that the closer the beams are to each other the closer Burst B-scan rate gets to the axial scan rate. Figure 4.13 shows two beams that will scan a sample, a microfluidic channel in this example, and for two different timestamps. The two beams are separated by ΔS, that corresponds to a time delay ΔT. After time t, less than the B-scan period T_{Bscan}, the two beams have travelled some distance x, less than the total sampling width W. It can be seen that there exists an overlapping region (light grey) where both beams have captured the same cross-sectional area. On either side of this region, highlighted with cyan and red the two non-overlapping region captured by each beam. Each of these regions is equal to ΔS.

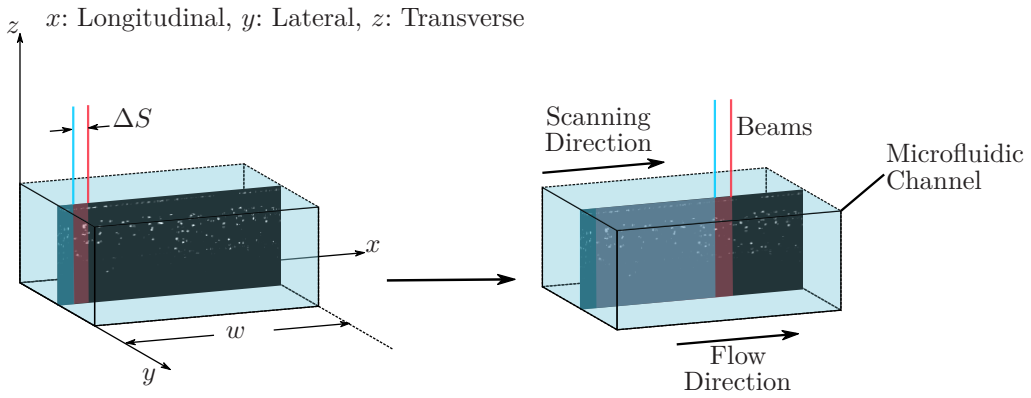

Figure 4.13: *Orientation of the sample (microfluidic channel) in relation to the scanning direction. The two beams are coplanar and are separated by a distance ΔS that induces a time delay ΔT between the acquired B-scans. As the scan progresses, there is an overlapping region captured by both beams but at a different time. Depending on ΔT, the two B-scans can have time delay equal to the time between two successive A-scans.*

Similarly, in Figure 4.14, it can be seen that both beams will travel a total distance of W. The B-scan period (T_{Bscan}) is also highlighted along with the time delta ΔT between each subframe.

Interestingly, the time between two sub-frames is adjustable as it depends on the distance between the two beams. The Burst B-scan rate approaches the A-scan rate, by minimising the separation between the two beams. Having this distance adjustable, will allow the acquisition of particles with different velocities to be measured without requiring a redesign of the optical setup. Notably, the inter-beam distance affects the generated parallax due to the separation. If the particle velocity is smaller than the B-scan rate, this parallax can be used to extract some information about the lateral depth.

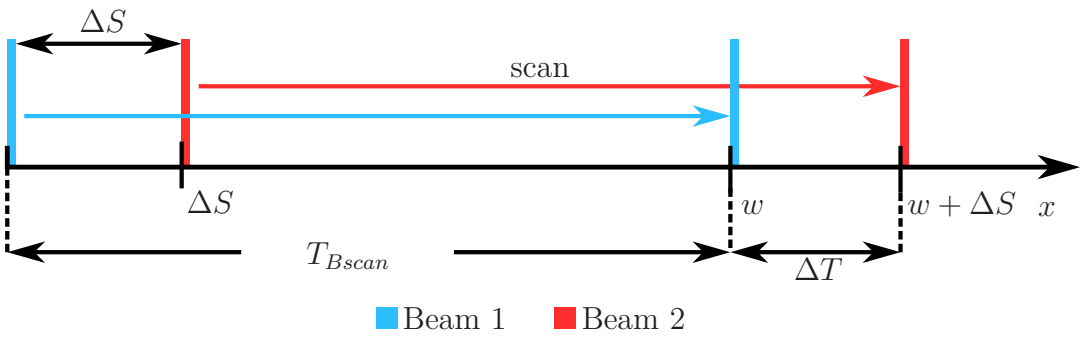

Figure 4.14: *The two beams are separated by distance ΔS that translates to a time difference ΔT between the acquisition of two subframes. The B-scan period T_{Bscan} is equal to the period of the single beam equivalent.*

4.5.1 2-component High Velocity Tracking

For particle tracking, capturing two frames with microseconds delay allows the detection of particle with higher velocities. Initially, the particles on both frames must be identified, linked and subsequently tracked for the remainder of the n-tuple frames. Let a system where eight A-scans compose one B-scan and the beam separation (ΔS) is equal to the distance travelled by the beam between to A-scans as shown in Figure 4.15. The scanning direction of the beams is the same as the flow direction inside the channel. The big red and blue rectangles represent the cross-sectional are captured by each B-scan. Subsequently, the rectangles inside represent the area captured by each A-scan. Also, the ones with the darker shade, correspond to the A-scan being captured.

For the 2-component high velocity tracking, during the acquisition of the first dual-frame, there is a time $T = t_1$ where a particle can be captured by the first beam "Beam 1" but is not by "Beam 2". Notably, scanning and flow directions are the same. In the next A-scan ($T = t_2$), while the particle has moved to the right it is not capture by "Beam 1" again, though the particle will be captured by "Beam 2".

The multi-beam overlapping mode, depending on the beam separation, allows the acquisition of sequential B-scans with a delay between frames up to the A-scan period ($^1/_{f_{\text{Ascan}}}$). As an example, a dual beam system with an A-scan rate of 96 kHz and 600 A-scans compose a B-scan image. Also, the width W of the scan is 3 mm, thus each A-scan will occupy 5 µm laterally. Then, the system will have an A-scan velocity equal to

$$v_{\text{Ascan}} = \frac{W}{600} \cdot f_{\text{Ascan}} = \delta x \cdot f_{\text{Ascan}} = 480\,\text{mm/s}\,, \tag{4.48}$$

where v_{Ascan} the scanning velocity of the scan in meters per second, W the width of the B-scan, and f_{Ascan} the sweep frequency of the laser.

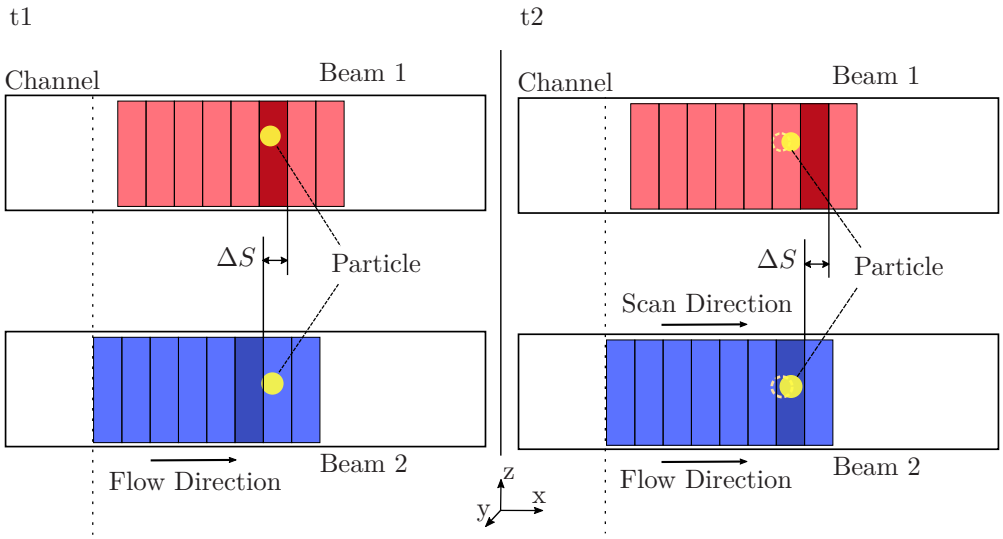

Figure 4.15: *2-component High Velocity Tracking. Two beams are separated by ΔS equal to the distance travelled between an A-scan. At $T = t_1$, a particle is captured only by the first beam. In the next A-scan, $T = t_2$, the particle has moved due to the flow but is captured by the second beam. This technique allows the tracking of particles, in two dimensions, with velocities that approach SS-OCT sweep rates.*

For a beam separation $\Delta S = 1$ or $\Delta S = 5\,\mu\text{m}$, the maximum particle velocity will be equal to v_{Ascan}, 480 mm/s. Similarly, for $\Delta S = 10$ or $\Delta S = 50\,\mu\text{m}$, the maximum particle velocity will drop to 48 mm/s. Figure 4.16 shows the maximum particle velocities that can be measured versus the beam separation for different lateral resolutions. From the graph, the maximum particle velocity drops significantly for beam separations above 60 µm.

Interestingly, as seen in Section 4.3.4, for high quality images the sweep of the galvanometer and the width of the scan must be selected appropriately so each A-scan represents the depth of a point with a diameter equal to the transverse resolution δx of the system. For the example above a lateral resolution of 5 µm was assumed, thus 600 axial scans should correspond to a length of 3 mm. If the lateral resolution was 2.5 µm then for the same width of 3 mm, 1200 would be required. As the step for each A-scan is now smaller, the velocity of the A-scan will decrease;

$$v_{\text{Ascan}} = \frac{W}{1200} \cdot f_{\text{Ascan}} = \delta x \cdot f_{\text{Ascan}} = 240\,\text{mm/s}\,, \tag{4.49}$$

thus, not only the beam separation can affect the maximum velocity measured, but also the lateral resolution. As a general rule, the lateral resolution must be chosen to allow the detection of the particles, while being large enough to allow faster moving particles to be measured.

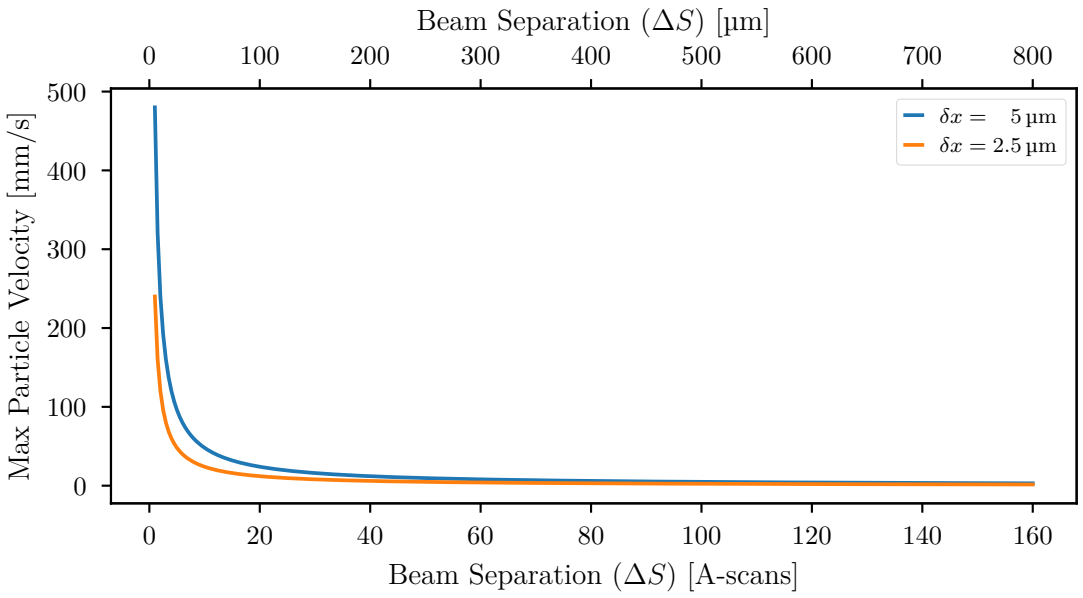

Figure 4.16: *The maximum particle velocity measured as a function of beam separation, for a system with f_{Ascan} equal to 96 kHz, scanning 3 mm with 600 (blue) and 1200 (orange) axial scans. The maximum velocity drop significantly above a beam separation of 50 µm. Additionally, the lateral resolution δx substantially affects the maximum velocity, as without changing the sweeping frequency the step for each A-scan decreases while the resolution increases.*

4.5.2 Comparison with Single Beam Scanning

Assuming that the velocity measurements for both single and multiple beam system are utilising particle tracking velocimetry then the maximum recorded velocity will depend on the size of captured B-scans, the lateral resolution, the A-scan rate, and the beam velocity. There are multiple other factors that affect the maximum particle velocity detected and due to the differences of both techniques it is difficult to make a straight comparison between the two. Thus,to make a fair comparison, the following assumptions will be made. For the particle tracking to work consistently each particle must appear at least a couple of B-scan frames. The minimum number of frames needed to calculate the velocity is two but not enough to make an accurate measurement. It will be fair to suggest that six frames are enough to be able to record the velocity; six frames translate to five velocity measurements for each particle. Therefore, the particle travelling at the maximum detectable distance will appear in six different B-scan images; slower moving particles will appear in more than six frames.

If the velocity of the beam is $v_{\text{Ascan}} = \delta x \cdot f_{\text{Ascan}}$ then the time δt required to

capture a single B-scan image that is W meters wide will be

$$\delta t = \frac{W}{v_{\text{Ascan}}} \,. \tag{4.50}$$

Also, as discussed in previous sections, the scanned distance W is selected appropriately to satisfy that the space between two successive A-scan is almost zero, where each A-scan samples an area with a diameter equal to the lateral resolution (δx). As the requirement for detectable particles is at least six frames, then the particle must cover a distance W in $\Delta t = 6\delta t$, i.e. the maximum particle velocity is given by

$$v^x_{\text{max}} = \frac{W}{6\delta t} = \frac{v_{\text{Ascan}}}{6} = \frac{\delta x f_{\text{Ascan}}}{6} \,, \tag{4.51}$$

where v^x_{max} is the maximum particle velocity at the direction parallel to the flow. Interestingly, the particle velocity depends on the scanning velocity of the beam or equivalently on the lateral resolution and the sweep rate of the laser, yet is independent of the scanning distance W.

For a dual beam system, the beam velocity will be the same but as there will be two beams for capturing the flow only three passes are required to capture six frames. However, there is a delay between two successive sub-frames (Equation (4.46)) thus the total time will be

$$\Delta t = 3\left(\frac{W}{v_{\text{Ascan}}} + \frac{\Delta S}{f_{\text{Ascan}}}\right) = 3\left(\frac{W + \delta x \Delta S}{v_{\text{Ascan}}}\right) \,, \tag{4.52}$$

where δx is the lateral resolution, ΔS the separation of the beams in A-scans, and W the scanned distance. Substituting (4.52) to particle velocity yields

$$v^x_{\text{max}} = \frac{W}{3\left(\frac{W+\delta x \Delta S}{v_{\text{Ascan}}}\right)} = \frac{v_{\text{Ascan}}}{3} \cdot \frac{W}{W + \delta x \Delta S} \,. \tag{4.53}$$

Evidently, for a scanning distance W equal to $\delta x \Delta S$ the maximum particle velocity will be the same as the single beam system. The maximum velocity is proportional to the scanning distance and as this distance increases the velocity approaches $v_{\text{Ascan}}/3$. It is clear from (4.51) and (4.53) that adding a second beam doubles the maximum particle velocity. Extending to six beams, the maximum velocity allowed to be recorded is equal to the velocity of the scanning beam.

As a numerical example using realistic values, assume that both systems have a 96 kHz swept laser and 10 µm lateral resolution; the beam velocity will be equal to $v_{\text{Ascan}} = 960\,\text{mm/s}$. Furthermore, for the dual beam system the beam separation will be $\delta x \delta S = 250\,\mu\text{m}$. Using the previous equations, the maximum particle velocity as a function of B-scan width W is shown in Figure 4.17.

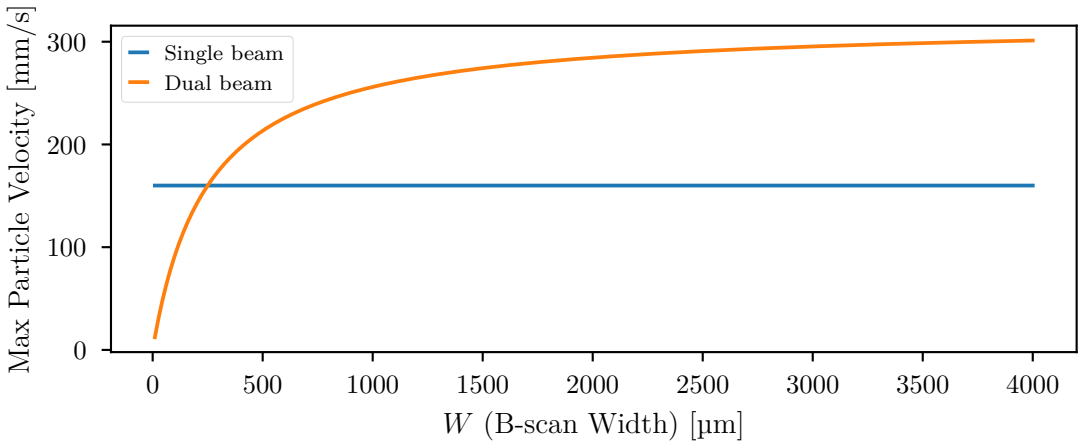

Figure 4.17: *For multi-beam systems the maximum particle velocity is proportional to the B-scan width W. At a B-scan width equal to the beam separation the velocity is the same as a single beam system.*

4.6 Multi Beam (Volumetric)

The volumetric multi-beam mode inherits all the optical properties from the multi beam coplanar (overlapping) mode. In this mode the beams are collinear in a line parallel to the longitudinal axis—same as with the other modes—but the scanning direction is now perpendicular to the longitudinal axis (x).

Figure 4.18 shows the orientation of the sample, in this case a microfluidic channel, in relation to the scanning and flow directions for the dual beam volumetric mode. The width W of the B-scan is also noted on the figure. From the figure it can be seen that the scanning direction of the beams is perpendicular to the flow of the channel. Additionally, the B-scan n-tuple frames are now captured simultaneously and correspond to a different, yet parallel, cross-sectional plane; unlike other modes.

This means that the time delay between sub-frame will be zero, though for particle tracking, the particle has to appear on all light sheets. For the dual beam example, for the particle with the highest detectable velocity, the particle will appear in the first light sheet (B-scan) on the first double-frame and on the second light sheet on the second double-frame. The time delay ΔT between the two double-frames is equal to the B-scan period, thus

$$\Delta T = T_{\text{Bscan}} = \frac{f_{\text{Ascan}}}{W}\,, \tag{4.54}$$

where W the B-scan width in units of A-scans per B-scan.

For a system with n beams the time delay will be the same, because a particle may

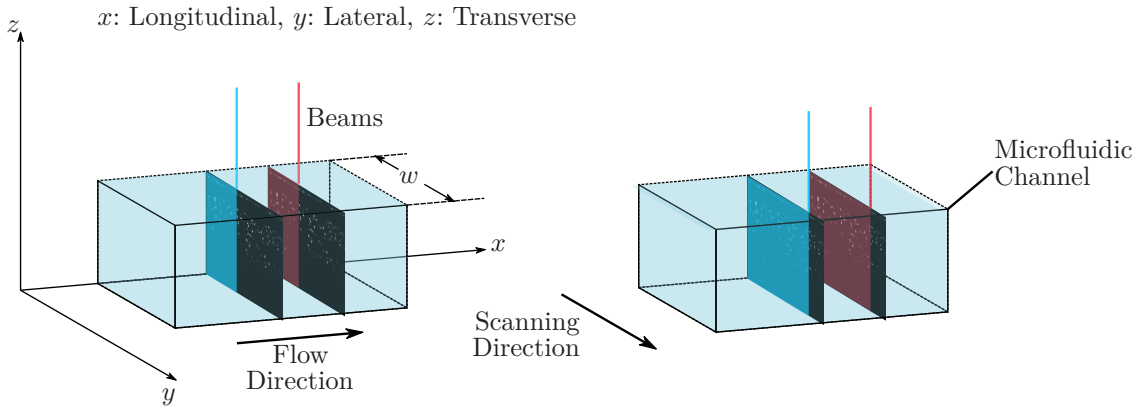

Figure 4.18: *Orientation of the sample (microfluidic channel) in relation to the scanning direction for a dual beam volumetric mode. The beams define two cross-sectional planes that are perpendicular to the longitudinal axis and thus to the flow direction. Compared to the other modes, the B-scans from all the beams are acquired simultaneously.*

have a velocity such as to make it appear on the first and last light sheets between two n-tuple frames. A particle that appears in light sheets between the first and the last will have a lower velocity.

As with the multi-beam coplanar (overlapping) mode, the beam separation ΔS determines the maximum particle velocity detected. The particle velocity $v_{\text{part.}}$ will be equal to the distance ΔS between two light beams, over the time it took for the particle to appear on both light sheets:

$$v^x_{\text{part.}} = \frac{\Delta S}{\Delta t}\,, \tag{4.55}$$

where $v_{\text{part.}}$ is the particle velocity, ΔS the beam separation, and Δt the time needed by the particle to travel a distance ΔS. When the particle appears on the first and last B-scan of two consecutive n-tuple frames, then Δt is equal to $2\Delta T$ and Equation (4.55) becomes

$$v^x_{\text{part.}} = \frac{\Delta S}{2\Delta T} = \frac{\Delta S}{2T_{\text{Bscan}}} = \Delta S \cdot \frac{f_{\text{Bscan}}}{2}\,, \tag{4.56}$$

where T_{Bscan} and f_{Bscan} are the B-scan period and frequency respectively.

Using Equation (4.56) and for ΔS from 1 µm to 1400 µm the particle velocity can be seen on Figure 4.19. Again, transverse resolution (δx) affects the maximum particle velocity detectable—more A-scans needed for the same B-scan width, thus the time between frames (ΔT) increases.

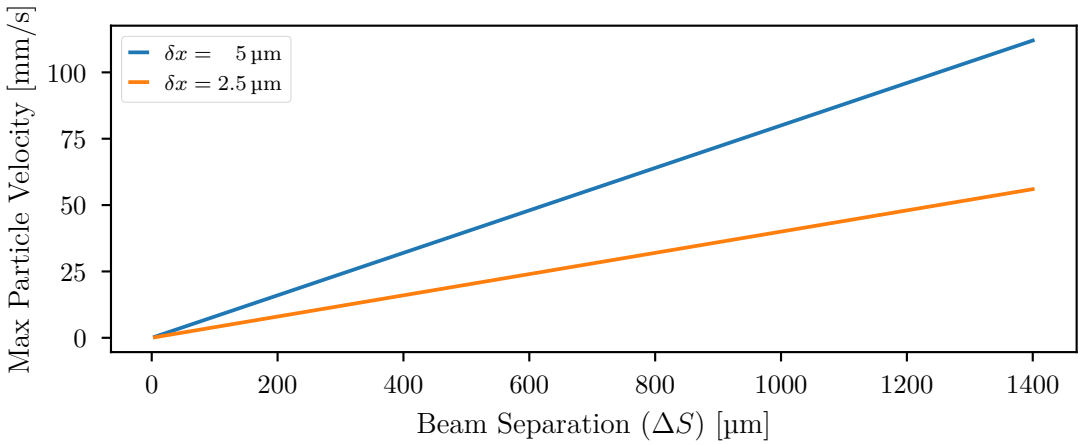

Figure 4.19: *The maximum particle velocity measured as a function of beam separation, for a system with f_{Ascan} equal to 96 kHz. The maximum velocity detected is proportional to the beam separation. For a particle to appear on both light sheets in successive frames, will have to travel a distance ΔS in twice the B-scan period ($2T_{\text{Bscan}}$).*

4.6.1 3-component Velocity Tracking

The multi-beam volumetric mode allows the tracking of particles in three dimensions, while requiring a single access port. This is useful in microfluidic velocity measurements, as it enables the tracking and mapping of complex and turbulent flows. Figure 4.20 shows a dual beam volumetric system scanning a microfluidic channel.

Assume that at time $T = t_1$, a particle is detected on the B-scan captured from the first beam. Because a B-scan is two-dimensional, the particle position on the image represents the particle position inside the channel on the $y - z$ plane. As the location of the first beam is known, that means the particle position on all dimensions is known, hence the term 3-component velocity tracking. At time $T = t_2$, the particle appear on the second B-scan captured from the second beam. Similar to the first B-scan, the particle position is detected for all dimensions. To calculate its velocity, the velocity for each dimension is measured.

The displacement in position between the two B-scans along with the time between the two frames ($\Delta t = t_2 - t_1$) gives the velocities v_y and v_z. For the velocity on x axis, the distance travelled is equal to beam separation ΔS and the time between the two frames is again Δt. Hence, the 3-component particle velocity is equal to

$$\|v_{\text{part.}}\| = \sqrt{v_x^2 + v_y^2 + v_z^2} = \sqrt{\left(\frac{\Delta S}{\Delta t}\right)^2 + \left(\frac{\Delta y}{\Delta t}\right)^2 + \left(\frac{\Delta z}{\Delta t}\right)^2}. \tag{4.57}$$

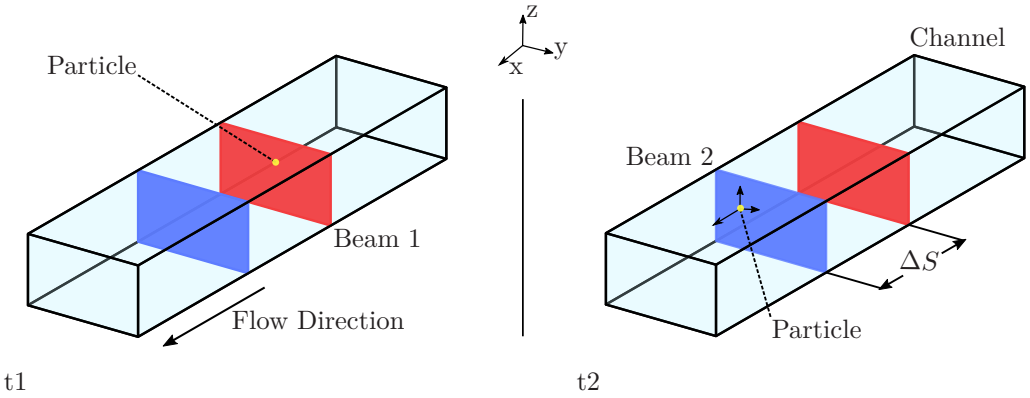

Figure 4.20: *3-component Velocity Tracking. At time t_1 a particle will appear in the light sheet generated by Beam 1 and its position will be recorded. At t_2, determined by ΔS and particle flow velocity, the particle will appear on the second light sheet generated by Beam 2. As the distance ΔS between the two light sheets, the displacement on $y-z$, and the time between particle appearances is known, the velocity of the particle can be calculated. Thus the velocity of the particle is known for all dimensions x, y, and z.*

4.7 Summary

In this chapter, the theory behind the operating principles of multi-beam OCT systems was discussed. Each multi-beam OCT system can fall into one of the following categories:

- Multi Beam — coplanar (non-overlapping)
- Multi Beam — coplanar (overlapping)
- Multi Beam — volumetric

The multiple beam coplanar system is an extension of the single beam SS-OCT, except for having multiple coplanar beams distributed along the transverse axis to scan the sample. In the non-overlapping variant of the multi-beam system, the beams are equally spaced. This mode generates a number of B-scan images equal to the number of beams, but each B-scan is only a portion of the sectioning width. To get the full B-scan image, all the sub-regions have to be stitched together.

For the second category, the beams are not distributed along the scanning path; rather, each beam is placed next to the other at a distance ΔS which is known as the beam separation. As the beams are scanned along the whole width of the sampling region, multiple B-scans will be generated that correspond to the same overlapping region plus some non-overlapping portion of the sample. This mode allows the acquisition of B-scan images where all contain a portion of the sample but corresponds to a different timestamp. The closer the beams are to each other,

the shorter the amount of time between each B-scan.

For the last mode, the beams are collinear in a line parallel to the longitudinal axis—same as with the other modes—but the scanning direction is now perpendicular to the longitudinal axis. Thus, multiple light planes are slicing the sample generating multiple B-scan images at different positions along the longitudinal axis.

Furthermore, in this chapter the factors that affect the resolution of the OCT system were discussed. Every OCT system has a depth (axial) and a lateral (transverse) resolution. The former is dependent on the laser centre wavelength and bandwidth, while the latter on the spot size and the focal length of the lens. Additionally, both the lateral resolution and depth of field are connected to the beam waist of the laser beam and the Numerical Aperture (NA) of the optics. The axial resolution is proportional to the bandwidth and inversely proportional to the square of the centre wavelength. Thus, to increase the axial resolution, the bandwidth must be increased or the centre wavelength must be decreased or both. Similarly, the lateral resolution increases as the beam waist decreases, but for this to happen the NA of the optics must be increased. However, increasing the NA of the system decreases the depth of field, thus only a small region inside the sample will be in focus.

Chapter 5

Design and Implementation of a Dual Beam OCT instrument

5.1 Introduction

This chapter is divided into three main parts. The first describes the process for constructing a dual fibre connector and the reasoning behind it. For the second part, the design (Section 5.3.1) and the implementation (Section 5.3.2) of an all-fibre OCT system is shown. Additionally, the coherence of the akinetic laser is measured using this setup.

For the third part, the system design of the all-fibre setup is improved (Section 5.4.1) using the knowledge gathered after the implementation. The implementation of the second system is discussed in Section 5.4.2. For the second implementation, effort was put to integrate the design in order to be able to fit inside an enclosure.

At the end of the chapter Section 5.5, a comparison is drawn for the two system implementations and future improvements are discussed for both.

5.2 Dual Fibre Pair

As discussed in Section 4.5 the addition of multiple beams to an OCT system will allow faster particle tracking to be realised. A difficulty that needs to be overcome in order to develop such a multi-beam system is how the multiple beams are delivered to the sample. There is the requirement that the beams should be close enough (a few A-scans apart) in order to gain a significant speed improvement. This is especially true for the multi-beam coplanar mode with overlapping acquisition regions.

In this work, a solution for a dual beam implementation is proposed. The solution is to combine two single-mode fibres into a ceramic ferrule designed for multi-mode fibres. In the following subsections, the process of constructing and the evaluation of this component is discussed.

5.2.1 Construction of the Fibre Pair

The fibres used for the setup are single-mode SMF-28e+ for 1550 nm and manufactured by Corning. They have a core diameter of 8.2 µm and a cladding diameter of 125 ±0.7 µm. For the dual fibre connector, the two fibres have to be brought as close as possible to minimise the distance between the two fibre cores in order to get the minimum separation in A-scans. Due to physical constraints the shortest distance between the two cores is equal to the cladding diameter, i.e. 125 ±0.7 µm. Then, the total space required for the pair is 250 µm.

A problem that arises is that the two fibres must stay together and aligned across experiments and be protected from accidental or environmental damage. The solution to this problem was given by utilising a multi-mode ferrule as a cage for two single-mode fibres. The dimensions of the fibre pair, when put side-by-side, are 250 µm by 125 µm. For this reason, a ceramic ferrule was used to encapsulate the two fibres. A diagram of the ferrule can be seen in Figure 5.1. The ferrule that was chosen for the dual fibre pair and has a length of 6.4 mm, bore size diameter of 270 µm, and outer diameter of 1.25 mm. The reason for using this ferrule is that the bore diameter allows the two fibres to fit inside.

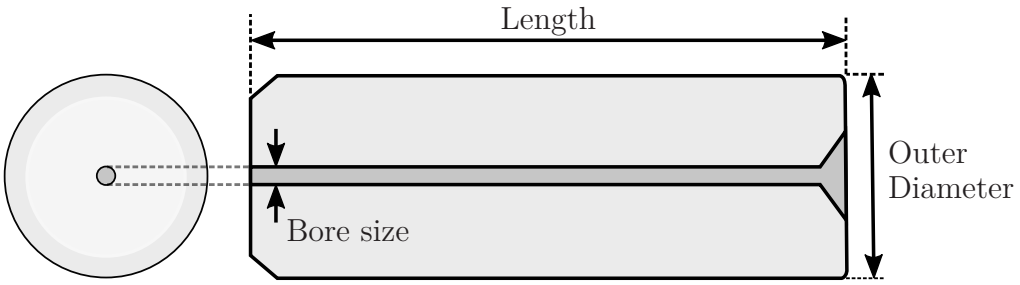

Figure 5.1: *Front view and side cross-section of the fibre ferrule. For the dual fibre connector, the ferrule used has a length of 6.4 mm, bore size diameter 270 µm, and outer diameter of 1.25 mm.*

To construct the connector, two fibre pigtails, like the one shown in Figure 5.2, are used. One end of the pigtail already has a connector, for example a FC/APC (Ferrule Connector/Angled Physical Contact), whereas the other end has a bare fibre. For

the two systems implemented for this project both SC/APC (Subscriber Connector) and FC/APC connectors were used.

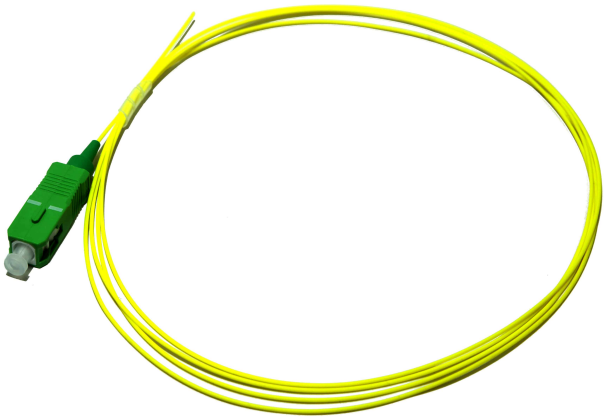

Figure 5.2: *Single-mode fibre pigtail with SC/APC connector. The bare end is used for the construction of the dual fibre. The fibre pigtail has a length of 1.5 m while the core and cladding diameters are 8.2 µm and 125 µm respectively.*

The pigtails used for the dual fibre in both OCT implementations had a length of 1.5 m. The only difference is that for the all-fibre system SC/APC connectors where used whereas in the integrated system the FC/APC connector was used instead. With the two pigtails selected and with the appropriate connector the dual fibre can be constructed. In summary the steps for constructing the dual fibre connector are the following:

- Strip 7 mm of the jacket and remove the coating of the bare fibre end for both pigtails using a fibre stripper similar to the ones for copper wire.
- Cleave the bare ends with a mechanical cleaver (diamond cutting wheel) to produce a clean flat end.
- Clean the fibre ends using Isopropyl Alcohol (IPA).
- Insert the two fibres through an FC/PC connector and subsequently into the ferrule and fill the bore hole with a high temperature epoxy adhesive (RT153F). Then heat the ferrule with a hot-air gun until the temperature reaches 120 °C. The adhesive colour will change on cure from straw through amber to red.
- After the epoxy is dry, proceed with hand-polishing the new dual fibre connector until the polishing angle is equal to 8°. The ferrule is placed on a FC/APC stainless steel polishing disk.

- The polishing happens in two stages: First, using a 30 µm aluminium oxide lapping film and then using a 1 µm diamond coated lapping film. De-ionised water is used for lubrication throughout polishing.

Extra care is taken at the polishing step because the epoxy is brittle and can be chipped away leaving an exposed fibre. A finished dual fibre ferrule can be seen in Figure 5.3. On Figure 5.3a the two inner circles (A) show the circumference of the two fibres. The circle (B) highlights the bore area where the two fibres are glued within. The outer surface (C) is the ceramic ferrule itself. As mentioned above, the epoxy can be chipped off while polishing the ferrule—this can be seen on Figure 5.3b where both the glue and a portion of cladding is removed from the left fibre.

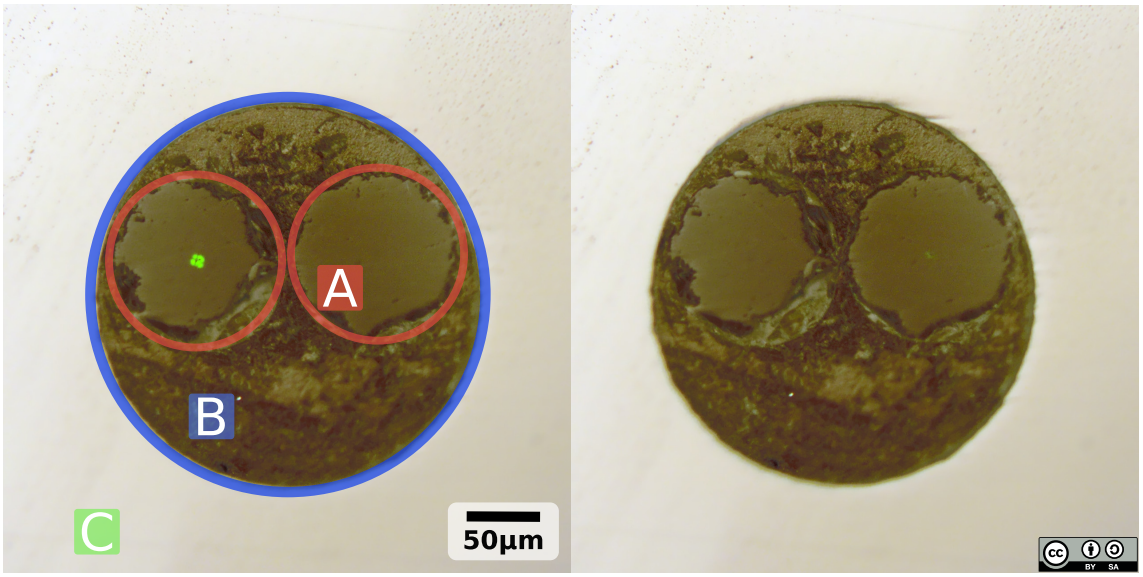

(a) *Left fibre illuminated* **(b)** *Right fibre illuminated*

Figure 5.3: *Microscope image of the end-face of the dual fibre pair (ferrule). On (a) the two fibres are enclosed in circles (A). The core-to-core distance is 125 µm while the bore diameter of the ferrule, that is filled with epoxy glue (B), is equal to 270 µm. The white material (C) around the fibres is the ceramic ferrule.*

In addition, to check the condition of the fibres inside the ferrule a green laser (532 nm) was used. The light from the laser is on both images, albeit for the right fibre the light is faint which is an indication of a damaged fibre. Furthermore, as the fibre is designed for 1550 nm and the wavelength of the green laser is below that, the fibre is multimoded and a higher-order mode exhibiting four spots can be seen on the left fibre (Figure 5.3a). It should be noted that for the experiments a new dual fibre bundle was prepared.

5.2.2 Physical Characteristics

Another reason for using the ferrule for mounting the two fibres is that it gives the ability to adjust the orientation of the fibres in relation to the sample. As described previously in Section 4.5, the beams must be collinear and coplanar relative to the cross-section of the sample. To ensure that the fibres were oriented properly in order to achieve coplanarity, an infrared camera was used. Additional information about this process can be found in Section 5.4.10.

A new fibre pair was constructed and inspected under a polarising microscope (Olympus BX51) at 50x magnification—an image of the end-face can be seen on Figure 5.4a. There is white light coming out of the two cores as light was coupled into the two fibres. The distance between the two cores was again 125 µm. In the image the polished ferrule is shown; it is evident that a portion of the cladding is removed from both fibres due to polishing. Apart from the damage on the cladding, no other issues were found and the fibre bundle was operational. Note that as the end is angle-polished, only the strip down the centre of the image can be in-focus.

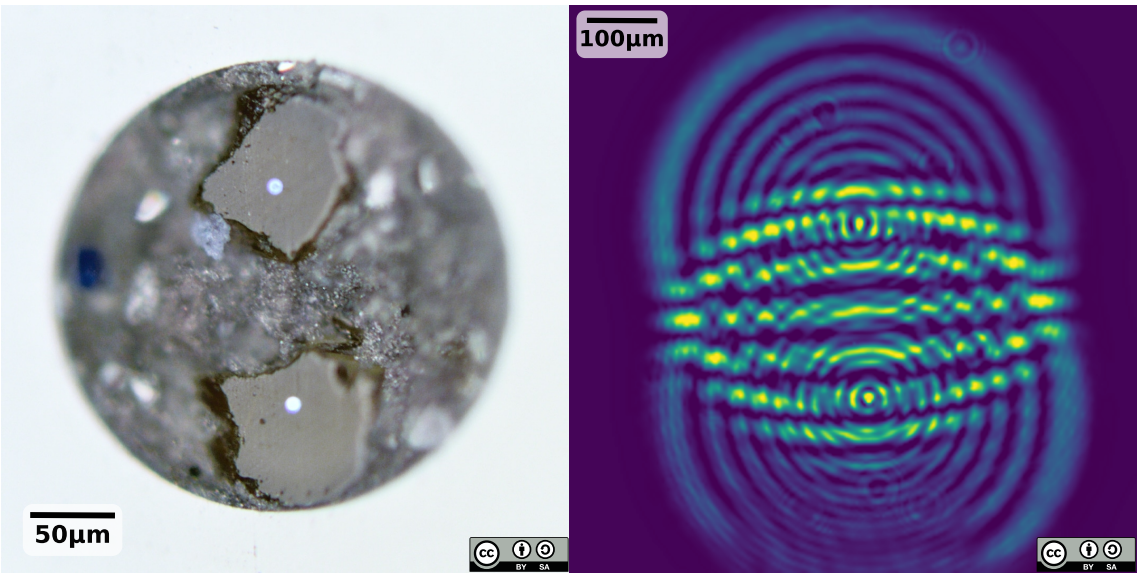

(a) *Microscope image of the dual fibre end-face* **(b)** *Fringe pattern of the dual-fibre pair*

Figure 5.4: *On (a) the dual fibre end-face can be seen while the two cores are illuminated. The separation of the single-mode fibres is 250 µm. The two fibres are glued inside the a ferrule with a 270 µm bore diameter. On (b), the fringe pattern for 1550 nm captured with an infrared camera. A colourmap is applied to increase the visibility of the fringes.*

With the akinetic laser that is used in the dual beam setup (Section 5.3.2), along with a Near Infrared (NIR) InGaAs CCD camera, the fringe pattern was recorded and is shown in Figure 5.4b. The strong fringes (yellow/green hue) that appear between

the cores are generated by the interference of the two fibres as their polarisation components match. The weak fringes (concentric cyan circles) are produced by self-interference introduced by reflections from the protective glass plate in front of the camera sensor. The visibility (fringe contrast) in this case is 67 % and was calculated using Equation (5.1) [46], assuming $I_{\max}$ is the maximum pixel brightness value in the image and $I_{\min}$ the lowest value above the background level.

$$\mathcal{V} = \frac{I_{\max} - I_{\min}}{I_{\max} + I_{\min}} \,. \tag{5.1}$$

5.3 Dual Beam All-Fibre Swept Source OCT

For the first implementation of the dual beam SS-OCT system an all-fibre approach was made. This means that the Michelson interferometer, which is the basis for optical coherence tomography, is implemented with fibre-optic components only. Using fibre based components makes the system, in comparison with a bulk-optic variant, more compact, more stable as there are no moving parts, and less complex. However, the fibre setup is susceptible to temperature and fibre bend induced polarisation effects.

5.3.1 System Design

This design of a dual beam OCT system borrows from the single beam fibre-optic OCT setup. In such a system, the interferometer is built using a fibre-coupler instead of a beam-splitter. In this case, as the system must deliver two beams to the sample, two fibre-couplers with 50% split ratio are used. As the laser only has one output, another fibre-coupler is used to split the light into each interferometer.

In order to use balanced detection and increase the Signal to Noise Ratio (SNR) a circulator is added in front of each coupler, as shown in Figure 5.5. Additionally, the circulator is used to prevent any laser damage caused by reflected light that returns to the laser. Each coupler introduces a phase change of 90° between the two outputs. A set of two lenses for the sample and each reference arm are used. For the reference arms, the lenses are placed before the mirror. The first lens collimates the divergent light coming out of the fibre end, while the second one which is placed at a focal length distance from the mirror focuses the collimated light beam. Similarly, a lens is placed before the galvanometer to collimate the light from the fibre bundle, while a second lens focuses the light on the sample. Both sample and reference arms have a free space portion and identical lenses allowing dispersion matching between them. In OCT only the difference in net propagation between reference and sample arms is preserved; thus, if the fibre and air path lengths in each arm are closely matched, the propagation between the arms can be considered as occurring in a

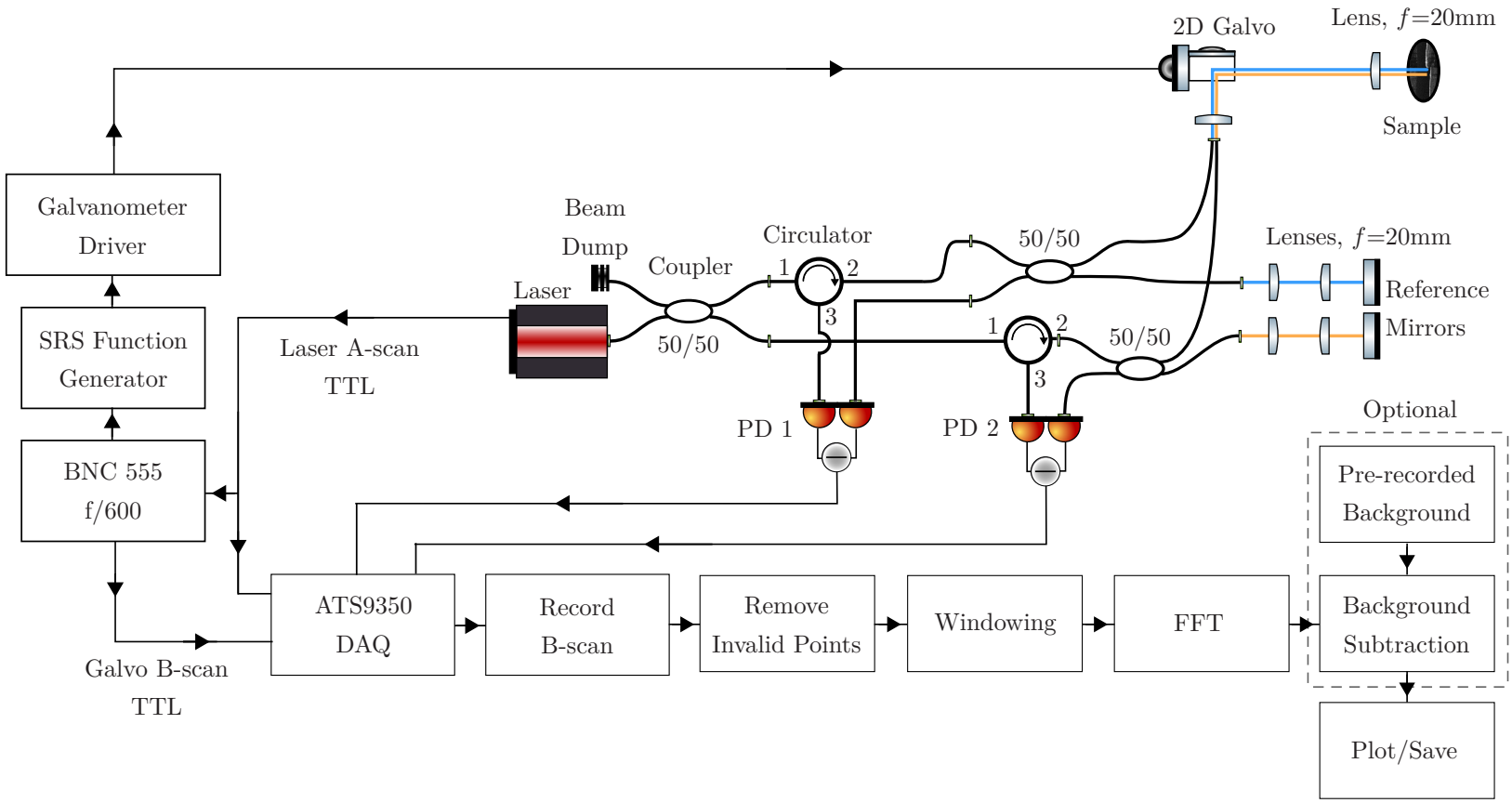

Figure 5.5: *Schematic diagram of the dual beam all-fibre optic setup. The coupler splits the light of the laser into two, one for each beam, and through the circulators each beam passes through another coupler to split the light between the sample and the laser. The reflected light passes through the couplers and is fed to the balanced detectors (PD 1 and 2). On the electrical side, the A-scan clock signal is connected to a frequency divider that divides it by 600 to generate the B-scan trigger signal that is used by the Data Acquisition card (DAQ) and the function generator that generates the signal to drive the galvanometer motor. After the DAQ, the invalid points of the A-scans are removed, the resulting arrays are windowed and an FFT is performed before the B-scan images are displayed.*

single medium. The lenses are achromatic doublets with anti-reflection coating for 1050 nm to 1620 nm, 20 mm focal length, and 8 mm aperture. Light reflected from the sample and the reference paths pass trough the coupler and undergo another 90° phase change. The two interference signals, one that returns to the circulator and one that goes directly to the photodetector, differ by 180°, thus balanced detection is achieved.

As for the electrical side of the setup, the A-scan clock signal that is generated by the laser is connected to a digital delay/pulse generator (BNC 555). The BNC 555 continually counts for 600 pulses of the clock and generates a short pulse after the 600th pulse. This short pulse will be known as the B-scan trigger, as it is used with the Data Acquisition card (ATS9350 DAQ) to signal the beginning of a new B-scan. Additionally, this trigger is used by the SRS function generator to synchronise the signal that drives the galvanometer with the B-scans. Finally, the output from the two balanced detectors (PD 1 and 2) is connected to the DAQ in order to capture the interferometric signal on the computer.

On the processing side, the software that was implemented for the project as described in Section 5.4.8 is used. The interferometric signal is recorded by the DAQ and using the Data Valid Vector (DVV), that was generated by the laser after its calibration, the invalid points from the captured data are removed.

Then, as the power output of the laser has a flat-top profile a Blackman-Harris window is applied on the data before the application of the Fast Fourier Transform (FFT). When the FFT is finished the spectra are bundled into two images and displayed on screen. Optionally, a background scan, that was captured before the placement of the sample, can be subtracted from the data to improve the SNR by removing static noise and cavity reflections.

5.3.2 Implementation

5.3.2.1 Optical Components

For this project, an akinetic laser was chosen for the swept source. The operating principles of the laser are described in Chapter 3. The laser specifications are shown in Table 5.1. It has an adjustable optical bandwidth with a range of 10 nm to 100 nm around a centre wavelength of 1.55 µm. The scanning range is limited by the manufacturer and is related to the efficiency of the sweep outside.

As mentioned in Section 4.3.1, the axial resolution of a swept source OCT setup will increase by either lowering the centre wavelength or increasing the bandwidth. Thus, the sweep width of the laser must be set to its maximum value of 100 nm. However, as discussed in Section 3.4.1 the sweep rate, sweep width, and points per

Table 5.1: *Specifications of Insight Photonic akinetic laser (SLE-101)*

Parameter	Value	Unit
Sweep width	10 to 100	nm
Optical Power	1 to 11	mW
Center wavelength	1.55	µm
Coherence length	40.00	mm
Sweep power profile	Flat Top	
Sweep speed (sweeps per second)	4000 to 100 000	
Number of measurement points	1 to 130 000	
Linear sweep parameter	linear in λ or frequency	
Sweep direction	forward in λ	

sweep are all linked together and changing one of them affects the other two, e.g. changing the sweep rate affects either one of the sweep width and the points per sweep or both. For an optimised discrete Fourier transform the number of points per sweep were chosen to be 4096. Additionally, the sweep rate is set to 96 kHz leading to a sweep width of 82 nm. Thus, the bandwidth of the laser is set—at every calibration—to 82 nm by setting the sweep rate and points per sweep to 96 kHz and 4096 respectively. Hence, the laser sweeps from 1525.90 nm to 1608.14 nm.

After each calibration, the laser, using its internal interferometer evaluates the sweep characteristics by calculating the Point Spread Function (PSF). This diagnostic information is retrieved from the laser and is used to determine its current condition. The laser condition should not change in a controlled environment, where the temperature and humidity are regulated. Temperature or humidity fluctuations, affect the SNR of the laser and it can be seen both on the diagnostic information and on the resulting images obtained by the OCT system. As an example, Table 5.2 shows the information retrieved from the laser after a calibration.

Table 5.2: *Example of akinetic laser calibration information*

Parameter	Value	Unit
PSF Peak to Side Lobe Ratio	48.2392	dB
PSF Peak to Noise Floor Ratio	63.6977	dB
Average Sum of Squared Errors (SSE)	0.0012	
Average Sliding RIN	0.2023	%
Maximum Sliding RIN	0.4696	%

To diagnose the laser condition, the “PSF Peak to Side Lobe” and “PSF Peak to Noise Floor” parameters are checked. When the output of the laser deteriorates, the peak to side-lobe ratio drops below 40 dB and lowers the contrast of the OCT image.

Similarly, when the peak to noise floor ratio decreases, the noise on the OCT image increases.

Additionally, the sweep rate affects the output of the laser. At lower sweep rates, the peak to side-lobe ratio increases, while as the sweep rate increases the peak to side-lobe ratio decreases. Thus, when high sweep rates are preferable, a compromise in OCT image quality is made.

As mentioned above, to increase the depth resolution, the bandwidth of the laser is set to 82 nm, but the maximum bandwidth is 100 nm. In order to maintain the resolution, the fibre-optic components used in the setup must allow the whole bandwidth to pass. The selected couplers, made by Gould Optics with part-number "45-W3255-50-22272" are made using Corning SMF28e fibres and have a bandwidth of $\pm$100 nm with a centre wavelength of 1550 nm. Furthermore, the two circulators (Thorlabs 6015-3-APC) have a bandwidth of 85 nm covering the range between 1525 nm to 1610 nm. Thus, the 82 nm bandwidth (sweep width) of the laser, set at the calibration stage, is preserved throughout the system. All the connectors used in the fibre-optic components, are angle-polished to minimise the back-reflections that will affect the signal quality.

For scanning the sample, a scanner head was constructed using an enclosure for a 2D galvanometer that is compatible with 30 mm cage components. This construction can be seen in Figure 5.6. The custom dual fibre bundle (A) is mounted on a mount (B) with x,y-axis translation and z-axis translation-rotation. This mount is connected to the cage (C) using four rods that are bolted to the side of the galvanometer enclosure. The beams from the fibre bundle are collimated using an achromatic doublet lens (D) that is placed between the cage and the fibre mount. Similarly, the focusing lens is the same as the collimating one and is mounted on (E). As the lateral resolution is dependent on the Numerical Aperture (NA), the collimator lens (Thorlabs AC080-020-C-ML) is mounted on a M12x0.5 Threaded Mount and has a 80 mm diameter, 20 mm focal length, and has anti-reflection coating for the 1050 nm to 1620 nm range. The inside of the cage where the two galvanometer mirrors are held in place can be seen in Figure 5.16b.

To construct the reference arms for the two beams, four 3-axis flexure stage blocks are used. For each beam, a set of two stages are used to hold the collimator lens after a fibre holder, as well as the focusing lens in front of a mirror. All four lenses are the same as the collimator from the sample arm, i.e. Thorlabs AC080-020-C-ML. The two stages of each set (C, D), as shown in Figure 5.7, are placed opposite to each other at a specific distance adjusted appropriately to ensure path length matching. On the input of each reference, a neutral density filter is placed after the collimator lens to regulate the amount of light and improve the interferometric signal. As the fibre portion between each coupler and the fibre holders at A, C, and D varies, the distance between each reference and the sample is different. Thus, the distance between the

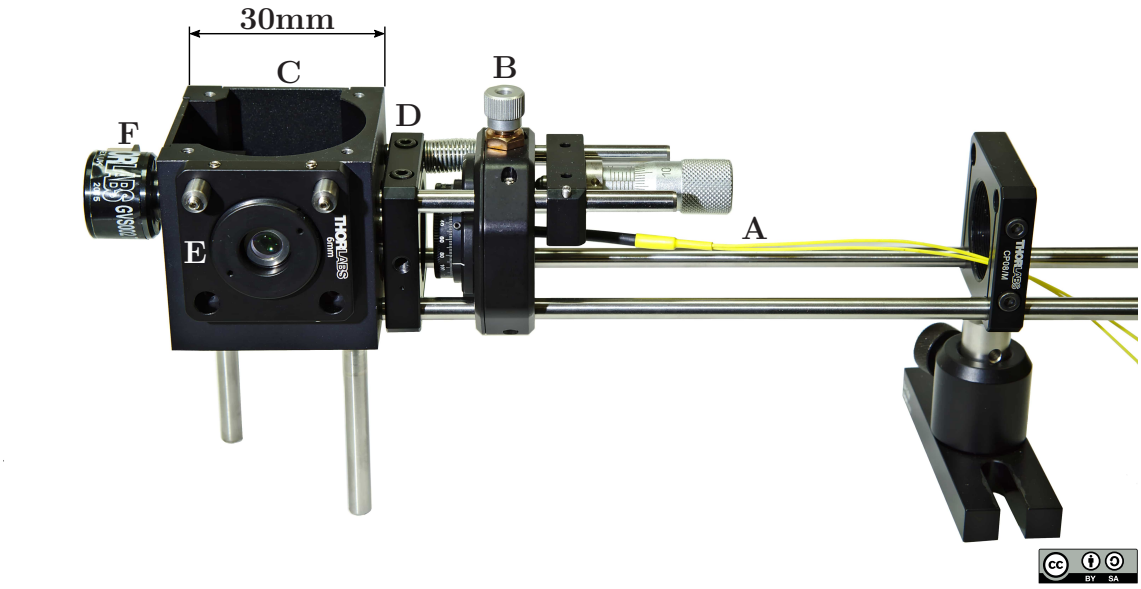

Figure 5.6: *Side view of the dual beam OCT galvanometer head. The OCT head is constructed using a 2D galvanometer (F) mounted on a 30 mm cage (C). On the sample facing side an achromatic doublet lens is mounted (E). On (D), another achromatic doublet is mounted and act as the collimator. The dual fibre (A) is mounted on a 4 degrees-of-freedom mount (B).*

reference collimator and the mirror is adjusted accordingly so that this optical path length is equal to that of the sample arm.

Additionally, on the top left of the picture a red fibre holder (B), that the dual fibre is coiled around, can be seen. The use of this holder is described in Section 5.3.3.

5.3.2.2 Electrical Components

On the electronics side of the setup, the laser generates a signal to indicate when a new sweep starts which corresponds to one A-scan. This signal is connected to both the acquisition card and a Berkeley Nucleonics Corporation (BNC) 555. The BNC 555 is a 2-channel delay pulse generator used to generate the trigger signal for the B-scan images. It has a delay range of 0 s to 100 s with a 1 ns resolution. The BNC 555 counts 600 pulses of the laser signal and generates a short pulse (known as the B-scan trigger) to indicate that a new B-scan must be captured.

Subsequently, this B-scan trigger is used as a synchronisation clock for the generation of the signal that will drive the galvanometer. The signal for the galvanometer is a 94% duty cycle sawtooth of 84 Hz and has an amplitude of 1.2 V. As the galvanometer can draw high current (spikes above 3A at quick signal transitions) which the function generator cannot supply, a galvanometer driver board is used. The driver

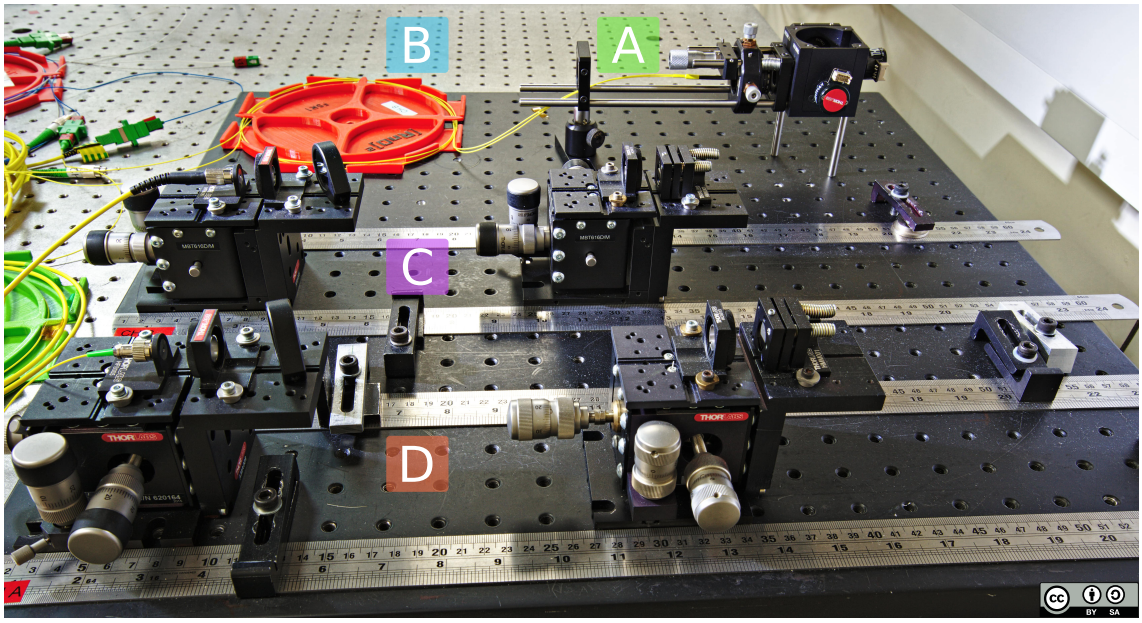

Figure 5.7: *Dual beam all-fibre optic setup. The dual fibre (A) is mounted on the galvanometer head. At the bottom left of the image, (C) and (D) are the two reference arms of the intereferometer.*

board is connected to ±15 V, 3 A power supply, thus it can amplify the signal to deliver enough current to move the galvanometer. The maximum voltage accepted by the galvanometer is ±10 V that corresponds to a sweep range of ±12°.

For the acquisition of the optical interferometric signals, two balanced photodetectors (Thorlabs PDB415C) with InGaAs[1] photodiodes are used. Table 5.3 highlights the specifications of these detectors.

Table 5.3: *Balanced photodetector specifications for Thorlabs PDB415C*

Parameter	Value	Unit
Detector Type	InGaAs	
Wavelength Range	800–1700	nm
Typical Max. Responsivity	1.00	A/W
Active Detector Diameter	0.30	mm
Bandwidth (3 dB)	100.00	MHz
Common Mode Rejection Ratio	>25.00	dB
Trans-impedance Gain	50.00×10^3	V/A
Minimum Noise-equivalent Power	6.99	$pW/\sqrt{Hz}$

[1]InGaAs: (Indium-Galium-Arsenide)

The selected photodetectors have a minimum Noise-equivalent Power (NEP) of $6.99\,\mathrm{pW}/\sqrt{\mathrm{Hz}}$ which is a measure of the sensitivity of the photodetector and is the sum of the electrical shot noise $\sigma^2_{\mathrm{sh,el}}$, the thermal noise σ^2_{th}, and any other excess amplifier noise σ^2_{amp}. By definition the NEP of a detector is the optical power incident to the detector that needs to be applied to equal the noise power from all sources in the detector; i.e. NEP is the optical power that results in a SNR of 1. The minimum detected optical power P_{min} is given by

$$P_{\mathrm{min}} = NEP(\lambda) \cdot \sqrt{BW} = \sigma^2_{\mathrm{th}} + \sigma^2_{\mathrm{sh,el}} + \sigma^2_{\mathrm{amp}} = \sigma^2_{\mathrm{BD}}\,, \tag{5.2}$$

where $NEP(\lambda)$ is wavelength-dependent NEP, BW the measurement bandwidth, and σ^2_{BD} is the balanced detector noise [154].

Limiting the bandwidth using additional electrical filters reduces the amount of noise and consequently the minimum optical power detected. Alternatively, increasing the averaging time t_{avg} for the measurements allows weaker signals to be detected. From Nyquist's theorem, the averaging time t_{avg} is dependent on the bandwidth and specifically is equal to

$$t_{\mathrm{avg}} = \frac{1}{2 \cdot BW}\,. \tag{5.3}$$

Solving for bandwidth on Equation (5.3) and substituting to Equation (5.2) the minimum detectable optical power will be

$$P_{\mathrm{min}} = NEP(\lambda) \times \sqrt{\frac{1}{2 \cdot t_{\mathrm{avg}}}} = \frac{1}{\sqrt{2}} \cdot \frac{NEP(\lambda)}{\sqrt{t_{\mathrm{avg}}}}\,. \tag{5.4}$$

Additionally, the noise spectral density (expressed in units of $\mathrm{A}/\sqrt{\mathrm{Hz}}$ or $\mathrm{V}/\sqrt{\mathrm{Hz}}$) can be calculated by multiplying NEP and detector's responsivity. From Equations (5.2) to (5.4), the selected photodetectors can detect a signal of 6.99 pW with a signal-to-ratio of 1 for a bandwidth of 1 Hz after 0.5 s averaging time. The NEP is inversely proportional to the square root of the averaging time, thus by increasing the averaging time to 50 seconds (x100) improves the NEP by a factor of 10. If the full bandwidth (DC–100 MHz) of the detector is used for the measurement, then the minimum optical power will be $P_{\mathrm{min}} = 69.9\,\mathrm{nW}$. The total noise power of the balanced receiver σ^2_{BD} contributes to the noise of the electrical signal detected in SS-OCT,

$$\sigma^2_{\mathrm{SS-OCT}} = \sigma^2_{\mathrm{BD}} + \sigma^2_{\mathrm{sh,opt}} + \sigma^2_{\mathrm{ex}}\,. \tag{5.5}$$

SS-OCT systems are operated in the shot noise limit, and as discussed in Section 4.3.9, the optical power of the reference signal (P_{ref}) is adjusted such that the total noise is governed by optical shot noise and not by the excess or the receiver noise.

5.3.3 Polarisation Effects

In the dual beam OCT setup the interferometer resides inside the last two beam-splitters. The interferometer will work only if the light coming back from the two arms (sample and mirror) shares the same polarisation state components. If the polarisation states are orthogonal, then the light would not interfere at the square-law photodetector (photodiode) and no image will be produced. The problem with having a fibre-optic interferometer is that the polarisation state inside the fibre changes uncontrollably, thus the OCT images will vary depending on the polarisation of the two arms. Additionally, the temperature and the stress applied on the fibre will affect the polarisation state. In contrast, on a bulk-optic system, the polarisation state of the light for both arms of the interferometer generally remains the same.

For the OCT system that was built for the experiments the polarisation effects were strong. An occasional draft would temporarily affect the visibility of the fringes. To minimise the effect, two different measures were applied, an active and a passive one. The passive measure was to minimise the stress on the fibres and lay all the fibre-spools as flat as possible to minimise the polarisation mode dispersion. This was accomplished using custom 3D-printed spool-holders—one can be seen in Figure 5.7 (indicated with B)—to contain the fibres, thus the change in polarisation due to stress was minimised. For the active measure, two polarisation state controllers (PSC) were inserted after the circulators and before the couplers. Hence, the polarisation controllers were adjusted for the highest possible visibility between measurements when the conditions were changed.

While the solution with the polarisation state controllers can be viable, the random nature of the changes in temperature and other parameters led to the decision of switching to a bulk-optic interferometer; but with fibre-optic light delivery. The bulk-optic interferometer setup is discussed in Section 5.4. Furthermore, a solution for the polarisation issues with minimum changes to the fibre-optic setup is discussed in Section 5.5.

5.3.4 Advantages and Disadvantages

The use of fibre-optic components for the implementation of an OCT setup has its advantages and disadvantages. Using fibre-optic components instead of the bulk-optic equivalents can make the overall design more compact. Additionally, in a fibre-optic setup balanced detectors can easily be added, thanks to the circulators. The introduction of balanced detection allows weaker signals to be detected, as it removes the common noise from the signal (Section 4.3.7).

Furthermore, the separate references give fine control over the path length distance

between sample and reference. This is particularly useful, as the construction of the dual fibre is not perfect and the two fibres inside the ferrule might be misaligned. But the two separate references can become a disadvantage as the setup becomes bulkier and requires additional space. Alternatively, a retro-reflector can be substituted for the two references allowing a more robust setup with the compromise of losing the ability to adjust the path difference separately for each beam.

While the fibre-optic setup has certain advantages, it has a major issue with polarisation. As mentioned previously, this issue can be minimised but needs constant adjustment as the environment changes. Additionally, it requires extra components complicating the design, which was considered as an advantage over a bulk-optic version of the setup.

As the problem with polarisation lies on the fibres that are inside the interferometer, a solution is given by modifying the fibre-setup and substituting the two interferometers (i.e couplers) with a single bulk-optic interferometer (beam-splitter). This substitution of the couplers with a bulk-optic beam-splitter is described in Section 5.4.

5.4 Integrated Dual Beam Swept Source OCT

As discussed previously in Section 5.3.3, the fibre-optic setup has polarisation issues as the fibres do not maintain the polarisation state. When the polarisation state between the sample and the reference is different, the fringe visibility is reduced. A solution to this issue is given by substituting a bulk-optic beam-splitter for the two couplers. The changes made to the previous design along with the new setup implementation is discussed in this section.

5.4.1 System Design

Using the design from Section 5.3.1 as the basis for the new setup, a set of changes were made in order to improve system stability and solve the polarisation issues that plagued the previous setup. The updated design that contains all the applied changes on the previous setup is shown in Figure 5.8. In place of the two couplers there is now a beam-splitter with a 90/10 split ratio. Additionally, the two ends of the dual fibre bundle are connected to the output of a circulator, while the dual-end is connected to the beam-splitter. After the beam-splitter, 90% of the light goes to the galvanometer and subsequently to the sample through the scan lens. Similarly, the other 10% of the light goes to either a mirror or a retro-reflector as shown. By limiting the reference power, the excess noise is reduced and the system operates in shot-noise-limited

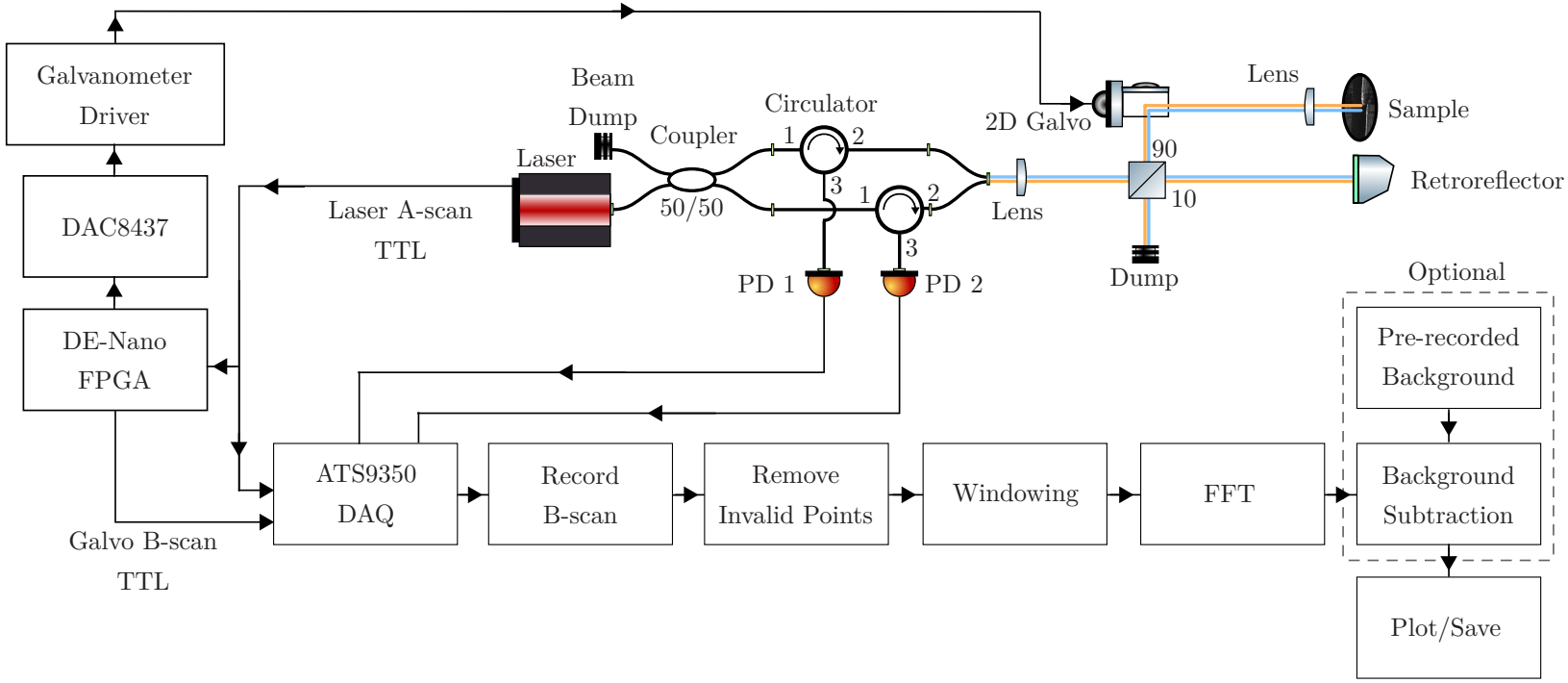

Figure 5.8: *Schematic diagram of the integrated dual beam optical setup and the post-processing stages. The coupler splits the light of the laser into two, one for each beam. Then, the light passes through the circulators which are used to direct the reflected light to the photodetectors (PD 1 and 2). On the second port of each circulator is connected one end of the dual fibre. Next, the light from the fibre pair is collimated and passes through a 90/10 non-polarising beam-splitter that splits 90% of the light to the sample and the remaining 10% is sent to the reference arm (retroreflector). On the electrical side, the A-scan clock signal is connected to an FPGA board to generate the B-scan trigger and the galvanometer driver signal. After the DAQ, the invalid points of the A-scans are removed, the resulting arrays are windowed and the FFT is performed before the B-scan images are displayed.*

detection. For these retro-reflecting prisms, the incident and reflected beams will be parallel to within 3″. Unless the incident and reflected beams strike the exact centre of the optic, they will not overlap but rather be shifted with respect to each other. However, even if the light for each beam does not couple with the same fibre is enough to produce interference. Yet, if a mirror was used instead of the retro-reflector, any misalignment will cause the light to be coupled to the wrong fibre. Thus, using a retro-reflector prism instead of a mirror reduces the number of lenses needed in the setup and simplifies the alignment process. Furthermore, the balanced detection is lost, as there is no *easy* way to extract a second interferometric signal with 180° phase difference. One way will be to substitute the dump at the beam-splitter with a second dual fibre bundle. But, that reduces the stability for re-coupling, while also increasing the number of components in the setup, as the removed couplers would have to be added again. At least, without the polarisation issues the signal-to-noise ratio is improved, thus the lack of balanced photodetectors does not have a huge impact on the signal integrity. Lastly, by using a 90/10 beam-splitter, the necessity to attenuate the light of the reference using neutral density filters is removed. The bandwidth of the photodetectors is limited to DC–50 MHz using electronic filters, thus the minimum detectable optical power is $P_{\min} = 49.4\,\text{nW}$.

Apart from solving the issues with polarisation, a few changes were made to the electronic side of the setup. These changes improve the usability of the system and allow it to be more compact. Specifically, the instruments used to generate the B-scan trigger and the sawtooth signal for the galvanometer are replaced by two electronic boards. The first (DE-nano), is a Field-programmable Gate Array (FPGA) board that is used for the generation of the trigger signals. The second (DAC8437), is a Digital-to-Analogue Converter (DAC) that takes as an input the digital representation of the signal and generates it analogue counterpart. Section 5.4.5 analyses the operating principles of these boards and discusses the advantages of this approach.

5.4.2 System Integration

As mentioned previously, one of the reasons to change the first design was to increase system stability by minimising the effects of environmental changes. This is achieved by enclosing all the components and controlling the temperature inside the enclosure. In order for this to happen, all the functions provided by separate instruments and external power supplies have to be integrated into the enclosure. By identifying the critical components that constitute the setup, the OCT instrument can be divided into *five* main parts. These are the *bulk-optic scan-head*, the *fibre-optic components*, the *data acquisition*, the *galvanometer driver*, and the *electrical power delivery*.

In the following sections, the operating principles of the parts and how they are integrated into the OCT instrument are discussed. The result of this process is the

dual beam OCT instrument of Figure 5.9. This portable enclosure contains all the necessary fibre-optic and electronic components for a dual beam OCT setup. The enclosure is a ventilated 3U rack mount case (Schroff 10225601) with a width of 520 mm, height of 153 mm, and depth of 500 mm. On the front of the instrument all the fibre-optic and galvanometer cables are connected. Similarly, all the electrical connections such as the outputs of the photodetectors, the B-scan trigger output, and the A-scan clock input are connected at the back.

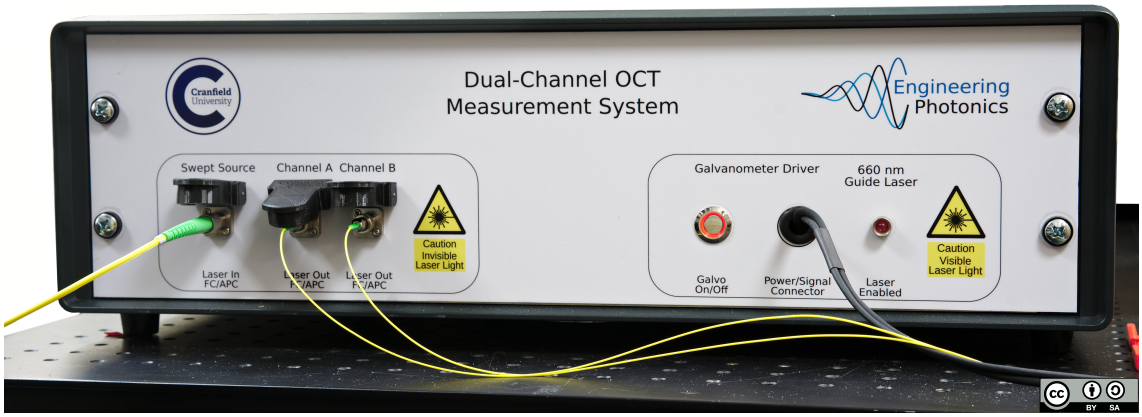

Figure 5.9: *Dual beam OCT instrument front panel. The fibre optic cables are connected to the left side of the panel. The leftmost connector is the laser input while the other two are the outputs for the dual fibre. On the right side of the panel, an on/off switch for the galvanometer and an indicator light for the guide laser can be seen.*

5.4.3 Dual Beam OCT Galvanometer Head

With the replacement of the couplers the dual fibre bundle no longer attaches to the galvanometer cage. Instead, the bundle is connected to the beam-splitter which in turn is connected to the galvanometer, thus a new OCT scanner head was constructed. In Figure 5.10 this OCT head is shown.

The dual fibre bundle (A) is mounted on the left with a precision 30 mm cage system rotation mount (B). After the fibre mount, a xy-translation mount (C) holds the collimating lens. The 90/10 beam-splitter is enclosed in a cage (G) located at the centre of the head—where the cage rods are connected on either side. On the right side of the beam-splitter, the focusing lens is held using the same xy-translation mount (D) as the collimator lens. A silver-coated mirror is mounted on a x-y translation and tilt mount (E). A mounting adapter (F) for the galvanometer is placed on top of the beam-splitter cage. Light coming from the beam-splitter is directed through

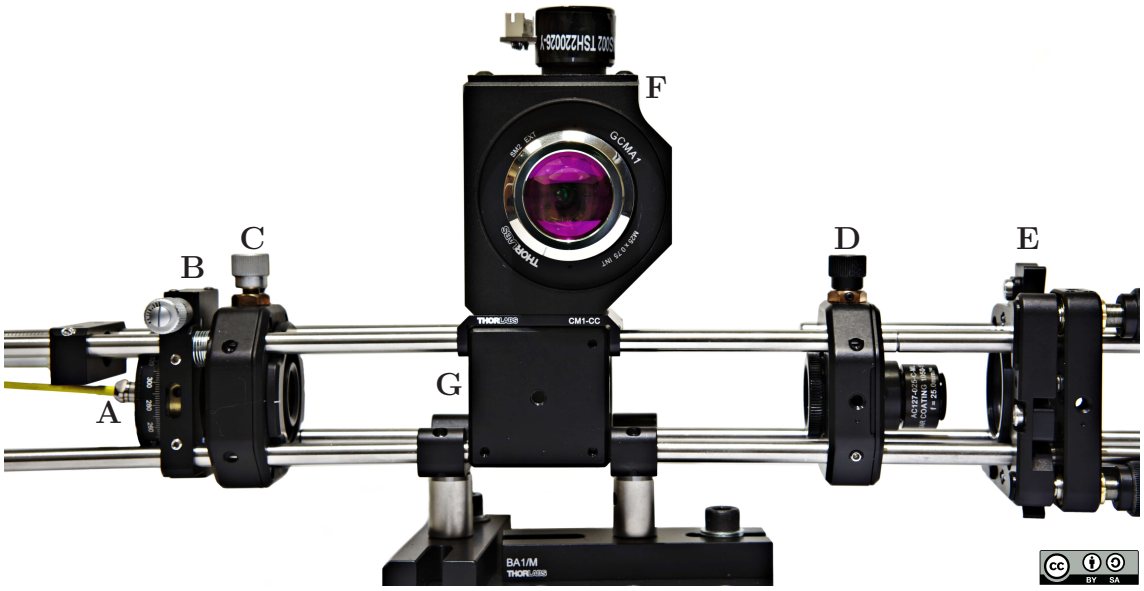

Figure 5.10: *Front view of the dual beam bulk-optic OCT scan head. On (A), the dual fibre is mounted on a precision 30 mm cage system rotation mount (B) while an xy-translation mount (C) holds the collimating lens. The focusing lens is held in place with an xy-translation mount (D) as the collimator. The reference mirror is mounted on an x-y translation and tilt mount (E). Underneath the galvanometer cage (F) and between the input and the reference, the 90/10 beam-splitter is enclosed (G).*

the input port, reflecting off both galvanometer mirrors, and then exiting through an OCT scan lens. The lenses used for collimation have a focal length of 25 mm and a diameter of 12.7 mm, while the scan lens has an effective focal length of 36 mm and a working distance of 25.1 mm.

5.4.4 Internal Components

Inside the enclosure and divided into *four* regions are the requisite parts that comprise the OCT system. A top view from inside the enclosure with these *four* regions highlighted is shown in Figure 5.11. The two photodetectors are located at the back (A) of the instrument, so their output can be connected to the back side of the enclosure. In front of the photodetectors (B), the coupler (top) and a stack of the two circulators (bottom) can be seen. The fibre-spool holders are custom-made using a 3D-printer. The diameter of the spool-holder is smaller than the one from the previous system because there are no issues with polarisation as discussed in Section 5.4.1.

On the right side, the power supplies (C) can be seen. Apart from the photodetector

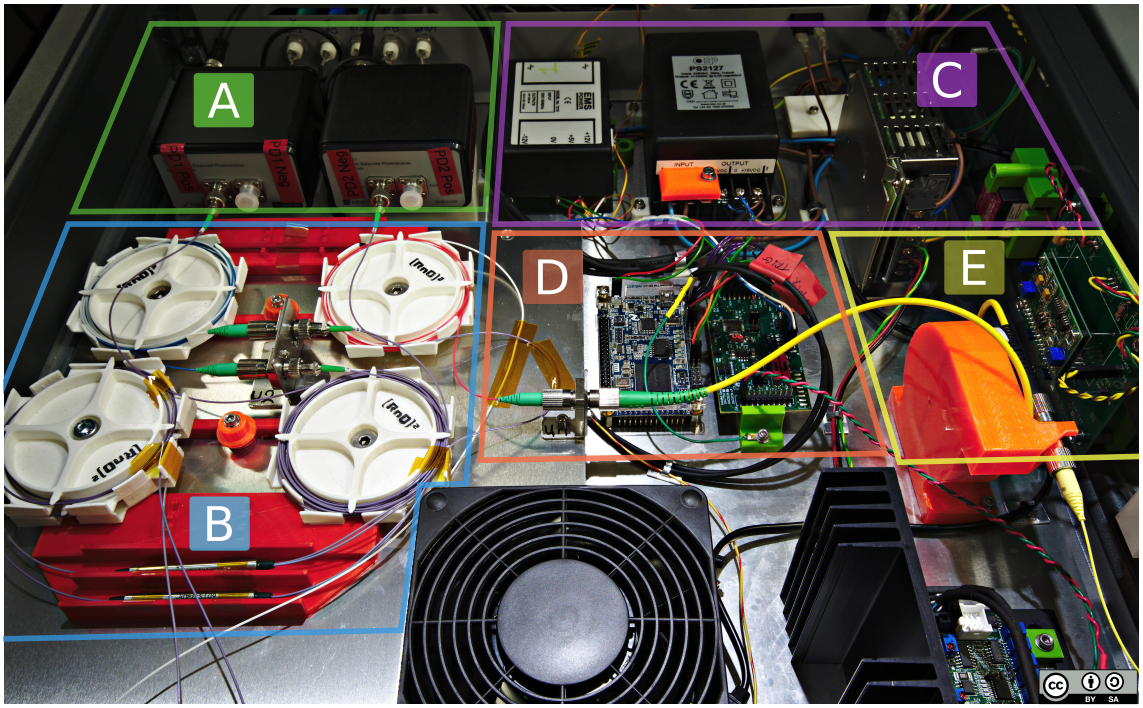

Figure 5.11: *The image shows the inside top view of the dual beam OCT instrument. The two photodetectors are located at the back (A) of the instrument behind of the coupler and circulators (B). On the right side, at the back (C) the power supplies and AC/DC converters can be seen. The FPGA and DAC boards (D) are located in front of the supplies. The twisted pair that comes from the DAC board is used for the galvanometer driver signal. On the right side of the enclosure (E), the guide laser and its driver are mounted.*

power supply which is a linear power supply—i.e. uses a transformer and analogue filters regulate the voltage, the rest are switching power supplies and use a Field-effect Transistor (FET) to switch the output rapidly as a way to reduce the output voltage. In summary, from left to right the power supplies are:

- EMS Power 7218; 5 V for FPGA and ±12 V for DAC
- OEP PS2127; 15 V for the photodetectors
- Tracopower TXL 035-1515D; ±15 V, 2.4 A for the galvanometer driver
- Tracopower TMLM 04112; 12 V for the guide laser

Furthermore, the FPGA and DAC boards (D) are located in front of the supplies. The red-green twisted pair that comes from the DAC board is used for the galvanometer driver signal. In Section 5.4.5 the design of these two boards is discussed.

Finally, the guide laser (Thorlabs LPS-660-FC) and its driver (Thorlabs EB2000) are mounted on the right side of the enclosure (E). The guide laser is a fibre-pigtailed

laser diode with 7.5 mW output power and a wavelength of 658 nm (red). In Figure 5.12, the inside of the box is shown while is operating. The fibre-coupler loops are illuminated as the 658 nm guide laser is connected to the coupler and a portion of light escapes the fibre loops. The light from the guide laser is highly attenuated as it is below the cut-off wavelength of the fibre-coupler, hence the light is faint and cannot be seen on the fibre-loops of the two circulators. For this reason, the guide laser was not used in the setup. Additionally, the green light from the FPGA indicates that the embedded code is functional, while the blue indicates that the board is properly powered.

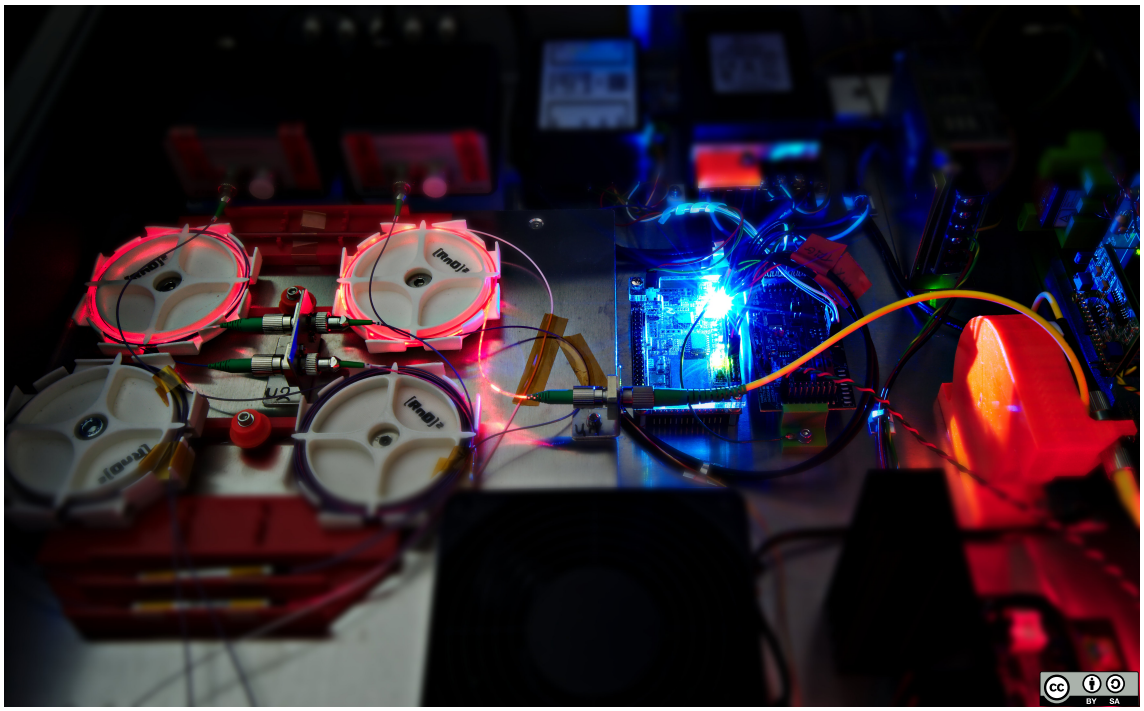

Figure 5.12: *Internal view of the OCT instrument while in operation. The colour of the lights on the FPGA board indicate that is fully operational. The guide laser (658 nm) is connected to the coupler; a portion of light escapes the fibre loops.*

5.4.5 Trigger Generation Using an FPGA

One of the main parts of the OCT setup is the generation of the trigger signals and the sawtooth for the galvanometer. Without these, the A-scan and consequently B-scan acquisitions would not be synchronised with the sweep of the galvanometer, thus leading to images where different portions will correspond to different sweeps. As the main objective is to fit all the components inside the enclosure, the instruments used for the generation of the triggering signals cannot be used. Therefore, their

functionality is replicated using the FPGA and DAC boards mentioned in previous sections.

For the generation of the trigger signals as well as the sawtooth for the galvanometer an FPGA development board was used. The downside of the FPGA board is that is not possible to output the analogue waveform for the galvanometer directly as the FPGA is oriented for digital signals. Therefore, a second development board that has an integrated Digital-to-Analogue Converter (DAC) is used alongside the FPGA. A close-up of the two boards from inside the box is shown in Figure 5.13

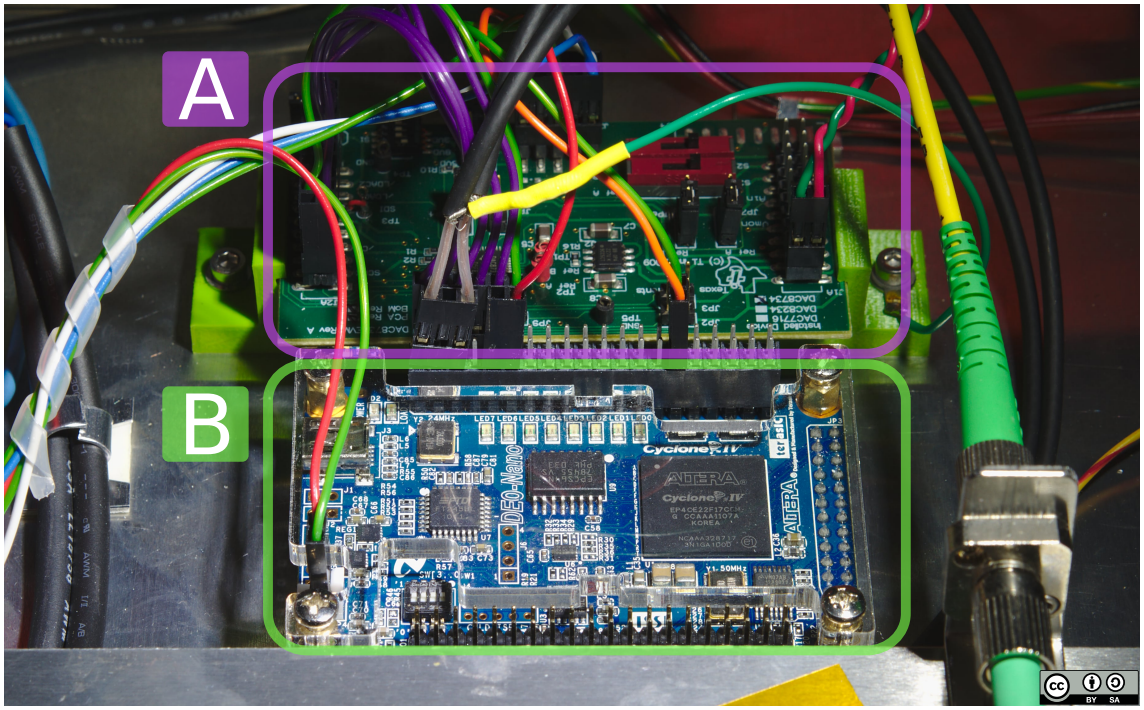

Figure 5.13: *A close-up of the DAC (A) and FPGA (B) boards that are inside the dual beam OCT instrument. The digital sawtooth signal is converted to an analogue signal and is sent to the galvanometer driver board (not shown in the picture).*

The two boards are connected with three wires and communicate using the Serial Peripheral Interface Bus (SPI) protocol. In summary, the FPGA (B) has a main 50 MHz clock signal. For SPI, a secondary clock of 25 MHz is generated and a new value for the sawtooth is calculated and sent to the DAC board at a rate of 352 kHz. Then, the DAC board (A) generates on its output the voltage that corresponds to that value. Over time the output voltage will be the analogue representation of the digital waveform.

5.4.5.1 Field-Programmable Gate Array (FPGA) board

The purpose of the FPGA is to replace the delay pulse generator (BNC 555) that was used in the first setup and in conjunction with the DAC to replace the function generator. The internal wiring of the FPGA is described using a hardware description language known as VHDL (VHSIC[2] Hardware Description Language) and is used in electronic design automation to describe digital and mixed-signal systems such as field-programmable gate arrays and integrated circuits.

The FPGA chip consist of a series of arithmetic logic units (ALU) which are combinational digital electronic circuits that perform arithmetic and bitwise operations on integer binary numbers. These units are connected to each other in order to perform complex operations such as counters, clock dividers, multipliers, etc. Using the VHDL language, the connections between the units is defined along with their specific operation. Small blocks consisting of a series of ALUs that perform a specific function can be abstracted and used as the primary blocks in more complex designs.

For the project, the top-level design of the FPGA can be considered to contain three main blocks. First, the B-scan trigger generator that takes the A-scan clock signal from the laser where it divides its frequency by the number of A-scans in one B-scan and generates a short pulse at the beginning of the next cycle. Second, a block that handles the generation of the sawtooth signal and the communication with the DAC board. Third, a block that uses the onboard led lights to signal the board's state of operation. The top-level block diagram of the FPGA code, with the three main blocks highlighted, can be seen in Figure 5.14. Starting for the "Bscan Trigger Generator" function, the A-scan trigger signal is connected as an input to the "Bscan_trig_gen" block. Connected as inputs to this block as well are the reset signal (RESET) and the FPGA 50 MHz clock (CLOCK_50). On every tick of the 50 MHz clock the "Bscan_trig_gen" block checks the voltage level on the trigger signal (START_SWEEP) and if there is a low-high transition increments the internal counter. When the counter reaches 600 it generates a short pulse on the B-scan trigger (BSCAN_TRIG) output. Additionally, on this block there is another output signal called "DAC_EN" which is used to reset the sawtooth generator block (sawtooth_gen) after 600 A-scans.

The "Update Sawtooth" function consists of two blocks, the "sawtooth_gen" and "slow_dac". Functionally, the "sawtooth_gen" block is similar to the B-scan generator block, as at its core is a binary counter. Furthermore, the reset signal (RESET) and the FPGA 50 MHz clock (CLOCK_50) are connected to the "sawtooth_gen" as well. However, there is additional logic that surrounds this counter.

First, the counter has two different counting steps $n = 1$ and $n = -16$. After a

[2]Very High Speed Integrated Circuit

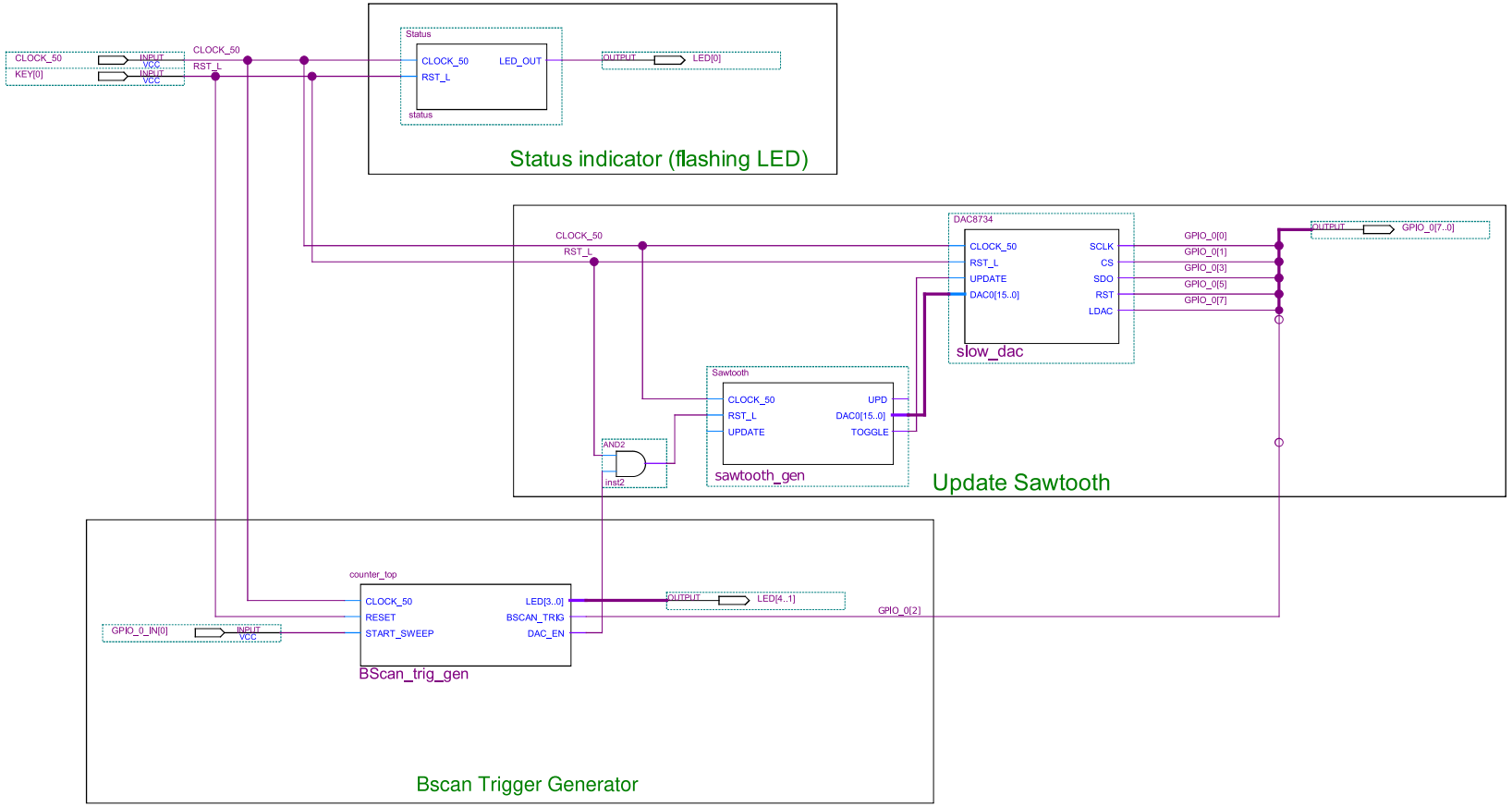

Figure 5.14: *The block diagram of the code executed by the FPGA board. It consists of three main blocks. The B-scan trigger generator that takes the A-scan clock signal from the laser where it divides the A-scan frequency by the number of A-scan in one B-scan. The sawtooth generator is enabled by the B-scan trigger and on every clock pulse of the FPGA it sends a command to the DAC8734 that communicates with the Digital-to-Analogue board and updates the output voltage. Last, the status indicator block generates a pulse that drives an LED diode on the FPGA board that is used as good condition indicator.*

reset, the 16 bit counter starts at the value of −1968 and is incremented by $n = 1$ on every 142nd FPGA clock pulse until its value is 1968. The number 1968 is selected as it is divisible by 16 and the range −1968 to 1968 will give a 94 % duty cycle with a frequency of ≈84 Hz as shown in Equations (5.7) and (5.8). When the value of the counter reaches 1968 the step n changes to $n = -16$, thus on every 142nd FPGA clock pulse the counter is decremented by 16 until it reaches the starting value of −1968. Additionally, every 142nd FPGA clock pulse, the state of the "TOGGLE" output is toggled to signal the "slow_dac" when to read the 16 bit counter value and update the signal on the DAC board.

As the FPGA clock is connected to the "slow_dac", the SPI clock is equal to 50 MHz thus the maximum DAC trigger rate is 438. However, as the 50 MHz clock of the FPGA is divided by 142, the update frequency of the sawtooth is 352.12 kHz. The total number of points in the sweep are equal to the number of points where the counter increments plus the number of points where the counter decrements:

$$\text{total points} = (1968 - (-1968)) + \frac{(1968 - (-1968))}{16} = 3936 + 246 = 4182\,. \quad (5.6)$$

The duty cycle of the sweep is given by the ratio between the points in each direction,

$$\text{duty cycle} = 100 - \frac{4182}{246} \times 100 = 100 - 5.88 = 94.12\%\,. \quad (5.7)$$

Furthermore, the frequency of the sawtooth is given by

$$f_{\text{saw}} = \frac{352.11\,\text{kHz}}{4182} = 84.20\,\text{Hz}\,. \quad (5.8)$$

Thus, the generated sawtooth has a frequency $f_{\text{saw}} = 84.20$ Hz with 94.12 % duty cycle and 4182 total number of points.

Finally, the last block is a status indicator that controls an on-board light emitting diode (LED) to signal that the board is functional. Again, this is a counter block that counts for 50×10^6 clock pulses in order to generate a 1 Hz square wave for the flashing LED.

5.4.5.2 Digital-to-Analogue Converter board

The Digital-to-Analogue converter board (DAC) is used for converting the sawtooth signal generated by the FPGA into an analogue voltage waveform that is sent to the galvanometer driver board. This is an evaluation board for the Integrated Circuit (IC) DAC8734 manufactured by Texas Instruments. The DAC8734 is a high-accuracy,

quad-channel, 16-bit digital-to-analogue converter (DAC) that operates from supply voltages of ±5 V to ±18 V in bipolar output mode, and from 5 V to 24 V in unipolar mode. Additionally, with a 5 V reference, the DAC8734 can be configured to output ±10 V, ±5 V, 0 V to 20 V, or 0 V to 10 V.

The specifications of the chip are shown in Table 5.4. For the OCT setup the DAC was configured to output a voltage of ±10 V which is inside the range of the galvanometer driver (Section 5.4.6). Furthermore, only one channel is used on the DAC, as for the system only B-scan sectioning is performed which requires only one mirror.

Table 5.4: *DAC8734 digital to analogue converter*

Parameter	Value	Unit
Channels	4	
Resolution	16	bit
Clock Rate (f_{clk})	<50	MHz
Trigger rate (f_{clk}=50 MHz)	438	kHz
Supply Voltage	2.7–5.5	V
Output Voltage	±5 to ±18	V

The clock for the SPI is set to 50 MHz (Section 5.4.5.1) but the sawtooth update frequency rounded to the second decimal place is 352.11 kHz. Considering that the sawtooth for the galvanometer has a frequency of ≈84 Hz, then in one period 4182 points will be generated. The sawtooth with 100% duty cycle would be the ideal signal to drive the galvanometer, as there will be little dead time between sweeps. Undoubtedly, the motors of the galvanometers are unable to rotate back at such a short time. Additionally, the current drawn by the motor at such a steep transition will be way above the range of the supply with a risk of damaging both. Thus, to protect the galvanometer and reduce the power requirements a 94% duty cycle is used.

To show the difference between the two waveforms in Figure 5.15 a 94% and 100% duty cycle sawtooth with a frequency of 84 Hz is plotted. For the 94% signal there is 700 µs of dead time when the mirror flies back to its starting position. For this 700 µs, the output of the B-scan image is erroneous, thus it is removed at post-processing.

5.4.6 Galvanometer and Driver Board

In the setup a small-beam dual-axis galvanometer (Thorlabs GVS002) with a maximum mechanical angle of ±12° is used. This galvanometer is used in conjunction

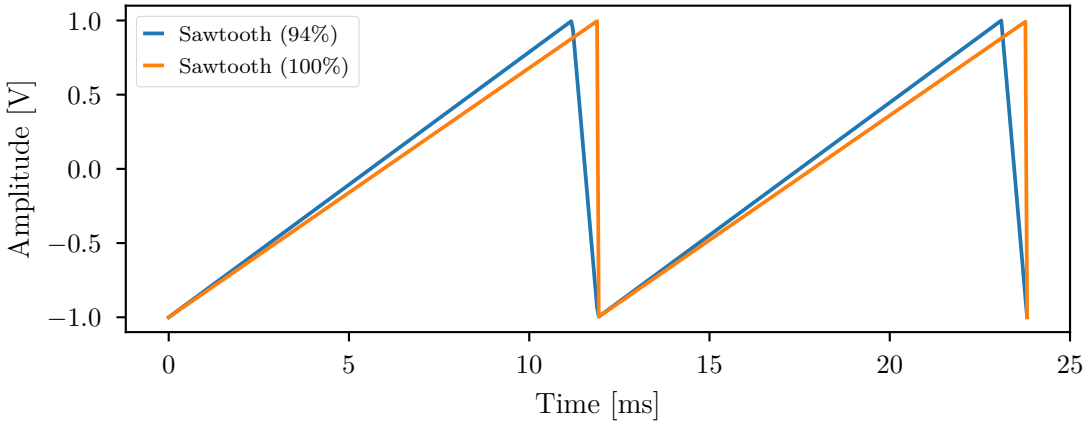

Figure 5.15: *The sawtooth with 100% duty cycle would be the ideal signal to drive the galvanometer. Due to physical limitations, imposed by the galvanometer motor, the sawtooth signal with 94% duty cycle is use instead. The timing of the signal is synced with the A-scan clock to minimise the amount of wasted A-scans.*

with a driver board (Thorlabs GVSM002/M) that accepts the signal from the DAC and after signal conditioning passes the signal to the motors. Table 5.5 summarises the specifications of both the galvanometer and its driver board.

Table 5.5: *Thorlabs GVSM002/M galvanometer and driver board specifications*

(a) *Galvanometer*

Parameter	Value	Unit
Resolution	70.0	µrad
Average Current	1.0	A
Peak Current	5.0	A
Input Beam Diameter	4.0	mm
Mechanical Angle X	±8.5	°
Optical Angle X	±17.0	°
Mechanical Angle Y	±12.5	°
Optical Angle Y	±25.0	°

(b) *Driver board*

Parameter		Value	Unit
Bandwidth	Square	100.00	kHz
	Sine	250.00	kHz
	Sawtooth	175.00	kHz
Power Supply	Current	1.25	A
	Peak	5.00	A
	Voltage	±15.00	V
Input Position Signal	Voltage	±10.00	V
	Scale	0.80	V/°
Output Position Signal	Scale	0.50	V/°

Based on the driver board specifications the DAC board must generate a dual bipolar ±10 V analogue output (differential) with a clocking frequency higher than 20 kS/s (kilo Samples/second). It is recommended to have higher sampling frequencies like 100 kS/s. Additionally, it is recommended the DAC to have 16 bit resolution and low impedance output (≤50 Ω). As mentioned in Section 5.4.5.2, the DAC has 16 bit resolution, is set to a bipolar output of ±10 V and the sampling rate is 352.11 kHz, i.e. 352 kS/s which is over thrice the recommended value of 100 kS/s.

Furthermore, the galvanometer draws an average current of 1 A while the driver board requires a power supply with a dual input voltage of ±15 V and 1.2 A on each rail. For this reason, the switching power supply for the driver board has a dual output of ±15 V and 2 A. Also, from the specifications of the galvanometer, the scan angle range is different for each motor. The mechanical scan angle range for the x-axis is ±8.5°, while for the y-axis is ±12.5°. Notably, the optical scan angles are twice the mechanical one and the scanning distance is given by

$$I = 2d \tan \Theta \,, \tag{5.9}$$

where I is the scanned distance on the sample surface, d the distance of the mirror to the sample and Θ the optical scan angle.

As an overview, Figure 5.16 shows (a) the galvanometer driver board for x-axis—each galvanometer motor has a specific driver board that is calibrated against—and (b) the view of the galvanometer mirrors inside the cage adapter.

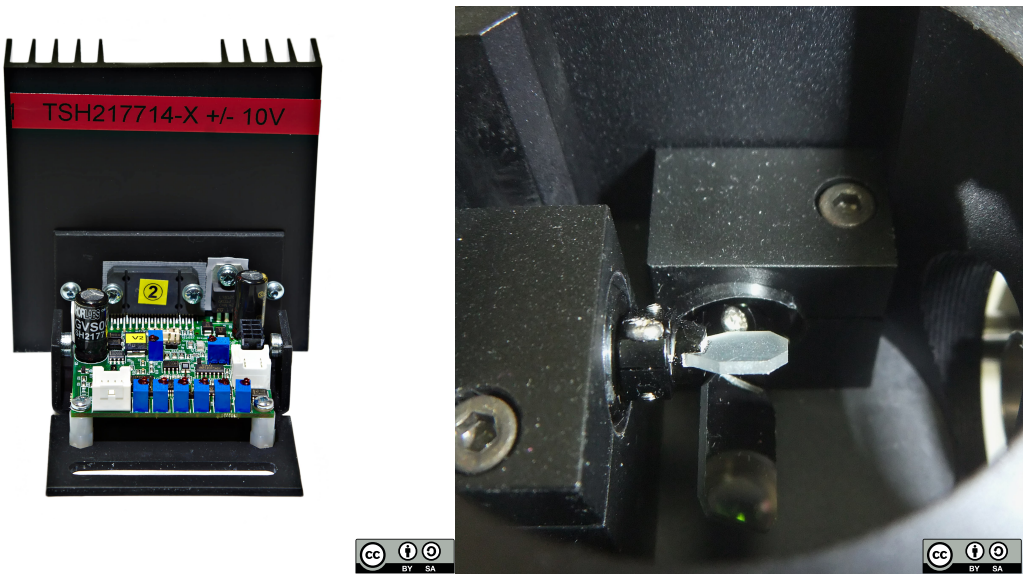

(a) *Galvanometer driver board and heatsink* **(b)** *A 2D galvanometer in a cage mount*

Figure 5.16: *The galvanometer driver (a) used inside the dual-beam OCT instrument and (b) the 2D galvanometer mounted inside a cage system mount as shown in Figure 5.6.*

5.4.7 Analogue-to-Digital Converter Board

For the acquisition of the signal from the photodetectors a Data Acquisition card (DAQ) is connected to the computer using the PCI Express (Peripheral Component Interconnect Express) interface. As one of the objectives of the project is to develop

a real-time dual beam OCT system, this acquisition board should have the following requirements:

- Dual channel support (Dual beam system)
- Trigger inputs (A-scan, B-scan triggers)
- The onboard Analogue-to-Digital Converter (ADC) should have at least 12 bit resolution
- Input bandwidth greater than the photodetectors (100 MHz)
- Sampling rate greater than 250 MS/s
- Data transfer rates above 800 MB/s

A DAQ card from AlazarTech[3] was selected satisfying all the requirements; Table 5.6 shows the specifications of this card.

Table 5.6: *ATS9350 data acquisition card specifications*

Parameter	Value	Unit
Channels	2	
Resolution	12	bit
Throughput	1800	MB/s
Sample Rate	500	MS/s
Bandwidth	250	MHz
Input Voltage (max)	±4	V

Notably, the selected card has an FPGA onboard that handles the communication with the computer, the onboard memory (SDRAM) where the captured data are temporarily saved, and the ADC's that digitise the analogue waveform in order to be stored. To better understand how the DAQ card operates the simplified block diagram is shown in Figure 5.17.

The board has five connectors, external clock (E CLK), two input channels (CH A, B), trigger input (TRIG IN), and an auxiliary bidirectional connection (AUX I/O). The external clock source is used as an input for a variable crystal oscillator (VCO) that generates the digitiser clock for the two channels (CLK A, B). On every pulse of these clocks, a new sample is taken by the analogue-to-digital converters (DAC). The input channels are connected to an input amplifier that will adjust the voltage level accordingly so the full-scale amplified signal uses the whole range of the 12 bit digitiser. To control when data are captured, a trigger input is connected to the positive input of a comparator. On the negative input of the comparator, the signal

[3]http://www.alazartech.com

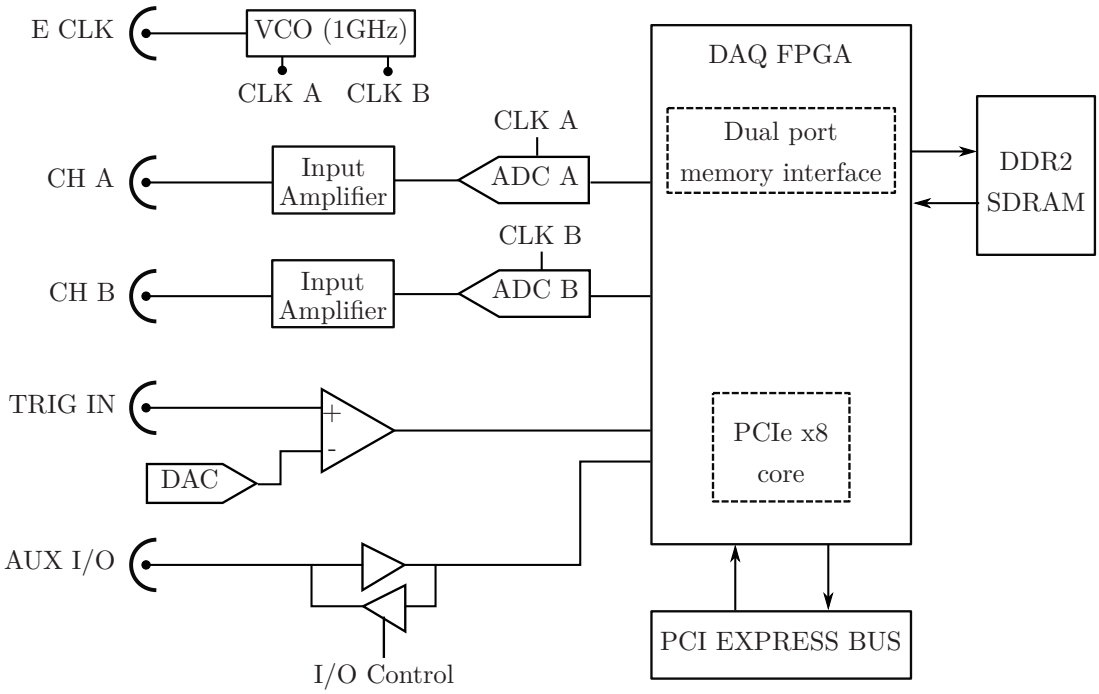

Figure 5.17: *Simplified block diagram of the data acquisition card.*

from an onboard digital-to-analogue converter is connected. Before the acquisition, the value of the digital-to-analogue converter is set; when the voltage level of the trigger input surpasses the DAC value the acquisition begins.

Finally, onboard there is an auxiliary input/output that can either be used as a secondary trigger input or as a digital output. In the former case, the trigger must be digital and its purpose is to enable the acquisition. Thus, if the voltage level on the auxiliary input is high and a valid trigger is generated by the TRIG IN, then acquisition begins. If the voltage level on the auxiliary input is low, when a valid trigger is generated by the TRIG IN is ignored and no acquisition takes place.

For the dual beam OCT system only CH A, CH B, TRIG IN, and AUX IN are used. The A-scan trigger signal from the laser is connected to TRIG IN, thus on every pulse a laser sweep (i.e. A-scan) is captured. On the acquisition card, the FPGA is set to capture data for 600 triggers before it stops. The B-scan trigger signal is connected on AUX IN and is used to re-arm the acquisition on the board so that another set of 600 A-scans can be captured. Thus, the A-scan and B-scan sweeps are synchronised with the one for the galvanometer,

5.4.8 Acquisition Software

As mentioned in Section 5.4.7, the raw interferometric signals from the two photodetectors (one for each beam), are digitised using a Data Acquisition card (DAQ). This card is connected to the instrumentation computer via PCI Express (Peripheral Component Interconnect Express) directly on to the motherboard. The card is directly connected to the computer, therefore the digitised data can transparently be transferred to system memory and accessed by the CPU for the calculation of the Fast Fourier Transform (FFT), before being displayed on the screen.

Due to the highly specialised hardware and the specificity of the work, a custom application and framework for the processing had to be made. Consequently, for the purposes of the project a software application was developed in parallel with the optical and electrical setup. The programming language used on most of the software is Python[4].

Apart from a small utility that performs the calibration of the laser before use, two main applications were written. The first one is an acquisition front-panel that controls the digitiser card, provides a real-time display of the two B-scan images—one per beam, and can capture a set of raw frames that are used for the flow tracking. As an example, a screenshot of the front-panel can be seen in Figure 5.18 where it shows the dual B-scan of a microfluidic chip seeded with particles. The front panel has four main areas A–D. From the top toolbar (A) the windowing functions and the size of the Fourier transform can be selected. Lowering the FFT size allows higher refresh rates of the images as it takes less time to compute the transform. With an FFT size of 2048 and both beams enabled a frame rate of 30 Hz, similar to video, can be achieved. Additionally, from the DVV tab, the amount to shift the Data Valid Vector before application can be set (in real-time). The “Save” tab on the toolbar gives the ability to capture a series of B-scans at the maximum scanning rate and store them on a custom file format for later use.

On the right side of the front panel (B) there is a histogram plot of the OCT images. The bins of the histogram correspond to the amplitude of the pixels in dB. Using the yellow sliders, a portion of the histogram can selected and only the pixels with amplitudes inside the range are shown. The remaining pixels are clipped; their amplitudes are clamped to the edge values of the range. This way, the contrast and the brightness can be adjusted to produce clear images with high contrast. Furthermore, the main viewing area is highlighted with (C). Inside this area the B-scan images from both beams are displayed. Finally, the bottom toolbar (D) displays information about the current acquisition such as acquisition rate, FFT calculation rate, and image plotting rate. On the right there is an adjustment for the refractive index. The

[4]Python Software Foundation. Python Language Reference, version 3.6. Available at http://www.python.org

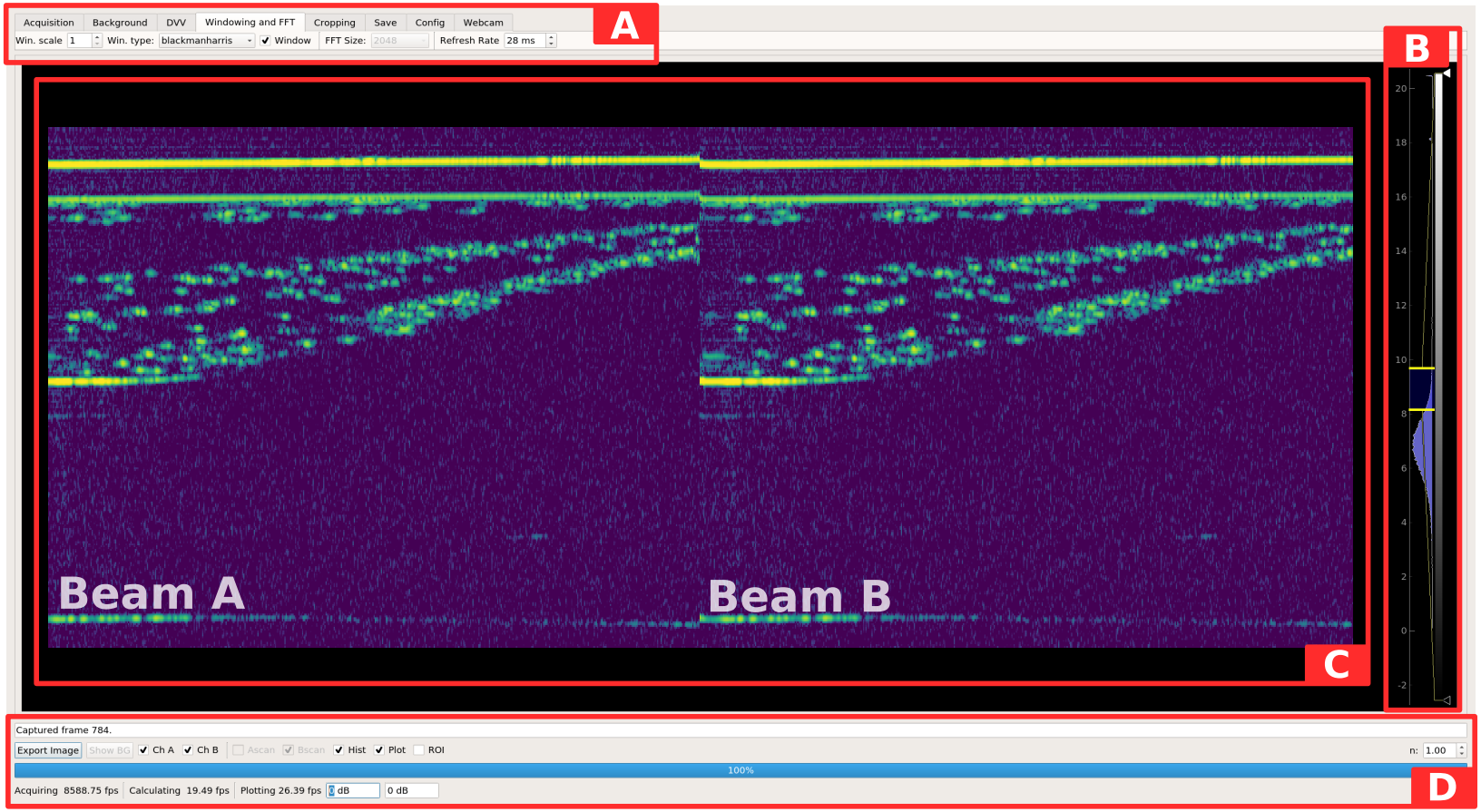

Figure 5.18: *Screenshot of the OCT acquisition software that was implemented specifically for the dual beam OCT system. The toolbar (A) gives the ability to change the configuration in real-time, while the histogram (B) allows the contrast of the image to be adjusted. It is a frontpanel that allows the B-scan images to be viewed in real-time for both beams simultaneously. The B-scan images (C) show the cross-section of a microfluidic chip seeded with particles.*

value can be changed to reflect the refractive index of the material been measured. This is needed for the scaling of the image as the depth resolution is dependent on the refractive index. The second application processes the recorded A-scan to produce the B-scan images and prepare them for the flow tracking. Detailed information about the second application can be found in Section 6.5.1 which describes how the application works and why it is needed for particle tracking.

As the purpose of the project is to enable particle tracking of high velocity microfluidic flows, there is a need to capture the data at the fastest possible rate, i.e. ≈80 Hz equal to the B-scan rate. A major limitation that had to be circumvented was the bottleneck on the storage, where the speed of the drive that the data are stored was not enough for continuous streaming. The problem arises from the nature of the data, because for a single a frame, for both beams, there are

$$\text{Frame size} = (2 \times 600 \times 4096 \times 16\,\text{bit}) = 78.6432 \times 10^6\,\text{bit} = 9.830\,\text{MB}\,. \quad (5.10)$$

And as the B-scan rate is 80 Hz it leads to 786.432 MB/s, while the fastest commercial Solid State Drive connected through the Serial ATA (SATA) interface can get up to a maximum 450 MB/s.

Nonetheless, there is a solution that is implemented on the current system, and makes use of a Non-Volatile Memory Express (NVMe) Drive that attaches directly to a PCI express slot. This drive has a maximum write speed of 1.8 GB/s and combined with 16 GB of DDR4 memory allows the acquisition of dual beam OCT data at 80 Hz for durations up to three seconds.

Lastly, the collected data are stored in the Hierarchical Data Format (HDF) [170], which is a set of file formats (HDF4, HDF5) designed to store and organize large amounts of data. It was originally developed at the US National Centre for Supercomputing Applications (NCSA) and is supported by The HDF Group, a non-profit corporation whose mission is to ensure continued development of HDF5 technologies and the continued accessibility of data stored in HDF. The file format was chosen as it an open format that guaranties the availability of data stored; as there are multiple implementations for reading this format. Apart from this fact, the file format has a truly hierarchical, filesystem-like data format. This means that within a single file all the dataset relevant to the acquisition can be grouped together under folders. Metadata are stored in the form of user-defined, named attributes attached to groups and datasets.

In this project a custom file format that builds upon HDF5 was specified in accordance with the principle that the results should be reproducible. The information is stored in three folders, *ascans*, *bscans*, and *dvv*. Inside the *ascans* and *bscans* folders the raw A-scans and B-scans are stored as a three-dimensional array (frames x (2x600) x 4096). Likewise, *dvv* folder contains the Data Valid Vector (DVV) along

with the amount to roll the vector before application. Finally, the metadata about the target are stored on the top-level directory as a table.

After the data are stored on the disk, the second application (Section 6.5.1) is used to calculate the full 4096 points Fast Fourier Transform (FFT) to generate the final B-scan images that are subsequently stored in the file for future processing or for reference.

5.4.9 Coherence Length

In order to measure the coherence length of the laser the implemented OCT setup was used. As discussed in Section 3.4.2, the optical path length difference over which the optical PSF drops to 50% is the coherence length of the source. Additionally, through the Wiener–Khintchine–Einstein theorem the power spectral density is equal to the autocorrelation function. To capture the autocorrelation of the system a mirror was placed in front of the sample arm, thus both arms have equal power and reflect the same amount of light.

In Figure 5.19 the optical setup used for the laser's coherence length measurement is shown. The two arms of the interferometer (A, B) were aligned separately and for (A) the mirror was mount on a translation stage which was bolted on the optical table. Additionally, the 50 MHz electronic filter was connected to the output of the photodetector. This means that the recorded coherence length will be lower than the coherence length of the laser. However, as the filter is used for the microfluidic measurements it provides an accurate measure of the coherence length and subsequently the imaging range of the OCT system.

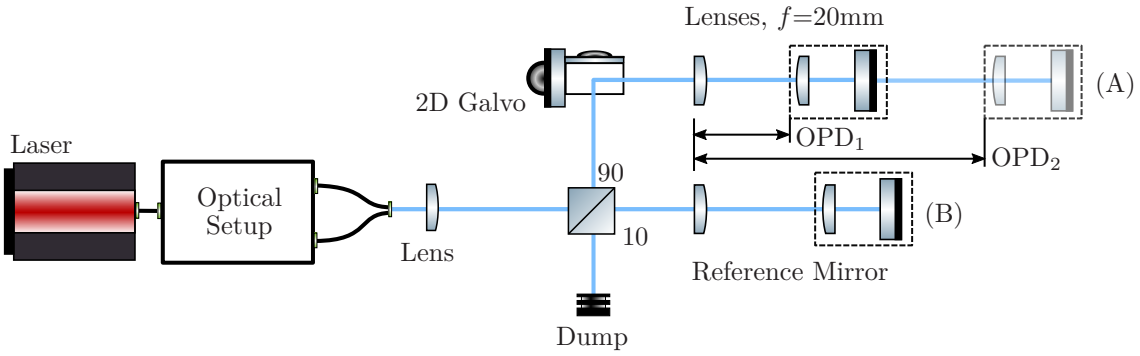

Figure 5.19: *Schematic diagram of optical setup for coherence measurement. The reference arm of the interferometer (B) is stationary, while the sample arm (A) is shifted backwards while measuring the optical power incident to the photodetector. During the measurement, the position of galvanometer was constant. Depending on the optical path difference (OPD) the output optical power varies.*

For the measurement, the mirror on the sample arm was positioned near zero path length OPD_1, Then, using the micrometer of the stage the mirror was pushed backwards to OPD_2 at 500 µm increments while acquiring the interference fringes from the photodetector. Using the acquisition software, the PSF was calculated and the peak was recorded for each position. The result of the measurements can be seen in Figure 5.20 where the peak optical power of the autocorrelation function is plotted against the optical path difference. The power drops by 3 dB at OPD = 6.5 mm resulting in an imaging depth of approximately 3 mm.

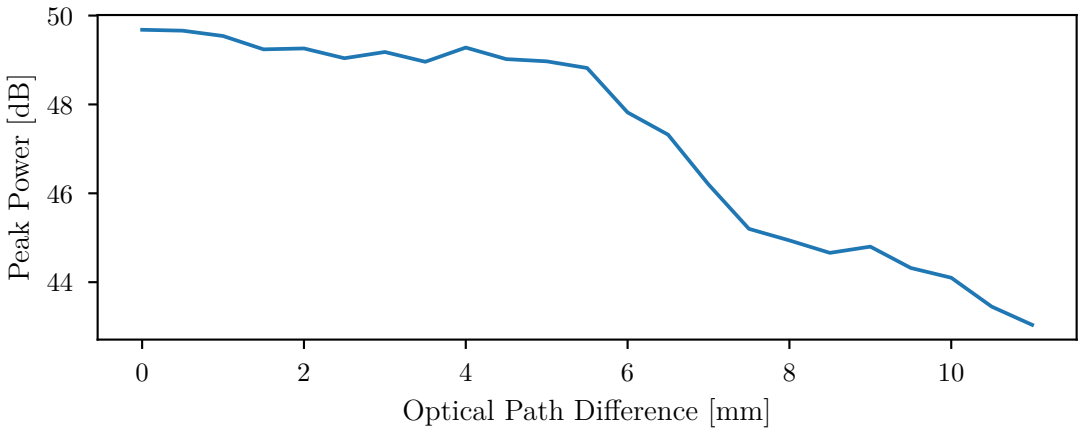

Figure 5.20: *The measured coherence length of the system. With the electronic filter the coherence is limited to 6.5 mm.*

5.4.10 Beam Waist Measurement

5.4.10.1 Measurement procedure

One of the main characteristics of an OCT system is the transverse (lateral) resolution. From Section 4.3.2.7, the lateral resolution is related to the beam waist radius of the Gaussian beam. More specifically, the lateral resolution δx is equal to

$$\delta x = 2w_0 \,. \tag{5.11}$$

Additionally, it can be calculated based on focal length, aperture of the lens, and centre wavelength,

$$\delta x = 2w_0 = \frac{4\lambda}{\pi}\frac{f}{d} \,, \tag{5.12}$$

where d is the spot size of the beam on the objective lens, f is the focal length.

However, instead of calculating the lateral resolution of the dual beam OCT system using the equations from Section 4.3.2.7, the resolution was measured with an experiment. For this experiment, an infrared camera was placed after the lens. A razor blade, mounted on a 3-axis stage, was inserted between the scan lens and the camera. The diagram of this setup is shown in Figure 5.21.

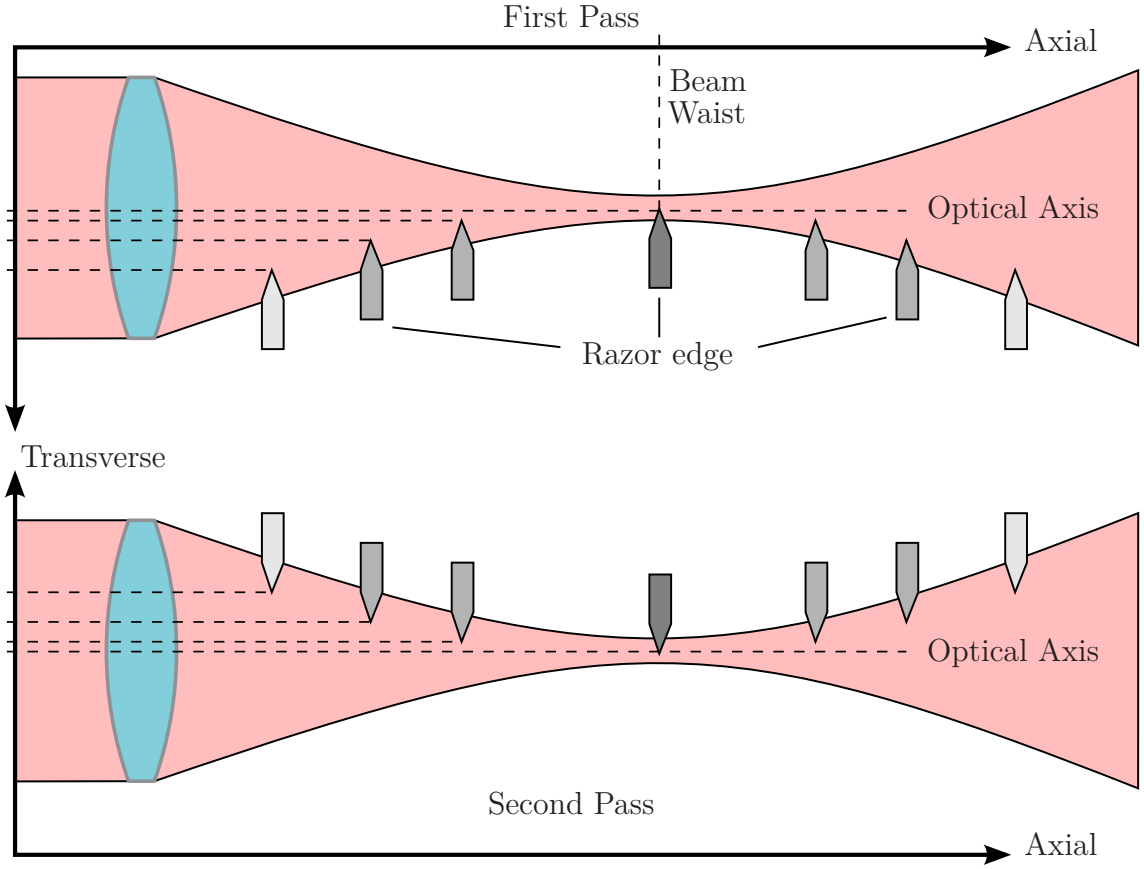

Figure 5.21: *Setup for the measurement of the beam waist for the dual beam OCT system. The razor edge is placed after the scan lens at a position closer than one focal length. Then, the razor is moved backwards in steps along the axial direction. At each step the edge is transversely translated towards the beam until it starts blocking it and the amount of translation is recorded. The process is repeated for the other side of the beam.*

The steps involved for the measurement of the beam waist are the following, starting for the first beam:

1. Place the razor edge close the scan lens at a distance less than the focal length of the lens.

2. Using the NIR InGaAs CCD camera (Hamamatsu C14041-10U) to see the beam, adjust the transverse position of the razor edge using the stage mi-

crometer so that the edge begins to cover the beam dropping the power by half.

3. Record the position of the micrometers for the axial and transverse direction.
4. Adjust the micrometer to obstruct the beam from the other side and record the position.
5. Using the micrometer, move the razor closer to the camera.
6. Repeat steps 2–5, until the position of the razor is past the beam waist.
7. Repeat steps 1–6 for the second beam.

After the above procedure a set of x and y positions will have been recorded, two x positions per y position per beam.

5.4.10.2 Razor blade holder

In order to perform the beam waist measurement the razor blades have to be at an appropriate height so that the beam can be obstructed. Thus, a 3D-printed holder that holds the two blades was constructed and is attached to a 3-axis flexure stage. An image of the finished holder can be seen in Figure 5.22, two razor blades are mounted at the end of the holder (A). The two razor blades are separated by 5 mm (measured with digital calipers) so the two beams can pass between them without being obstructed. The blades themselves are ≈40 mm long and ≈22 mm wide. The 3D-printed holder is bolted on a 3-axis flexure stage (B), thus with micrometer precision the razor can be positioned in both the axial and transverse direction of the beam. Figure 5.23 demonstrates how the razor blade holder was positioned for the measurement.

5.4.10.3 Beam waist profile

With the recorded positions for the beams and after calculating the absolute distances between the sides of the beams, the two beam waist profiles can be plotted. The result is shown in Figure 5.24.

The points on the graph represent the recorded positions while the solid lines with the shaded regions around them represent the polynomial fit on the data and the confidence interval respectively. From the graph is seems that the two beams are diverging which indicates a slight misalignment of the two fibres in the ferrule. Additionally, based on the measurement, the two beam waists are 10 µm for the first and 15 µm for the second beam.

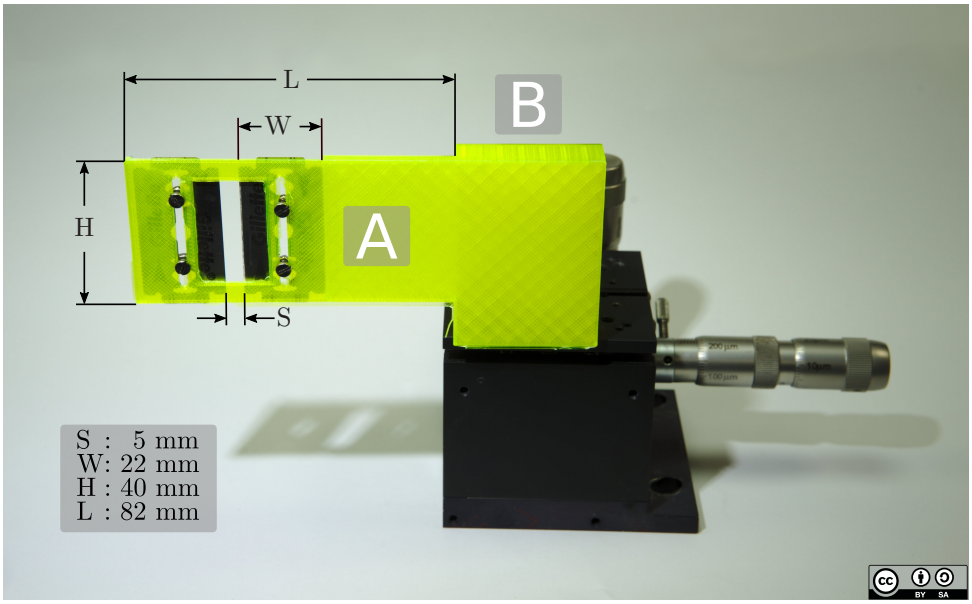

Figure 5.22: *The image shows the 3D-printed razor blades holder (B). The blades are screwed in place side by side at the end of the holder (A). The holder is secured on a 3-axis flexure stage offering fine control over the x-y translation of the razor blades.*

5.5 Summary and Future Work

In this chapter, the process of designing and developing two different dual beam OCT systems was discussed. First, the design of a fibre-optic system was shown along with its development. However, this system had issues with polarisation that was affecting the signal-to-noise ratio and consequently the image quality of OCT. An interim solution was proposed which utilised polarisation state controllers (PSC) to minimise the polarisation effects.

Secondly, a different approach was proposed which uses a bulk-optic beam-splitter as the interferometer for both beams. This solution removed any polarisation effects that were plaguing the early prototype. Apart from solving the polarisation issues, this second system was designed to be more compact and minimise the effects of environmental changes. Additionally, an experiment was made in order to measure the beam waist of the beams to determine the lateral resolution of the system.

Nevertheless, the issues with the first system could have been solved with a different approach. But, the required components weren't available at the time of the development. As mentioned in Section 5.3.2.1 the bandwidth of the fibre components had to be at least equal to that of the laser, in this case 82 nm, to guarantee that the depth resolution of the system will be high. However, these components now exist so the all-fibre system can be realised without the problems described previously.

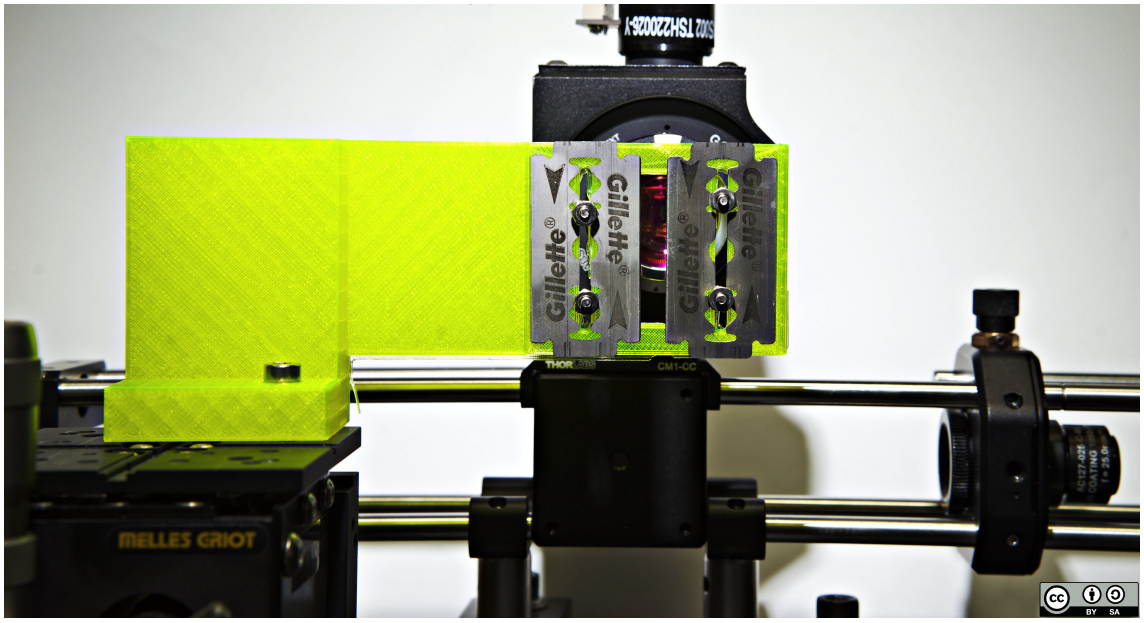

Figure 5.23: *The razor blade holder, mounted on a 3-axis flexure stage, is placed in front of the OCT scan head for the measurement of the beam waist.*

This fibre design utilises polarisation maintaining components to maintain the state of polarisation across the whole optical path. Nowadays, Polarisation Maintaining (PM) couplers exist with bandwidths equal to the non-PM equivalent.

Furthermore, with the PM solution the balanced detection can still be used for further noise reduction. Figure 5.25 shows the design of a dual beam system using polarisation maintaining components. The setup assumes that the light from the laser is not polarised and that the circulators are not polarisation maintaining. Similar to Figure 5.5, polarisation state controllers are placed at second port of each circulator. This way the state of polarisation can be altered before it enters the couplers. Additionally, in front of the PM couplers an In-Line Polariser (ILP) is placed, thus independent of the state at the input of the ILP the output will always be a linear polarised light. So, independent of the polarisation state after the circulator, the polarisation state is rotated using the PSC to match the linear state and maximise the amount of light that passes through the ILP. Lastly, as the couplers are polarisation maintaining, the linear state is maintained, thus the system is free of signal issues due to polarisation. If the laser has a polarisation-maintaining output, the PSC and ILP can be removed as long as the circulators are polarisation maintaining. However, existing PM circulators have a bandwidth of 60 nm which is lower than the non-PM circulators with bandwidths of 85 nm.

Finally, another area of improvement is the fibre pair. A future development can be to substitute 50 µm fibres for the 125 µm ones. The benefits of this approach will

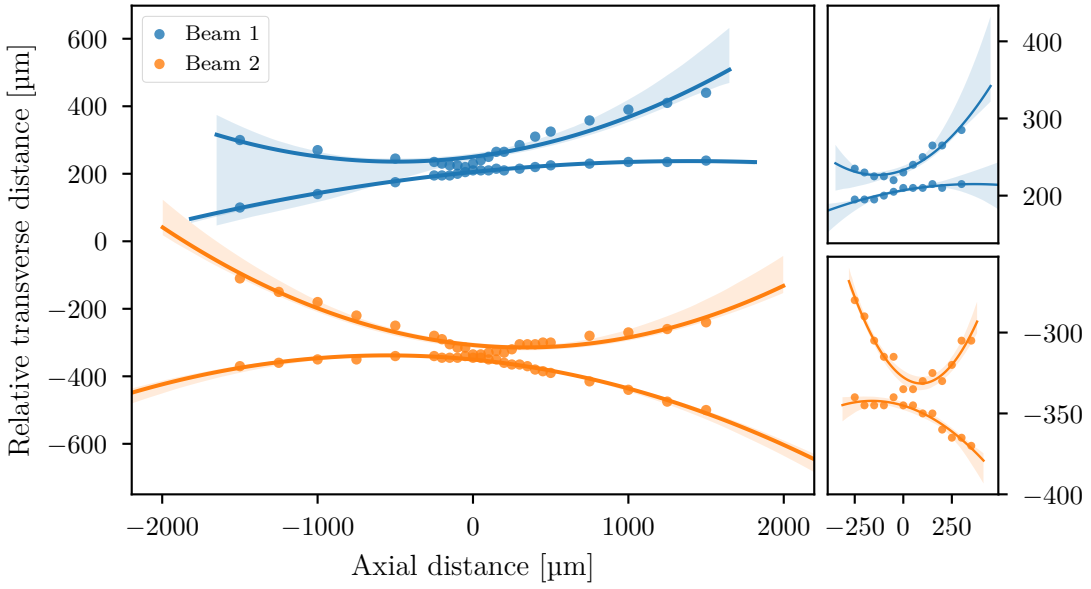

Figure 5.24: *The beam waists of the two beam are shown. The points correspond to the measured values while the solid lines are a second degree polynomial fit on the data. The two beams seem to diverge, an indication that the fibres inside the ferrule are misaligned. The two sub-figures on the right show a close-up of the beam waist.*

be twofold. First, it will allow for smaller beam spacing, increasing the maximum measured velocity of particles. Second, more than two fibres can fit into the bundle. Thus, by appropriately choosing—depending the application—which two fibres to use from the bundle, the beam spacing can be varied, as the chosen fibres can either be adjacent (small spacing) or not (large spacing). Another possibility will be to use the extra fibres as references by silver plating their ends, thus becoming low reflectance mirrors. Then there will be no need for the 90/10 beam-splitter currently used and it will make the OCT scan head more compact. However, as the fibre couplers will be again inside the interferometer the polarisation issued will be relevant. Yet, the issues can be overcome using the polarisation maintaining solution described previously. The only issue with a fibre interferometer that uses a bulk optic reference is dispersion compensation. Usually, dispersion compensation is performed by matching optical materials and path lengths in the two interferometer arms. This was done for the fibre setup shown in Section 5.3.2. Another approach is to compensate numerically during post-processing, but usually is computationally intensive. Although, as demonstrated by Wojtkowski et al., high-speed approximate dispersion compensation can be performed with no increase in computational time compared to standard spectral domain OCT [171].

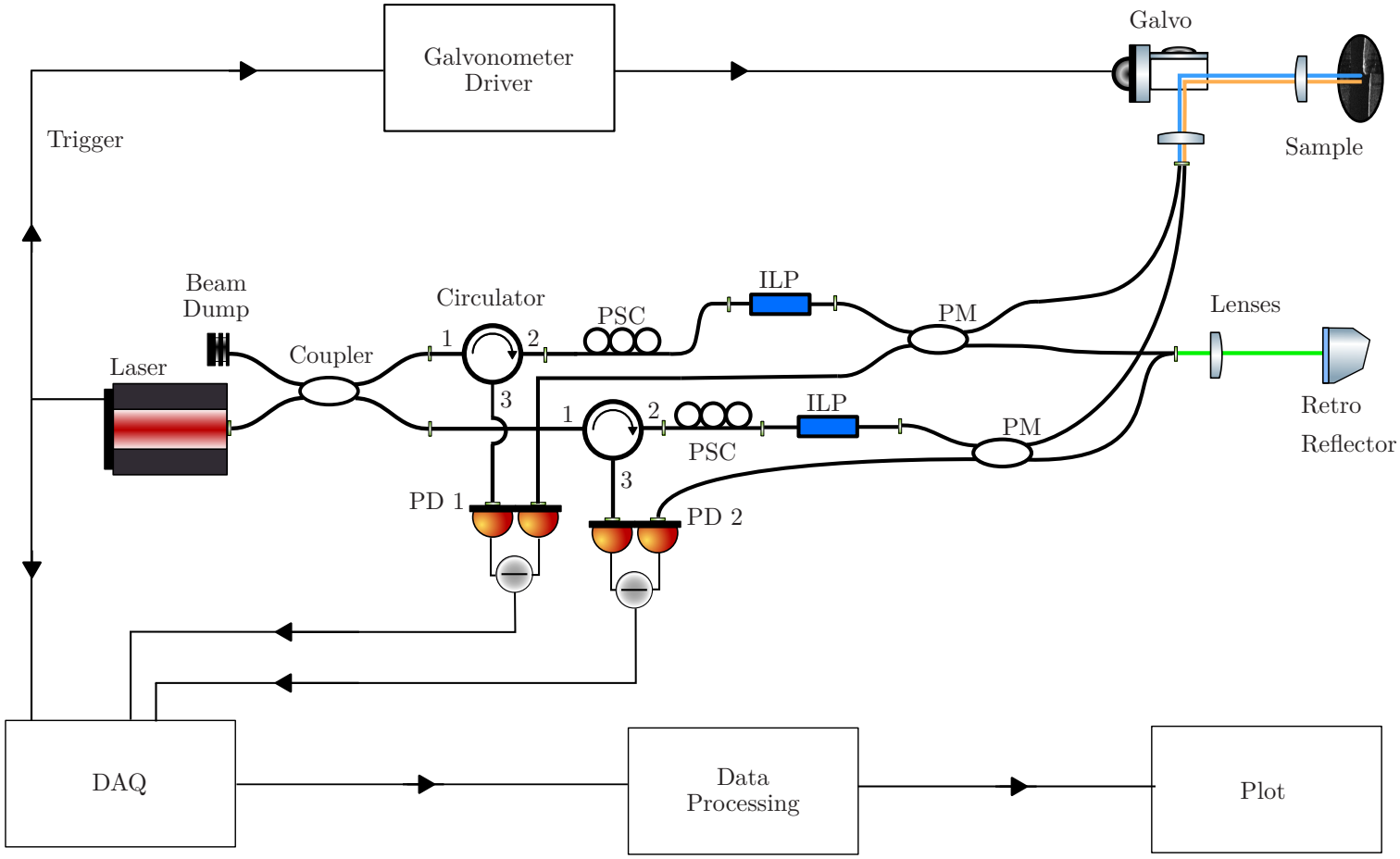

Figure 5.25: *Schematic diagram of a polarisation maintaining dual beam optical setup. Using the polarisation state controlers (PSC) and the inline linear polarisers (ILP) the state of polarisation is fixed and is maintained by the polarisation maintaining (PM) couplers.*

Chapter 6

Microfluidic Velocity Measurements Using Dual Beam OCT

6.1 Introduction

In this chapter, the acquisition process of flow profiles using a dual beam OCT system is presented. Additionally, the results from the processing of the acquired data along with other findings are shown. The targets used for the flow tracking are polymer-based microfluidic chips that were used as flow-channels.

In the first two sections, the physical properties of the microfluidic chips, that were chosen as the targets for the evaluation of the dual beam OCT system, are shown along with the preparation procedure of the colloidal suspension of latex particles that is used for the particle tracking measurements.

In Section 6.4, the microfluidic setup used for the experiments is presented. Additionally, details about the acquisition and processing software are shown. The post-processing of the measurements for calculating the flow profiles is discussed in Section 6.5. It covers the topics of B-scan image conditioning, particle identification, linking particles into trajectories, calculating particle velocities and presenting the flow information.

Furthermore, Section 6.7, shows the effects of pump flow pulsation on particle velocity and the difficulties it imposes on the calculation of the flow profiles.

At the end of the chapter, the results and possible improvements for future research are discussed, before concluding with a brief summary.

6.2 Microfluidic Chips

In order to evaluate the integrated dual beam OCT system (Section 5.4) as an instrument for capturing B-scan images that can be used for particle tracking velocimetry, two different microfluidic chips with rectangular microfluidic channels were investigated—as the velocity profile of such channels is known (square or cylindrical channels exhibit a laminar flow characterised by Hagen–Poiseuille equation, also known as the Hagen–Poiseuille law).

These microfluidic chips are used as sample preparation chips for lab on a chip applications and have the format of a microscopy slide (75.5 mm x 25.5 mm x 1.5 mm) and are equipped with female mini Luer connectors. Their key microfluidic elements are reaction chambers of various volumes (Figures 6.1 and 6.27) can for example be used as nucleic acid extraction devices via magnetic beads simply via applying beads and sample and by using an external magnet to hold the beads in place. These procedures can be done completely manually with a pipette—besides the magnet no additional equipment is necessary—or semi-automated with normal peristaltic pumps found in most life science labs.

The chips were sourced from *microfluidic ChipShop*[1], a company, that started in 2002 as a spin-off from the Fraunhofer Institute for Applied Optics and Precision Engineering and the Application Centre for Microtechnology Jena. For the evaluation, a rhombic and a reaction chamber chip were chosen.

Specifically, the rhombic chip with part-number "12-0918-0194-01" (Figure 6.1) has a 250 µl chamber and a lid thickness of 175 µm. It has two microfluidic channels that are 30.7 mm long, and 8.8 mm wide and 800 µm deep. Each channel, at both ends has two ports that are used either as inputs or outputs and there is a triangle to push liquid to the sides before it merges closer to the centre of the channel. The purpose of the two ports and the triangle is to encourage mixing of the two components to be reacted. This chip was chosen because was the one with the deepest channel, not for its mixing abilities. For the experiments, only one port at each end was used, the other was capped with a mini Luer cap.

Similarly, the reaction chamber chip with part-number "12-1405-0556-03" (Figure 6.2) has eighteen channels with 20 µl volume. Each channel is 700 µm deep; the length and width are 10.8 mm and 2.4 mm respectively. Additionally, the reaction chip has a single input port on either end as well as an inclination to gradually let the particles into the channel. This slope is 12° and it can be seen on the two B-scan images shown in Figure 6.3 and captured using the dual beam OCT system that was developed (Chapter 5). The image on the left has the channel filled with the particle solution and due to the difference of the refractive index the channel appears deeper

[1] http://www.microfluidic-chipshop.com/

compared to the right image, taken with the channel filled with air. Furthermore, the total thickness 2.09 mm can be seen on the image as well as the lid a thickness of 175 µm.

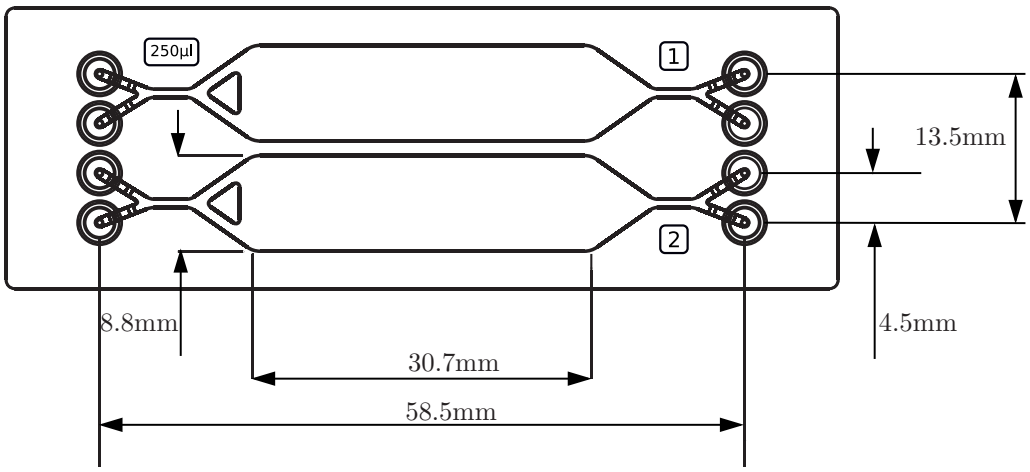

Figure 6.1: *Top view of PMMA Rhombic Chamber Chip with 250 µl chamber. This microfluidic chip has two channels that are 800 µm deep. The length and width of each channel is 30.7 mm and 8.8 mm respectively. The lid thickness is 175 µm.*

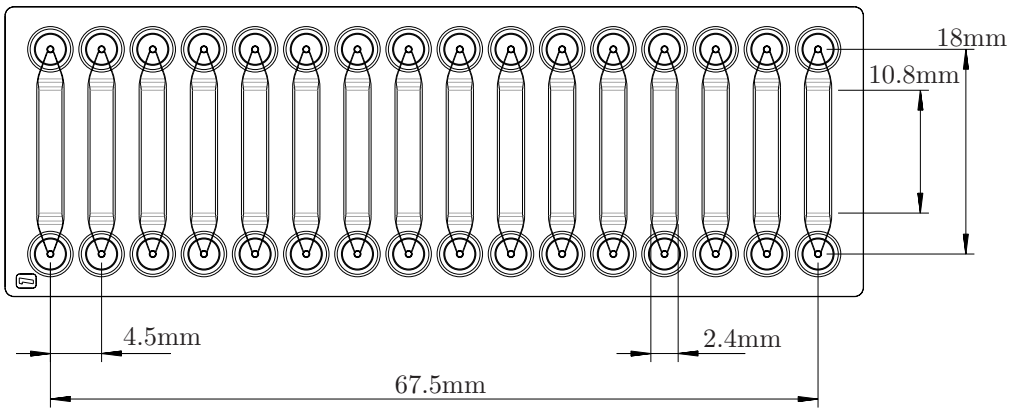

Figure 6.2: *Top view of reaction chamber chip (Fluidic 556) with chamber volume of 20 µl. Polycarbonate (PC) Reaction Chamber Chip with 20 µl chamber. This microfluidic chip has sixteen channels that are 700 µm deep and feature a slope on either side. The length and width of each channel is 10.8 mm and 2.4 mm respectively. The lid thickness is 175 µm*

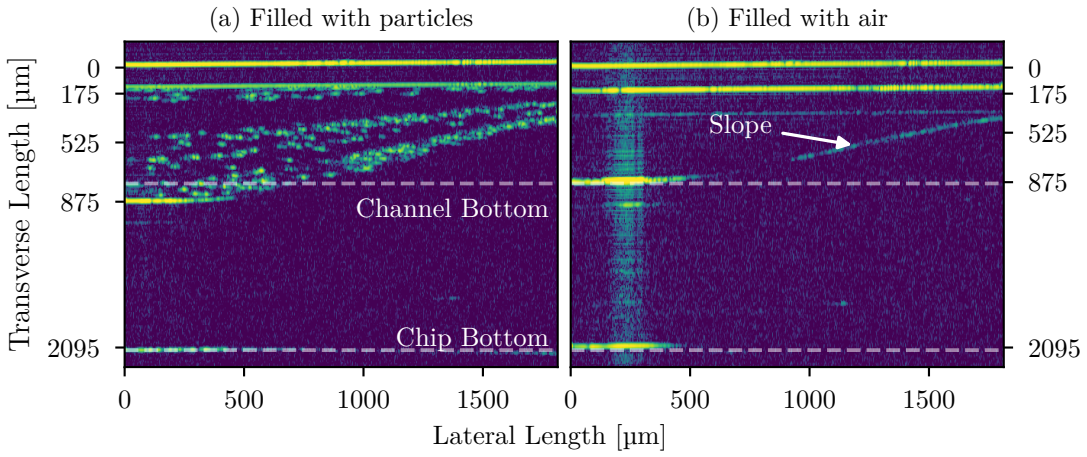

Figure 6.3: *OCT images of the reaction chamber chip. Filled with a particle-glycerol solution (a) and empty (b). Additionally, the bottom of the channel is further down on (a) as it is filled with a particle-glycerol solution altering the refractive index, thus changing the scaling. The lid has a thickness of 175 µm. and on (b), the slope of the channel can be seen.*

6.3 Preparation of Latex Spheres for Microfluidic Imaging

In order to characterise the flow profile generated by the different chip designs colloidal suspensions of latex spheres which can be used as imaging targets were prepared. The requirements of the OCT system require targets that are within the resolution of the system; greater than 10 µm for this system.

The size of the latex particles makes colloidal preparations difficult to maintain as the particles will naturally settle over time. The glycerol-solution used for the experiments described in later sections was prepared using the following procedure[2] for creating a suspension with the correct density in order to ensure that the particles are held at neutral buoyancy (1.05 g/ml). Additionally, the size of the particle has to be sufficiently small to track accurately the flow, yet large enough to be detected by the OCT system.

[2]The procedure was created by Dr. Matthew Partridge (department's chemist) after private communication.

6.3.1 Particle Drag Forces (Stokes Number)

The equation of motion for a spherical particle in a fluid has been called the BBO (Basset–Boussinesq–Oseen) equation. Assuming there is no acceleration of the relative velocity between the particle and the conveying fluid the BBO equation of motion can be simplified to

$$m\frac{\mathrm{d}v}{\mathrm{d}t} = F_{\mathrm{ss}} + F_{\mathrm{g}} + F_{\mathrm{bu}} = \overbrace{-3\pi\eta_{\mathrm{f}} d_{\mathrm{p}} f v}^{\text{Drag force}} + \overbrace{mg - \rho_{\mathrm{g}} V_{\mathrm{p}} g}^{\text{Net body forces}}, \tag{6.1}$$

where m is the mass of the particle, v the velocity of the particle, F_{ss} the steady-state drag forces, F_{g} the force of gravity, F_{bu} the buoyant force, η_{f} the viscosity of the fluid, d_{p} the diameter of the particle, f the drag factor (ratio of drag coefficient to Stokes drag), ρ_{f} is the fluid density, and V_{p} the volume of displaced fluid (equal to particle volume) [172]. It is assumed that v is positive in the direction of gravity (downward). The definition of the drag factor is

$$f = \frac{C_{\mathrm{d}}}{24}\frac{\rho_{\mathrm{f}}|u-v|d_{\mathrm{p}}}{\eta_{\mathrm{f}}}, \tag{6.2}$$

where C_{d} is the drag coefficient, ρ_{f} the fluid density, u the fluid velocity, v the particle velocity, d_{p} the particle diameter, and η_{f} the fluid viscosity [172]. From Equation (6.2) the relative Reynolds number can be defined as

$$Re_{\mathrm{r}} = \frac{\rho_{\mathrm{f}}|u-v|d_{\mathrm{p}}}{\eta_{\mathrm{f}}}. \tag{6.3}$$

The Reynolds number is a dimensionless quantity that is defined as the ratio of the inertial forces ($\rho_{\mathrm{f}}|u-v|d_{\mathrm{p}}$) to the viscous forces (η_{f}). Substituting Re_{r} to Equation (6.2), yields

$$f = \frac{C_{\mathrm{d}}}{24} Re_{\mathrm{r}}. \tag{6.4}$$

Last, the drag coefficient is defined as

$$C_{\mathrm{d}} = \frac{24}{Re_{\mathrm{r}}}. \tag{6.5}$$

Thus, when the advective inertial forces are small compared with viscous forces ($Re_{\mathrm{r}} \ll 1$) the type of the flow is known as "Stokes flow" and the drag factor is equal to 1. With respect to laminar and turbulent flow regimes: laminar flow occurs at low Reynolds numbers, where viscous forces are dominant, and is characterized by smooth, constant fluid motion; turbulent flow occurs at high Reynolds numbers and is dominated by inertial forces, which tend to produce chaotic eddies, vortices and other flow instabilities.

In Equation (6.1) the mass of the particle can be written in relation to particle density and volume ($m = \rho_\mathrm{p} V_\mathrm{p}$) yielding

$$\frac{\pi d_\mathrm{p}^3}{6}\rho_\mathrm{p}\frac{\mathrm{d}v}{\mathrm{d}t} = -3\pi\eta_\mathrm{f} d_\mathrm{p} f v + \frac{\pi d_\mathrm{p}^3}{6} g(\rho_\mathrm{p} - \rho_\mathrm{f})\,. \tag{6.6}$$

Once the particle reaches terminal (settling) velocity $v = v_\mathrm{T}$ there is no more acceleration; all the forces cancel out and the terminal velocity is equal to

$$\begin{aligned} 3\pi\eta_\mathrm{f} d_\mathrm{p} f v_\mathrm{T} &= \frac{\pi d_\mathrm{p}^3}{6} g(\rho_\mathrm{p} - \rho_\mathrm{f}) \\ \Longrightarrow \qquad v_\mathrm{T} &= \frac{g d_\mathrm{p}^2(\rho_\mathrm{p} - \rho_\mathrm{f})}{18\eta_\mathrm{f} f} = \frac{g}{f}\frac{d_\mathrm{p}^2\rho_\mathrm{p}}{18\eta_\mathrm{f}}(1 - \frac{\rho_\mathrm{f}}{\rho_\mathrm{p}})\,. \end{aligned} \tag{6.7}$$

From Equation (6.7), the particle velocity response time can be defined as

$$t_\mathrm{V} = \frac{d_\mathrm{p}^2\rho_\mathrm{p}}{18\eta_\mathrm{f}}\,. \tag{6.8}$$

The particle response time corresponds to the time needed for a particle released from rest to achieve 63% of the free stream velocity [172]. Based on Equations (6.7) and (6.8), for Stokes flow and $\rho_\mathrm{p}/\rho_\mathrm{f} \ll 1$ the terminal velocity reduces to

$$v_\mathrm{T} = g \cdot t_\mathrm{V}\,. \tag{6.9}$$

Similarly, when the particle density is equal to the fluid density, i.e. $\rho_\mathrm{p} = \rho_\mathrm{f}$, the settling (terminal) velocity is zero and the particles are neutrally buoyant. Based on the previous equations, for a tracer particle that accurately tracks the fluid flow the Reynolds number Re_r must be low to assure laminar flow, the particle density almost equal to fluid density, and the particle velocity response time to be sufficiently small. For the last criterion, a dimensionless quantity called "Stokes number" has been defined in honour to George Gabriel Stokes. Stokes number, St_V, is defined as the ratio of the characteristic particle response time t_V to the time characteristic of the flow field t_F,

$$St_\mathrm{V} = \frac{t_\mathrm{V}}{t_\mathrm{F}}\,. \tag{6.10}$$

For example, the characteristic time for the flow through a pipe may be D_H/U where D_H is the hydraulic diameter of the pipe and U is the flow velocity. In this case the Stokes number becomes

$$St_\mathrm{V} = \frac{t_\mathrm{V} U}{D_\mathrm{H}}\,. \tag{6.11}$$

However, for shapes such as squares, rectangular or annular ducts where the height and width are comparable, the characteristic dimension for internal-flow situations is taken to be the hydraulic diameter, D_H, defined as $D_\mathrm{H} = 4A/P$ where A is the

cross-sectional area, and P is the wetted perimeter. The wetted perimeter for a channel is the total perimeter of all channel walls that are in contact with the flow.

If $St_\mathrm{V} \ll 1$ the response time of the particles is much less than the characteristic time associated with the flow field. Thus, the particles will have ample time to respond to changes in flow velocity; the particle and fluid velocities will be nearly equal (velocity equilibrium). For $St_\mathrm{V} \gg 1$, the particle will have essentially no time to respond to the fluid velocity changes. From a practical point of view it can be stated that the condition $St_\mathrm{V} < 0.1$ returns an acceptable flow tracing accuracy with errors below 1% [173].

Last, for accurately tracking of the flow, the concentration of particles must be chosen to be high enough to meet the required temporal resolution requirements while being low enough to insure single realization operation. Single realization operation is achieved when the probability of more than one particle occurring simultaneously in the detection volume is less than 0.5% [174]. Assuming a random homogeneous distribution of the particles, the probability of having N_p particles in a volume V will follow a Poisson distribution,

$$P(N_\mathrm{p}) = \frac{\overline{N_\mathrm{p}}^{N_\mathrm{p}}}{N_\mathrm{p}!} \mathrm{e}^{-\overline{N_\mathrm{p}}}\,, \tag{6.12}$$

where $\overline{N_\mathrm{p}}$ is the Poisson parameter and expresses the mean number of particles simultaneously in the volume V. The Poisson parameter can be written in terms of the mean concentration $\overline{n_\mathrm{p}}$ as $\overline{N_\mathrm{p}} = \overline{n_\mathrm{p}} V$. The condition for single realisation is $\overline{N_\mathrm{p}} < 0.1$ [174]. Thus, the particle concentration must satisfy the following condition

$$\overline{n_\mathrm{p}} \leq \frac{0.1}{V_\mathrm{d}}\,, \tag{6.13}$$

where V_d is the detection volume. A lower particle concentration will lead to a lower particle rate, hence, a longer measurement duration to reach a given accuracy.

6.3.2 Scattering Properties of Tracer Particles

Based on the Stokes number, discussed in the previous section, small particles are required to fulfil the fluid-mechanical requirements of tracers. However, as an opposing requirement, the particles should scatter enough light in order to be visible. Typical particle dimensions are on the order of a micrometer for gas (i. e. air) flows, and tens of micrometers for liquid (i. e. water) flows. For optical systems like µPIV, LDV, OCT the scattering of light by these particles occurs in the so-called Mie regime [173], where the particle diameter d_p is larger than the light wavelength λ. For this reason, techniques such as PIV usually employ tracer particles that contain a fluorescent dye; the light absorbed by the dye is emitted at a longer wavelength.

The Mie scattering of a spherical particle depends on the sphere diameter d_p, the refractive index of the particle m (relative to the refractive index of the surrounding medium), and the wavelength of the light λ. The Mie parameter $x_\mathrm{M} = \pi d_\mathrm{p}/\lambda$ governs the scattering amplitude. A typical Mie scattering diagram is shown on Figure 6.4 where the scattering amplitudes of two particles are plotted against the scattering angle θ_s. A scattering angle of 0° corresponds to forward scattering while 180° to backscattering. At the operating wavelength of the OCT system (i.e. 1.55 µm in air or 1.05 µm in glycerol), the Mie parameters for the two spheres are

$$x_\mathrm{M}(3) = \frac{3\pi\,\mu\mathrm{m}}{1.05\,\mu\mathrm{m}} = 7.37, \qquad x_\mathrm{M}(10) = \frac{10\pi\,\mu\mathrm{m}}{1.05\,\mu\mathrm{m}} = 29.88\,. \tag{6.14}$$

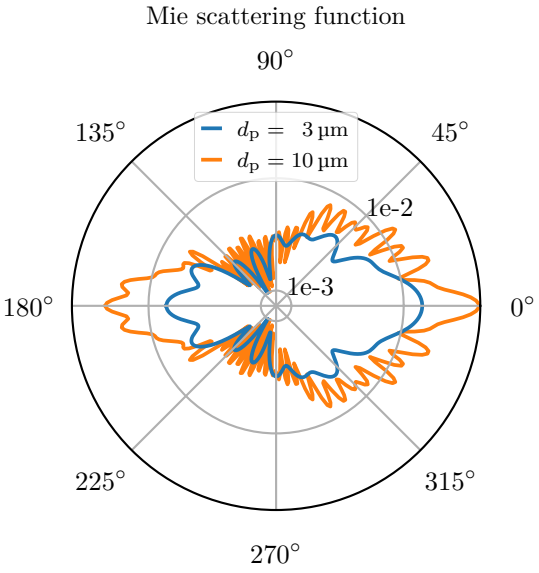

Figure 6.4: *Mie scattering cross-section of a polystyrene particle. The particles have a diameter of 3 µm and 10 um respectively. The scattering amplitude is proportional to particle size. Additionally, at scattering angles of 90° and 270° the amplitude is almost zero. This is why single camerea PIV needs a much stronger light source compared with other techniques that operate in forward/back scattering mode.*

From the figure it can be seen that the 10 µm particle scatters more light (in both horizontal directions) than the 3 µm. Additionally, at a scattering 90° and 270°, e.g. for single-camera PIV with the optical axis normal to the light-sheet plane, the scattering amplitude is generally very low. This is why PIV needs a much stronger light source than e.g. LDA or OCT, which operate in near-forward or near-backward scattering mode. Apart from the particle size, Mie scattering depends on the relative refractive index. Figure 6.5 shows the Mie scattering efficiency as a function of wavelength for different sized particles suspended in different media. Here, the two media are glycerol, as it was used in the experiments, and benzene. The refractive

indices are 1.4746 and 1.501 respectively. The refractive index m of the polystyrene spheres is 1.5717 [175]. The solid lines in the graph correspond to particles suspended in glycerol; the dashed lines correspond to particles suspended in benzene. At lower wavelengths the scattering efficiency is increases independent of particle size. This correlates with the Mie parameter x_{M} as it is inversely proportional to the wavelength. Interestingly, for glycerol at wavelengths between 1.15 µm to 1.55 µm the scattering efficiency of the 10 µm particle is higher than the larger 14 µm. This means, that the 10 µm is a good candidate for tracing flows in glycerol as it small in size yet it has higher scattering efficiency.

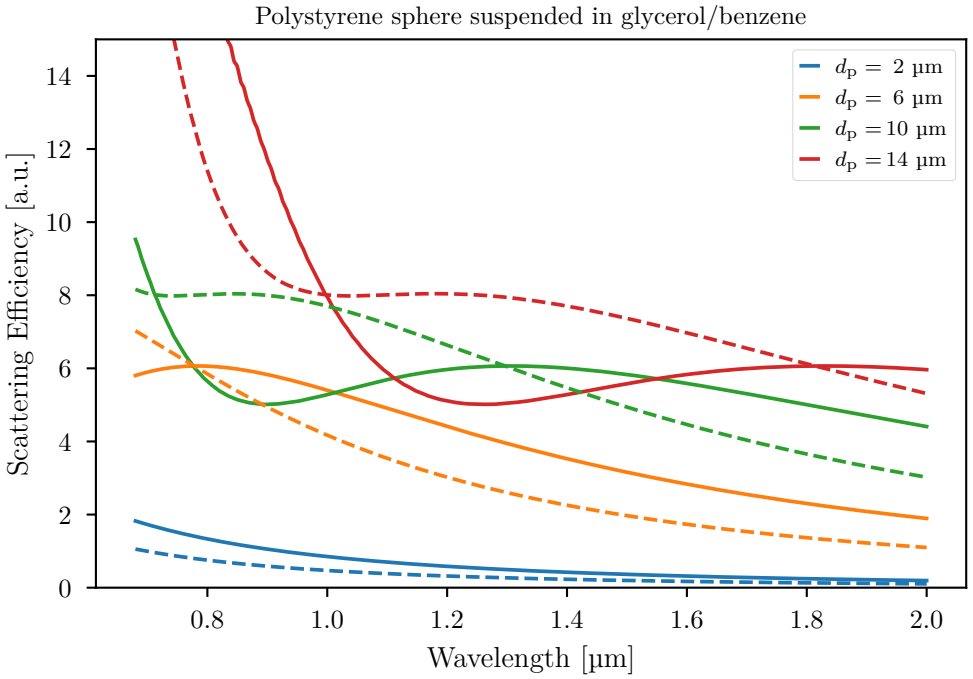

Figure 6.5: *Mie scattering efficiency of polystyrene spheres suspended in different media. The efficiency curves for different particle diameters d_{p} are plotted against wavelength. The solid lines correspond to spheres in glycerol while the dashed lines to spheres suspended in benzene.*

6.3.3 Particle Preparation Procedure

The micro-particles, used for the measurements, are based on polystyrene with a diameter $d_{\mathrm{p}} = (10.0 \pm 0.2)\,\mu\mathrm{m}$ and a density of $\rho_{\mathrm{p}} = 1.05\,\mathrm{g/ml}$. These particles are suspended in a glycerol-based solution. The refractive indices of polystyrene and glycerol are 1.5717 and 1.4746 respectively. Additionally, the viscosity of glycerol

[2]For the Mie scattering graphs the python library miepython by Scott Prahl was used.

is $\eta_\mathrm{f} = 0.95\,\mathrm{Pa}\cdot\mathrm{s}$. Using the equations discussed in Section 6.3.1 and particularly Equation (6.8) the particle velocity response time is

$$t_\mathrm{V} = \frac{d_\mathrm{p}^2 \rho_\mathrm{p}}{18\eta_\mathrm{f}} = 6.14\,\mathrm{ns}\,. \tag{6.15}$$

Assuming the flow velocities in the experiments to be below 20 mm/s and the flow density ρ_f equal to particle density, then the relative Reynolds number will be

$$Re_\mathrm{r} = \frac{\rho_\mathrm{f}|u-v|d_\mathrm{p}}{\eta_\mathrm{f}} = 0.000221\,. \tag{6.16}$$

As Reynolds number is well below 1 then the flow will be laminar. Last, for Stokes number t_F is needed, but it can be calculated based on the dimensions of the channel and the expected flow velocities. For the rhombic chamber chip the cross-sectional area A is equal to $0.8\,\mathrm{mm} \times 8.8\,\mathrm{mm} = 7.04\,\mathrm{\mu m}^2$ and the wetted perimeter $P = 19.2\,\mathrm{mm}$. For a velocity of 20 mm/s, the characteristic flow time is equal to $t_\mathrm{F} = 4A/PU = 73.33\,\mathrm{ms}$ yielding a Stokes number of

$$St_\mathrm{V} = \frac{t_\mathrm{V}}{t_\mathrm{F}} = \frac{6.14\,\mathrm{ns}}{73.33\,\mathrm{ms}} = 83.73 \times 10^{-9}\,. \tag{6.17}$$

As the Stokes number is less than 0.1 the flow tracing accuracy error is below 1%. Similarly for the reaction chip, the characteristic flow time is equal to $t_\mathrm{F} = 54.19\,\mathrm{ms}$ and the resulting Stokes number is $St_\mathrm{V} = 113.30 \times 10^{-9}$. While the St_V for the reaction chip is larger than the Stokes number for the rhombic chip it is lower than unity.

For 5 ml of 1% Latex sphere solution, a 250 ml solution of Phosphate Buffered Saline (PBS) is prepared by dissolving one PBS tablet in 250 ml of deionised water. The tablet takes approximately an hour to dissolve fully. Gentle agitation of the bottle can speed this up. Then, 1.12 g of glycerol is put into a 10 ml glass vial. Using a 5 ml measuring cylinder 3.60 ml of PBS is measured out. The PBS is added to the glycerol and the mixture must be swirled gently to mix, while 5 µl of Polysorbate 20, that is used to prevent biofilm growth from contamination, is added to the solution. Both the glycerol and Polysorbate 20 take approximately ten minutes to dissolve into the solution. Later, 500 µl of latex spheres are extracted and added to the solution while mixing. The final solution will have a self-life of approximately one month. After that, it should be disposed of into the waste water system.

Notably, the materials used, are the basis for soap making. Thus, the prepared solution tends to produce soap bubbles that fill the channel when the liquid is pumped.

6.4 Acquisition of Flow Measurements

In order to evaluate the dual beam OCT system, as an instrument for capturing microfluidics flows, a simple microfluidic setup was prepared. This setup consists of a set of syringes to hold the micro-particle solution that is used for the tracking of the flow, a microfluidic preparation sample as the target, and a syringe pump which holds the syringe and either pushes or pulls the plunger.

For the acquisition of the measurements the integrated dual beam OCT system described in Section 5.4 was used. Then, using the acquisition software, the raw signals are saved in a container file format along with extra information about the acquisition, including, but not limited to, microfluidic chip part-number, glycerol solution, particle size, setup configuration.

Later, in a process similar to digital photography, the raw data are developed into a series of B-scan images and used for the particle tracking.

6.4.1 Microfluidic Setup

In the microfluidic part of the setup, a 1 ml plastic syringe from Terumo is driven by the syringe pump. The syringe has a 0.8 mm diameter needle and is connected to 0.031 inch internal diameter Cole-Parmer c-flex tubing. Connected on the other side of the tube is the microfluidic chip using a mini Luer adapter. On the other side, the chip is connected, with the same adapter and tubing material, to a 10 ml plastic syringe serving as a reservoir.

The syringe pump is a Nexus 3000 by Chemyx and uses a stepper motor screw drive system for pushing and pulling the attached syringes. Table 6.1 contains the specifications of the pump. The stepper motor improves the repeatability of the pumping, as it has a fine control on the movement of the syringe plunger. But it has the downside—as discussed in Section 6.7—that induces a flow speed fluctuation inversely proportional to the flow rate as a percentage of the set flow rate, i.e. at low flow rates the pump speed fluctuation increases.

For the experiments the syringe is mounted on the spring-loaded syringe holder as seen in Figure 6.6 and the syringe type and volume is set on the pump using the embedded user interface. The pump can then be operated manually or be set to automatically operate between infusion and withdrawal even at different pump flow rates.

Connected to the syringe, using c-flex tubing, is the microfluidic chip. The chip is placed in a custom 3D printed holder that, apart from securing in place, it holds it at a certain height and distance from the OCT scanning head. For the reaction chamber

Table 6.1: *The specifications of the Nexus 3000 syringe pump that was used for the experiments*

(a) *Pump flow rates*

Parameter	Value	Unit
Syringe Size	<140.00	ml
Minimum Flow Rate	12.00	pl/min
Maximum Flow Rate	500.00	ml/min
Minimum Speed	1.95	nm/s
Maximum Speed	3.60	mm/s

(b) *Stepper motor*

Parameter	Value	Unit
Screw Travel Per Revolution	1.50	mm
Motor Steps Per Revolution	200.00	
Screw Travel Per Step	3.75	µm
Microsteps Per Step	128.00	
Screw Travel Per Microstep	29.30	nm

chip, the holder can be seen in Figure 6.7. On the left (A), the fibre-pair is mounted on a precision 30 mm cage system rotation mount along with a xy-translation mount for the collimating lens. On the right (B), the focusing lens ($f = 25\,\text{mm}$) is held in place in front of the reference mirror with the same xy-translation mount as the collimator. The holder is mounted on a XY translation stage with a rotating platform allowing 360° of continuous rotation and 13 mm linear travel along either axis.

Using the stage, the sample can be appropriately placed in front of the scan lens a focal length distance apart, while it allows, both the region to be scanned (y-axis translation) and the angle of the target in relation to the scanning lens (z-axis rotation). The latter is used to reduce the direct reflection of the microfluidic chip surface that reduces the visibility of the particles and is caused by the difference of the refractive index between the two interfaces. In OCT imaging, the brightness of the horizontal lines, that appear between two interfaces inside the sample, is approximately proportional to the refractive index change. Hence, when the laser light penetrates the chip, the refractive index changes by 0.467 for PMMA ($n = 1.467$) or 0.584 for PC ($n = 1.584$), while when the light enters the channel that is filled with the glycerol-based solution the change is 0.115 (1.467 for PMMA to 1.352 for glycerol) [175]. Last, polystyrene has a refractive index of 1.5717 at 1052 nm, which corresponds to a change of 0.163 between the micro-particles and glycerol. Hence, the return signal from the air/chip interface is greater than that of the glycerol/particle interface.

6.5 Dual Beam OCT for Flow Velocimetry

As mentioned in Section 5.4.8, two software applications were written. The first controls the digitiser card, provides a real-time display of the two B-scan images—one per beam, and can capture a set of raw frames that are used for the flow tracking. Whereas the second processes the raw data to produce the B-scan images used for particle detection.

Figure 6.6: *The syringe pump (Nexus 3000 by Chemyx) that is used for the infusion and withdrawal of the micro-particle solution. Using a stepper motor screw drive (C) the pusher block (A) pushes or pulls the syringe plunger for infusion, or for withdrawal respectively. The syringe is mounted on the spring-loaded syringe holder (B).*

After getting a set of B-scan images, in the form of raw A-scans, using the procedure that was highlighted in a previous section; the A-scans will be "developed" into a series of B-scan frames. These frames, separately for each beam, will be adjusted for contrast and then cropped in size before being processed by the particle tracking algorithm.

As an outline, the procedure of preparing and processing the series of B-scans is the following:

Developing the B-scans: The A-scans are loaded into the software, the DVV is applied and FFT is performed.

Adjusting the B-scans: Contrast is set, the images are cropped, and are exported as image files (Section 6.5.1).

Feature Detection: Using a particle size estimate the particles are located in the series of frames.

Linking Particles: After locating the particles, a linking algorithm tries to link a particle from one frame to the same one on the next (Section 6.5.2).

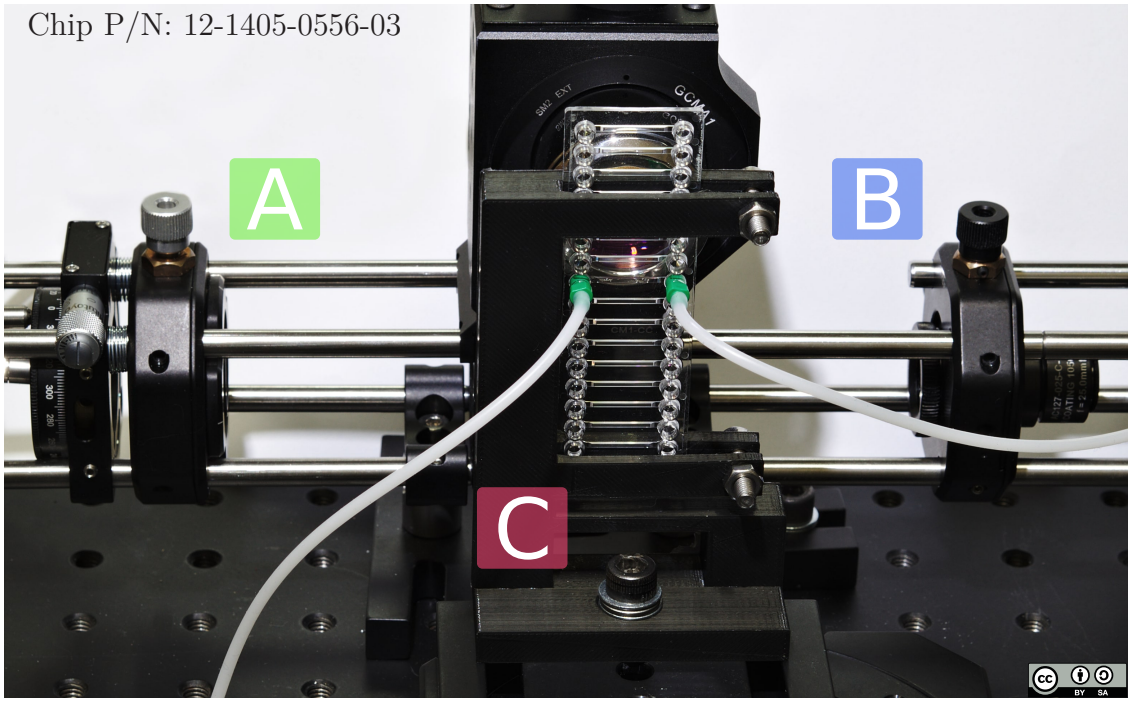

Figure 6.7: *Front view. A microfluidic chip (reaction chamber chip) is held in place with a bespoke 3D printed chip holder (C) in front of the OCT scanning head. The dual-fibre end is mounted on (A) where the beam is collimated and directed to the beam splitter that will split the light to the reference mirror (B) and to the galvanometer head.*

Particle Velocity Estimation: The particles, being now linked into particle trajectories, are processed individually and using the change in position between two frames the velocity is calculated (Section 6.6).

6.5.1 B-scan Post-Processing

The process of generating the series of B-scans from the captured A-scan involves the use of the second application developed specifically for this project. The main uses are:

- To load the raw data file, playback the frames at any frame rate, and read the attributes.
- To perform the Fast Fourier Transform at the maximum number of points; which cannot be done at the time of the acquisition.
- To export a processed data file for future use.
- To adjust the contrast of the B-scan images and perform image cropping.

- To measure distances inside the target.
- To perform a basic and manual calculation of the flow speed by locating the particles manually and measuring the travelled distance over a series of frames.

A screenshot of the application can be found in Figure 6.8. To adjust the contrast, the software has a separate histogram widget (blue rectangles) for each image, as it is difficult for the two images to have the same exposure at the time of acquisition. The exposure difference occurs as the length of the fibres is not perfectly matched between the arms and the use of on reference mirror does not allow independent path length matching between beams. The histogram displays the frequencies of the pixel intensities which correspond to the amplitude (in dB) of the FFT. Using the yellow sliders a portion of pixels intensities is selected. For the two images in Figure 6.8 the selected portion of the histogram differs. With this selection, the pixels of the image with an amplitude above or below the selected range are set to the edge values of the selected region.

Furthermore, the application is able to perform length measurements. By adjusting the ends of the green line (Figure 6.8) the length in pixels is translated to physical length. The optical scaling of the setup as well as the resolution of the OCT system is taken into account. However, the refractive index needs to be set to the appropriate value for the material being measured. As an example, the green line on the left image is set to measure the depth of the channel. On the left toolbar the "delta y" reading has a value of 699 µm as the images show the reaction chamber chip that has a 700 µm deep channel.

The standard procedure of post-processing the B-scans is:

- Load the raw data file, and perform the FFT.
- Adjust the contrast of the B-scan images using the histogram widget.
- Crop the images to include only the microfluidic channel; it reduces the filesize of the images and increases the speed of the tracking algorithm, because it does not try to locate particles outside the channel.
- Export the B-scans as an image sequence of TIFF[3] image files.

Notably, before the FFT, the invalid points are removed from the raw A-scans to produce 1200 arrays with 2875 valid points—for a single frame. Then, for each array a Blackman-Harris window is applied, and subsequently the arrays are padded with zeroes on either side. The reasoning behind the application of a Blackman-Harris window and the order of windowing and padding can be found in Chapter A.

[3]Tagged Image File Format, abbreviated TIFF or TIF. Supports 32 bit floating-point numbers for storing pixel information, thus it retains the dynamic range of the image.

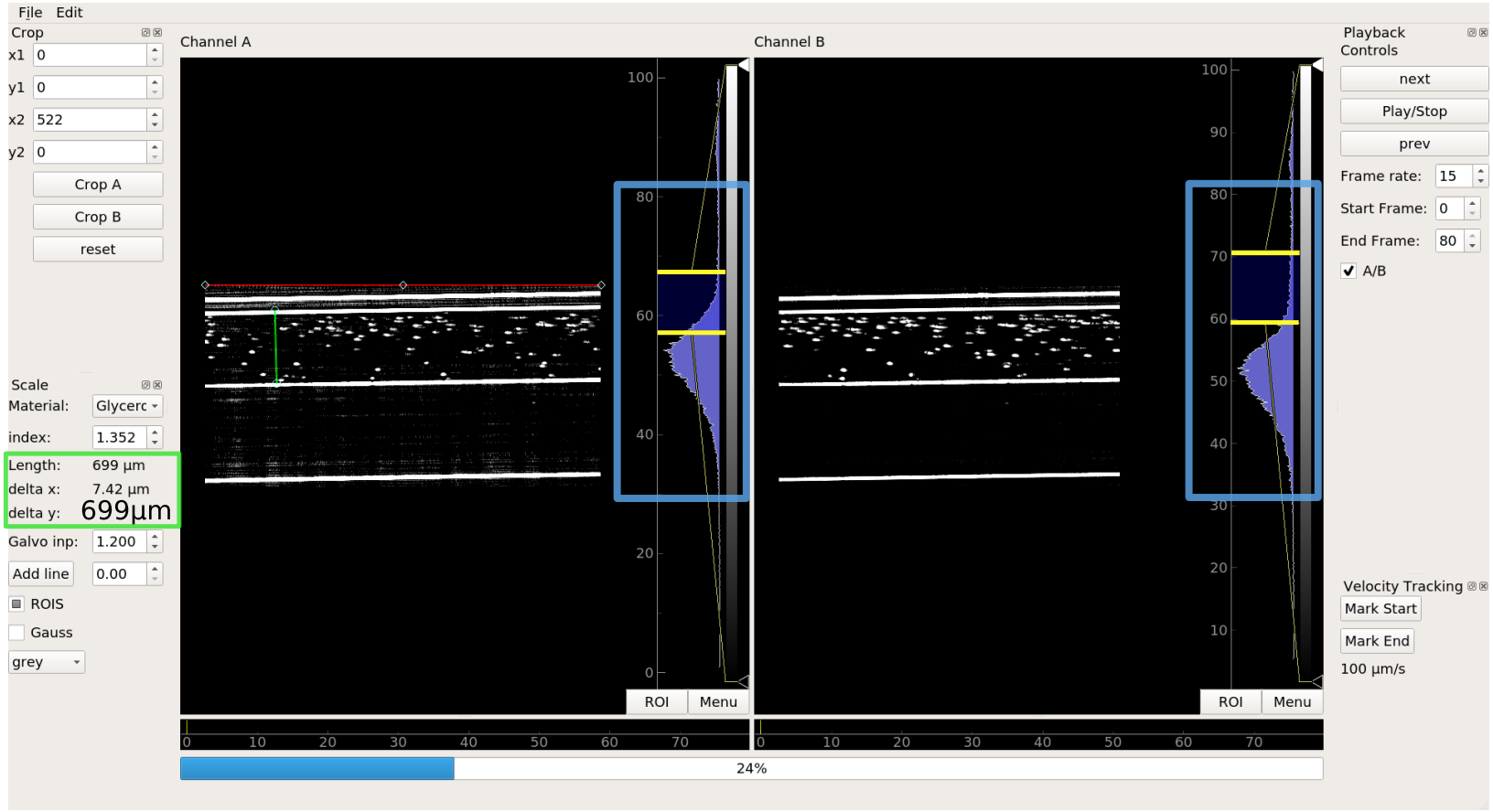

Figure 6.8: *Screenshot of the B-scan post-processing softare that was implemented specifically for the dual beam OCT system. The images show the cross-section of the 700 µm deep reaction chamber chip filled with particles. It can display the captured data file and perform various manipulations on the images. Additionally, it can be used to measure lengths and calculate velocities.*

After the FFT is performed, the next step is to select an appropriate region on the histogram that will be used as a threshold and give an adequate contrast to the images. As an illustration, Figure 6.9 shows the resulting images—along with the corresponding histograms—for four different pixel intensity regions. The frequency axis of the histograms is in logarithmic scale. For (d) the full range of intensities is selected and is used as a reference. In addition, the histogram of the reference is shown as an orange line in all four. It is clear from the histograms that the frequency of pixel intensities increase at the edges of the selected ranges due to pixels outside the range being set to the edge values.

Furthermore, in (b) the contrast is high and the background noise has been suppressed. Similarly, (c) suppresses the majority of the noise, the particles have enough separation, and the lines are visible; thus this is the best image for particle tracking. Finally, in (a) the lines are almost indistinguishable from noise.

Optimally, there should be an area around the particles that is fairly dark (consistent refractive index) to assist the detection of the particles. There is an upper threshold for the number of particles and how close they are, above this threshold the particle-linking algorithm will fail. The step above tries to solve this issue by assuring that the particles have enough separation.

Although, when the images are exported as 32 bit floating-point TIFF files, is more sensible to only adjust the black point and leave the white point to its maximum value. This way, only the lower values (such as noise) will be crushed into black; the brighter parts will keep their dynamic range. Last, the images are cropped to the size of the channel and exported as an image sequence. After this step, the images are ready to be used with the flow tracking software as discussed in the next section.

6.5.2 Particle Identification and Tracking

After the generation of the image sequence, the flow tracking can be performed. As discussed in Section 2.2.2, particle tracking velocimetry can be used for recording flow fields with comparable accuracy as PIV. Due to the simplicity of particle tracking, especially in laminar flows, the PTV method was select for the particle tracking. Ultimately, both methods will be used and a more detailed comparison can be drawn, as typically PTV uses cameras for capturing the tracer particles whereas here OCT is used instead. Notably, for highly turbulent flows will be more appropriate to use the three-component scanning method along with PIV for flow tracking. For the flow tracking, the Python programming language was used again as there is a software package for finding blob-like features in video, tracking them through time, and analysing their trajectories. It implements and extends the widely-used Crocker–Grier algorithm [176] in Python.

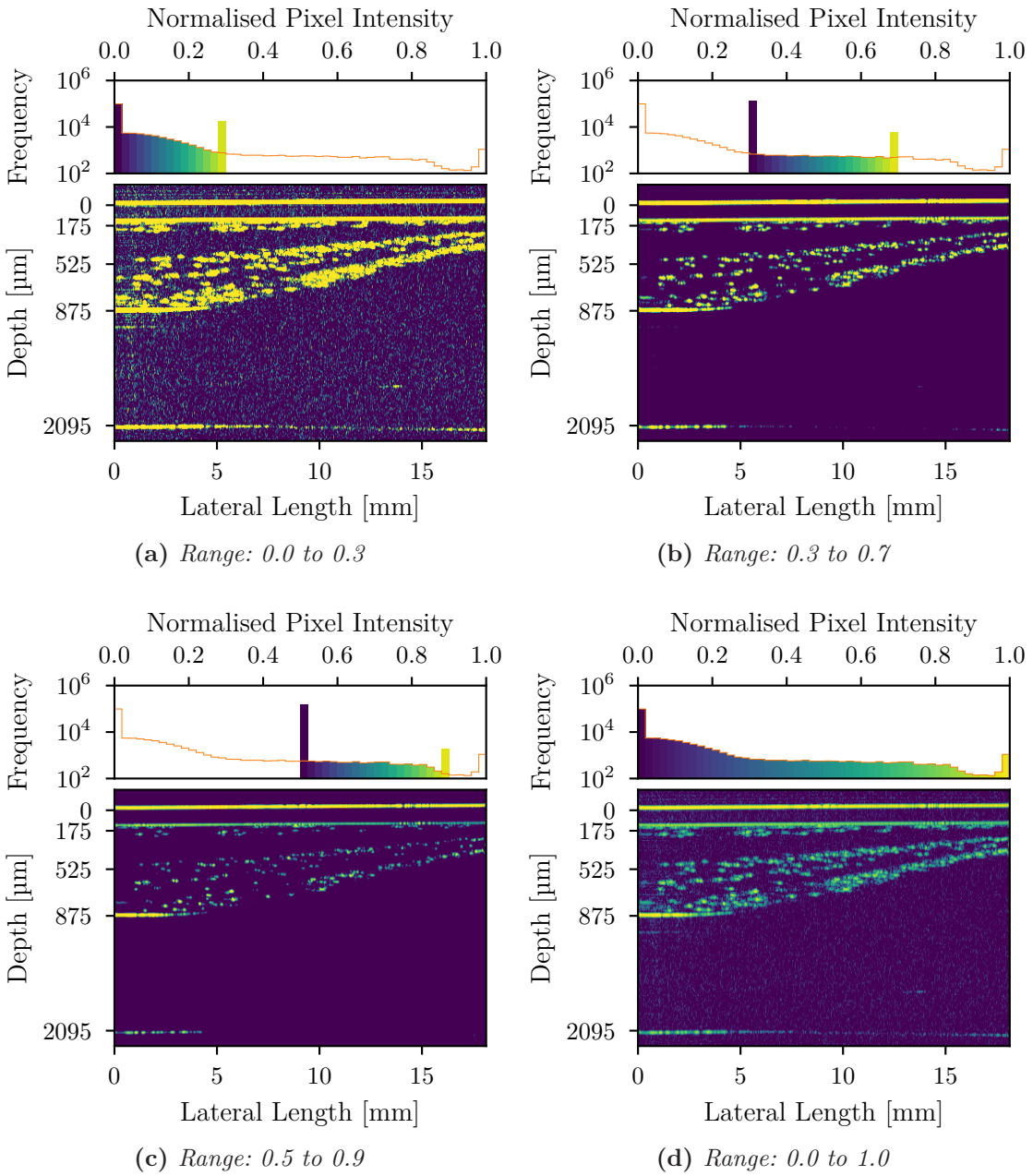

(a) *Range: 0.0 to 0.3*

(b) *Range: 0.3 to 0.7*

(c) *Range: 0.5 to 0.9*

(d) *Range: 0.0 to 1.0*

Figure 6.9: *B-scan images for different areas of pixel intensities. (d) is used as a reference as it contains the full range. A smaller range is selected for the others. The orange line corresponds to the histogram of (d). (a) and (b) are examples of low and high contrast respectively.*

This library is *trackpy* (version 0.3.2) developed by Allan et al. [177]. In addition, it has a prediction framework that helps track particles in fluid flows, or other scenarios where velocity is correlated between time steps. Using this software library and

building upon it, a custom procedure was developed for the purposes of this project.

The flow of the algorithm can be seen in Figure 6.10. The first step is to identify the size of the micro-particles in pixels—the size can be different in each image dimension—and use this value(s) to locate the particles in each frame. Locate all peaks of brightness, characterize the neighbourhoods of the peaks and take only those with given total brightness ("mass"). The *mass* attribute corresponds to the integrated brightness of a particle, i.e. is the summation of the brightness values of all pixels that define the particle. Particles will be identified by their mass and only if their size is equal or lower to the estimate. Then, the algorithm will measure the eccentricity of each feature (particle) and calculate the centroid of each one. Optionally, a smaller region can be isolated and used for the rest of the process. This way, misidentified features for particles can be eliminated, thus producing a more accurate flow profile. After all the particles are located on all frames, the identified particles must be linked together between frames to form a particle trajectory. In this step, the frames are compared in successive pairs and the particles on one frame will be matched with the particle that has the highest probability of being the same particle on the next frame. To find the matching particle, the original algorithm was assuming that the particles move freely in space with Brownian motion. In this case, is known that the particles move linearly in a single direction due to the laminar flow. For this reason, the predictive framework of the library is used. A comparison between the Channel Flow and Brownian predictor can be found in Section 6.6.

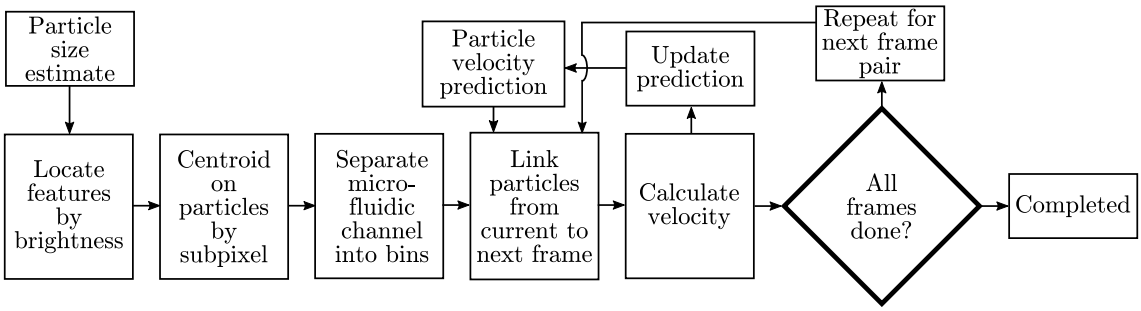

Figure 6.10: *Particle tracking algorithm flowchart using the Channel Flow predictor. With the Flow predictor, a velocity profile is generated on every frame couple and is used to predict the next particle position.*

Here, using the Channel Flow predictor (included in trackpy library), the channel is divided height-wise into bins of equal size. The number of bins is chosen based on the amount of identified particles inside the channel, usually the number of bins is between 25 to 30. For the first frame pair, the velocity of each particle is assumed to be zero. As an input, the maximum allowed displacement of a particle is given. If a particle has travelled a distance less than the maximum allowed one and is in the same bin for both frames, then that particle will be matched successfully with its

counterpart on the second frame. After linking all the matching particles, a velocity profile is calculated and is used to predict the new particle location for the next frame. This process continues till there are no new frames left. When the process is done, a table is produced that contains the x-y location of each particle through the frames. Table 6.2 is an excerpt of such a table.

6.5.3 Single Beam Particle Tracking

For the single beam particle, the rhombic chamber chip was used. The scanning configuration is shown in Figure 6.11. The laser beam is scanned along the x axis, i.e. the direction of the flow. Hence, the depth information is extracted along the z axis which corresponds to the depth of the channel.

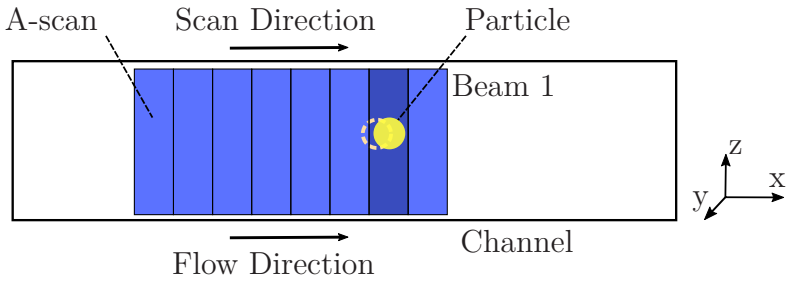

Figure 6.11: *A single beam measurement configuration with the scanning direction being the same as the flow.*

The linked trajectories can be plotted using the particle column as an identifier to colour each particle and x, y columns for their positions across a set of frames resulting in Figure 6.12. The length of the trajectory can be used as a coarse indicator of a particle's velocity. For example, the first particle on Table 6.2 with identifier `0` travelled approximately 60 µm, as the speed is lower on the edges than at the centre due to Poiseuille flow were the velocity profile as a function of depth is a paraboloid. In comparison, particle 5, due to its transverse location travelled laterally from roughly 450 µm over a span of half a second.

In order to calculate the velocity profile, the table is grouped by particle and the two deltas (Δx and Δy) are calculated for each consecutive frame pair. For the single beam processing the deltas are divided by the frame rate, yielding the particle velocity along each dimension and for the period of two frames. By taking the mean across the frames, the average velocity is calculated.

If in a capture, the two beams are not well aligned, there is still a lot of information that can be extracted. For example, in Figure 6.13, the two beams focused at different depths. As the overlap of the beams was small, the B-scans were processed

Table 6.2: *An excerpt of a table generated after particle linking. Using the particle column the trajectory information of each particle can be extracted. The size means the radius of gyration of its Gaussian-like profile.*

Particle	Frame	X [µm]	Y [µm]	Mass [a.u.]	Size [a.u.]
0	1	1071.0	42.5	4544.07	2.67
1	1	404.0	198.9	9846.38	3.01
2	1	498.1	205.4	8064.18	2.95
0	2	1074.9	42.5	4657.77	2.59
1	2	413.6	199.4	9734.39	2.99
2	2	507.9	205.3	8388.58	2.96

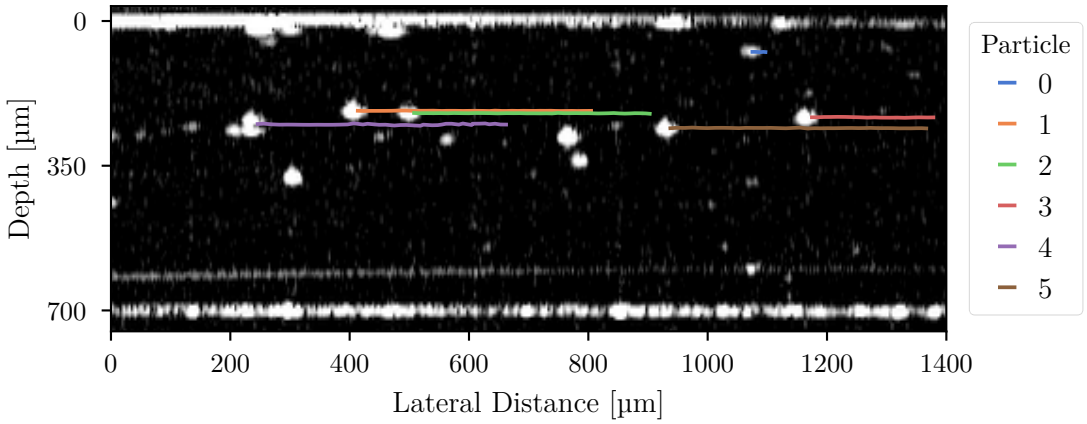

Figure 6.12: *Particle trajectories generated by linking particles across a series of frames using particle tracking velocimetry techniques.*

individually and then the extracted trajectories were merged into a single table, while maintaining the beam identifier. Hence, for the velocity profile depicted in Figure 6.13, the particle velocities are plotted with different colours to differentiate between the two beams. The grey line represents the flow profile and is a second order polynomial fitting of the particle velocities. Moreover, the shaded region around the fit is 95% confidence interval; in regions with a high amount of recorded velocities the area is minimised as the measurement error is lower. Regardless, by merging the two datasets, the calculated fit from the data matches the velocity profile that is expected for these types of Poiseuille flows. However, the spread of particle velocities for the same depth is not expected, and the cause for this variation is discussed in Section 6.7.

This multi-focal approach can be deliberately exploited to allow particle velocity tracking on deeper channels. Additionally, a similar multi-focal system has been

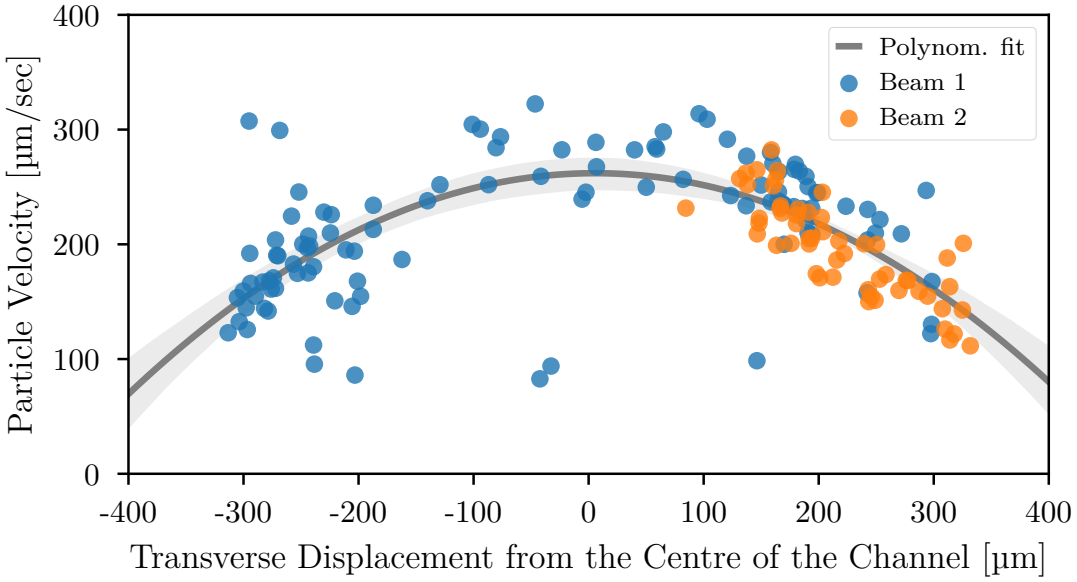

Figure 6.13: *Velocity profile of a rhombic chamber chip when beams are focused at different depths. The two beams were focused at different depths and as a result the multi-beam particle tracking technique was not applied. The shaded region around the second degree fit corresponds to the 95% confidence interval, which at regions with a high amount of samples is minimised.*

demonstrated [178] and it utilises four beams focused at different depths to achieve a B-scan image with longer depth of focus compared to the single beam equivalent. Not only that, this type of multi-focal OCT system is commercially available (Michelson Diagnostics, Vivosight). For the dual beam system the only drawback using this approach is that it sacrifices the imaging speed.

6.5.4 Dual Beam Particle Tracking

The configuration for dual beam particle tracking is the same as before but with the addition of a second beam with an offset. As shown in Figure 6.14, the two beams are separated by ΔS and the beams are scanned synchronously along the flow direction. In the figure, the active A-scans are indicated with a darker colour while the coloured regions indicate the cross-sectional area covered by each beam.

The tracking of particles between two beams utilises the same algorithm as for single beam tracking but poses a few difficulties. These difficulties arise from the fact that the images between two beams are not identical in brightness, focus, and contrast. Extra care is taken at the B-scan post-processing step to ensure that the

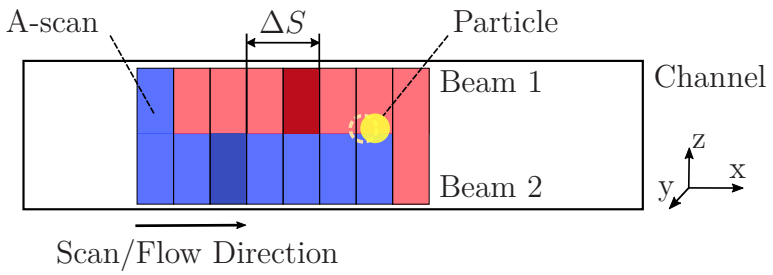

Figure 6.14: *A dual beam measurement configuration with the scanning direction being the same as the flow.*

two sets of images look as if it was from a single beam system.

In order to process the dual beam measurement, the images from both channels are interleaved in the time domain—so that the even frames correspond to the images from the first beam and the odd frames to the second. The transition between frames from the same beam will be called an intra-frame, while the one between beams will be called inter-frame. On an intra-frame transition—mainly used in single beam processing—the time step δt_0 is equal to the B-scan rate, but for the inter-frame transition there are two cases: from beam 1 to beam 2 and vice versa. When added together, the two time steps, δt_1 and δt_2, will be equal to the B-scan rate. This way, at the velocity calculation step, the two frames are checked and depending on the transition of the beam the appropriate time step is used.

However, this step is not that straightforward; let's take as an example Figure 6.15, which shows two frames (acquired simultaneously), one from each beam, and has the identified particles for each frame annotated with either a blue or an orange circle. The red line highlights a set of particles to show their lateral displacement due to the flow. Notably, the particles with solid circles around appear and are successfully identified on both beams. Still, there are a couple particles that are only identified on one of the two beams; these are highlighted with dashed circles instead of solid ones. Alternatively, there are features identified as particles like the two on second beam at the bottom right corner.

For all these particles the intra-frame time step will be used, but to complicate things further, a particle might be missed for a few frames and reappear again. This can be due different reasons such as turbulence moving the particle laterally in and out of the light-sheet, or due to change in light conditions changing the exposure of the frame. Nevertheless, for these particles the time step must be computed by adding the intervals of all the transitions that should have happened.

For example, assume that the time step δt_0 for intra-frame transition is 12.5 ms and for inter-frame $\delta t_1 = 2.5$ ms and $\delta t_2 = 10$ ms depending the transition. Now, assume a particle appears on frame *20* (first beam) and the same particle reappears

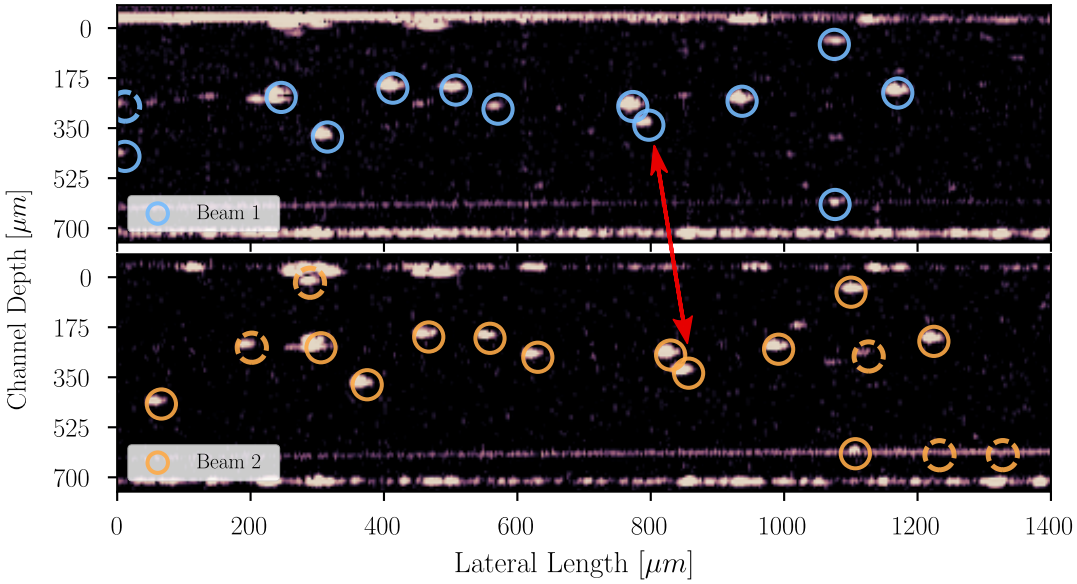

Figure 6.15: *The located particles are annotated with either solid blue or orange circles depending on the beam. It can be seen that while most of the particles are identified on both beams, there are couple of particles, dashed circles, on one beam only. The red line indicates that the connected particles are the same.*

on frame *25* (second beam) as in Figure 6.16.

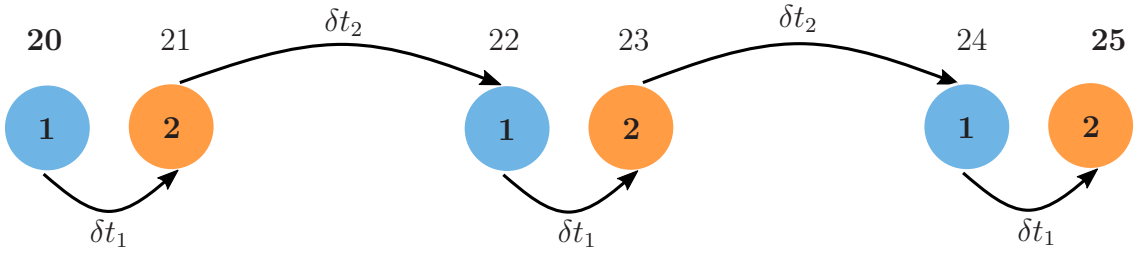

Figure 6.16: *Transitions between beams and time deltas for three pair of frames.*

Then, there will be three 1→2 transitions (2.5 ms) and two 2→1 transitions (10 ms). The total time between the two will be

$$\Delta t = 3 \cdot 2.5\,\text{ms} + 2 \cdot 10\,\text{ms} = 27.5\,\text{ms}\,. \tag{6.18}$$

As a general rule the total time between any odd number of frames m, the time step $\Delta t(m)$ will be

$$\Delta t(m) = \begin{cases} \frac{m+1}{2}\delta t_1 + \frac{m-1}{2}\delta t_2, & \text{for } 1\to 2 \\ \frac{m-1}{2}\delta t_1 + \frac{m+1}{2}\delta t_2, & \text{for } 2\to 1 \end{cases}. \tag{6.19}$$

The tracking results shown in this chapter use that approach to calculate the velocity of the particles, even if said particles disappear for a small amount of frames.

To help demonstrate the difficulties mentioned above, Figure 6.17 shows the particle trajectories. Each point on the plot is assigned either a blue or an orange dot depending on the beam that the particle was located in. The most notable trajectories or regions are assigned with a letter from *A* to *D*. For *A* and *B* the spacing between the two colours is changing throughout the trajectory. It starts sparse at *A*, then it gets smaller and it expands again at *B*. As the timing between the inter-frames is constant, this is an indication that the velocity varies in time—this is caused by flow fluctuations generated by the pump and is discussed in Section 6.7. On *C*, the particle appears intermittently on Beam 1 up until the mark of 0.5 mm, then it appears only on Beam 2. Last, for *D* the particle only appeared on the second beam and it was missed for a few frames before the last one.

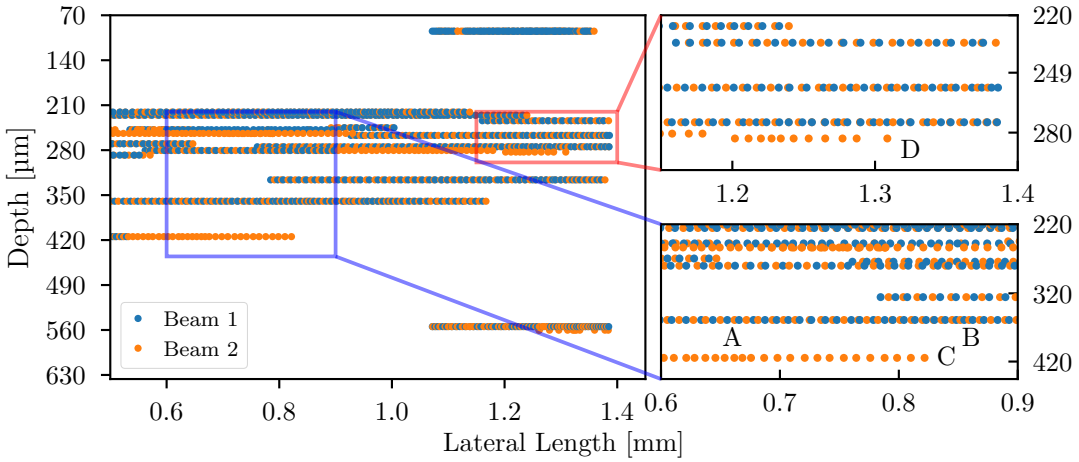

Figure 6.17: *Particle trajectories for dual beam tracked particles. Each point represents a tracked location. Indicated with letters A to D are regions and trajectories that highlight various issues. At A and B the spacing between the particle locations vary, indicating a shift in particle velocity. For C, the particle was intermittently identified on the first beam and on D, the particle was identified only on the second beam.*

In summary, to calculate the instantaneous particle velocities along the flow direction—iteratively for each particle and frame pair—the distance travelled Δx is computed by subtracting the x-axis positions for the pair, then the time step Δt is calculated using Equation (6.19). The last step is to calculate the instantaneous velocity Δv, which is equal to $\Delta x / \Delta t$.

6.6 Velocity Profile Analysis

As mentioned in Section 6.2 for the experiments two microfluidic chips were used, a rhombic chamber and a reaction chamber chip. Additionally, using the standard procedure from Section 6.3, a 10% colloidal suspension of latex micro-particles was prepared. For the first set of experiments the rhombic chamber chip was used along with the 10% latex-glycerol solution. Unfortunately, the first batch of the micro-particle solution did not have neutral density, leading to buoyant particles. This affected the measurements as the particles will float at the centre of the channel and above, thus missing measurement points at the bottom of the channel.

Despite the issue some initial measurements were taken and used to evaluate particle tracking approaches. The mature Brownian predictor was used at first for the linking of particles into trajectories followed by the Channel Flow predictor. The pump was set to a moderate flow rate (80 µl/min) so the particle velocities to be within the prediction window of the algorithm. The flow velocity in a square channel is given by the Plane Poiseuille flow equation. Assuming the distance between the top and bottom of the channel is h and a constant pressure gradient G is applied in the direction of flow, then the velocity distribution $u(y)$ and the volume flow rate Q per unit length are

$$u(y) = \frac{G}{2\eta} y(h-y) = -y^2 \frac{G}{2\eta} + yh\frac{G}{2\eta} \quad \text{and} \quad Q = \frac{Gh^3}{12\eta}\,, \tag{6.20}$$

where η is the dynamic viscosity of the liquid.

As the velocity in a Poiseuille flow as a function of depth is a quadratic polynomial (parabola), a second degree polynomial fit is used for the estimation of the profiles.

In Figure 6.18, the two polynomial fittings along with data points were plotted. Additionally, a B-scan image of the channel is shown on the left and the two dashed lines are the delimiters of the channel. A pink line is added on both graphs to indicate the maximum depth at which particles were detected. The velocities were divided into 20 bins and the mean was calculated for each bin. Furthermore, the error bars on the profile correspond to the Standard Deviation (SD) that was calculated for the binned velocities. The two solid lines are the polynomial fits and the shaded thickness on the fits represents the 95% confidence interval. As for the two predictors, the Brownian is on par with the channel one at lower velocities, but at roughly 80 µm/s and above the error margins on the Brownian predictor increase while the two fittings diverge. While the Brownian predictor can produce adequate results exploiting the low speeds, it is inappropriate for high speed flow tracking in channel flows as it does not accommodate fast movement in one direction. Additionally, for all the experiments microfluidic channels were used as target devices, thus the Channel Flow predictor was chosen.

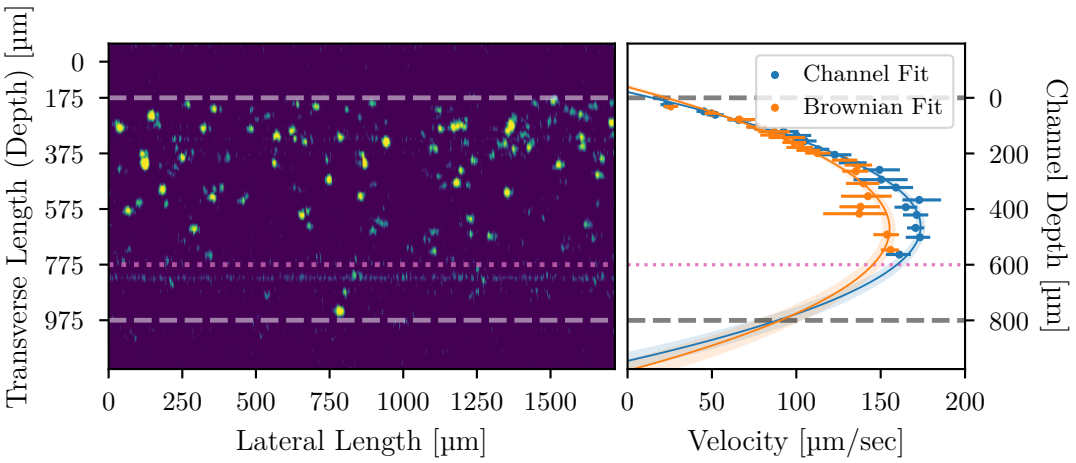

Figure 6.18: *On (a), a B-scan image of the channel with the particles. The 10% glycerol-solution used was buoyant leading to floating particle above the centreline. On (b), the particles velocities and the polynomial fits for both tracking predictors. The pink line on both plots highlights the depth at which no particles were detected. The velocities were divided into 20 bin were the means and standard deviation was calculated (points and error bars). The solid lines are the polynomial fits and the shaded thickness represents the 95% confidence interval of the fit. At lower velocities the two predictors are on par in both particle velocity and standard deviation. In contrast, at higher velocities the Channel Flow predictor has lower error margins.*

A set of measurements with different pump speeds was acquired with a new mixture of a 10% glycerol solution. This new mixture was closer to neutral density and as a result the particles were present throughout the depth of the channel, even on the deeper rhombic chamber one. On the initial tracking and velocity analysis it was made evident that there was something wrong with the velocities. While the profile fit was following the Poiseuille profile as expected, the velocities were too disparate. After closer inspection and by calculating the polynomial fit on a small set of frames it was revealed that the velocity fluctuates over time.

In Figure 6.19, the polynomial fit is calculated for two frame ranges, 37 to 42 and 25 to 37. While the shape of the profiles is almost identical, the velocities of the profile calculated at the frame range 37 to 42 are higher. This was due to the fluctuations generated by the syringe pump and is further explained in Section 6.7.

To understand how the velocity of the particles was changing over time the particle velocities were plotted against time as shown in Figure 6.20. Despite the different particle velocities, which is natural as particles at different depths have a lower or higher velocity, a trend can be observed. The velocity increases for the first hundred milliseconds, and after 200 ms it starts a decline with some minor bursts until it rises sharply after 800 ms.

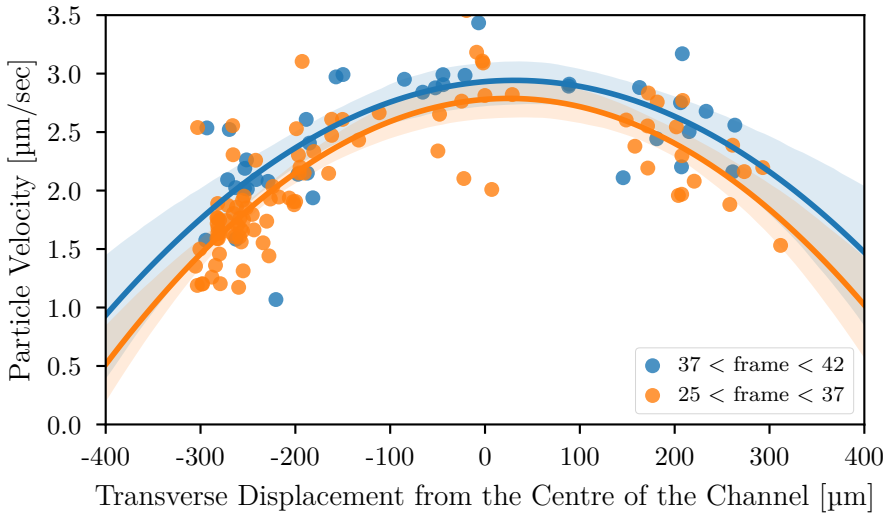

Figure 6.19: *Velocity profiles of rhombic chamber chip at different time spans. The polynomial fit was computed for two frame ranges, 37 to 42 (blue) and 25 to 37 (orange). The velocities at the 37 to 42 range are higher overall indicating a fluctuation in velocity.*

Apparently, the pump speed fluctuates around the value it is set—on the graph, the velocity fluctuates around 800 µm/s. In the next section, a closer look is taken on what causes this fluctuation while it demonstrates that the dual beam OCT system can be used as a diagnostic tool for these issues.

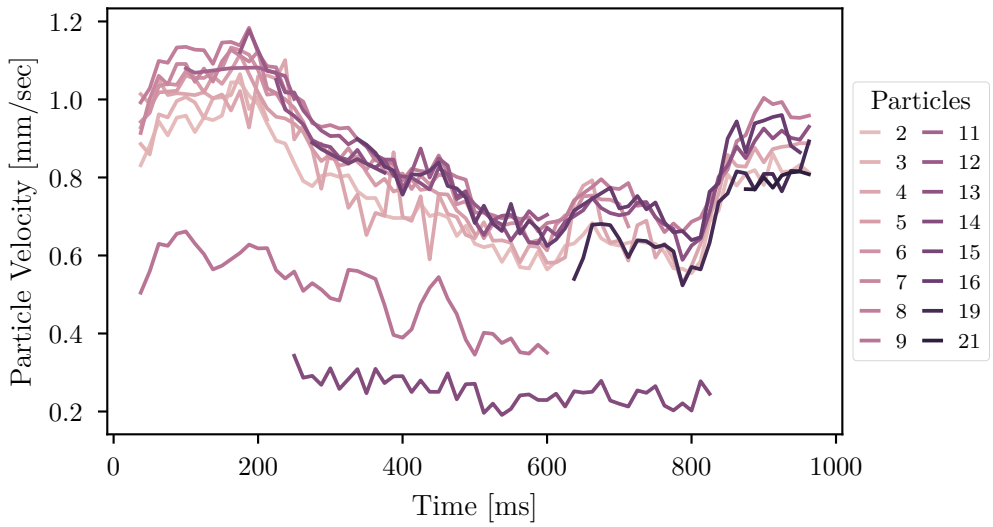

Figure 6.20: *Particle velocity versus time. Apart from particles having different velocities, there is an overall trend with velocity fluctuating around a certain value.*

6.7 Pump Flow Pulsation

After some initial measurements it was observed that the velocity fluctuates widely instead of being constant. In order to troubleshoot the issue and discover what might be causing this a series of measurements were taken. For these measurements the reaction chamber chip was used.

On this run of measurements, to guarantee particles will appear across the whole depth of the channel a shallower channel (700 µm) compared to the rhombic chip (800 µm) was used. The pump was set to three different flow rates: 40 µl/min, 200 µl/min, and 400 µl/min. For the first two measurement the acquisition time was set to one second while for the last measurement, the acquisition time was set to three seconds to ensure that enough particles will be recorded. Table 6.3 summarises the attributes of each measurement.

Table 6.3: *Set of measurements for the analysis of pump speed fluctuation*

No	Pump Speed	Time [sec]	Particle concentration
1	40 µl/min	1	10%
2	200 µl/min	1	10%
3	400 µl/min	3	10%

6.7.1 Flow Pulsation Effects on Particle Velocity

After the measurements, the acquired data were processed as discussed in previous sections. The tracked particle velocities were plotted against time and polynomial fittings were computed on velocities as a function of both channel depth and time. In Figure 6.21, a scatter plot of the recorded velocities along the polynomial fit can be seen. The data for the plot come from the third flow measurement with the pump set to 400 µl/min. The polynomial fit shows that the velocity varies sinusoidally while increases with time. If a polynomial fit for the velocity profile was applied for the whole time span of the acquisition it would have big error margins, leading to the conclusion that there is an issue with the particle-glycerol solution or the instrument.

Additionally, on the right side of Figure 6.21, two velocity profile fits are shown. Each profile was calculated on the recorded velocities at a different time slice and subsequently on a different set of B-scan images. The blue profile corresponds to the first trough located at 340 ms to 360 ms while the orange profile to the last peak at 580 ms to 610 ms. There is a difference of ≈1.5 mm/s between the two profiles at 350 µm.

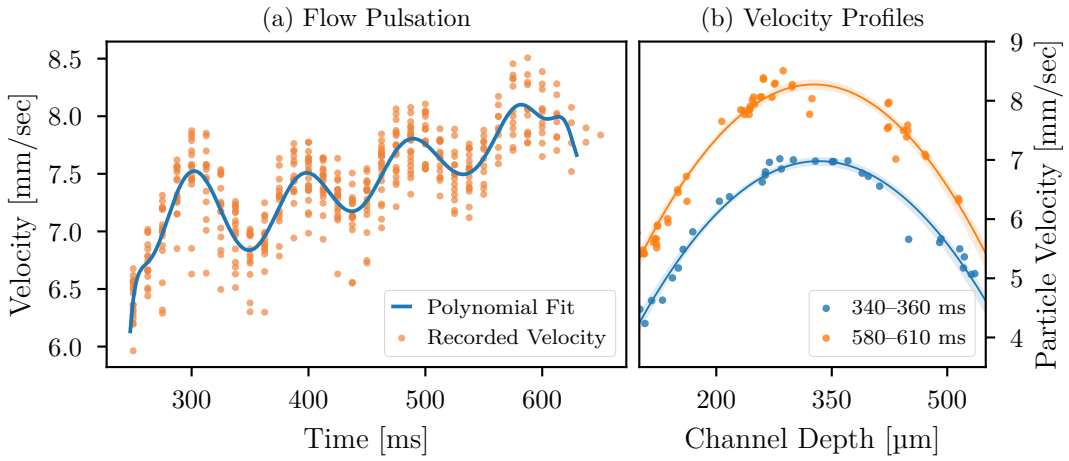

Figure 6.21: *On (a), particle velocities are plotted against time and a polynomial fit is shown. On (b), two polynomial fits where computed for different time ranges.*

In order to assert that the recorded velocities are correct and the instrument performs as expected the flow rates were calculated. Assuming a channel with dimensions w,h,l and a constant flow velocity v along l, then the flow rate Q is given by

$$Q = v \cdot A = v \cdot w \cdot h\,, \tag{6.21}$$

where Q is the flow rate, v the average velocity, A the channel surface area, w and h the width and height of the channel respectively.

As the velocity is not constant across the cross-sectional area, the area is divided into n smaller areas. Then for each area A_i the velocity v_i is considered constant and the flow rate Q_i can be computed using Equation (6.21). The total flow rate will be equal to the sum of the individual flow rates,

$$Q = \sum_{i}^{n} v_i \cdot A_i\,. \tag{6.22}$$

Using the formula from (6.22) the flow rate as a function of time was computed for all measurements. Subsequently, the mean and standard deviation was computed. As it can be seen in Figure 6.22, the mean values are close to the setting of the pump. However, the standard deviation is getting lower when the pump speed increases.

Apparently, these fluctuations are induced by the mechanical oscillations of the stepper motor used in the syringe pump. The effects of the pump motor oscillations on the flow rate have already been researched. In 2013, it was demonstrated that the stepper motor inside the pump is a source of fluctuations in microfluidic flows. This was achieved by using a liquid–liquid system with an ultra-low inter-facial tension and comparing the frequencies of the ripples observed at the interface to that of

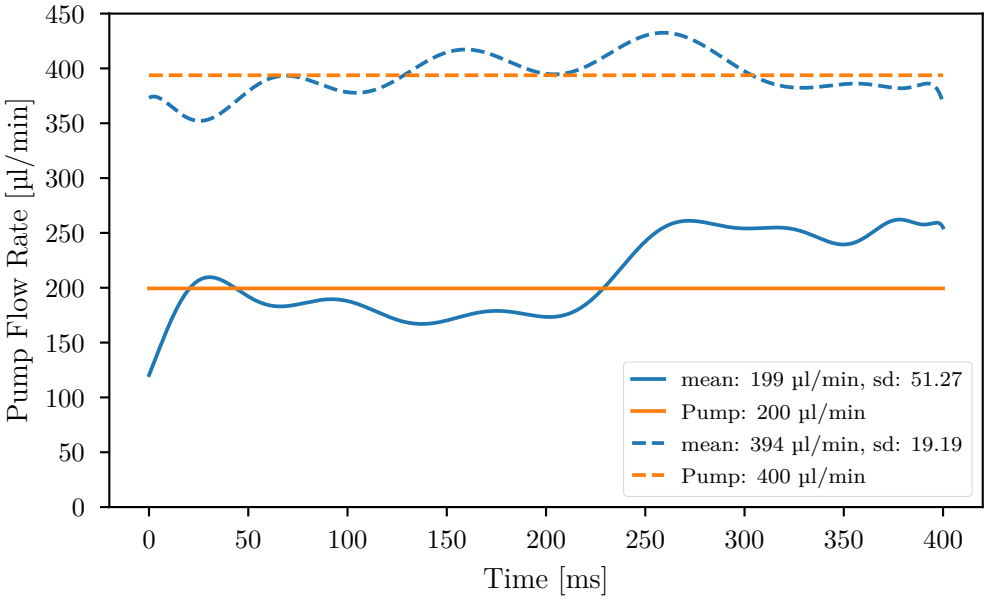

Figure 6.22: *Flow rate pulsation for different flow rates. The solid and dashed lines correspond to the second and third measurement respectively.*

the pulsation of the stepper motor [179]. Interestingly, the flow fluctuation does not have the square wave profile of the pump but rather a sinusoidal one. This is due to the tubing used to connect the syringe with the channel and more specifically to the elasticity of the tubing. The tubing is analogous to a low-pass filter like an RC circuit in electronics. From the Fourier series is known that a square wave is an infinite sum of sine waves, thus with the tubing the square wave is filtered and only the lower frequencies are passed through. This is shown in Figure 6.23 where the the pump fluctuation (a) is Fourier transformed (b) to reveal the base frequency of the fluctuation and subsequently of the stepper motor. The Fourier transforms have a DC component equal to the average flow rate. Moreover, the frequency of the fluctuation is proportional to the flow rate, i.e. high frequency components for higher flow rates. However, the amplitude of those components is inversely proportional to the flow rate, thus increasing the flow rate decreases the amount of fluctuations.

Additionally, in 2015, a mathematical model on the effect of the frequency of the pump on the normalized amplitude of pressure fluctuations was proposed and verified experimentally over a range of typical operating conditions [180]. The authors concluded that the normalized amplitude of pressure fluctuations decreases as the frequency of the pump increases and the elasticity of the channel material decreases which coincides with the finding presented here.

To understand the nature of the flow fluctuations the previous measurements were

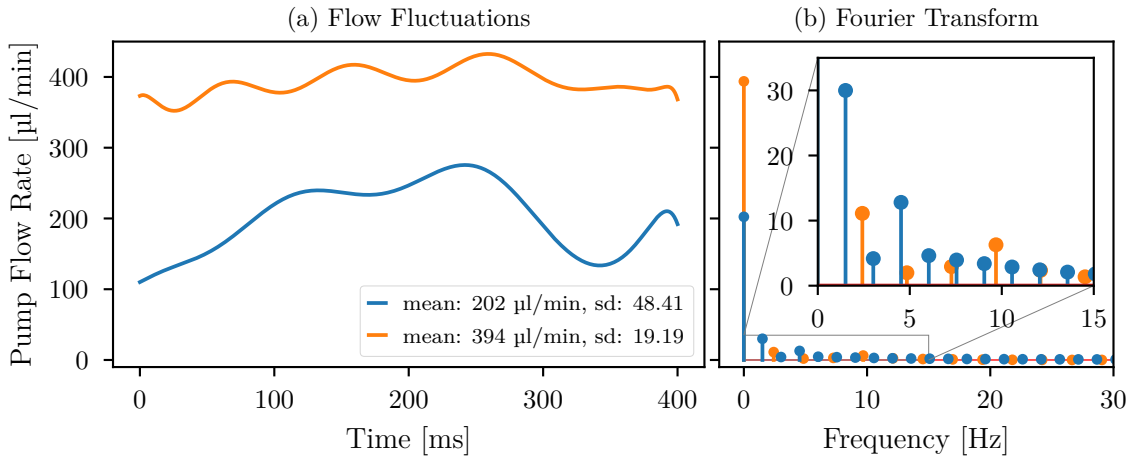

Figure 6.23: *On (a), the flow rate over time for different flows whereas on (b), the Fourier transforms of the flow rates is shown. The DC component of the Fourier transform corresponds to the average flow rate. For low flow rates there are lower frequency components with large amplitudes compared to higher flow rates with high frequency components of smaller amplitudes.*

used for the calculation of polynomial surface fittings for the velocity against channel depth and time. The results presented in Figures 6.24 to 6.27 show the development of velocity in two dimensions, depth and time. Each figure contains two graphs, the first with the recorded velocities projected in three-dimensional space along with a polynomial surface fit represented as a wireframe and the second with polynomial surface alone. On both sub-figures and on either 2D plane (Velocity-Time, Velocity-Depth) a contour is plotted. These contours help visualise the cross-section along the corresponding plane.

For Figure 6.24, the measurement used the rhombic chamber chip and the syringe plunger was driven by hand. As a result, the flow doesn't exhibit a sinusoidal modulation, instead the velocity increases slowly as the pressure on the plunger builds up and suddenly plummets as the pressure is released. At the end, the velocity rises slightly due to plunger's suction. At first glance, in Figures 6.25 to 6.27 where the syringe pump was set to three different flow rates and the reaction chip was used, there are no signs of sinusoidal modulation. Upon closer inspection, on each fitted surface it can be seen that the width of the bulges decreases meaning that the frequency of the pulsation increases. In Figure 6.27 where the pump speed was set to 400 µl/min—the maximum for the set of measurements—the frequency of the bulges is the highest and their amplitude the lowest, i.e. smaller fluctuations.

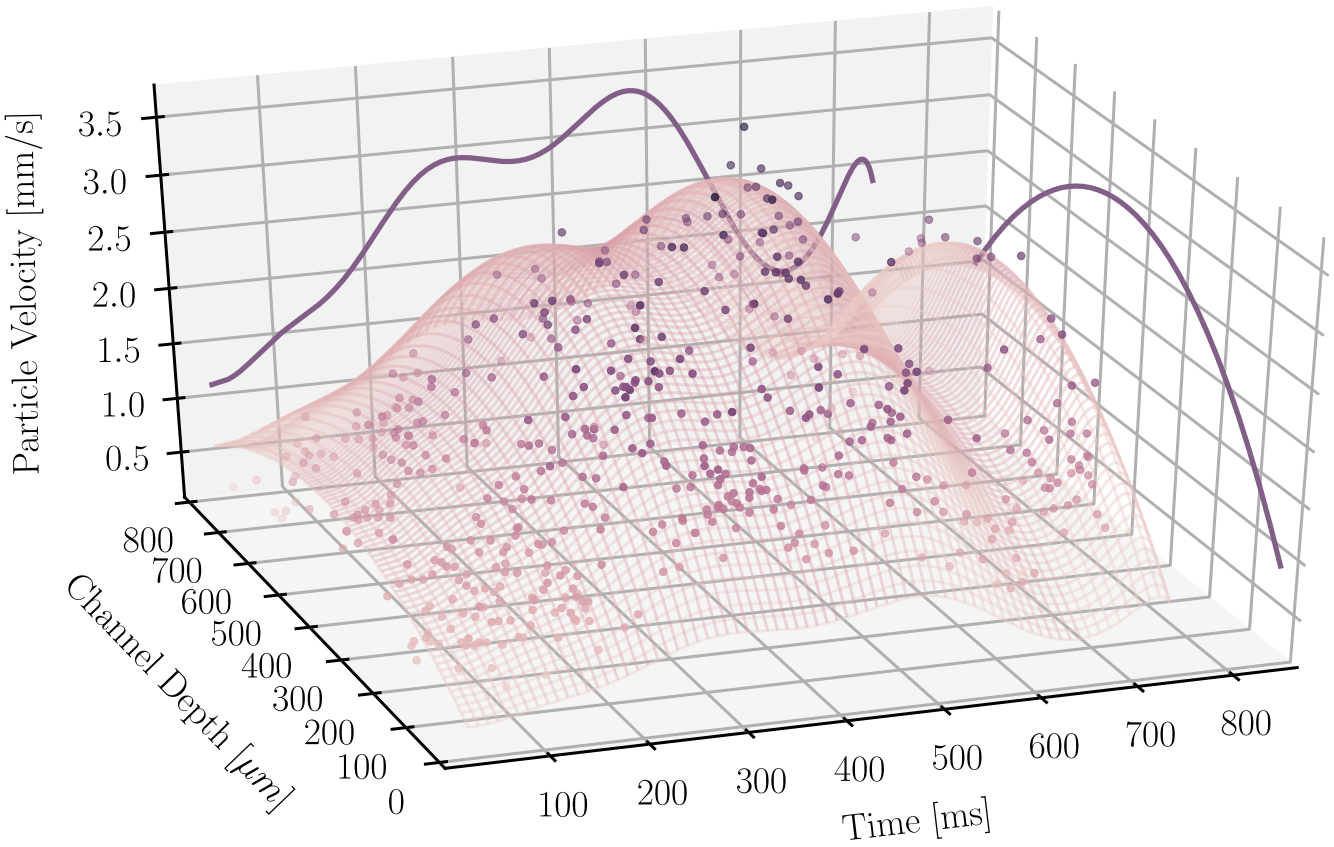

Figure 6.24: *Flow velocity across channel depth over time for the rhombic chamber chip. The flow was generated by applying pressure to the syringe manually. (a) Each dot represents the velocity of each particle, while the wireframe is the polynomial fitted surface. (b) The surface corresponds to the two-dimensional polynomial fit of the tracked particle velocity. The two lines projected on the two planes correspond to the polynomial fit of the particle velocity either over time, or across the channel depth.*

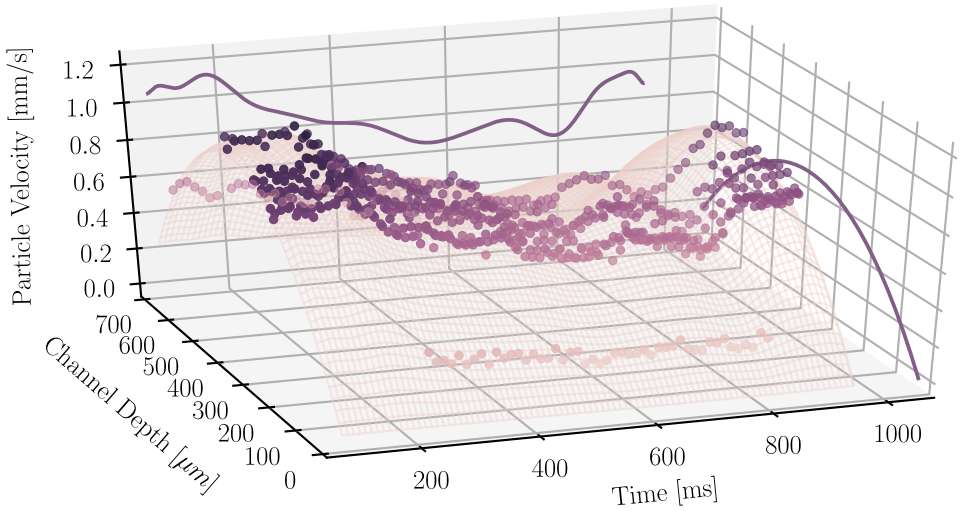

(a)

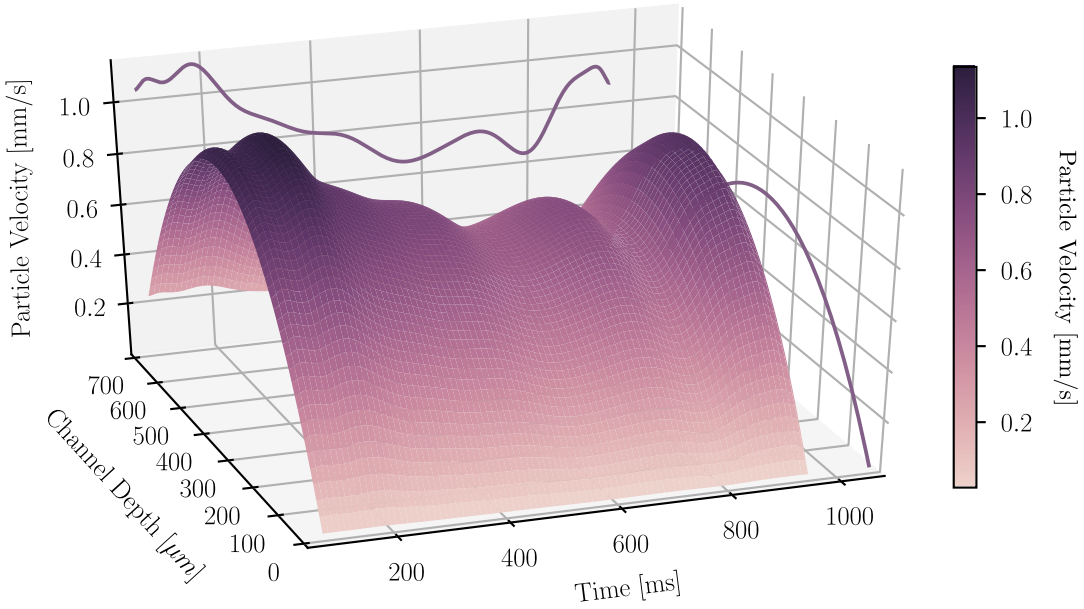

(b)

Figure 6.25: *Flow velocity profile over time for reaction chip (40 µl/min). (a) Each dot represents the velocity of each particle, while the wireframe is the polynomial fitted surface. (b) The surface corresponds to the two-dimensional polynomial fit of the tracked particle velocity. The two lines projected on the two planes correspond to the polynomial fit of the particle velocity either over time, or across the channel depth.*

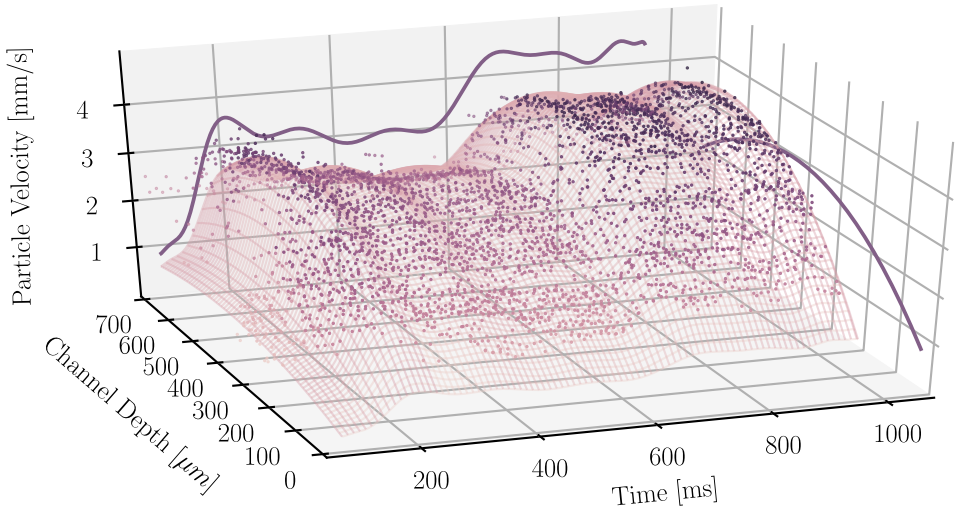

(a)

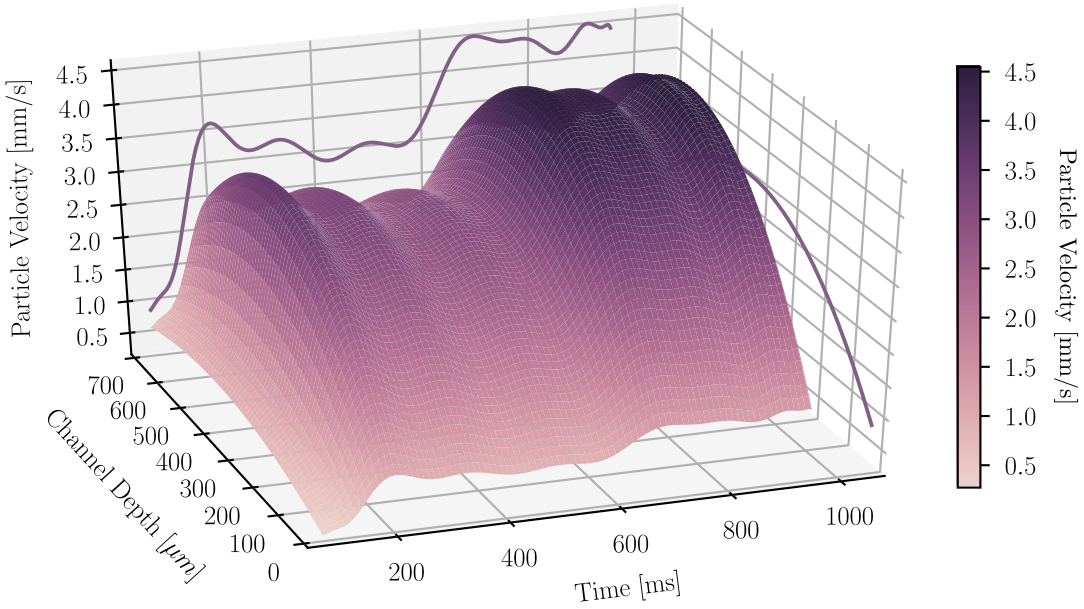

(b)

Figure 6.26: *Flow velocity profile over time for reaction chip (200 µl/min). (a) Each dot represents the velocity of each particle, while the wireframe is the polynomial fitted surface. (b) The surface corresponds to the two-dimensional polynomial fit of the tracked particle velocity. The two lines projected on the two planes correspond to the polynomial fit of the particle velocity either over time, or across the channel depth.*

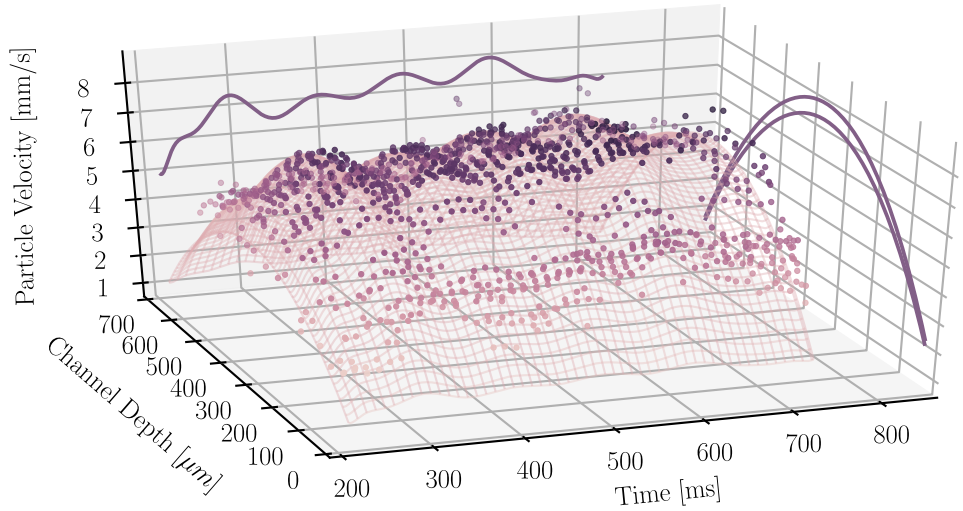

(a)

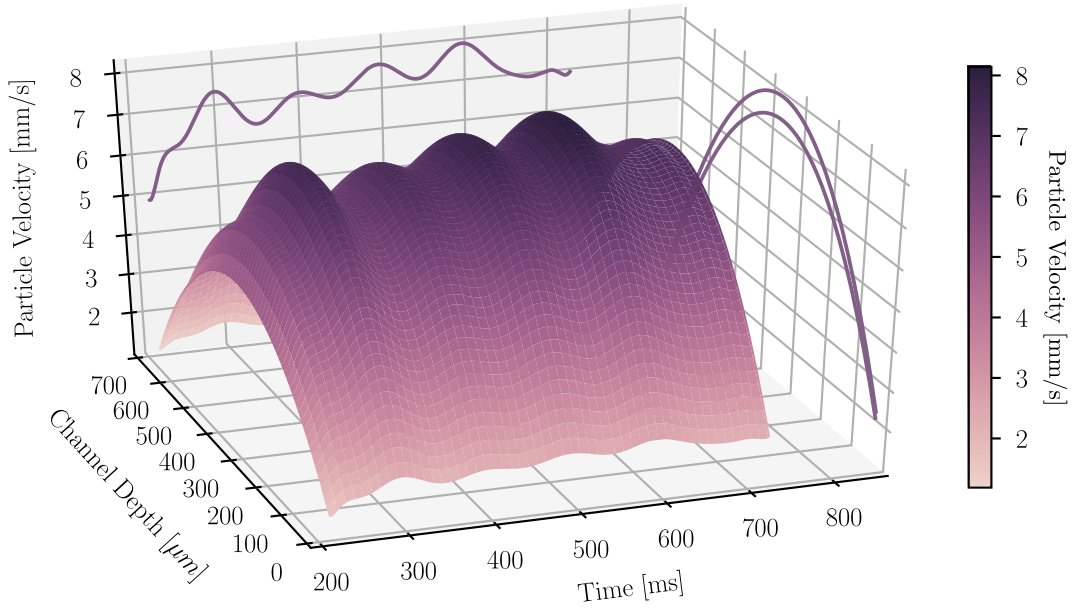

(b)

Figure 6.27: *Flow velocity profile over time for reaction chip (400 µl/min). (a) Each dot represents the velocity of each particle, while the wireframe is the polynomial fitted surface. (b) The surface corresponds to the two-dimensional polynomial fit of the tracked particle velocity. The two lines projected on the two planes correspond to the polynomial fit of the particle velocity either over time, or across the channel depth.*

6.8 Summary and Future Work

6.8.1 Summary

A novel approach on tracking particles in microfluidic channels using a B-scan images captured by a dual beam swept source OCT system is shown in this chapter. Using this approach, a set of experiments were performed to showcase the usability of the proposed OCT system and its applicability on measuring particle velocities in microfluidic chambers.

Two microfluidic chips were used for the experiments. These chips had rectangular chambers with different dimensions and were used because the flow profiles in this kind of chambers are known. Thus, the performance and accuracy of the tracking algorithm could be measured. Moreover, the principles of operation for the tracking algorithm along with the inherent difficulties of tracking particles between the two measurement beams were presented. As a result, measurements were performed for different flow rates and the tracking algorithm was able to detect particle velocities up to 8 mm/s. Using polynomial surface fitting the particle velocities were computed for both depth and time producing three-dimensional velocity profiles that show how the velocity is changing overtime at different depths inside the channel.

Furthermore, the microfluidic setup that was used for the measurements is shown, as well as the procedure of producing colloidal suspensions with latex micro-particles. A syringe pump was used in order to have a steady flow with a known flow rate for the calibration of the OCT system. Additionally, the effects of the pump on flow rate was examined and showed that this kind of flow pump introduces unwanted pulsations. These pulsations are inversely proportional to the flow rate of the pump, i.e. as the flow rate increases the percentage of the pulsation decreases.

Finally, as a whole this chapter shows how a novel dual beam OCT system was used as an instrument for the characterisation of microfluidic channels and the research behind the flow fluctuations induced by syringe pumps. Also, there is a discussion about the future steps and what improvements can be made to both the system and the tracking algorithm.

6.8.2 Future Work

Based on the results presented in this chapter, it is possible to use the dual beam SS-OCT system for the acquisition of flow measurements in microfluidic chambers. Additionally, with particle tracking velocimetry (PTV) techniques, the velocity information can be extracted from the series of OCT images. As seen in Section 6.7,

when a syringe pump is used for the infusion of liquid into the microfluidic channels a flow pulsation is induced.

Furthermore, as this kind of pump is used for the previous experiments, it seems reasonable to investigate this phenomenon further and analyse the effects for a series of different syringes and microfluidic chambers. Thus, a mathematical model can be devised and later corroborated with experimental measurements. Then, when for all the subsequent experiments the pump pulsation can be taken into account and using the acquired mathematical formulas the equipment will be set accordingly in order to minimise the induced fluctuations.

Additionally, the particle tracking algorithm needs improvements in particle identification and cross beam linking of particles. Now, the images from the two beams need to be comparable in contrast and brightness. Optimally, the algorithm must be able to perform the identification of the particles between beams separately and accommodate for brightness fluctuations or particle size variations. This will improve the linking of the particles between frames and beams, as more particles will be identified that now are missing. Also, by identifying more particles a better flow profile can be calculated.

Last, instead of using particle tracking techniques, PIV can be used instead. However, this requires to alter the optical setup so that can operate in the volumetric mode discussed in Section 4.6. Then, to perform 3-component velocity tracking, the captured B-scan images will be processed using a cross-correlation algorithm similar to PIV. This will allow the calculation of particle velocities in three dimensions simultaneously, thus turbulence inside the microfluidic chamber can be detected. With the ability to measure particle velocities in turbulent flows, more complex microfluidic channels can be analysed.

Chapter 7

Conclusions and Further Work

7.1 Conclusion

During the PhD project, two different dual-beam SS-OCT systems were developed. The first was implemented using fibre-optic components for the majority of the setup apart from the reference arms of the interferometer and the galvanometer in the sample arm. In this implementation the fibre-optic couplers are part of the interferometer and as discussed in Section 5.3.3 there were issues with the polarisation of light. For the second implementation, the interferometer uses a non-polarising beam-splitter with a 90/10 split ratio while the light delivery is accomplished with optical fibres exactly like the previous system.

The main objective of this project was to construct an optical system capable of high-speed imaging of microfluidic flows in sub-mm channels. To achieve this objective, Swept Source Optical Coherence Tomography (SS-OCT) was chosen as the central component of the system, as it provides background noise rejection, high SNR, and high-speed imaging. As OCT is an established imaging technique, the novelty of this thesis lies partly in the utilisation of state-of-the-art swept lasers—achieving ultra high-speed line scan rates—but mainly in multiplexing multiple light beams to scan the sample simultaneously, which has the potential to increase the imaging rate.

Additionally, in the course of implementing this novel system, effort was put into producing a modular design while reducing the number of components required, thus minimising the optical complexity. This was achieved with the use of common fibre-optic components for the wavelength of 1550 nm, which is commonly used in telecommunications. An advantage of these components over their bulk-optic equivalents is that they have no moving parts, so they have less wear and tear. Furthermore, for the implementation of the second system, custom-made electronic circuits were

designed and built for the generation of the control and triggering signals. For the signal generation, a Field-programmable Gate Array (FPGA) board was used in conjunction with a Digital-to-Analogue Converter (DAC) board. The FPGA board was triggered by the laser and was used to synchronise the signals for the galvanometer.

Moreover, for the acquisition of the signals and in order to provide a real-time preview of the images acquired, a custom software solution was implemented. For the development of the software various optimisations were used in order to multiplex the signals and display the computed B-scan images for two channels simultaneously with high frame-rates. Depending on the scan length across the sample, frame-rates up to 80 or 35 frames per second—for single and dual[1] OCT beam acquisition respectively—were accomplished. Also, streaming to disk acquisition was achieved with 80 frames per second for both beams simultaneously.

Apart from the software for the acquisition of the signals, a second program was developed for performing various common manipulations on the captured data. These include cropping, brightness and contrast adjustments, length measurements—while taking into account the refractive index of the material, and basic flow velocity measurements. For the storage of the raw datasets, a custom file format was developed that is based on the open Hierarchical Data Format (HDF). This custom file format can store the raw waveforms along with information about the acquisition, like sampling rates, or in this case additional data like the Data Invalid Vector (DIV) (Section 3.4.4). Furthermore, for the acquisition of laboratory flows, the file holds information about the microfluidic chips used in the experiment, particle size and concentration, and custom metadata. Last, it is designed to store and organize large amounts of data which is the case for this project.

For the second part of the project, the implemented system was used for velocity measurements in microfluidic chambers. In order to perform the measurements a 10% particle solution based on glycerol was used. For the controlled infusion of this solution a syringe pump was used along with a 1 ml syringe. Using a set of introductory measurements a channel-flow particle tracking algorithm was developed for the dual beam system. It has been demonstrated here that the dual beam OCT system combined with the particle tracking algorithm is able to identify and track 10 µm particles that travel with velocities of up to 8 mm/s.

From the experiments it was identified that the syringe pump induces pulsations that vary depending on the pump flow speed. The amplitude of the fluctuation that is induced by the pump is inversely proportional of the pump speed. Thus, to minimise the effects of the pulsation a higher pump speed must be used if the process requires a steady flow. Using the proposed OCT system these fluctuations were captured and

[1]For dual-beam acquisition the extra amount of data to be copied add an additional overhead, thus further reducing the frame rate.

analysed as shown in Section 6.7. The results presented in this thesis, align with the ones found previously by other researchers[179,180].

Summarising, this thesis proposes a dual beam SS-OCT system for the measurement of particle velocities in microfluidic flows. A dual beam system was implemented and experimentally tested for the measurement of particle velocities in laboratory flows using microfluidic chips with rectangular channels. The specifications of the system are summarised in Table 7.1. The integrated OCT system operates at the centre wavelength of 1550 nm and has a resolution of 10 µm in both axes, Longitudinal and transverse. For the light delivery to the interferometer, a custom-made fibre bundle has been constructed using two single-mode fibre pigtails. The fibre bundle is angle-polished to reduce back-reflections and thus increase the Signal to Noise Ratio (SNR). Furthermore, the B-scan frame-rate is equal to 80 Hz while the beam separation in A-scans is 56. Based on the lateral resolution (10 µm) and assuming that the scanning length is appropriately chosen the beam separation in length units is equal to 560 µm. From the equations discussed in Section 4.5.2, the maximum particle velocity will be in the range of 200 mm/s to 280 mm/s. Adjusting the numerical aperture of the system, thus altering the lateral resolution, velocities approaching 1 m/s can be realised. Last, for the storage of the acquired datasets, an open file format was developed to hold both the raw data and the metadata of each acquisition. By using an open and well documented format, the future availability of the data can be ensured.

Finally, for the microfluidic measurements, it has been demonstrated that the system is capable of measuring particles velocities for flows at least up to 400 µl/min; which for the microfluidic chips used, corresponds to particle velocities of 8 mm/s. Additionally, the phenomenon of flow speed fluctuations induced by a syringe pump was captured and it has been demonstrated that in order to reduce the flow fluctuation the pump speed must be increased.

7.2 Further Work

As discussed in previous chapters (Chapters 5 and 6), there are still some improvements to be made. Mainly, there are four areas, that can be improved. These are the fibre bundle, the polarisation control, the particle tracking algorithm, and the volumetric velocity measurements.

First, for the fibre bundle, a future development can be to substitute 50 µm fibres for the 125 µm ones. This will allow for smaller beam spacing, increasing the maximum measured velocity of particles. Additionally, with smaller fibres, more can fit inside the bundle, allowing better control of the beam spacing.

Table 7.1: *Dual beam swept source OCT system specifications*

Parameter	Value	Unit
Points per Sweep	4096.00	
Max. Optical Power	11.00	mW
Coherence Length	40.00	mm
Centre Wavelength	1550.00	nm
Sweep Width	82.00	nm
Sweep frequency	96.00	kHz
Sweep Power Profile	Flat Top	
Axial Resolution (air)	10.00	µm
Transverse Resolution (air)	10.00	µm
A-scans per B-scan	600.00	
B-scan Frame-rate	82.00	frames/second
B-scan Image Dimensions	600 x 2048	pixel
B-scan Image Pixel Count	1.22	Mpixel
Beam Separation	56.00	A-scans

Second, the fibre-optic system is prone to polarisation issues as the fibre-optic portion of the system is part of the interferometer. A possible solution, as proposed in Section 5.5, will be to use polarisation maintaining components. Furthermore, it allows the use of balanced detection, further increasing the SNR.

Third, as discussed in Section 6.8.2, the particle tracking algorithm needs improvements in particle identification and cross beam linking of particles. Optimally, the algorithm must be able to perform the identification of the particles between beams separately and accommodate for brightness fluctuations or particle size variations. This will improve the linking of the particles between frames and beams, as more particles will be identified that now are missing.

Finally, there are changes to be made on the setup to allow volumetric scanning of the channel. These changes will allow the three-component measurement of particle velocities. The advantage of volumetric scanning, apart from the ability to record all three velocity vectors simultaneously without requiring an additional access port, is that it will allow higher particle velocities to be recorded. This is achieved by increasing the distance between the two beam while maintaining the current scanning distance across the sample. Moreover, using PIV techniques (e.g. cross-correlation) on the captured images instead of Particle Tracking Velocimetry (PTV) ones, turbulent flows can be analysed. There are preliminary results on the work of volumetric scanning with the dual beam system. Figure 7.1 shows the volumetric side views of the reaction chamber chip used in the experiments. The top and bottom channels correspond to each light beam.

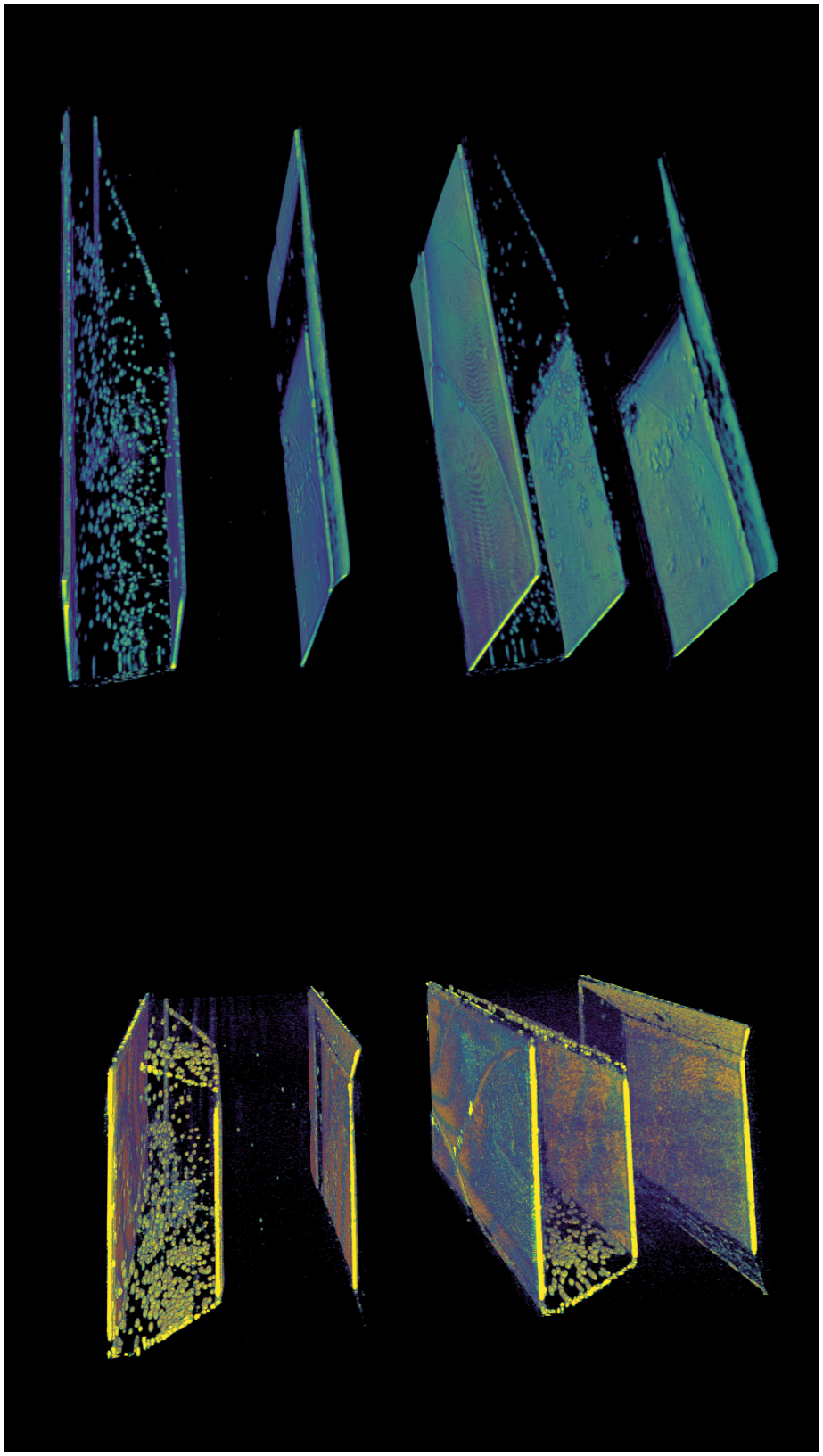

Figure 7.1: *Volumetric view of microfluidic channel. Side views of the reaction chamber chip for both beams.*

List of Publications

Conferences

- E. Rigas, J. M. Hallam, H. D. Ford, T. O. H. Charrett and R. P. Tatam, 'Depth-resolved monitoring of fluidic flows at m/s velocities and micrometre resolution using Optical Coherence Tomography via a single optical fibre access port', *Physics in Food Manufacturing Conference*, Edinburgh, UK, (11th Jan. 2018)
- E. Rigas, J. M. Hallam, H. D. Ford, T. O. H. Charrett and R. P. Tatam, 'Dual-plane optical coherence tomography imaging for velocity measurement in small-scale flows', *Photonex 2017*, (12th Oct. 2017)
- E. Rigas, J. M. Hallam, H. D. Ford, T. O. H. Charrett and R. P. Tatam, 'Microfluidic velocity measurement using dual-plane optical coherence tomography imaging', *4th EOS Conference on Optofluidics (EOSOF 2017)*, vol. 1, European Optical Society, pp. 9–11, (26th June 2017), ISBN: 9781510849341

Peer Review Papers

- E. Rigas, J. M. Hallam, H. D. Ford, T. O. H. Charrett and R. P. Tatam, 'Dual-channel OCT for Velocity Measurement in Microfluidic Channels', *26th International Conference on Optical Fibre Sensors (OFS-26)*, Lausanne, Vaud Switzerland, (28th Sept. 2018)

- **Invited Paper:** E. Rigas, J. M. Hallam, H. D. Ford, T. O. H. Charrett and R. P. Tatam, 'Dual sensing-light-sheet OCT for microfluidic PTV', *Interferometry XIX*, San Diego, California United States, (23rd Aug. 2018)

- E. Rigas, J. M. Hallam, H. D. Ford, T. O. H. Charrett and R. P. Tatam, 'Paired OCT Sensing-Light-Sheets For Rapid Microfluidic PTV', *19th International Symposium on Applications of Laser and Imaging Techniques to Fluid Mechanics*, Lisbon, Portugal, (16th June 2018)
- **Best Paper Award:** E. Rigas, J. M. Hallam, H. D. Ford, T. O. H. Charrett and R. P. Tatam, 'Multi-plane optical coherence tomography imaging for micro-fluidic velocity measurement', *European Advanced Materials Congress 2017*, (24th Aug. 2017)

Appendix A

Windowing and Padding for FFT

A.1 Windowing

In signal processing, a window function, also known as apodisation function, is a mathematical function that is zero-valued outside a chosen interval. A characteristic example of such function is a rectangular window that has a constant value at a specified interval and is zero for the rest of the function domain. When a signal is multiplied by the window, only a portion of the original signal at the window interval remains and is zero elsewhere. Typically, the window functions are non-negative, smooth, and "bell-shaped" curves. The most common use case of window functions is in spectral analysis. In order to perform the analysis, the time domain signal is transformed using Fourier. For continuous, non-repetitive signals the spectral content is calculated over certain time periods. In order to calculate the Fourier transform in one or more finite intervals the transform is applied on the product of the waveform and the window function. Notably, any window will affect the spectral estimate, even the rectangular one.

To demonstrate the effects of windowing on the interferometric signal and to compare different functions the following window types are chosen: Gaussian, Blackman-Harris, Hamming, and Flat-top. In Figure A.1 the four windows can be seen. The Gaussian window has a standard deviation of 7 in order to match the width of Blackman-Harris. Apart from the Gaussian window, the rest fall in the family of cosine-sum windows.

The periodic cosine-sum windows are commonly used in real-time applications that require both windowed and non-windowed (rectangularly windowed) transforms, because the windowed transforms can be efficiently derived from the non-windowed transforms by convolution. The Hamming window is based on the Hann (also known as *Hanning*) window named after Julius von Hann. By using a different value for

the first coefficient the Hamming window cancels the first side-lobe of the Hann window, giving it a height of about one-fifth that of the Hann window. Similarly, the Blackman-Harris window, is a generalization of the Hamming family, produced by adding more shifted *sinc* functions, meant to minimize side-lobe levels. Last, a flat top window is a partially negative-valued window that has minimal scalloping loss in the frequency domain. It is usually utilised in spectrum analysers for the measurement of amplitudes of sinusoidal frequency components. Drawbacks of the broad bandwidth are poor frequency resolution and high noise bandwidth.

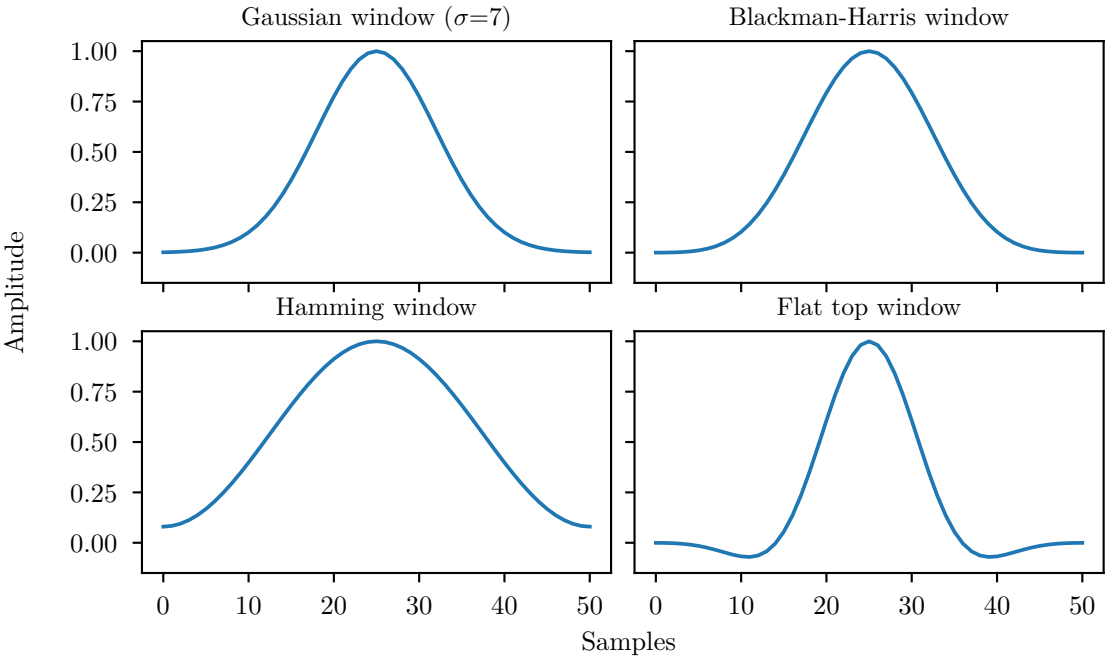

Figure A.1: *Four different window functions with equal number of samples are shown. The Blackman-Harris and Flat-top windows are fall to zero on either side of the peak. In contrast, the Gaussian and Hamming windows approach zero but never reach it.*

Windowing of a simple waveform like $\cos(\omega t)$ causes its Fourier transform to develop non-zero values—commonly called spectral leakage—at frequencies other than ω. The leakage is the worst near ω compared to frequencies farthest from ω. This can be seen in all four windows of Figure A.2, however each window has a different amount of leakage. A common metric that can be seen are the width of the main lobe and the peak level of the side-lobes, which respectively determine the ability to resolve comparable strength signals and disparate strength signals. Based on the graph, the Blackman-Harris window has a high peak to side-lobe ratio (PSR), hence is usually applied in cases where the waveform consists of disparate strength signals.

In contrast, a Hamming window has a narrower main lobe width allowing the resolution of signals with comparable strength and frequency. However, the PSR is the worst compared to the other three. Furthermore, the Gaussian window shows slightly worse than average main lobe width while has a good PSR. Last, the flat-top window while it has very good PSR, it has the worst main lobe width for OCT applications as it lowers the axial considerably. However, for use cases such as peak detection and power measurements, the flatness of the peak is rather desirable.

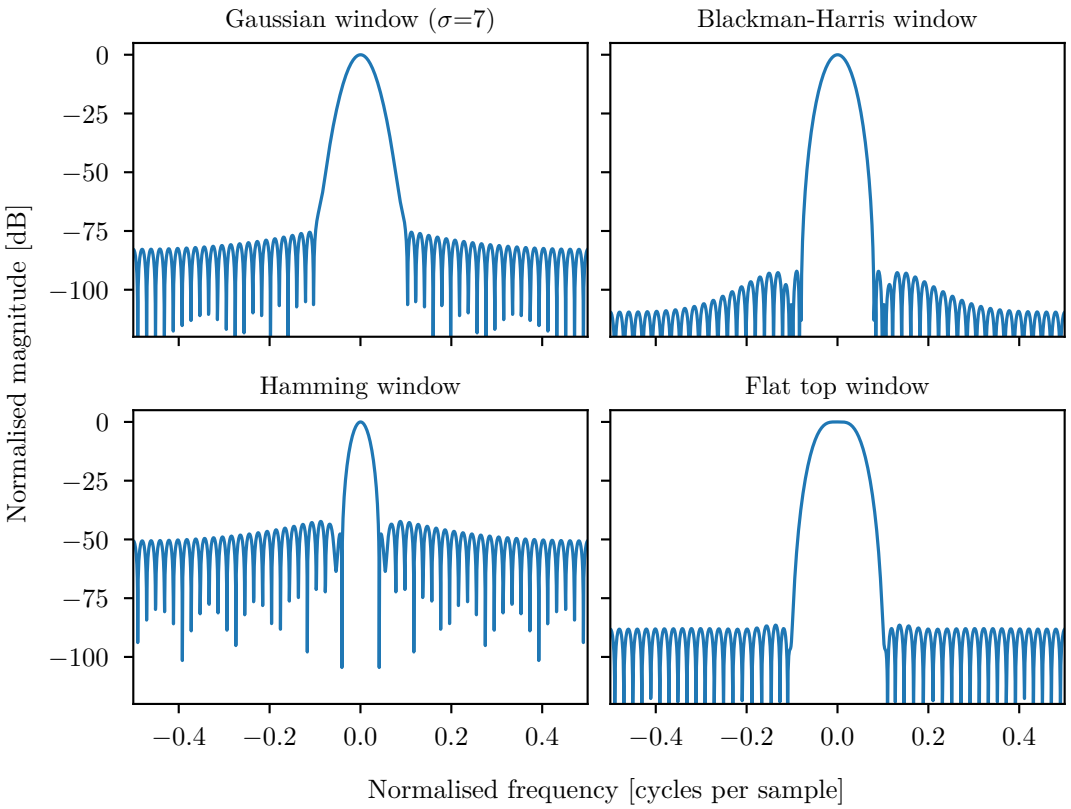

Figure A.2: *Fourier transforms of window functions. A Gaussian window leads to average main lobe widths and peak to side-lobe ratios. A Hamming window gives narrow widths at the cost of average dynamic range, while a Blackman-Harris window works inversely. Last, the Flat-top window features a flat-top that assist in power measurements.*

If the waveform under analysis comprises two sinusoids of different frequencies, leakage can interfere with the ability to distinguish them spectrally. If the strength of one sinusoid is weaker, then leakage from the stronger can obscure the weaker one's presence. But if the frequencies are similar, leakage can render them unresolvable even when the sinusoids are of equal strength. For comparing the different windows, the amplitude of the Fourier transform is plotted against normalised frequency as shown in Figure A.3.

The rectangular window has excellent resolution characteristics for sinusoids of comparable strength, but it is a poor choice for sinusoids of disparate amplitudes. This characteristic is sometimes described as low dynamic range. At the other extreme of dynamic range are the windows with lower resolution (wide main lobe) and sensitivity—the ability to reveal relatively weak sinusoids in the presence of additive random noise. That is because the noise produces a stronger response with high-dynamic-range windows than with high-resolution windows. Thus, high-dynamic-range windows are most often justified in wideband applications, where the spectrum being analysed is expected to contain many components of various amplitudes. Between the extremes window such as Hamming and Hann can be found.

In summary, spectral analysis involves a trade-off between resolving comparable strength components with similar frequencies and resolving disparate strength components with dissimilar frequencies. That trade-off occurs when the window function is chosen. In this project, the raw data are stored giving the ability to use different windowing functions and keep the one that produces better results.

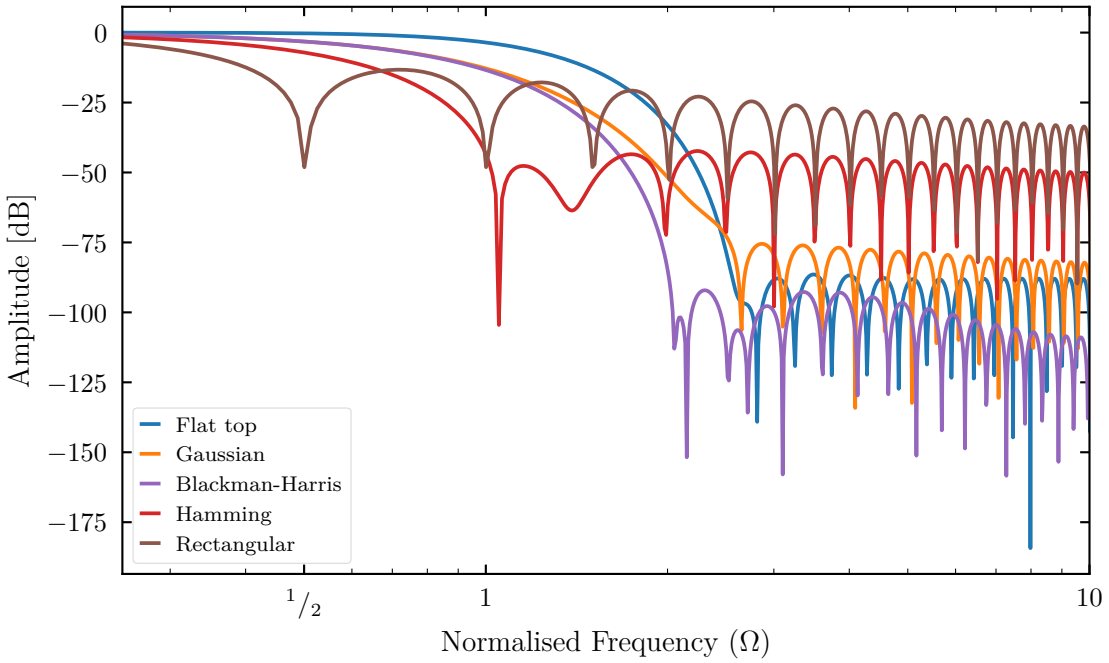

Figure A.3: *Window functions in the frequency domain ("spectral leakage"). The rectangular window is the best choice resolving comparable strength signals while is the worst choice for disparate strength signals. The Blackman-Harris window is appropriate when high dynamic range is desired.*

A.2 Padding

For the evaluation of the Discrete Fourier Transform (DFT) of a digital signal x a finite-length sequence $x[n]$ is needed. A long sequence might be truncated by a window function of length L resulting in two cases: $L \leq N$ and $L = I \cdot N$, for some integer I. When $L = I \cdot N$ a cycle of x_N reduces to a summation of I blocks of length N. Usually, N is chosen to be a power of 2 as it reduces the computation time in computers. The decimation of sampled data in one domain (time or frequency) produces aliasing in the other, and vice versa. The x_N summation is mathematically equivalent to aliasing, leading to decimation in frequency, leaving only DTFT samples least affected by spectral leakage.

The same results can be obtained by computing and decimating an L-length DFT, but that is not computationally efficient. When $L \leq N$, in order to take advantage of a fast Fourier transform algorithm for computing the DFT, the summation is usually performed over all N terms, even though $N - L$ of them are zeros. Therefore, the case $L < N$ is often referred to as zero-padding.

As mentioned before, the padding must be applied after the application of the window. For illustration, a signal composed by two sinusoids will be used;

$$x(t) = 0.5 \cdot sin(2\pi f_1 t) + 0.12 \cdot sin(2\pi f_2 t) + 5\,, \tag{A.1}$$

where f_1 and f_2 the frequency of each sinusoid.

The frequencies are selected to be $f_1 = 6$ and $f_2 = 15$ Hz. The resulting signal can be seen in Figure A.4. Additionally, the amplitude of the FFT is plotted against the normalised frequency.

Assume that the captured signal has $L = 1512$ samples. For the FFT, $N = 2048$ samples are required. To resolve the issue, the input array is padded with $N - L = 2048 - 1512 = 536$ zeroes. For this example, there are two cases: zero-pad the array first and apply the window, or apply the window and zero-pad the resulting array. The following figures, Figures A.5 and A.6, show the padded signal and its Fourier transform.

In Figure A.5, the signal is zero-padded before the application of a Blackman-Harris window. It is clear, that the windowing function is abruptly cut off at the point where the padding begins. As a result, the SNR of the Fourier is very poor and in addition spectral leakage has been introduced. Furthermore, on the Fourier domain, there are no signs of the windowing function, i.e. increased dynamic range, peak widening. Moreover, the padding increases the spacing of the frequency creating a zoomed-in effect. Thus, a frequency scaling must be applied to adjust the spacing.

In contrast, for Figure A.6 a Blackman-Harris window of size 1512 is applied to the signal before zero-padding. As the window reaches zero before the padding, there

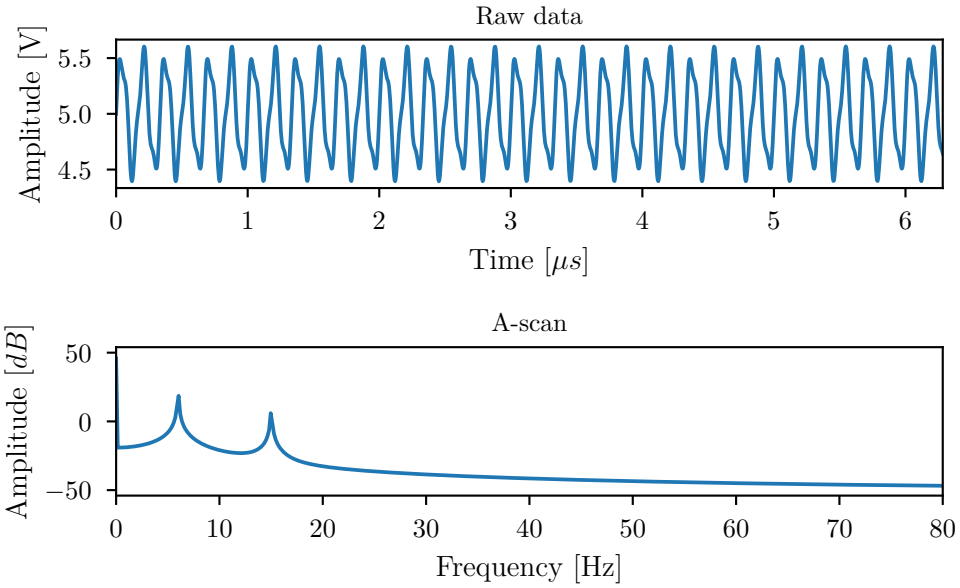

Figure A.4: *Top: The waveform of the time domain signal. Bottom: The Fourier transform of the signal. Two peaks (at 6 and 15 Hz) appear on the Fourier transform and correspond to the frequencies of the two cosines that the signal is composed off.*

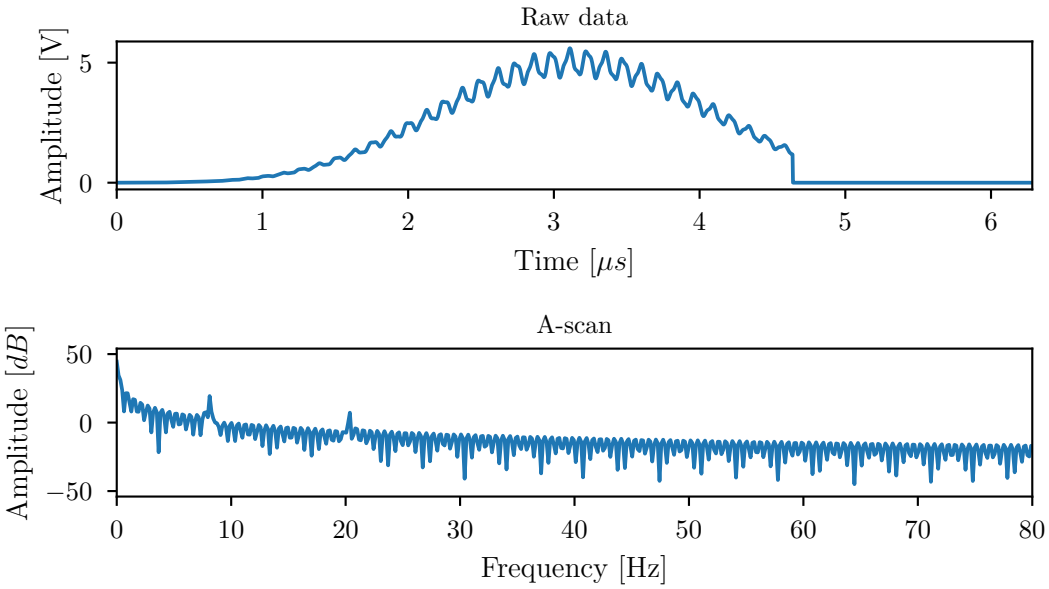

Figure A.5: *Top: The time domain signal is zero-padded and a Blackman-Harris window is applied. Because the signal is zero-padded first, the window is abruptly cut off. Bottom: The Fourier transform of the padded signal. Compared to the original, the SNR has been reduced and the spectral leakage has been increased.*

is a smooth transition. The result is increase dynamic range and decreased spectral leakage. However, in both cases the frequency spacing is altered and needs to be adjusted.

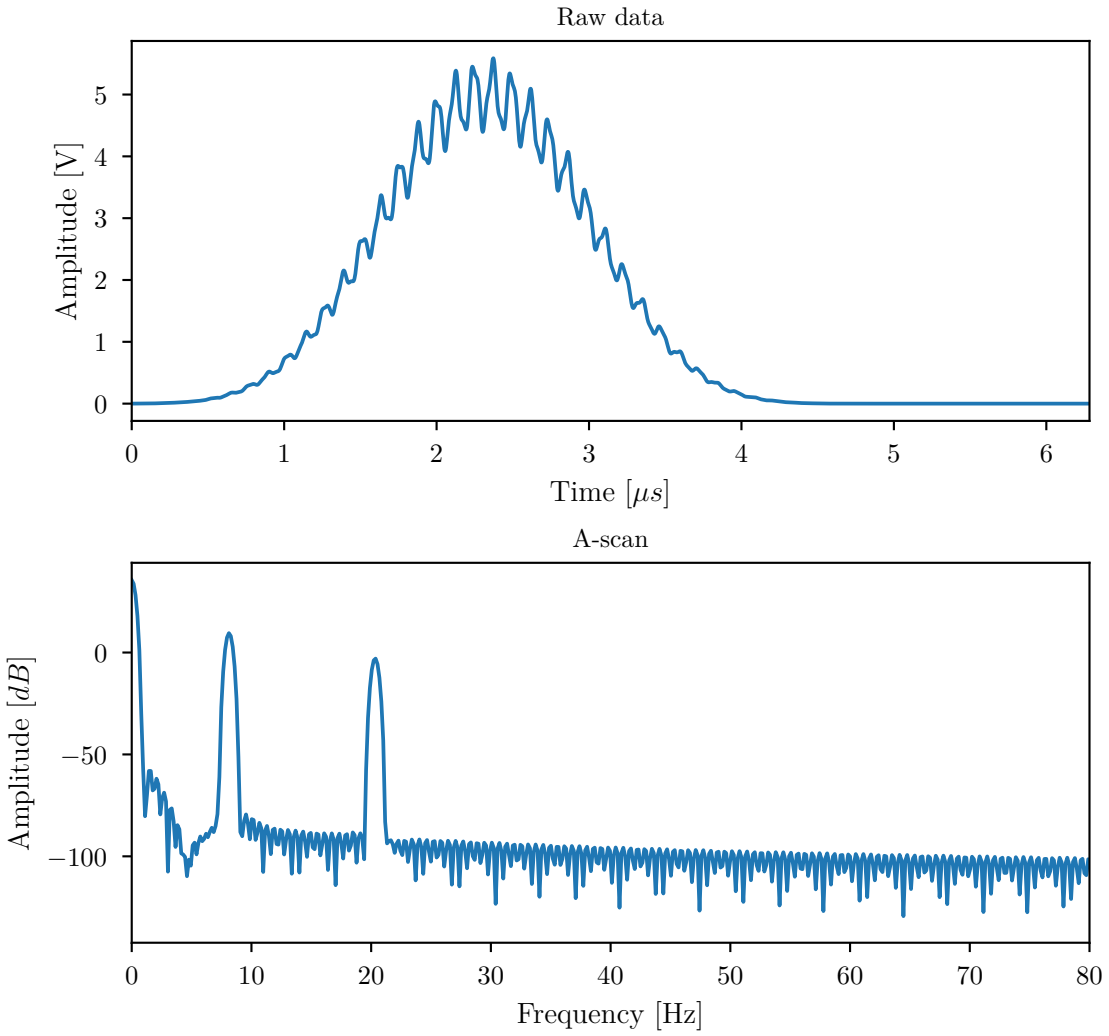

Figure A.6: *Top: A Blackman-Harris window is applied to the signal before padding. Bottom: The Fourier transform of signal. Compared to the original, the SNR has been increased, but the frequency spacing has changed.*

References

[1] A. Günther, S. Yasotharan, A. Vagaon, C. Lochovsky, S. Pinto, J. Yang, C. Lau, J. Voigtlaender-Bolz and S. Bolz, 'A microfluidic platform for probing small artery structure and function.' *Lab on a Chip*, vol. 10, no. 18, pp. 2341–2349, (2010), DOI: 10.1039/c004675b

[2] C. M. Moore, S. D. Minteer and R. S. Martin, 'Microchip-based ethanol/oxygen biofuel cell.' *Lab on a Chip*, vol. 5, no. 2, pp. 218–225, (2005), DOI: 10.1039/b412719f

[3] M. G. Khan and Ã. Amir Fartaj, 'A review on microchannel heat exchangers and potential applications', *International Journal of Energy Research*, vol. 35, no. July 2010, pp. 553–582, (2011), DOI: 10.1002/er

[4] E. Oosterbroek and A. van den Berg, 'Preface', ed. by R. E. Oosterbroek and A. van den Berg, *Lab on a Chip*, Elsevier, Amsterdam, pp. v–vi, (2003), ISBN: 978-0-444-51100-3, DOI: 10.1016/B978-044451100-3/50000-0

[5] M. Wojtkowski, R. Leitgeb, A. Kowalczyk, T. Bajraszewski and A. F. Fercher, 'In vivo human retinal imaging by Fourier domain optical coherence tomography.' *Journal of Biomedical Optics*, vol. 7, no. 3, pp. 457–463, (2002), DOI: 10.1117/1.1482379

[6] J. F. de Boer, B. Cense, B. H. Park, M. C. Pierce, G. J. Tearney and B. E. Bouma, 'Improved signal-to-noise ratio in spectral-domain compared with time-domain optical coherence tomography.' *Optics Letters*, vol. 28, no. 21, pp. 2067–2069, (2003), DOI: 10.1364/OL.28.002067

[7] T. Pfohl, F. Mugele, R. Seemann and S. Herminghaus, 'Trends in Microfluidics with Complex Fluids', *Chemical Physics*, vol. 4, no. 12, pp. 1291–1298, (2003), DOI: 10.1002/cphc.200300847

[8] G. V. Kaigala, R. D. Lovchik and E. Delamarche, 'Microfluidics in the "Open Space" for Performing Localized Chemistry on Biological Interfaces', *Angewandte Chemie International Edition*, vol. 51, no. 45, pp. 11224–11240, (2012), DOI: 10.1002/anie.201201798

[9] J. Berthier, K. A. Brakke and E. Berthier, 'Introduction', *Open Microfluidics*, Wiley-Blackwell, chap. 0, pp. 1–11, ISBN: 9781118720936, DOI: 10.1002/9781118720936.ch0

[10] S. Bouaidat, O. Hansen, H. Bruus, C. Berendsen, N. K. Bau-Madsen, P. Thomsen, A. Wolff and J. Jonsmann, 'Surface-directed capillary system; theory, experiments and applications', *Lab on a Chip*, vol. 5, no. 8, pp. 827–836, 8 (2005), DOI: 10.1039/B502207J

[11] B. P. Casavant, E. Berthier, A. B. Theberge, J. Berthier et al., 'Suspended microfluidics', *Proceedings of the National Academy of Sciences*, vol. 110, no. 25, pp. 10111–10116, (2013), DOI: 10.1073/pnas.1302566110

[12] J. Berthier, K. A. Brakke and E. Berthier, 'Paper-Based Microfluidics', *Open Microfluidics*, Wiley-Blackwell, chap. 7, pp. 229–256, ISBN: 9781118720936, DOI: 10.1002/9781118720936.ch7

[13] H. Chang and L. Y. Yeo, *Electrokinetically-Driven Microfluidics and Nanofluidics*, 1 edition, Cambridge University Press, Cambridge ; New York, 508 pp., ISBN: 978-0-521-86025-3

[14] Thales SA, 'Electrodes for a device operating by electrically controlled fluid displacement', US4569575A, J. P. L. Pesant, M. Hareng, B. Mourey and J. N. Perbet, 1986

[15] W. Martinez Andres, T. Phillips Scott, J. Butte Manish and M. Whitesides George, 'Patterned Paper as a Platform for Inexpensive, Low-Volume, Portable Bioassays', *Angewandte Chemie International Edition*, vol. 46, no. 8, pp. 1318–1320, (2007), DOI: 10.1002/anie.200603817

[16] T. San Park and J. Yoon, 'Smartphone detection of Escherichia coli from field water samples on paper microfluidics', *IEEE Sensors Journal*, vol. 15, no. 3, pp. 1902–1907, (2015)

[17] P. Galajda, J. Keymer, P. Chaikin and R. Austin, 'A Wall of Funnels Concentrates Swimming Bacteria', *Journal of Bacteriology*, vol. 189, no. 23, pp. 8704–8707, (2007), DOI: 10.1128/JB.01033-07

[18] L. Angelani, R. Di Leonardo and G. Ruocco, 'Self-Starting Micromotors in a Bacterial Bath', *Physical Review Letters 102, 048104 (2009)*, vol. 102, no. 4 (2009), DOI: 10.1103/PhysRevLett.102.048104

[19] A. Sokolov, M. M. Apodaca, B. A. Grzybowski and I. S. Aranson, 'Swimming bacteria power microscopic gears', *Proceedings of the National Academy of Sciences of the United States of America*, vol. 107, no. 3, pp. 969–974, (2010), DOI: 10.1073/pnas.0913015107

[20] R. Di Leonardo, L. Angelani, G. Ruocco, V. Iebba, M. P. Conte, S. Schippa, F. De Angelis, F. Mecarini and E. Di Fabrizio, 'A bacterial ratchet motor', *Proceedings of the National Academy of Sciences*, vol. 107, no. 21, pp. 9541–9545, (2010), DOI: 10.1073/pnas.0910426107

[21] S. Grilli, L. Miccio, V. Vespini, A. Finizio, S. D. Nicola and P. Ferraro, 'Liquid micro-lens array activated by selective electrowetting on lithium niobate substrates', *Optics Express*, vol. 16, no. 11, pp. 8084–8093, (2008), DOI: 10.1364/OE.16.008084

[22] P. Ferraro, L. Miccio, S. Grilli, A. Finizio, S. D. Nicola and V. Vespini, 'Manipulating Thin Liquid Films for Tunable Microlens Arrays', *Opt. Photon. News*, vol. 19, no. 12, pp. 34–34, (2008), DOI: 10.1364/OPN.19.12.000034

[23] R. Ellson, M. Mutz, B. Browning, J. Lawrence Lee, J. Michael F. Miller and J. Roeland Papen, 'Transfer of Low Nanoliter Volumes between Microplates Using Focused Acoustics—Automation Considerations', *Journal of the Association for Laboratory Automation*, vol. 8, no. 5, pp. 29–34, (2003), DOI: 10.1016/S1535-5535-03-00011-X

[24] R. Ellson, 'Picoliter: enabling precise transfer of nanoliter and picoliter volumes', *Drug Discovery Today*, vol. 7, no. 5, S32–S34, (2002), DOI: 10.1016/s1359-6446(02)02176-1

[25] X. Yin, A. Scalia, L. Leroy, C. M. Cuttitta et al., 'Hitting the target: fragment screening with acoustic *in situ* co-crystallization of proteins plus fragment libraries on pin-mounted data-collection micromeshes', *Acta Crystallographica Section D Biological Crystallography*, vol. 70, no. 5, pp. 1177–1189, (2014), DOI: 10.1107/S1399004713034603

[26] U. Demirci and G. Montesano, 'Single cell epitaxy by acoustic picolitre droplets', *Lab on a Chip*, vol. 7, no. 9, p. 1139, (2007), DOI: 10.1039/b704965j

[27] E. R. Choban, L. J. Markoski, A. Wieckowski and P. J. Kenis, 'Microfluidic fuel cell based on laminar flow', *Journal of Power Sources*, vol. 128, no. 1, pp. 54–60, (2004), DOI: 10.1016/j.jpowsour.2003.11.052

[28] S. A. M. Shaegh, N. Nguyen and S. H. Chan, 'A review on membraneless laminar flow-based fuel cells', *International Journal of Hydrogen Energy*, vol. 36, no. 9, pp. 5675–5694, (2011), DOI: 10.1016/j.ijhydene.2011.01.063

[29] A. Voigt, C. Bayer, K. Shirai, L. Büttner and J. Czarske, 'Laser Doppler field sensor for high resolution flow velocity imaging without camera.' *Applied Optics*, vol. 47, no. 27, pp. 5028–5040, (2008), DOI: 10.1364/AO.47.005028

[30] S. Weisse, M. Heydt, T. Maier, S. Schulz, J. P. Spatz, M. Grunze, T. Haraszti and A. Rosenhahn, 'Flow conditions in the vicinity of microstructured interfaces studied by holography and implications for the assembly of artificial actin networks.' *Physical Chemistry Chemical Physics : PCCP*, vol. 13, no. 29, pp. 13395–13402, (2011), DOI: 10.1039/c1cp20153k

[31] M. Dienerowitz, M. Lee, G. Gibson and M. Padgett, 'Measuring nanoparticle flow with the image structure function.' *Lab on a Chip*, vol. 13, no. 12, pp. 2359–63, (2013), DOI: 10.1039/c3lc00028a

[32] J. G. Santiago, S. T. Wereley, C. D. Meinhart, D. J. Beebe and R. J. Adrian, 'A particle image velocimetry system for microfluidics', *Experiments in Fluids*, vol. 25, no. 4, pp. 316–319, (1998), DOI: 10.1007/s003480050235

[33] C. D. Meinhart, S. T. Wereley and J. G. Santiago, 'PIV measurements of a microchannel flow', *Experiments in Fluids*, vol. 27, no. 5, pp. 414–419, (1999), DOI: 10.1007/s003480050366

[34] M. T. Roberts, A. Mohraz, K. T. Christensen and J. A. Lewis, 'Direct flow visualization of colloidal gels in microfluidic channels', *Langmuir*, vol. 23, no. 17, pp. 8726–8731, (2007), DOI: 10.1021/la700562m

[35] H. Kinoshita, S. Kaneda, T. Fujii and M. Oshima, 'Three-dimensional measurement and visualization of internal flow of a moving droplet using confocal micro-PIV', *Lab on a Chip*, vol. 7, pp. 338–346, 3 (2007), DOI: 10.1039/B617391H

[36] K. Shinohara, Y. Sugii, A. Aota, A. Hibara, M. Tokeshi, T. Kitamori and K. Okamoto, 'High-speed micro-PIV measurements of transient flow in microfluidic devices', *Measurement Science and Technology*, vol. 15, no. 10, p. 1965, (2004)

[37] Y. Sugii, R. Okuda, K. Okamoto and H. Madarame, 'Velocity measurement of both red blood cells and plasma of in vitro blood flow using high-speed micro PIV technique', *Measurement Science and Technology*, vol. 16, no. 5, p. 1126, (2005)

[38] T. Dracos, 'Particle Tracking Velocimetry (PTV)', ed. by T. Dracos, *Three-Dimensional Velocity and Vorticity Measuring and Image Analysis Techniques: Lecture Notes from the Short Course held in Zürich, Switzerland, 3–6 September 1996*, ERCOFTAC Series, Springer Netherlands, Dordrecht, pp. 155–160, (1996), ISBN: 978-94-015-8727-3, DOI: 10.1007/978-94-015-8727-3_7

[39] S. FU, P. H. Biwole and C. Mathis, 'A Comparative Study of Particle Image Velocimetry (PIV) and Particle Tracking Velocimetry (PTV) for Airflow Measurement' (2015)

[40] F. Alberini, L. Liu, E. H. Stitt and M. J. H. Simmons, 'Comparison between 3-D-PTV and 2-D-PIV for determination of hydrodynamics of complex fluids in a stirred vessel', *Chemical Engineering Science*, vol. 171, pp. 189–203, (2017), DOI: 10.1016/j.ces.2017.05.034

[41] S. Fu, P. H. Biwole and C. Mathis, 'Numerical and experimental comparison of 3D Particle Tracking Velocimetry (PTV) and Particle Image Velocimetry (PIV) accuracy for indoor airflow study', *Building and Environment*, vol. 100, pp. 40–49, (2016), DOI: 10.1016/j.buildenv.2016.02.002

[42] A. K. Tieu, M. R. Mackenzie and E. B. Li, 'Measurements in microscopic flow with a solid-state LDA', *Experiments in Fluids*, vol. 19, no. 4, pp. 293–294, (1995), DOI: 10.1007/BF00196478

[43] M. Schmidt, E. Wassner and H. Münstedt, 'Setup and Test of a Laser Doppler Velocimeter for Investigations of Flow Behaviour of Polymer Melts', *Mechanics of Time-Dependent Materials*, vol. 3, no. 4, pp. 371–393, (1999), DOI: 10.1023/A:1009820500869

[44] S. Schuberth and H. Münstedt, 'Simultaneous measurements of velocity and stress distributions in polyisobutylenes using laser-Doppler velocimetry and flow induced birefringence', *Rheologica Acta*, vol. 47, no. 1, pp. 111–119, (2008), DOI: 10.1007/s00397-007-0219-2

[45] J. König, A. Voigt, L. Büttner and J. Czarske, 'Precise micro flow rate measurements by a laser Doppler velocity profile sensor with time division multiplexing', vol. 21, p. 074005, (2010)

[46] M. Born and E. Wolf, *Principles of Optics*, Cambridge University Press, Cambridge; New York, ISBN: 978-1-139-64418-1

[47] E. Beaurepaire, A. C. Boccara, M. Lebec, L. Blanchot and H. Saint-Jalmes, 'Full-field optical coherence microscopy', *Optics Letters*, vol. 23, no. 4, p. 244, (1998), DOI: 10.1364/OL.23.000244

[48] A. Dubois, L. Vabre, A. Boccara and E. Beaurepaire, 'High-resolution full-field optical coherence tomography with a Linnik microscope.' *Applied Optics*, vol. 41, no. 4, pp. 805–812, (2002), DOI: 10.1364/AO.41.000805

[49] S. V. der Jeught, A. Bradu and A. G. Podoleanu, 'Real-time resampling in Fourier domain optical coherence tomography using a graphics processing unit', *Journal of Biomedical Optics*, vol. 15, no. 3, pp. 15 - 15 - 3, (2010), DOI: 10.1117/1.3437078

[50] Z. Chen and J. Zhang, 'Doppler Optical Coherence Tomography', ed. by W. Drexler and J. G. Fujimoto, *Optical Coherence Tomography: Technology and Applications*, Springer International Publishing, Cham, pp. 1289–1320, (2015), ISBN: 978-3-319-06419-2, DOI: 10.1007/978-3-319-06419-2_42

[51] Z. Chen, T. E. Milner, D. Dave and J. S. Nelson, 'Optical Doppler tomographic imaging of fluid flow velocity in highly scattering media.' *Optics Letters*, vol. 22, no. 1, pp. 64–66, (1997), DOI: 10.1364/OL.22.000064

[52] D. Piao, N. G. Chen, Q. Zhu, N. K. Dutta and L. L. Otis, 'Imaging of fluid flow velocity using Doppler optical coherence tomography: preliminary results', *Proceedings of the IEEE 27th Annual Northeast Bioengineering Conference (Cat. No.01CH37201)*, IEEE, pp. 55–56, (2001), ISBN: 0-7803-6717-0, DOI: 10.1109/NEBC.2001.924717

[53] G. Liu, L. Chou, W. Jia, W. Qi, B. Choi and Z. Chen, 'Intensity-based modified Doppler variance algorithm: application to phase instable and phase stable optical coherence tomography systems', *Optics Express*, vol. 19, no. 12, pp. 11429–11440, (2011), DOI: 10.1364/OE.19.011429

[54] Z. Chen, T. E. Milner, S. Srinivas, X. Wang, A. Malekafzali, M. J. C. van Gemert and J. S. Nelson, 'Noninvasive imaging of in vivo blood flow velocity using optical Doppler tomography', *Optics Letters*, vol. 22, no. 14, p. 1119, (1997), DOI: 10.1364/OL.22.001119

[55] J. A. Izatt, M. D. Kulkarni, S. Yazdanfar, J. K. Barton and A. J. Welch, 'In vivo bidirectional color Doppler flow imaging of picoliter blood volumes using optical coherence tomography', *Optics Letters*, vol. 22, no. 18, p. 1439, (1997), DOI: 10.1364/OL.22.001439

[56] Y. Zhao, Z. Chen, C. Saxer, S. Xiang, J. F. de Boer and J. S. Nelson, 'Phase-resolved optical coherence tomography and optical Doppler tomography for imaging blood flow in human skin with fast scanning speed and high velocity sensitivity.' *Optics Letters*, vol. 25, no. 2, pp. 114–116, (2000), DOI: 10.1364/OL.25.000114

[57] V. J. Srinivasan, S. Sakadžić, I. Gorczynska, S. Ruvinskaya, W. Wu, J. G. Fujimoto and D. A. Boas, 'Quantitative cerebral blood flow with Optical Coherence Tomography', *Optics Express*, vol. 18, no. 3, pp. 2477–2494, (2010), DOI: 10.1364/OE.18.002477

[58] Y. Jia, P. O. Bagnaninchi, Y. Yang, A. E. Haj, M. T. Hinds, S. J. Kirkpatrick and R. K. Wang, 'Doppler optical coherence tomography imaging of local

fluid flow and shear stress within microporous scaffolds', *Journal of Biomedical Optics*, vol. 14, no. 3, p. 034014, (2009), DOI: 10.1117/1.3130345

[59] Y. Ahn, W. Jung and Z. Chen, 'Optical sectioning for microfluidics: secondary flow and mixing in a meandering microchannel.' *Lab on a Chip*, vol. 8, no. 1, pp. 125–133, (2008), DOI: 10.1039/b713626a

[60] Z. Y. Shen, M. Wang, Y. H. Ji, Y. H. He, X. S. Dai, P. Li and H. Ma, 'Transverse flow velocity quantification using optical coherence tomography with correlation', *Laser Physics Letters*, vol. 8, no. 4, pp. 318–323, (2011), DOI: 10.1002/lapl.201010126

[61] S. Cito, Y. Ahn, J. Pallares, R. M. Duarte, Z. Chen, M. Madou and I. Katakis, 'Visualization and measurement of capillary-driven blood flow using spectral domain optical coherence tomography', *Microfluidics and Nanofluidics*, vol. 13, no. 2, pp. 227–237, (2012), DOI: 10.1007/s10404-012-0950-6

[62] M. Baltussen, P. Anderson, F. Bos and J. den Toonder, 'Inertial flow effects in a micro-mixer based on artificial cilia.' *Lab on a Chip*, vol. 9, no. 16, pp. 2326–2331, (2009), DOI: 10.1039/b901660k

[63] A. Szkulmowska, M. Szkulmowski, D. Szlag, A. Kowalczyk and M. Wojtkowski, 'Three-dimensional quantitative imaging of retinal and choroidal blood flow velocity using joint Spectral and Time domain Optical Coherence Tomography', *Optics Express*, vol. 17, no. 13, pp. 10584–10598, (2009), DOI: 10.1364/oe.17.010584

[64] D. M. Bukowska, L. Derzsi, S. Tamborski, M. Szkulmowski, P. Garstecki and M. Wojtkowski, 'Assessment of the flow velocity of blood cells in a microfluidic device using joint spectral and time domain optical coherence tomography.' *Optics Express*, vol. 21, no. 20, pp. 24025–38, (2013), DOI: 10.1364/OE.21.024025

[65] S. Jonas, D. Bhattacharya, M. K. Khokha and M. A. Choma, 'Microfluidic characterization of cilia-driven fluid flow using optical coherence tomography-based particle tracking velocimetry', *Biomedical Optics Express*, vol. 2, no. 7, pp. 2022–2034, (2011), DOI: 10.1364/BOE.2.002022

[66] J. Lauri, J. Czajkowski, R. Myllylä and T. Fabritius, 'Measuring flow dynamics in a microfluidic chip using optical coherence tomography with 1 mu m axial resolution', *Flow Measurement and Instrumentation*, vol. 43, pp. 1–5, (2015), DOI: 10.1016/j.flowmeasinst.2015.02.001

[67] B. Potsaid, B. Baumann, D. Huang, S. Barry, A. E. Cable, J. S. Schuman, J. S. Duker and J. G. Fujimoto, 'Ultrahigh speed 1050nm swept source / Fourier domain OCT retinal and anterior segment imaging at 100,000 to 400,000 axial scans per second', *Optics Express*, vol. 18, no. 19, pp. 20029–20048, (2010), DOI: 10.1364/OE.18.020029

[68] A.-H. Dhalla, K. Shia and J. A. Izatt, 'Efficient sweep buffering in swept source optical coherence tomography using a fast optical switch', *Biomedical Optics Express*, vol. 3, no. 12, p. 3054, (2012), DOI: 10.1364/boe.3.003054

[69] D. Huang, E. a. Swanson, C. P. Lin, J. S. Schuman et al., 'Optical Coherence', *Science (New York, N.Y.)* Vol. 254, no. 5035, pp. 1178–1181, (1991), PMCID: PMC4638169, PMID: 1957169

[70] W. Drexler, U. Morgner, F. X. Kärtner, C. Pitris, S. a. Boppart, X. D. Li, E. P. Ippen and J. G. Fujimoto, 'In vivo ultrahigh-resolution optical coherence tomography', *Optics Letters*, vol. 24, no. 17, pp. 1221–1223, (1999), DOI: 10.1364/OL.24.001221

[71] B. Povazay, K. Bizheva, a. Unterhuber, B. Hermann et al., 'Submicrometer axial resolution optical coherence tomography.' *Optics Letters*, vol. 27, no. 20, pp. 1800–1802, (2002), DOI: 10.1364/OL.27.001800

[72] J. F. de Boer, R. Leitgeb and M. Wojtkowski, 'Twenty-five years of optical coherence tomography: the paradigm shift in sensitivity and speed provided by Fourier domain OCT [Invited]', *Biomedical Optics Express*, vol. 8, no. 7, p. 3248, (2017), DOI: 10.1364/boe.8.003248

[73] S. H. Yun, C. Boudoux, G. J. Tearney and B. E. Bouma, 'High-speed wavelength-swept semiconductor laser with a polygon-scanner-based wavelength filter', *Optics Letters*, vol. 28, no. 20, pp. 1981–1983, (2003), DOI: 10.1364/OL.28.001981

[74] M. Bonesi, D. Churmakov and I. Meglinski, 'Study of flow dynamics in complex vessels using Doppler optical coherence tomography', *Measurement Science and Technology*, vol. 18, 11, pp. 3279–3286, (2007), DOI: 10.1088/0957-0233/18/11/003

[75] D. Bukowska, M. Szkulmowski, I. Gorczynska, A. Kowalczyk and M. Wojtkowski, 'Microfluidics analysis of blood using joint spectral and time domain optical coherence tomography', ed. by J. A. Izatt, J. G. Fujimoto and V. V. Tuchin, *Optical Coherence Tomography and Coherence Domain Optical Methods in Biomedicine XVI*, vol. 8213, SPIE, 82132R–82132R–6, (2012), DOI: 10.1117/12.911070

[76] J. Czajkowski, J. Lauri, R. Sliz, P. Fält, T. Fabritius, R. Myllylä and B. Cense, 'Sub-micron resolution, high-speed spectral domain optical coherence tomography in quality inspection for printed electronics', *SPIE*, vol. 8430, 84300K–84300K–8, (2012), DOI: 10.1117/12.922443

[77] M. Wojtkowski, a. Kowalczyk, R. Leitgeb and a. F. Fercher, 'Full range complex spectral optical coherence tomography technique in eye imaging.' *Optics Letters*, vol. 27, no. 16, pp. 1415–1417, (2002), DOI: 10.1364/OL.27.001415

[78] P. Targowski, M. Wojtkowski, A. Kowalczyk, T. Bajraszewski, M. Szkulmowski and I. Gorczyńska, 'Complex spectral OCT in human eye imaging in vivo', *Optics Communications*, vol. 229, no. 1-6, pp. 79–84, (2004), DOI: 10.1016/j.optcom.2003.10.041

[79] J. A. Izatt, M. A. Choma and A.-H. Dhalla, 'Theory of Optical Coherence Tomography', ed. by W. Drexler and J. G. Fujimoto, *Optical Coherence Tomography: Technology and Applications*, Springer International Publishing, Cham, pp. 65–94, (2015), ISBN: 978-3-319-06419-2, DOI: 10.1007/978-3-319-06419-2_3

[80] M. Wojtkowski, V. Srinivasan, T. Ko, J. Fujimoto, A. Kowalczyk and J. Duker, 'Ultrahigh-resolution, high-speed, Fourier domain optical coherence tomography and methods for dispersion compensation.' *Optics Express*, vol. 12, no. 11, pp. 2404–2422, (2004), DOI: 10.1364/OPEX.12.002404

[81] R. Leitgeb, W. Drexler, A. Unterhuber, B. Hermann, T. Bajraszewski, T. Le, A. Stingl and A. Fercher, 'Ultrahigh resolution Fourier domain optical coherence tomography.' *Optics Express*, vol. 12, no. 10, pp. 2156–2165, (2004), DOI: 10.1364/OPEX.12.002156

[82] T. C. Chen, B. Cense, M. C. Pierce, N. Nassif, B. H. Park, S. H. Yun, B. R. White, B. E. Bouma, G. J. Tearney and J. F. de Boer, 'Spectral domain optical coherence tomography: ultra-high speed, ultra-high resolution ophthalmic imaging.' *Archives of Ophthalmology*, vol. 123, no. 12, pp. 1715–1720, (2005), DOI: 10.1001/archopht.123.12.1715

[83] M. Wojtkowski, V. Srinivasan, J. G. Fujimoto, T. Ko, J. S. Schuman, A. Kowalczyk and J. S. Duker, 'Three-dimensional retinal imaging with high-speed ultrahigh-resolution optical coherence tomography', *Ophthalmology*, vol. 112, no. 10, pp. 1734–1746, (2005), DOI: 10.1016/j.ophtha.2005.05.023

[84] Y. Zhang, B. Cense, J. Rha, R. S. Jonnal, W. Gao, R. J. Zawadzki, J. S. Werner, S. Jones, S. Olivier and D. T. Miller, 'High-speed volumetric imaging of cone photoreceptors with adaptive optics spectral-domain optical coherence tomography.' *Optics Express*, vol. 14, no. 10, pp. 4380–4394, (2006), DOI: 10.1364/OE.14.004380

[85] D. Litwiller, 'CCD vs. CMOS', *Photonics Spectra*, vol. 35, no. 1, pp. 154–158, (2001)

[86] H. Helmers and M. Schellenberg, 'CMOS vs. CCD sensors in speckle interferometry', *Optics and Laser Technology*, vol. 35, no. 8, pp. 587–595, (2003), DOI: 10.1016/S0030-3992(03)00078-1

[87] B. Potsaid, I. Gorczynska, V. J. Srinivasan, Y. Chen, J. Jiang, A. Cable and J. G. Fujimoto, 'Ultrahigh speed spectral / Fourier domain OCT ophthalmic imaging at 70,000 to 312,500 axial scans per second.' *Optics Express*, vol. 16, no. 19, pp. 15149–15169, (2008), DOI: 10.1364/OE.16.015149

[88] K. Zhang and J. U. Kang, 'Graphics Processing Unit-Based Ultrahigh Speed Real-Time Fourier Domain Optical Coherence Tomography', *IEEE Journal of Selected Topics in Quantum Electronics*, vol. 18, no. 4, pp. 1270–1279, (2012), DOI: 10.1109/JSTQE.2011.2164517

[89] J. Su, J. Zhang, L. Yu, H. G Colt, M. Brenner and Z. Chen, 'Real-time swept source optical coherence tomography imaging of the human airway using a microelectromechanical system endoscope and digital signal processor', *Journal of Biomedical Optics*, vol. 13, no. 3, p. 030506, (2008), DOI: 10.1117/1.2938700

[90] I. V. Larina, K. Furushima, M. E. Dickinson, R. R. Behringer and K. V. Larin, 'Live imaging of rat embryos with Doppler swept-source optical coherence tomography', *Journal of Biomedical Optics*, vol. 14, no. 5, pp. 5–7, (2009), DOI: 10.1117/1.3241044

[91] V. Jayaraman, J. Jiang, H. Li, P. Heim, G. Cole, B. Potsaid, J. G. Fujimoto and A. Cable, 'OCT Imaging up to 760 kHz Axial Scan Rate Using Single-Mode 1310nm MEMS-Tunable VCSELs with >100nm Tuning Range', PDPB2, (2011), DOI: 10.1364/cleo_si.2011.pdpb2

[92] B. Potsaid, V. Jayaraman, J. G. Fujimoto, J. Jiang, P. J. S. Heim and A. E. Cable, 'MEMS tunable VCSEL light source for ultrahigh speed 60kHz - 1MHz axial scan rate and long range centimeter class OCT imaging', ed. by J. A. Izatt, J. G. Fujimoto and V. V. Tuchin, *Optical Coherence Tomography and Coherence Domain Optical Methods in Biomedicine XVI*, SPIE, San Francisco, California, USA, p. 82130M, (2012), DOI: 10.1117/12.911098

[93] M. Gora, K. Karnowski, M. Szkulmowski, B. J. Kaluzny, R. Huber, A. Kowalczyk and M. Wojtkowski, 'Ultra high-speed swept source OCT imaging of the anterior segment of human eye at 200 kHz with adjustable imaging range.' *Optics Express*, vol. 17, no. 17, pp. 14880–14894, (2009), DOI: 10.1364/OE.17.014880

[94] I. Grulkowski, J. J. Liu, B. Potsaid, V. Jayaraman, C. D. Lu, J. Jiang, A. E. Cable, J. S. Duker and J. G. Fujimoto, 'Retinal, anterior segment and full eye imaging using ultrahigh speed swept source OCT with vertical-cavity surface emitting lasers', *Biomedical Optics Express*, vol. 3, no. 11, p. 2733, (2012), DOI: 10.1364/BOE.3.002733

[95] R. J. Santoro, A. C. Fernandez-Pello, F. L. Dryer and I. Glassman, 'Application of a two-component LDV to the measurement of flows induced by flames

propagating over condensed fuels', *Applied Optics*, vol. 17, no. 23, pp. 3843–3850, (1978), DOI: 10.1364/AO.17.003843

[96] D. García-Vizcaíno, F. Dios and J. R. A. R. A. Comeron, 'One-wavelength two-component laser Doppler velocimeter system for surface displacement monitoring', *Optical Engineering*, vol. 47, no. 12, pp. 47 - 47 - 11, (2008), DOI: 10.1117/1.3050421

[97] W. Drexler and J. Fujimoto, *Optical Coherence Tomography - Technology and Applications | Wolfgang Drexler | Springer*, ed. by W. Drexler and J. Fujimoto, vol. 1, Springer Berlin Heidelberg, Berlin, chap. 11, ISBN: 978-3-540-77550-8

[98] M. A. Choma, K. Hsu and J. A. Izatt, 'Swept source optical coherence tomography using an all-fiber 1300-nm ring laser source', *Journal of Biomedical Optics*, vol. 10, no. 4, pp. 044009–044009–6, (2005), DOI: 10.1117/1.1961474

[99] K. Liu and M. G. Littman, 'Novel geometry for single-mode scanning of tunable lasers', *Optics Letters*, vol. 6, no. 3, pp. 117–118, (1981), DOI: 10.1364/OL.6.000117

[100] T. Day, M. F. Brownell and I. Wu, 'Widely tunable external cavity diode lasers', ed. by Y. Shevy, *Laser Frequency Stabilization and Noise Reduction*, vol. 2378, SPIE, p. 35, (1995), DOI: 10.1117/12.208238

[101] M. Wippich and K. L. Dessau, 'Tunable lasers enhance fiber sensors', *ResearchGate*, vol. 39, no. 3, pp. 89–94, (2003)

[102] L. A. Kranendonk, R. J. Bartula and S. T. Sanders, 'Modeless operation of a wavelength-agile laser by high-speed cavity length changes', *Optics Express*, vol. 13, no. 5, pp. 1498–1507, (2005), DOI: 10.1364/OPEX.13.001498

[103] Santec Corporation, *50kHz high-speed, Wide range Swept Source, Datasheet, CODE-200907-TH-MT-CPY*, HSL-2100-HW, HSL-2100-HW-C-E, version 1.0, Santec Corporation, Inner Vision.

[104] Axsun, *High Speed 1310nm Swept Source for OCT*, AXSUN Technologies

[105] Santec Corporation, *Optical Coherence Tomography, HSL application note 2010-E/Volume.1.1 201005-A4-TH-MT-print*, Santec Corporation, Inner Vision.

[106] Y. Okabe, Y. Sasaki, M. Ueno, T. Sakamoto et al., '200 kHz swept light source equipped with KTN deflector for optical coherence tomography', *Electronics Letters*, vol. 48, no. 4, pp. 201–202, (2012), DOI: 10.1049/el.2011.4057

[107] R. Huber, M. Wojtkowski, K. Taira, J. G. Fujimoto and K. Hsu, 'Amplified, frequency swept lasers for frequency domain reflectometry and OCT imaging: design and scaling principles', *Optics Express*, vol. 13, no. 9, pp. 3513–3528, (2005), DOI: 10.1364/OPEX.13.003513

[108] R. Huber, M. Wojtkowski and J. G. Fujimoto, 'Fourier Domain Mode Locking (FDML): A new laser operating regime and applications for optical coherence tomography', *Optics Express*, vol. 14, no. 8, pp. 3225–3237, (2006), DOI: 10.1364/OE.14.003225

[109] B. Pezeshki, E. Vail, J. Kubicky, G. Yoffe et al., '20-mW widely tunable laser module using DFB array and MEMS selection', *IEEE Photonics Technology Letters*, vol. 14, no. 10, pp. 1457–1459, (2002), DOI: 10.1109/LPT.2002.802392

[110] V. J. Srinivasan, R. Huber, I. Gorczynska, J. G. Fujimoto, J. Y. Jiang, P. Reisen and A. E. Cable, 'High-speed, high-resolution optical coherence tomography retinal imaging with a frequency-swept laser at 850 nm', *Optics Letters*, vol. 32, no. 4, pp. 361–363, (2007), DOI: 10.1364/OL.32.000361

[111] D. C. Adler, Y. Chen, R. Huber, J. Schmitt, J. Connolly and J. G. Fujimoto, 'Three-dimensional endomicroscopy using optical coherence tomography', *Nature Photonics*, vol. 1, no. 12, pp. 709–716, (2007), DOI: 10.1038/nphoton.2007.228

[112] J. Lewandowski, M. Duelk and C. Velez, 'Light Source, and Optical Coherence Tomography Module', US20140098829A1, J. Lewandowski, M. Duelk and C. Velez, 2014

[113] X. Liu, S. Chen, D. Cui, X. Yu and L. Liu, 'Spectral estimation optical coherence tomography for axial super-resolution', *Optics Express*, vol. 23, no. 20, p. 26521, (2015), DOI: 10.1364/OE.23.026521

[114] J. Kilby, ed. by Texas Instruments, URL: http://www.ti.com/corp/docs/kilbyctr/jackbuilt.shtml

[115] G. Moore, 'Cramming More Components onto Integrated Circuits', *Proceedings of the IEEE*, vol. 86, IEEE, (1998)

[116] R. Huber, 'FDML (incl. Parallelization)', ed. by W. Drexler and J. G. Fujimoto, *Optical Coherence Tomography: Technology and Applications*, Springer International Publishing, Cham, pp. 741–787, (2015), ISBN: 978-3-319-06419-2, DOI: 10.1007/978-3-319-06419-2_25

[117] B. R. Biedermann, W. Wieser, C. M. Eigenwillig, T. Klein and R. Huber, 'Dispersion, coherence and noise of Fourier domain mode locked lasers', *Optics Express*, vol. 17, no. 12, pp. 9947–61, (2009), DOI: 10.1364/OE.17.009947

[118] G. Y. Liu, A. Mariampillai, B. A. Standish, N. R. Munce, X. Gu and I. A. Vitkin, 'High power wavelength linearly swept mode locked fiber laser for OCT imaging', *Optics Express*, vol. 16, no. 18, p. 14095, (2008), DOI: 10.1364/oe.16.014095

[119] V. Jayaraman, J. Jiang, B. Potsaid, M. Robertson et al., 'VCSEL Swept Light Sources', ed. by W. Drexler and J. G. Fujimoto, *Optical Coherence Tomography: Technology and Applications*, Springer International Publishing, Cham, pp. 659–686, (2015), ISBN: 978-3-319-06419-2, DOI: 10.1007/978-3-319-06419-2_23

[120] C. Gierl, T. Gruendl, P. Debernardi, K. Zogal et al., 'Surface micromachined tunable 1.55 μm-VCSEL with 102 nm continuous single-mode tuning', *Optics Express*, vol. 19, no. 18, pp. 17336–17343, (2011), DOI: 10.1364/OE.19.017336

[121] Y. Zhou, M. C. Y. Huang and C. J. Chang-Hasnain, 'Tunable VCSEL with ultra-thin high contrast grating for high-speed tuning', *Optics Express*, vol. 16, no. 18, pp. 14221–14226, (2008), DOI: 10.1364/OE.16.014221

[122] L. A. Coldren, 'Multi-section tunable laser with differing multi-element mirrors', US4896325 A, L. A. Coldren, 1990

[123] R. Schatz, *Advances in Widely Tunable Lasers*, Laboratory of Photonics, Royal Institute of Technology

[124] B. Pezeshki, 'Tunable optical device using a scanning MEMS mirror', 6791694, B. Pezeshki, 2004

[125] A. J. Ward, D. J. Robbins, G. Busico, E. Barton et al., 'Widely tunable DS-DBR laser with monolithically integrated SOA: design and performance', *IEEE Journal of Selected Topics in Quantum Electronics*, vol. 11, no. 1, pp. 149–156, (2005), DOI: 10.1109/JSTQE.2004.841698

[126] C. Doyle, *Structural health monitoring 2003: from diagnosis & prognostics to structural health management ; proceedings of the 4th International Workshop on Structural Health Monitoring, Stanford University, Stanford, CA, September 15 - 17, 2003*, DEStech Publications, Lancaster, Pa, chap. structural health monitoring using optical fibre strain sensing systems, ISBN: 978-1-932078-20-6

[127] M. Kuznetsov, W. Atia, B. Johnson and D. Flanders, 'Compact ultrafast reflective Fabry-Perot tunable lasers for OCT imaging applications', ed. by J. A. Izatt, J. G. Fujimoto and V. V. Tuchin, *Optical Coherence Tomography and Coherence Domain Optical Methods in Biomedicine XIV*, vol. 7554, SPIE, 75541F–75541F–6, (2010), DOI: 10.1117/12.842567

[128] S. O'Connor, M. A. Bernacil and D. Derickson, 'Generation of high speed, linear wavelength sweeps using sampled grating distributed Bragg reflector lasers', *LEOS 2008 - 21st Annual Meeting of the IEEE Lasers and Electro-Optics Society*, IEEE, pp. 147–148, (2008), DOI: 10.1109/LEOS.2008.4688531

[129] M. P. Minneman, J. Ensher, M. Crawford and D. Derickson, 'All-semiconductor high-speed akinetic swept-source for OCT', ed. by J. Popp, *Optical Sensors and Biophotonics III*, vol. 8311, SPIE, pp. 831116–831116–10, (2011), DOI: 10.1117/12.912119

[130] J. Ensher, P. Boschert, K. Featherston, J. Huber, M. Crawford, M. Minneman, C. Chiccone and D. Derickson, 'Long coherence length and linear sweep without an external optical k-clock in a monolithic semiconductor laser for inexpensive optical coherence tomography', ed. by J. A. Izatt, J. G. Fujimoto and V. V. Tuchin, *Optical Coherence Tomography and Coherence Domain Optical Methods in Biomedicine XVI*, vol. 8213, SPIE, p. 7, (2012), DOI: 10.1117/12.911477

[131] M. Minneman, J. Ensher, M. Crawford, M. Bonesi et al., 'Akinetik Swept Sources', *Optical Coherence Tomography: Technology and Applications*, ed. by W. Drexler and J. G. Fujimoto, Springer International Publishing, Cham, pp. 687–739, ISBN: 978-3-319-06419-2, DOI: 10.1007/978-3-319-06419-2_24

[132] M. Minneman, J. Ensher, M. Crawford, M. Bonesi et al., 'Akinetik Swept Sources', ed. by W. Drexler and J. G. Fujimoto, *Optical Coherence Tomo-*

graphy: Technology and Applications, Springer International Publishing, Cham, pp. 687–739, (2015), ISBN: 978-3-319-06419-2, DOI: 10.1007/978-3-319-06419-2_24

[133] W. Drexler and J. G. Fujimoto, eds., *Optical Coherence Tomography - Technology and Applications | Wolfgang Drexler | Springer*, vol. vol. 1, chap. 11, ISBN: 978-3-319-06418-5

[134] J. D. Ellis, *Field Guide to Displacement Measuring Interferometry*, SPIE, ISBN: 978-0-8194-9800-7, DOI: 10.1117/3.1002328

[135] C. E. Saxer, J. F. d. Boer, B. H. Park, Y. Zhao, Z. Chen and J. S. Nelson, 'High-speed fiber–based polarization-sensitive optical coherence tomography of in vivo human skin', *Optics Letters*, vol. 25, no. 18, pp. 1355–1357, (2000), DOI: 10.1364/OL.25.001355

[136] B. J. Vakoc, S. H. Yun, J. F. d. Boer, G. J. Tearney and B. E. Bouma, 'Phase-resolved optical frequency domain imaging', *Optics Express*, vol. 13, no. 14, pp. 5483–5493, (2005), DOI: 10.1364/OPEX.13.005483

[137] F. Delorme, H. Nakajima, C. Alletru, S. Slempkes and B. Pierre, 'A new distributed Bragg reflector laser for improved tuning', *IEEE Photonics Technology Letters*, vol. 6, no. 9, pp. 1085–1087, (1994), DOI: 10.1109/68.324676

[138] A. Dhalla, D. Nankivil and J. A. Izatt, 'Complex conjugate resolved heterodyne swept source optical coherence tomography using coherence revival', *Biomedical Optics Express*, vol. 3, no. 3, pp. 633–649, (2012), DOI: 10.1364/BOE.3.000633

[139] J. Kim, D. T. Miller, E. Kim, S. Oh, J. Oh and T. E. Milner, 'Optical coherence tomography speckle reduction by a partially spatially coherent source', *Journal of Biomedical Optics*, vol. 10, no. 6, pp. 064034–064034–9, (2005), DOI: 10.1117/1.2138031

[140] G. J. Tearney, E. A. Swanson, J. G. Fujimoto, B. E. Bouma, S. A. Boppart and B. Golubovic, 'Rapid acquisition of in vivo biological images by use of optical coherence tomography', *Optics Letters*, vol. 21, no. 17, pp. 1408–1410, (1996), DOI: 10.1364/OL.21.001408

[141] S. H. Yun, G. J. Tearney, B. J. Vakoc, M. Shishkov et al., 'Comprehensive volumetric optical microscopy in vivo', *Nature Medicine*, vol. 12, no. 12, pp. 1429–1433, (2006), DOI: 10.1038/nm1450

[142] G. J. Tearney, S. Waxman, M. Shishkov, B. J. Vakoc et al., 'Three-Dimensional Coronary Artery Microscopy by Intracoronary Optical Frequency Domain Imaging', *JACC: Cardiovascular Imaging*, vol. 1, no. 6, pp. 752–761, (2008), DOI: 10.1016/j.jcmg.2008.06.007

[143] B. Liu and M. E. Brezinski, 'Theoretical and practical considerations on detection performance of time domain, Fourier domain, and swept source optical coherence tomography', *Journal of Biomedical Optics*, vol. 12, no. 4, pp. 044007–044007–12, (2007), DOI: 10.1117/1.2753410

[144] S. Yazdanfar, C. Yang, M. V. Sarunic and J. A. Izatt, 'Frequency estimation precision in Doppler optical coherence tomography using the Cramer-Rao lower bound', *Optics Express*, vol. 13, no. 2, pp. 410–416, (2005), DOI: 10.1364/OPEX.13.000410

[145] S. H. Yun, G. J. Tearney, J. F. d. Boer, N. Iftimia and B. E. Bouma, 'High-speed optical frequency-domain imaging', *Optics Express*, vol. 11, no. 22, pp. 2953–2963, (2003), DOI: 10.1364/OE.11.002953

[146] R. V. Kuranov, A. B. McElroy, N. Kemp, S. Baranov, J. Taber, M. D. Feldman and T. E. Milner, 'Gas-Cell Referenced Swept Source Phase Sensitive Optical Coherence Tomography', *IEEE Photonics Technology Letters*, vol. 22, no. 20, pp. 1524–1526, (2010), DOI: 10.1109/LPT.2010.2055842

[147] E. A. Swanson and S. R. Chinn, 'Method and apparatus for performing optical frequency domain reflectometry', 6160826, E. A. Swanson and S. R. Chinn, 2000

[148] S. L. Miller and D. G. Childers, *Probability and random processes: with applications to signal processing and communications*, 2nd. ed, Academic Press, Boston, MA, 611 pp., ISBN: 978-0-12-386981-4

[149] P. Stoica and R. L. Moses, *Spectral analysis of signals*, Pearson/Prentice Hall, Upper Saddle River, N.J, 452 pp., ISBN: 978-0-13-113956-5

[150] M. Choma, M. Sarunic, C. Yang and J. Izatt, 'Sensitivity advantage of swept source and Fourier domain optical coherence tomography', *Optics Express*, vol. 11, no. 18, p. 2183, (2003), DOI: 10.1364/OE.11.002183

[151] A. Desjardins, B. Vakoc, M. Suter, S.-H. Yun, G. Tearney and B. Bouma, 'Real-Time FPGA Processing for High-Speed Optical Frequency Domain Imaging', *IEEE Transactions on Medical Imaging*, vol. 28, no. 9, pp. 1468–1472, (2009), DOI: 10.1109/TMI.2009.2017740

[152] E. P. Goodwin and J. C. Wyant, *Field Guide to Interferometric Optical Testing (SPIE Field Guide Series Vol. FG10)*, SPIE field guides v. FG10, SPIE Publications, Bellingham, Wash, 100 pp., ISBN: 978-0-8194-6510-8

[153] B. E. Bouma, G. J. Tearney, B. Vakoc and S. H. Yun, 'Optical Frequency Domain Imaging', ed. by W. Drexler and J. G. Fujimoto, *Optical Coherence Tomography: Technology and Applications*, Springer International Publishing, Cham, pp. 225–254, (2015), ISBN: 978-3-319-06419-2, DOI: 10.1007/978-3-319-06419-2_8

[154] M. Duelk and K. Hsu, 'SLEDs and Swept Source Laser Technology for OCT', ed. by W. Drexler and J. G. Fujimoto, *Optical Coherence Tomography: Technology and Applications*, Springer International Publishing, Cham, pp. 527–561, (2015), ISBN: 978-3-319-06419-2, DOI: 10.1007/978-3-319-06419-2_19

[155] J. E. Greivenkamp and S. of Photo-optical Instrumentation Engineers, *Field guide to geometrical optics*, SPIE, Bellingham, Wash. (1000 20th St. Bellingham WA 98225-6705 USA), ISBN: 978-0-8194-7816-0

[156] A. D. Aguirre, C. Zhou, H.-C. Lee, O. O. Ahsen and J. G. Fujimoto, 'Optical Coherence Microscopy', ed. by W. Drexler and J. G. Fujimoto, *Optical Coherence Tomography: Technology and Applications*, Springer International Publishing, Cham, pp. 865–911, (2015), ISBN: 978-3-319-06419-2, DOI: 10.1007/978-3-319-06419-2_29

[157] A. E. Siegman, *Lasers*, University Science Books, Mill Valley, California, ISBN: 978-0-935702-11-8

[158] W. Drexler, Y. Chen, A. D. Aguirre, B. Považay, A. Unterhuber and J. G. Fujimoto, 'Ultrahigh Resolution Optical Coherence Tomography', ed. by W. Drexler and J. G. Fujimoto, *Optical Coherence Tomography: Technology and Applications*, Springer International Publishing, Cham, pp. 277–318, (2015), ISBN: 978-3-319-06419-2, DOI: 10.1007/978-3-319-06419-2_10

[159] I. Grulkowski, J. J. Liu, B. Potsaid, V. Jayaraman, A. E. Cable and J. G. Fujimoto, 'Ultrahigh Speed OCT', ed. by W. Drexler and J. G. Fujimoto, *Optical Coherence Tomography: Technology and Applications*, Springer International Publishing, Cham, pp. 319–356, (2015), ISBN: 978-3-319-06419-2, DOI: 10.1007/978-3-319-06419-2_11

[160] ETSI, *Digital Video Broadcasting (DVB); Specification for the use of Video and Audio Coding in Broadcasting Applications based on the MPEG-2 Transport Stream*, Standard ETSI TS 101 154 V2.4.1, European Telecommunications Standards Institute, 2018

[161] CIPA, *Guideline for Noting Digital Camera Specifications in Catalogs*, tech. rep. CIPA DCG-001-Translation-2014, Camera & Imaging Products Association (CIPA), 2014

[162] H. Nyquist, 'Thermal Agitation of Electric Charge in Conductors', *Physical Review*, vol. 32, no. 1, pp. 110–113, (1928), DOI: 10.1103/PhysRev.32.110

[163] J. B. Johnson, 'Thermal Agitation of Electricity in Conductors', *Physical Review*, vol. 32, no. 1, pp. 97–109, (1928), DOI: 10.1103/PhysRev.32.97

[164] W. Schottky, 'Über spontane Stromschwankungen in verschiedenen Elektrizitätsleitern', *Annalen der physik*, vol. 362, no. 23, pp. 541–567, (1918), DOI: 10.1002/andp.19183622304

[165] H. J. Carmichael, 'Spectrum of squeezing and photocurrent shot noise: a normally ordered treatment', *Journal of the Optical Society of America B: Optical Physics*, vol. 4, no. 10, pp. 1588–1603, (1987), DOI: 10.1364/josab.4.001588

[166] S. Shin, U. Sharma, H. Tu, W. Jung and S. A. Boppart, 'Characterization and Analysis of Relative Intensity Noise in Broadband Optical Sources for Optical Coherence Tomography', *IEEE Photonics Technology Letters*, vol. 22, no. 14, pp. 1057–1059, (2010), DOI: 10.1109/LPT.2010.2050058

[167] W.-C. Kuo, C.-M. Lai, Y.-S. Huang, C.-Y. Chang and Y.-M. Kuo, 'Balanced detection for spectral domain optical coherence tomography', *Optics Express*, vol. 21, no. 16, pp. 19280–19291, (2013), DOI: 10.1364/OE.21.019280

[168] Z. Lu, D. K. Kasaragoda and S. J. Matcher, 'Performance comparison between 8 and 14 bit-depth imaging in polarization-sensitive swept-source optical coherence tomography', ed. by J. G. Fujimoto, J. A. Izatt and V. V. Tuchin, *Optical Coherence Tomography and Coherence Domain Optical Methods in Biomedicine XV*, vol. 7889, SPIE, pp. 7889 - 7889 - 9, (2011), DOI: 10.1117/12.874605

[169] R. J. Adrian, 'Twenty years of particle image velocimetry', *Experiments in Fluids*, vol. 39, no. 2, pp. 159–169, (2005), DOI: 10.1007/s00348-005-0991-7

[170] HDF Group, 'Hierarchical data format, version 5' (2014)

[171] M. Wojtkowski, V. Srinivasan, T. Ko, J. Fujimoto, A. Kowalczyk and J. Duker, 'Ultrahigh-resolution, high-speed, Fourier domain optical coherence tomography and methods for dispersion compensation', *Optics Express*, vol. 12, no. 11, pp. 2404–2422, (2004), DOI: 10.1364/OPEX.12.002404

[172] C. T. Crowe, J. D. Schwarzkopf, M. (of Halle-Wittenberg, G. Sommerfeld and Y. Tsuji, *Multiphase flows with droplets and particles*, ed. by C. T. Crowe, 2nd ed, CRC Press, Boca Raton, 494 pp., ISBN: 978-1-4398-4050-4

[173] C. Tropea, A. L. Yarin and J. F. Foss, eds., *Springer Handbook of Experimental Fluid Mechanics*, Springer handbooks, Springer, Berlin, 1557 pp., ISBN: 978-3-540-30299-5

[174] H. E. Albrecht, M. Borys, N. Damaschke and C. Tropea, *Laser Doppler and Phase Doppler Measurement Techniques*, 1st ed., Experimental Fluid Mechanics, Springer-Verlag Berlin Heidelberg, 756 pp., ISBN: 978-3-642-08739-4

[175] M. N. Polyanskiy, *Refractive index database*, URL: https://refractiveindex.info (visited on 23/05/2018)

[176] J. C. Crocker and D. G. Grier, 'Methods of digital video microscopy for colloidal studies', *Journal of colloid and interface science*, vol. 179, no. 1, pp. 298–310, (1996)

[177] D. Allan, T. Caswell, N. Keim and C. van der Wel, *trackpy: Trackpy v0.3.2*, 2016, DOI: 10.5281/zenodo.60550

[178] J. Holmes, 'Theory and applications of multi-beam OCT', *1st Canterbury Workshop on Optical Coherence Tomography and Adaptive Optics*, vol. 7139, International Society for Optics and Photonics, p. 713908, (2008), DOI: 10.1117/12.821006

[179] Z. Li, S. Y. Mak, A. Sauret and H. C. Shum, 'Syringe-pump-induced fluctuation in all-aqueous microfluidic system implications for flow rate accuracy', *Lab on a Chip*, vol. 14, no. 4, pp. 744–749, (2014), DOI: 10.1039/C3LC51176F

[180] W. Zeng, I. Jacobi, D. J. Beck, S. Li and H. A. Stone, 'Characterization of syringe-pump-driven induced pressure fluctuations in elastic microchannels', *Lab on a Chip*, vol. 15, no. 4, pp. 1110–1115, (2015), DOI: 10.1039/C4LC01347F